In Germany, a coronavirus expert becomes explainer-in-chief p. 462

Intrinsically photosensitive retinal ganglion cells pp. 471 & 527

Crises are no excuse: Maintain high scientific standards p. 476

Science

$15

1 MAY 2020

AAAS

SPEEDY CERAMICS

Rapid heating for high-throughput synthesis p. 521

THE BRAIN PRIZE

LADIES AND GENTLEMEN, THE WINNERS ARE...

Professor Huda Zoghbi
Baylor College of Medicine, USA

Professor Sir Adrian Bird
University of Edinburgh, UK

The Brain Prize 2020 is awarded to Professor Huda Zoghbi and Sir Adrian Bird for their fundamental and pioneering work on Rett syndrome. Their work established the importance of epigenetic regulation in both brain development and the maintenance of normal adult brain function. It also points to novel opportunities for treatment of this and other neurodevelopmental disorders.

THE BRAIN PRIZE SELECTION COMMITTEE

Richard Morris, United Kingdom – Chairman
Story Landis, USA – Vice-Chairwoman
Catherine Dulac, USA
Geoffrey Donnan, Australia
Irene Tracey, United Kingdom
Joseph Coyle, USA
Mu-ming Poo, China
Ole Petter Ottersen, Sweden
Philip Scheltens, The Netherlands

LUNDBECK FOUNDATION

CONTENTS

1 MAY 2020 • VOLUME 368 • ISSUE 6490

PHOTO: VOLKER LANNERT

QQ群: 970508760

NEWS

IN BRIEF

452 News at a glance

IN DEPTH

455 The mystery of the pandemic's 'happy hypoxia'
Doctors debate how to treat patients with low blood oxygen but without trouble breathing
By J. Couzin-Frankel

456 COVID-19 shot protects monkeys
Vaccine from Chinese firm uses old-fashioned "killed" virus *By J. Cohen*

457 Scientists discover upsides of virtual meetings
As the COVID-19 pandemic pushes conferences online, audiences grow *By M. Price*

458 Critics say EPA's 'transparency' rules would favor industry
Agency could consider studies available only by cumbersome Freedom of Information Act requests *By J. Mervis*

459 Carbon dioxide increase may promote 'insect apocalypse'
Study links low-nutrient plants to fewer grasshoppers *By E. Pennisi*

460 Autistic people take the helm of studies
Trend brings new focus on well-being of autistic adults *By E. Willingham*

461 Cancer DNA blood test gets real-world trial
Early detection test spots tumors in 26 women, but also produces false positives *By J. Kaiser*
PODCAST

FEATURES

462 The coronavirus czar
The COVID-19 pandemic has made German virologist Christian Drosten an unlikely cult figure *By K. Kupferschmidt*

INSIGHTS

PERSPECTIVES

466 What future awaits the Sun?
Stellar data question the notion that the Sun is stemming its magnetic activity cycle
By Â. R. G. Santos and S. Mathur
REPORT p. 518

467 Profiling prostate biology
Prostate luminal secretory cells can function as facultative stem cells *By K. Kelly*
RESEARCH ARTICLE p. 497

469 π^0 decay precision-tests the chiral anomaly
More precise neutral pion lifetime measurements probe quantum symmetry breaking *By H. B. Meyer*
REPORT p. 506

470 Exercised cytokines promote endurance
Muscle tissue secretory response to exercise promotes beneficial metabolism
By J. C. Correia and J. L. Ruas
RESEARCH ARTICLE p. 488

471 Dampening light sensitivity
An inhibitory signal from the retina limits the response to light
By J. Ding and W. Wei
REPORT p. 527

473 Cytokine release syndrome in severe COVID-19
Lessons from arthritis and cell therapy in cancer patients point to therapy for severe disease
By J. B. Moore and C. H. June

475 Philip W. Anderson (1923–2020)
Intellectual giant of condensed matter physics
By P. A. Lee and N. P. Ong

POLICY FORUM

476 Against pandemic research exceptionalism
Crises are no excuse for lowering scientific standards *By A. J. London and J. Kimmelman*

BOOKS *ET AL.*

478 Tinctures of time and Schrödinger's virus
Literature and science converge in a pandemic *By L. Campos*

480 The other public health crisis
Social connection is critical, but many struggle to form and maintain meaningful relationships *By J. Schug*

LETTERS

481 Brazil policy invites marine invasive species
By R. J. Miranda et al.

481 Brazil threatens indigenous lands
By L. Ferrante and P. M. Fearnside

482 Call for transparency of COVID-19 models
By C. M. Barton et al.

483 Errata

RESEARCH

IN BRIEF

484 From *Science* and other journals

REVIEW

487 Antimicrobial peptides
Antimicrobial peptides: Application informed by evolution *B. P. Lazzaro* et al.
REVIEW SUMMARY; FOR FULL TEXT: DX.DOI.ORG/10.1126/SCIENCE.AAU5480

RESEARCH ARTICLES

488 Immunometabolism
Interleukin-13 drives metabolic conditioning of muscle to endurance exercise
N. H. Knudsen et al.
RESEARCH ARTICLE SUMMARY; FOR FULL TEXT: DX.DOI.ORG/10.1126/SCIENCE.AAT3987
PERSPECTIVE p. 470

489 Coronavirus
Substantial undocumented infection facilitates the rapid dissemination of novel coronavirus (SARS-CoV-2) *R. Li* et al.

493 Coronavirus
The effect of human mobility and control measures on the COVID-19 epidemic in China
M. U. G. Kraemer et al.

497 Tissue regeneration
Regenerative potential of prostate luminal cells revealed by single-cell analysis
W. R. Karthaus et al.
PERSPECTIVE p. 467

REPORTS

506 Nuclear physics
Precision measurement of the neutral pion lifetime *I. Larin* et al.
PERSPECTIVE p. 469

510 Nanophotonics
Three-dimensional cross-nanowire networks recover full terahertz state
K. Peng et al.

513 Catalysis
Water-promoted interfacial pathways in methane oxidation to methanol on a CeO_2-Cu_2O catalyst
Z. Liu et al.

518 Stellar physics
The Sun is less active than other solar-like stars *T. Reinhold* et al.
PERSPECTIVE p. 466; PODCAST

521 Ceramics
A general method to synthesize and sinter bulk ceramics in seconds
C. Wang et al.

527 Neuroscience
A noncanonical inhibitory circuit dampens behavioral sensitivity to light *T. Sonoda* et al.
PERSPECTIVE p. 471

532 Superconductivity
Ferromagnetic order beyond the superconducting dome in a cuprate superconductor *T. Sarkar* et al.

534 Mesoscopic physics
Evidence for an edge supercurrent in the Weyl superconductor $MoTe_2$ *W. Wang* et al.

DEPARTMENTS

445 Editorial
COVID-19 amidst Ebola's retreat
By John Ditekemena

447 Editorial
A COVID-19 recovery for climate
By Daniel Rosenbloom and Jochen Markard

542 Working Life
Clocking your work *By Anouschka Foltz*

ON THE COVER

Heat from two carbon strips surrounding an oxide mixture sinters the particles into a dense ceramic composite. Conventional ceramic sintering techniques are limited by long processing times and poor compositional control. To overcome these constraints, an ultrafast high-temperature sintering method has been developed to fabricate ceramic materials from oxide precursors in ~10 seconds, enabling rapid screening and discovery of high-performance ceramics. See page 521.
Image: Jiaqi Dai and Liangbing Hu

Science Staff 446
Science Careers 538

SCIENCE (ISSN 0036-8075) is published weekly on Friday, except last week in December, by the American Association for the Advancement of Science, 1200 New York Avenue, NW, Washington, DC 20005. Periodicals mail postage (publication No. 484460) paid at Washington, DC, and additional mailing offices. Copyright © 2020 by the American Association for the Advancement of Science. The title SCIENCE is a registered trademark of the AAAS. Domestic individual membership, including subscription (12 months): $165 ($74 allocated to subscription). Domestic institutional subscription (51 issues): $2148; Foreign postage extra: Air assist delivery: $98. First class, airmail, student, and emeritus rates on request. Canadian rates with GST available upon request, GST #125488122. Publications Mail Agreement Number 1069624. **Printed in the U.S.A.**
Change of address: Allow 4 weeks, giving old and new addresses and 8-digit account number. **Postmaster:** Send change of address to AAAS, P.O. Box 96178, Washington, DC 20090–6178. **Single-copy sales:** $15 each plus shipping and handling available from backissues.sciencemag.org; bulk rate on request. **Authorization to reproduce** material for internal or personal use under circumstances not falling within the fair use provisions of the Copyright Act can be obtained through the Copyright Clearance Center (CCC), www.copyright.com. The identification code for *Science* is 0036-8075. *Science* is indexed in the *Reader's Guide to Periodical Literature* and in several specialized indexes.

PHOTO: KLEIN AND HUBERT/MINDEN PICTURES

EDITORIAL

COVID-19 amidst Ebola's retreat

In April, the Democratic Republic of the Congo (DRC) was on the verge of good news—announcing an end to its tenth (and the world's second largest) Ebola outbreak. Unfortunately, since 10 April, new Ebola cases have been reported in Beni, the epicenter of the Ebola outbreak. Although the DRC has long struggled with political unrest, armed conflict, poverty, and infectious diseases, it must remain committed to ending the Ebola crisis while also applying the lessons learned in tackling this old viral enemy to combat a new one—severe acute respiratory syndrome–coronavirus 2 (SARS-CoV-2), the cause of coronavirus disease 2019 (COVID-19).

Reported cases of COVID-19 in the DRC so far (442 cases, 28 deaths) are probably underestimations given the lack of testing in a country whose weak health system serves 89 million people. The perception of COVID-19's impact among the DRC Congolese is likely to be dwarfed by their experience with the more lethal Ebola virus (2279 deaths among 3461 infected since August 2018). As less than 5% of the DRC's 59,000-km network of roads are usable, the expansion of COVID-19 to rural provinces may be slow. But once COVID-19 gains a strong foothold in the DRC, its elimination could take much longer.

> "...once COVID-19 gains a strong foothold... its elimination could take much longer."

A major lesson learned from the DRC's response to Ebola is that people's distrust of authorities and outsiders can delay responses to disease. Illegal poaching and lumber trade, mining, and war-related displacement of people to Congo's rain forests likely damaged the forest in ways that increased contact between people and animal reservoirs of Ebola virus. The Congolese became increasingly wary of authorities and others who were stripping resources and stoking corruption, violence, and poverty. Health workers had to establish local trust through clear communication and transparency about the disease and treatments. Eventually, the Congolese were open to a vaccination campaign and other measures that brought the current outbreak under control.

But there is an air of optimism in and about the DRC. The near successful campaign against Ebola, the first peaceful democratic transition of power in 2019, economic growth over the past 2 years, and anticorruption reforms aimed at individuals and industries have been positive changes for the nation. The new government must launch a strong response to COVID-19 without compromising the last leg of the Ebola response. Indeed, the system developed for managing Ebola is now being absorbed by the COVID-19 task force.

How can this be accomplished? Public–private partnerships such as the DRC's Investment Promotion fund can upgrade labs and test centers and pay for test kits. Existing internationally funded programs such as those from the World Bank, African Development Bank, and World Health Organization, could be leveraged until additional COVID-19 funds can be acquired. Last month, the government announced a new National Solidarity Fund against COVID-19 that includes representation by the religious sector, a welcome step that should be duplicated for other outbreaks. Hand-washing stations must be created and the importance of face covering must be communicated by authorities and health workers. Only 4% of the 11 million residents of Kinshasa follow the latter recommendation. The DRC's Ebola contact tracing experts and field epidemiology graduates can train volunteer university students to carry out COVID-19 contact tracing. Similarly, surge capacity can be developed through intensive training of graduates of medical (>2000/year), nursing (>7000/year), and laboratory technical schools to boost testing and to triage patients. Increasing temporary bed capacity to isolate the ill (in school and university buildings) should be considered.

The DRC government must also address pandemic-induced economic hardships—that is, the loss of daily wages for the 73% of the population who survive on less than $1.90 a day, as businesses, farming, and other livelihoods begin to close. Private sector food banks have emerged, but they should be sustained by government engagement with the private sector and the United Nations World Food Programme. The United Nations Organization Stabilization Mission in the Democratic Republic of the Congo (MONUSCO) and DRC's defense infrastructure can jointly help facilitate distribution.

Difficult days are ahead for the DRC in its fight against Ebola and COVID-19, in addition to measles, malaria, and cholera. This is a time for national unity and optimism and partnerships with the global community to ensure that disease threats are faced head-on.

–John Ditekemena*

PHOTO: ERIC BOND

John Ditekemena is an associate professor at Kinshasa School of Public Health, University of Kinshasa, Democratic Republic of the Congo. john.ditekemena@unikin.ac.cd

*I thank S.H. Ebrahim for helpful input on this commentary.

10.1126/science.abc4859

Science AAAS

Editor-in-Chief Holden Thorp, hthorp@aaas.org

Executive Editor Monica M. Bradford

Editors, Research Valda Vinson, Jake S. Yeston **Editor, Insights** Lisa D. Chong

DEPUTY EDITORS Julia Fahrenkamp-Uppenbrink (UK), Stella M. Hurtley (UK), Phillip D. Szuromi, Sacha Vignieri **SR. EDITORIAL FELLOW** Andrew M. Sugden (UK) **SR. EDITORS** Gemma Alderton (UK), Caroline Ash (UK), Brent Grocholski, Pamela J. Hines, Paula A. Kiberstis, Marc S. Lavine (Canada), Steve Mao, Ian S. Osborne (UK), Beverly A. Purnell, L. Bryan Ray, H. Jesse Smith, Keith T. Smith (UK), Jelena Stajic, Peter Stern (UK), Valerie B. Thompson, Brad Wible, Laura M. Zahn **ASSOCIATE EDITORS** Michael A. Funk, Priscilla N. Kelly, Tage S. Rai, Seth Thomas Scanlon (UK), Yury V. Suleymanov **LETTERS EDITOR** Jennifer Sills **LEAD CONTENT PRODUCTION EDITORS** Harry Jach, Lauren Kmec **CONTENT PRODUCTION EDITORS** Amelia Beyna, Jeffrey E. Cook, Chris Filiatreau, Julia Katris, Nida Masiulis, Suzanne M. White **SR. EDITORIAL COORDINATORS** Carolyn Kyle, Beverly Shields **EDITORIAL COORDINATORS** Aneera Dobbins, Joi S. Granger, Jeffrey Hearn, Lisa Johnson, Maryrose Madrid, Ope Martins, Shannon McMahon, Jerry Richardson, Hilary Stewart (UK), Alana Warnke, Alice Whaley (UK), Anita Wynn **PUBLICATIONS ASSISTANTS** Jeremy Dow, Alexander Kief, Ronmel Navas, Brian White **EXECUTIVE ASSISTANT** Jessica Slater **ASI DIRECTOR, OPERATIONS** Janet Clements (UK) **ASI SR. OFFICE ADMINISTRATOR** Jessica Waldock (UK)

News Editor Tim Appenzeller

NEWS MANAGING EDITOR John Travis **INTERNATIONAL EDITOR** Martin Enserink **DEPUTY NEWS EDITORS** Elizabeth Culotta, Lila Guterman, David Grimm, Eric Hand (Europe), David Malakoff **SR. CORRESPONDENTS** Daniel Clery (UK), Jon Cohen, Jeffrey Mervis, Elizabeth Pennisi **ASSOCIATE EDITORS** Jeffrey Brainard, Catherine Matacic **NEWS REPORTERS** Adrian Cho, Jennifer Couzin-Frankel, Jocelyn Kaiser, Kelly Servick, Robert F. Service, Erik Stokstad, Paul Voosen, Meredith Wadman **INTERNS** Eva Frederick, Rodrigo Perez Ortega **CONTRIBUTING CORRESPONDENTS** Warren Cornwall, Ann Gibbons, Mara Hvistendahl, Sam Kean, Eli Kintisch, Kai Kupferschmidt (Berlin), Andrew Lawler, Mitch Leslie, Eliot Marshall, Virginia Morell, Dennis Normile (Shanghai), Elisabeth Pain (Careers), Charles Piller, Michael Price, Tania Rabesandratana (Barcelona), Emily Underwood, Gretchen Vogel (Berlin), Lizzie Wade (Mexico City) **CAREERS** Donisha Adams, Rachel Bernstein (Editor), Katie Langin (Acting Editor) **COPY EDITORS** Julia Cole (Senior Copy Editor), Cyra Master (Copy Chief) **ADMINISTRATIVE SUPPORT** Meagan Weiland

Creative Director Beth Rakouskas

DESIGN MANAGING EDITOR Marcy Atarod **GRAPHICS MANAGING EDITOR** Alberto Cuadra **PHOTOGRAPHY MANAGING EDITOR** William Douthitt **WEB CONTENT STRATEGY MANAGER** Kara Estelle-Powers **SENIOR DESIGNER** Chrystal Smith **DESIGNER** Christina Aycock **GRAPHICS EDITOR** Nirja Desai **INTERACTIVE GRAPHICS EDITOR** Xing Liu **SENIOR SCIENTIFIC ILLUSTRATORS** Valerie Altounian, Chris Bickel **SCIENTIFIC ILLUSTRATOR** Alice Kitterman **SENIOR GRAPHICS SPECIALISTS** Holly Bishop, Nathalie Cary **SENIOR PHOTO EDITOR** Emily Petersen **PHOTO EDITOR** Kaitlyn Dolan

Chief Executive Officer and Executive Publisher Sudip Parikh

Publisher, Science Family of Journals Bill Moran

DIRECTOR, BUSINESS SYSTEMS AND FINANCIAL ANALYSIS Randy Yi **DIRECTOR, BUSINESS OPERATIONS & ANALYSIS** Eric Knott **DIRECTOR OF ANALYTICS** Enrique Gonzales **MANAGER, BUSINESS OPERATIONS** Jessica Tierney **SENIOR BUSINESS ANALYST** Cory Lipman, Meron Kebede **FINANCIAL ANALYST** Alexander Lee **ADVERTISING SYSTEM ADMINISTRATOR** Tina Burks **SENIOR SALES COORDINATOR** Shirley Young **DIGITAL/PRINT STRATEGY MANAGER** Jason Hillman **QUALITY TECHNICAL MANAGER** Marcus Spiegler **ASSISTANT MANAGER DIGITAL/PRINT** Rebecca Doshi **SENIOR CONTENT SPECIALISTS** Steve Forrester, Jacob Hedrick, Antoinette Hodal, Lori Murphy **DIGITAL PRODUCTION MANAGER** Lisa Stanford **CONTENT SPECIALIST** Kimberley Oster **ADVERTISING PRODUCTION OPERATIONS MANAGER** Deborah Tompkins **DESIGNER, CUSTOM PUBLISHING** Jeremy Huntsinger **SR. TRAFFIC ASSOCIATE** Christine Hall **SPECIAL PROJECTS ASSOCIATE** Sarah Dhere

ASSOCIATE DIRECTOR, BUSINESS DEVELOPMENT Justin Sawyers **GLOBAL MARKETING MANAGER** Allison Pritchard **DIGITAL MARKETING MANAGER** Aimee Aponte **JOURNALS MARKETING MANAGER** Shawana Arnold **MARKETING ASSOCIATES** Tori Velasquez, Mike Romano, Ashley Hylton **DIGITAL MARKETING SPECIALIST** Asleigh Rojanavongse **SENIOR DESIGNER** Kim Huynh

DIRECTOR AND SENIOR EDITOR, CUSTOM PUBLISHING Sean Sanders **ASSISTANT EDITOR, CUSTOM PUBLISHING** Jackie Oberst

DIRECTOR, PRODUCT & PUBLISHING DEVELOPMENT Chris Reid **DIRECTOR, BUSINESS STRATEGY AND PORTFOLIO MANAGEMENT** Sarah Whalen **ASSOCIATE DIRECTOR, PRODUCT MANAGMENT** Kris Bishop **SR. PRODUCT ASSOCIATE** Robert Koepke **DIGITAL PRODUCT STRATEGIST** Michael Hardesty **SPJ ASSOCIATE** Samantha Bruno Fuller

DIRECTOR, INSTITUTIONAL LICENSING Iquo Edim **ASSOCIATE DIRECTOR, RESEARCH & DEVELOPMENT** Elisabeth Leonard **MARKETING MANAGER** Kess Knight **SENIOR INSTITUTIONAL LICENSING MANAGER** Ryan Rexroth **INSTITUTIONAL LICENSING MANAGER** Marco Castellan **MANAGER, AGENT RELATIONS & CUSTOMER SUCCESS** Judy Lillibridge **SENIOR OPERATIONS ANALYST** Lana Guz **FULFILLMENT COORDINATOR** Melody Stringer **SALES COORDINATOR** Josh Haverlock

DIRECTOR, GLOBAL SALES Tracy Holmes **US EAST COAST AND MID WEST SALES** Stephanie O'Connor **US WEST COAST SALES** Lynne Stickrod **US SALES MANAGER, SCIENCE CAREERS** Claudia Paulsen-Young **US SALES REP, SCIENCE CAREERS** Tracy Anderson **ASSOCIATE DIRECTOR, ROW** Roger Goncalves **SALES REP, ROW** Sarah Lelarge **SALES ADMIN ASSISTANT, ROW** Bryony Cousins **DIRECTOR OF GLOBAL COLLABORATION AND ACADEMIC PUBLISHING RELATIONS, ASIA** Xiaoying Chu **ASSOCIATE DIRECTOR, INTERNATIONAL COLLABORATION** Grace Yao **SALES MANAGER** Danny Zhao **MARKETING MANAGER** Kilo Lan **ASCA CORPORATION, JAPAN** Kaoru Sasaki (Tokyo), Miyuki Tani (Osaka) **COLLABORATION/CUSTOM PUBLICATIONS/JAPAN** Adarsh Sandhu

DIRECTOR, COPYRIGHT, LICENSING AND SPECIAL PROJECTS Emilie David **RIGHTS AND LICENSING COORDINATOR** Jessica Adams **RIGHTS AND PERMISSIONS ASSOCIATE** Elizabeth Sandler **CONTRACTS AND LICENSING ASSOCIATE** Lili Catlett

---

MAIN HEADQUARTERS
Science/AAAS
1200 New York Ave. NW
Washington, DC 20005

SCIENCE INTERNATIONAL
Clarendon House
Clarendon Road
Cambridge, CB2 8FH, UK

SCIENCE CHINA
Room 1004, Culture Square
No. 59 Zhongguancun St.
Haidian District, Beijing, 100872

SCIENCE JAPAN
ASCA Corporation
Sibaura TY Bldg. 4F, 1-14-5
Shibaura Minato-ku
Tokyo, 108-0073 Japan

EDITORIAL
science_editors@aaas.org

NEWS
science_news@aaas.org

INFORMATION FOR AUTHORS
sciencemag.org/authors/science-information-authors

REPRINTS AND PERMISSIONS
sciencemag.org/help/reprints-and-permissions

MEDIA CONTACTS
scipak@aaas.org

MULTIMEDIA CONTACTS
SciencePodcast@aaas.org
ScienceVideo@aaas.org

INSTITUTIONAL SALES AND SITE LICENSES
sciencemag.org/librarian

PRODUCT ADVERTISING & CUSTOM PUBLISHING
advertising.sciencemag.org/products-services
science_advertising@aaas.org

CLASSIFIED ADVERTISING
advertising.sciencemag.org/science-careers
advertise@sciencecareers.org

JOB POSTING CUSTOMER SERVICE
employers.sciencecareers.org
support@sciencecareers.org

MEMBERSHIP AND INDIVIDUAL SUBSCRIPTIONS
sciencemag.org/subscriptions

MEMBER BENEFITS
aaas.org/membercentral

AAAS BOARD OF DIRECTORS
CHAIR Steven Chu
PRESIDENT Claire M. Fraser
PRESIDENT-ELECT Susan G. Amara
TREASURER Carolyn N. Ainslie
CHIEF EXECUTIVE OFFICER Sudip Parikh
BOARD Cynthia M. Beall, Rosina M. Bierbaum, Ann Bostrom, Stephen P.A. Fodor, S. James Gates, Jr., Laura H. Greene, Kaye Husbands Fealing, Maria M. Klawe, Robert B. Millard, Alondra Nelson, William D. Provine

Science serves as a forum for discussion of important issues related to the advancement of science by publishing material on which a consensus has been reached as well as including the presentation of minority or conflicting points of view. Accordingly, all articles published in *Science*—including editorials, news and comment, and book reviews—are signed and reflect the individual views of the authors and not official points of view adopted by AAAS or the institutions with which the authors are affiliated.

BOARD OF REVIEWING EDITORS (Statistics board members indicated with **(S)**)

Adriano Aguzzi, *U. Hospital Zürich*
Takuzo Aida, *U. of Tokyo*
Leslie Aiello, *Wenner-Gren Foundation*
Judith Allen, *U. of Manchester*
Sebastian Amigorena, *Institut Curie*
James Analytis, *U. of California, Berkeley*
Paola Arlotta, *Harvard U.*
Johan Auwerx, *EPFL*
David Awschalom, *U. of Chicago*
Clare Baker, *U. of Cambridge*
Nenad Ban, *ETH Zürich*
Franz Bauer, *Pontificia Universidad Católica de Chile*
Ray H. Baughman, *U. of Texas at Dallas*
Peter Bearman, *Columbia U.*
Carlo Beenakker, *Leiden U.*
Yasmine Belkaid, *NIAID, NIH*
Philip Benfey, *Duke U.*
Gabriele Bergers, *VIB*
Bradley Bernstein, *Mass. General Hospital*
Alessandra Biffi, *Harvard Med. School*
Peer Bork, *EMBL*
Chris Bowler, *École Normale Supérieure*
Ian Boyd, *U. of St. Andrews*
Emily Brodsky, *U. of California, Santa Cruz*
Ron Brookmeyer, *U. of California, Los Angeles* **(S)**
Christian Büchel, *UKE Hamburg*
Dennis Burton, *Scripps Research*
Carter Tribley Butts, *U. of California, Irvine*
György Buzsáki, *New York U. School of Med.*
Blanche Capel, *Duke U.*
Annmarie Carlton, *U. of California, Irvine*
Nick Chater, *U. of Warwick*
Zhijian Chen, *UT Southwestern Med. Ctr.*
Ib Chorkendorff, *Denmark TU*
James J. Collins, *MIT*
Robert Cook-Deegan, *Arizona State U.*
Alan Cowman, *Walter & Eliza Hall Inst.*
Carolyn Coyne, *U. of Pittsburgh*
Roberta Croce, *VU Amsterdam*
Jeff L. Dangl, *U. of North Carolina*
Tom Daniel, *U. of Washington*
Chiara Daraio, *Caltech*
Nicolas Dauphas, *U. of Chicago*
Frans de Waal, *Emory U.*
Claude Desplan, *New York U.*
Sandra Díaz, *Universidad Nacional de Córdoba*
Ulrike Diebold, *TU Wien*
Hong Ding, *Inst. of Physics, CAS*
Jennifer Dionne, *Stanford U.*
Dennis Discher, *U. of Penn.*
Gerald Dorn, *Washington U. in St. Louis*
Jennifer A. Doudna, *U. of California, Berkeley*
Bruce Dunn, *U. of California, Los Angeles*
William Dunphy, *Caltech*
Christopher Dye, *U. of Oxford*
Todd Ehlers, *U. of Tübingen*
Jennifer Elisseeff, *Johns Hopkins U.*
Tim Elston, *U. of North Carolina*
Andrea Encalada, *U. San Francisco de Quito*
Nader Engheta, *U. of Penn.*
Karen Ersche, *U. of Cambridge*
Barry Everitt, *U. of Cambridge*
Vanessa Ezenwa, *U. of Georgia*
Michael Feuer, *The George Washington U.*
Toren Finkel, *U. of Pittsburgh Med. Ctr.*
Gwenn Flowers, *Simon Fraser U.*
Peter Fratzl, *Max Planck Inst. Potsdam*
Elaine Fuchs, *Rockefeller U.*
Eileen Furlong, *EMBL*
Jay Gallagher, *U. of Wisconsin*
Daniel Geschwind, *U. of California, Los Angeles*
Karl-Heinz Glassmeier, *TU Braunschweig*
Ramon Gonzalez, *U. of South Florida*
Elizabeth Grove, *U. of Chicago*
Nicolas Gruber, *ETH Zürich*
Hua Guo, *U. of New Mexico*
Kip Guy, *U. of Kentucky College of Pharmacy*
Taekjip Ha, *Johns Hopkins U.*
Christian Haass, *Ludwig Maximilians U.*
Sharon Hammes-Schiffer, *Yale U.*
Wolf-Dietrich Hardt, *ETH Zürich*
Louise Harra, *U. College London*
Jian He, *Clemson U.*
Carl-Philipp Heisenberg, *IST Austria*
Ykä Helariutta, *U. of Cambridge*
Janet G. Hering, *Eawag*
Hans Hilgenkamp, *U. of Twente*
Kai-Uwe Hinrichs, *U. of Bremen*
Lora Hooper, *UT Southwestern Med. Ctr.*
Fred Hughson, *Princeton U.*
Randall Hulet, *Rice U.*
Auke Ijspeert, *EPFL*
Akiko Iwasaki, *Yale U.*
Stephen Jackson, *USGS and U. of Arizona*
Kai Johnsson, *EPFL*
Peter Jonas, *IST Austria*
Matt Kaeberlein, *U. of Washington*
William Kaelin Jr., *Dana-Farber Cancer Inst.*
Daniel Kammen, *U. of California, Berkeley*
V. Narry Kim, *Seoul Nat. U.*
Robert Kingston, *Harvard Med. School*
Nancy Knowlton, *Smithsonian Institution*
Etienne Koechlin, *École Normale Supérieure*
Alexander L. Kolodkin, *Johns Hopkins U.*
Julija Krupic, *U. of Cambridge*
Thomas Langer, *Max Planck Inst. Cologne*
Mitchell A. Lazar, *U. of Penn.*
Ottoline Leyser, *U. of Cambridge*
Wendell Lim, *U. of California, San Francisco*
Jianguo Liu, *Michigan State U.*
Luis Liz-Marzán, *CIC biomaGUNE*
Jonathan Losos, *Washington U. in St. Louis*
Ke Lu, *Chinese Acad. of Sciences*
Christian Lüscher, *U. of Geneva*
Jean Lynch-Stieglitz, *Georgia Inst. of Tech.*
Fabienne Mackay, *U. of Melbourne*
Anne Magurran, *U. of St. Andrews*
Oscar Marín, *King's College London*
Charles Marshall, *U. of California, Berkeley*
Christopher Marx, *U. of Idaho*
Geraldine Masson, *CNRS*
C. Robertson McClung, *Dartmouth College*
Rodrigo Medellín, *U. Nacional Autónoma de México*
Graham Medley, *London School of Hygiene & Tropical Med.*
Jane Memmott, *U. of Bristol*
Baoxia Mi, *U. of California, Berkeley*
Edward Miguel, *U. of California, Berkeley*
Tom Misteli, *NCI, NIH*
Yasushi Miyashita, *U. of Tokyo*
Alison Motsinger-Reif, *NIEHS, NIH* **(S)**
Daniel Nettle, *Newcastle U.*
Daniel Neumark, *U. of California, Berkeley*
Beatriz Noheda, *U. of Groningen*
Helga Nowotny, *Vienna Science, Research & Tech. Fund*
Rachel O'Reilly, *U. of Birmingham*
Harry Orr, *U. of Minnesota*
Pilar Ossorio, *U. of Wisconsin*
Andrew Oswald, *U. of Warwick*
Isabella Pagano, *Istituto Nazionale di Astrofisica*
Margaret Palmer, *U. of Maryland*
Elizabeth Levy Paluck, *Princeton U.*
Jane Parker, *Max Planck Inst. Cologne*
Giovanni Parmigiani, *Dana-Farber Cancer Inst.* **(S)**
Samuel Pfaff, *Salk Inst. for Biological Studies*
Julie Pfeiffer, *UT Southwestern Med. Ctr.*
Matthieu Piel, *Institut Curie*
Kathrin Plath, *U. of California, Los Angeles*
Martin Plenio, *Ulm U.*
Katherine Pollard, *U. of California, San Francisco*
Elvira Poloczanska, *Alfred-Wegener-Inst.*
Julia Pongratz, *Ludwig Maximilians U.*
Philippe Poulin, *CNRS*
Jonathan Pritchard, *Stanford U.*
Félix A. Rey, *Institut Pasteur*
Trevor Robbins, *U. of Cambridge*
Joeri Rogelj, *Imperial College London*
Amy Rosenzweig, *Northwestern U.*
Mike Ryan, *U. of Texas at Austin*
Mitinori Saitou, *Kyoto U.*
Shimon Sakaguchi, *Osaka U.*
Miquel Salmeron, *Lawrence Berkeley Nat. Lab*
Nitin Samarth, *Penn. State U.*
Jürgen Sandkühler, *Med. U. of Vienna*
Alexander Schier, *Harvard U.*
Wolfram Schlenker, *Columbia U.*
Susannah Scott, *U. of California, Santa Barbara*
Rebecca Sear, *London School of Hygiene & Tropical Med.*
Vladimir Shalaev, *Purdue U.*
Jie Shan, *Cornell U.*
Beth Shapiro, *U. of California, Santa Cruz*
Jay Shendure, *U. of Washington*
Steve Sherwood, *U. of New South Wales*
Brian Shoichet, *U. of California, San Francisco*
Robert Siliciano, *Johns Hopkins U. School of Med.*
Lucia Sivilotti, *U. College London*
Alison Smith, *John Innes Centre*
Richard Smith, *U. of North Carolina* **(S)**
Mark Smyth, *QIMR Berghofer*
Pam Soltis, *U. of Florida*
John Speakman, *U. of Aberdeen*
Tara Spires-Jones, *U. of Edinburgh*
Allan C. Spradling, *Carnegie Institution for Science*
V. S. Subrahmanian, *Dartmouth College*
Ira Tabas, *Columbia U.*
Sarah Teichmann, *Wellcome Sanger Inst.*
Rocio Titiunik, *Princeton U.*
Shubha Tole, *Tata Inst. of Fundamental Research*
Wim van der Putten, *Netherlands Inst. of Ecology*
Reinhilde Veugelers, *KU Leuven*
Bert Vogelstein, *Johns Hopkins U.*
Kathleen Vohs, *U. of Minnesota*
David Wallach, *Weizmann Inst. of Science*
Jane-Ling Wang, *U. of California, Davis* **(S)**
David Waxman, *Fudan U.*
Jonathan Weissman, *U. of California, San Francisco*
Chris Wikle, *U. of Missouri* **(S)**
Terrie Williams, *U. of California, Santa Cruz*
Ian A. Wilson, *Scripps Research* **(S)**
Yu Xie, *Princeton U.*
Jan Zaanen, *Leiden U.*
Kenneth Zaret, *U. of Penn. School of Med.*
Jonathan Zehr, *U. of California, Santa Cruz*
Xiaowei Zhuang, *Harvard U.*
Maria Zuber, *MIT*

EDITORIAL

A COVID-19 recovery for climate

In response to the coronavirus disease 2019 (COVID-19) pandemic, countries are launching economic recovery programs to mitigate unemployment and stabilize core industries. Although it is understandably difficult to contemplate other hazards in the midst of this outbreak, it is important to remember that we face another major crisis that threatens human prosperity—climate change. Leveraging COVID-19 recovery programs to simultaneously advance the climate agenda presents a strategic opportunity to transition toward a more sustainable post–COVID-19 world.

The climate and COVID-19 crises are global and unprecedented in their level of disruption, and require coordinated responses by policy-makers, businesses, and broader society. But they are also different. The pandemic directly threatens individuals and health systems, whereas climate change undermines broader natural and human systems. COVID-19 requires responses within days and weeks, whereas reactions to the climate crisis appear less acute. Nevertheless, science suggests that climate impacts will worsen the longer we wait. So, we are faced with overlapping crises that require immediate societal mobilization.

Yet, as nations marshall massive resources to mitigate the economic and social impacts of COVID-19, they may be missing the chance to address climate change. Indeed, earlier experiences show that policy responses to major calamities, such as the 2008 global financial crisis and the Millennium drought in Australia, tend to focus on stabilizing incumbent industries, technologies, and practices rather than seizing the opportunity for sustainable transformation.

At this early stage of the pandemic, we are witnessing how worldwide lockdowns have decreased air pollution and greenhouse gas emissions because of reduced transportation, electricity generation, and industrial production. This shows how intertwined modern economic life and fossil fuels have become, and suggests consideration of climate implications in economic recovery plans.

However, there is variation in political responses to COVID-19. The United States has rolled back certain environmental regulations and appears poised to direct stimulus funds toward reinvigorating the fossil fuel industry. The German Council of Economic Experts submitted a 110-page report on the coronavirus crisis without mentioning climate change or sustainability. By contrast, 17 European climate and environment ministers called on the European Commission to make the Green Deal central to the recovery following the pandemic.

Where, then, should we begin to focus in building back jobs and the economy while also transitioning toward a more sustainable future? One strategy would be to use recovery funds to stimulate innovation for the low-carbon energy transition. This might involve promoting new infrastructure, business models, and industrial capacity in renewable energy technology, energy storage, electric vehicles, and charging stations through tax credits and other measures. An example would be supporting the diffusion of electric delivery vehicles, given the rise in e-commerce. But transitioning entire sectors is a long-term endeavor that requires continuous adaptation and attention to context. There may also be opportunities to build on social changes catalyzed by COVID-19 such as remote working, video conferencing, e-commerce, and reduced air travel. Science must explore how such changes can be made durable and contribute to low-carbon pathways.

> **"...COVID-19 recovery... presents a strategic opportunity to transition toward a more sustainable... world."**

A complementary strategy is to harness disruption to accelerate the decline of carbon-intensive industries, technologies, and practices. COVID-19 has temporarily destabilized businesses, economic activity, and consumption. This can be leveraged to accelerate the phase-out of coal-fired power, which is already part of the climate action plans of several countries, including Canada, the United Kingdom, Finland, and Germany. Destabilization has also affected the oil and gas industry, with the price of U.S. oil futures turning negative for the first time in history and global demand for oil estimated to reach a 25-year low. These circumstances can be harnessed to transition away from fossil fuels toward clean alternatives. To drive this change, it is important not to bail out fossil fuel companies and industries. Support must instead flow to affected workers and communities in the form of temporary relief, retraining, and retirement benefits.

COVID-19 recovery programs can lay the foundation for a more sustainable and prosperous future. Nations should not squander this opportunity.

–Daniel Rosenbloom and Jochen Markard

Daniel Rosenbloom is a Social Sciences and Humanities Research Council Postdoctoral Fellow in the Department of Political Science, University of Toronto, Toronto, Ontario, Canada. daniel.rosenbloom@utoronto.ca

Jochen Markard is a senior researcher in the Group of Sustainability and Technology, Department of Management, Technology and Economics, ETH Zurich, Zurich, Switzerland. jmarkard@ethz.ch

10.1126/science.abc4887

CAPITAL CITY, CAPITAL IDEAS: BEIJING AS CHINA'S NATIONAL SCIENCE AND TECHNOLOGY INNOVATION CENTER

If you had to name a city in China where you could find over half of the top scientific experts in the nation, your answer would have to be Beijing. As the capital of China, Beijing has led the nation's development on many fronts, particularly innovation. The city is transforming itself into a national science and technology innovation center.

Science and technology (S&T) is a crucial factor in the development of a nation and of society as a whole. History has shown that scientific revolutions can change the world. Nations that led the most revolutionary scientific advancements, from steam power to electricity, to the emergence of computers and the internet, became global leaders in industry, commerce, and culture. As China grows to become the world's second largest economy, the country also strives to be a superpower in innovation.

Beijing is at the forefront of this scientific revolution. The city has made plans to develop cutting-edge technologies such as 5G, artificial intelligence (AI), and intelligent connected vehicles. It aims to foster key industries in each of its districts and apply the technology they bring to daily management of the city, improving the quality of urban life.

As an innovation center, Beijing will also play the lead role in coordinating development in the surrounding region and the rest of the country. In 2019, agreements made between Beijing, Tianjin city, and Hebei Province totaled RMB 30 billion (USD 4.3 billion). In addition, Beijing strongly supports the Xiong'an New Area, a core development hub of the Beijing–Tianjin–Hebei economic triangle. In Tibet, Xinjiang, and Inner Mongolia, Beijing's technological innovations have lifted many out of poverty. In Xinjiang, technologies that improve soil quality and increase crop yields helped increase the average annual income of over 100 families by RMB 4,950 (USD 704) in 2019.

An open environment

The city is also a pivot point for interaction among some of the world's best S&T institutes. Activities such as the Zhongguancun Forum, the Beijing International Academic Season, the China–Italy Science, Technology and Innovation Week, and the Beijing Design Week form a platform of communication for scientists, entrepreneurs, and investors around the globe. Meanwhile, Beijing has rolled out a plan to advance scientific innovation and interaction as part of the "One Belt, One Road" initiative, a global strategy to develop infrastructure and other projects in several countries, involving multilayer cooperation in S&T. According to the plan, Beijing will foster international conversation and cooperation in scientific innovation, open up its resources to the world, aid local companies to expand overseas, and attract international talent to the city.

As it transforms itself into an S&T hub, Beijing is revising its policies to welcome international talent. As President Xi Jinping put it, innovation should happen in an open environment. "We should never close our doors," he says, "but should leverage the all possibilities, plan, and push forward innovation with a global vision."

The Beijing Municipal Science & Technology Commission (BMSTC) has been the "central nervous system" of strategic planning for Beijing's S&T development, conducting research, communicating

PHOTO: SHUTTERSTOCK/DOUG MCLEAN

Beijing is an innovation hub, as seen from the increasing number of buildings in its skyline.

with stakeholders, and supervising and implementing policies. Since 2017, it has generated detailed annual plans—for as many as 220 projects each year.

Such development has already borne fruit: In 2019, the GDP per person in Beijing surpassed RMB 164,000 (USD 23,617)—the same level as found in some developed countries and regions.

Robust R&D investment

Beijing is among the Chinese cities that provides scientists and entrepreneurs with the most funding, and it is careful about where it invests this money.

R&D investment is the source and motive for innovation. Modest strengthening of R&D investment advances technology and spurs innovation, in turn promoting economic development and enhancing the competitiveness of a city and a country.

In 2018, Beijing invested RMB 187 billion (USD 26.9 billion) in R&D—an increase of 18.4% over the previous year, ranking third in the country. The intensity of R&D investment (ratio of R&D expenditure to regional GDP) was 5.7%, ranking first in the country and surpassing some developed countries.

In addition to the continuous increase in investment, Beijing is also constantly optimizing its R&D funding by attaching greater importance to fundamental science research. The proportion of investment in basic research in the city continues to increase: In 2018, investment in basic research was RMB 27.8 billion (USD 4 billion), about one quarter of the total for the whole country and an increase of 19.5% over the previous year.

Five major fields comprise 96.5% of Beijing's funding. Among them, over half (52.5%) of the investments in 2018 went to scientific research and the technical services industry, while 18.2% went to the telecommunications industry and the software and information technology services industry. The manufacturing and education industries received 14.2% and 11.5%, respectively.

In addition, Beijing's companies are increasing their R&D expenditures in groundbreaking technologies and emerging areas such as 5G, AI, integrated circuits, the Internet of Things, quantum science, big data, and medicine and health. The total enterprise R&D expenditure was RMB 78.1 billion (USD 11.2 billion) in 2018, a 26.2% increase from the previous year.

2019 saw Beijing's efforts rewarded with multiple scientific breakthroughs. Researchers at Peking University invented LEAPER (leveraging endogenous ADAR [adenosine deaminase acting on RNA] for programmable editing of RNA), a new gene-editing technique that increases the efficiency and accuracy of editing defective cells. Scientists at the Institute of Physics, Chinese Academy of Sciences, succeeded in folding a layer of graphene thinner than 0.2 nm, which creates materials with unique features that could function as electronic components in phones and computers. Tsinghua University produced Tianjic, a chip with hybrid coding schemes that not only accommodates machine-learning algorithms, but could also function in brain-inspired circuits. Beijing scientists were responsible for eight of China's top 10 scientific advances for 2019, as announced by the Ministry of Science and Technology on February 27.

Some of the latest technologies, such as AI robots, facial recognition, and 5G data transmission, have been implemented in public infrastructures such as the Daxing International Airport and used for public events such as the 2019 Beijing International Horticultural Exhibition.

Beijing's companies are helping to provide 5G technology for China, as shown in this picture.

PHOTO: BMSTC

Beijing is aiming for a greener, more efficient, and more intelligent development strategy. It is trading scale for quality, and will maintain its strong R&D investments, particularly in these 10 high-tech industries: next-generation IT, integrated circuits, medicine and health, smart equipment, energy saving and environmental protection, future smart cars, new materials, AI, software and information services, and technology services industries.

Drivers of innovation: Academic institutes and enterprises

Beijing's innovation is driven by its many academic institutions and enterprises. The city boasts more than half of the country's top colleges and universities, including Tsinghua University, Peking University, and the Chinese Academy of Sciences. It is also home to numerous domestic and foreign S&T enterprises.

An important contributor to this drive is Beijing's high-tech companies. They are characterized by high-innovation input and output, which play an important supporting role in economic and social development. For example, almost all the city's IT enterprises have invested strategically in AI, which is vital for China's long-term growth. As of today, Beijing has five of the world's top 100 AI companies and 60% of the nation's AI talent.

(TOP) Huairou Science City Earth simulator. (BOTTOM) Design view of the High Energy Photon Source (HEPS) at Huairou Science City.

The high-tech companies currently in Beijing have steadily grown their research teams and R&D input over the past few years. Their R&D investment increased by 41.8% from 2016 to 2018, from RMB 192.6 billion (USD 27.7 billion) to RMB 273 billion (USD 28.8 billion). Meanwhile, the per capita R&D expenditure for S&T personnel increased from RMB 226,700 (USD 32,584) in 2016 to RMB 280,700 (USD 40,345) in 2018, also showing year-on-year growth.

Meanwhile, foreign enterprises and their research teams have become an indispensable part of Beijing's drive to innovate. They directly apply their R&D to the Chinese market and help raise the level of collaboration in the city. Beijing welcomes such efforts and is reinvigorating its policies to help grow S&T innovation. Its policymakers believe a key to speeding the movement of technological innovation from the laboratory to production is to establish policies that provide efficient pathways for such transition—an agenda the city has been working on for years.

National laws, such as the "Law on Promoting the Transformation of Scientific and Technological Achievements," as well as Beijing's own regulations and plans, serve as such pathways. In 2019, Beijing issued the "Regulation of the Beijing Municipality on Promoting the Transformation of Scientific and Technological Achievements," which is the first national policy to make institutional arrangements for the reform of ownership of S&T achievements in the form of local regulations, effectively solving bottleneck problems such as the ownership of those achievements.

With policies such as this, researchers have found it easier to industrialize their innovations. In 2017, Beijing ranked first in China in terms of the total value of contracts signed by scholars at colleges and research institutions for transformation of scientific achievements, reaching RMB 3.3 billion (USD 480 million), according to a 2019 report published by the government-affiliated National Center for Science and Technology Evaluation.

Embracing international talent with friendly policies

A skilled labor force is one of Beijing's greatest advantages—and one of which it is very proud. It has an abundance of experts, along with impressive S&T resources both in terms of quantity and quality. There are more than 90 colleges and universities in Beijing, more than 1,000 scientific research institutes, and more than 180 National Key Laboratories and engineering technology research centers, as well as half of the nation's academicians. About half of the first prizes for national S&T achievements and many of the top 10 S&T advancements are credited to Beijing each year.

Beijing has offered support in three major areas to high-level experts from outside the country:

First, foreign experts enjoy shortened approval times for a permanent stay in China—as short as 50 days—and those who meet certain criteria are allowed to apply for permanent residency (a Chinese green card). For people holding a foreign expert visa, the period of validity is as long as 10 years, and one is allowed to stay in the nation for 180 days consecutively. The visas will be approved on the second day of application and are free. Foreign experts could be exempted for certain

PHOTOS: BMSTC

documents and offline procedures when coming to Beijing for innovative work in fields such as science, finance, and education.

Secondly, the city encourages foreign high-level talent to take the lead in undertaking national S&T projects as well as programs such as the National Natural Science Foundation's Outstanding Youth Program. They can also be nominated for national S&T awards.

Last but not least, the city also takes care of accommodating foreign talent and educating their children. Beijing has fostered international talent communities in Chaoyang District, Zhongguancun Street, Changping's Future Science City, and other areas, so that foreign experts can have full access to medical support, housing, and education. They enjoy the same level of welfare and medical insurance as Beijing citizens do, and are provided translational services at designated hospitals. Their children can choose to enter either public or private schools.

Innovative entrepreneurship: Beijing as an incubation hub

For companies that are looking for a vigorous business environment, Beijing is one of the best choices they could make.

The city has carried out ongoing reforms to make public services more easily accessible to the private sector, alleviating the burden of middle- and small-sized enterprises and facilitating the flow of capital and talent. In the World Bank's 2019 report "Doing Business," Beijing ranks No. 28 in the world, surpassing some European Union countries and Organization for Economic Cooperation and Development (OECD) members. It made the top 30 in indicators such as "starting a business," "getting electricity," "registering property," "protecting minority investors," and "enforcing contracts."

Beijing is developing a more active innovation system, a better innovation ecosystem, and a bigger innovation space. It welcomes world-class S&T companies to come and grow there.

Beijing has a long history of incubation. It launched its first incubator platform, the Beijing High-Tech Start-Up Service Center, 31 years ago in 1989. Since then, it has evolved with time and has now formed a multifield, multimode incubation system that integrates global resources.

At present, there are more than 500 incubators in the city, occupying an area of 5 million square meters. Numerous startups and teams are in incubation, of which 300 are listed companies and 13 are unicorn companies (privately held startup companies valued at USD 1 million). These companies have produced more than 325,000 jobs.

There is no doubt that incubators speed up innovation in Beijing. In 2018, the city's incubating enterprises held 86,112 valid intellectual property rights, an increase of 42.2% over 2017; the total investment obtained in 2018 was RMB 47.8 billion (USD 6.9 billion), an increase of 62.6% over 2017. Incubators and startups have become an important carrier for Beijing to accelerate the implementation of its innovation-driven development strategy.

Science and technology are the future of Beijing. The city is gathering its strength to offer a world-class S&T platform.

Sponsored by

北京市科学技术委员会
Beijing Municipal Science & Technology Commission

PHOTO: BMSTC

Beijing hosted the 2019 Zhongguancun Forum and held a subforum for innovative young talent.

NEWS

> "I have not seen any projections of sea level rise slowing down as a result of the COVID crisis."
>
> **Brian Strong**, chief resilience officer for San Francisco, which is trying to balance the growing cost of the virus with a $5 billion upgrade to its sea wall, in *The New York Times*.

Among those wearing masks last week was Nancy Pelosi (D–CA), speaker of the U.S. House of Representatives, preparing to vote on an economic stimulus measure.

IN BRIEF

Edited by **Jeffrey Brainard**

DISPATCHES FROM THE PANDEMIC

WHO advises against 'passports'

PUBLIC HEALTH | The World Health Organization cautioned governments against introducing documents—"immunity passports"—that declare people immune to COVID-19 after they test positive for antibodies to the new coronavirus. Authorities in some countries had floated the idea that people with such records could return to workplaces and restart stalled economies without worsening the pandemic. But, "There is no evidence that people who have recovered from COVID-19 and have antibodies are protected from a second infection," the agency wrote in a scientific brief issued 24 April. The antibodies, created by the immune system's response to the disease, may not protect well or for long. Some people who seemed to have cleared the virus have later tested positive again. It isn't known whether they suffered a relapse of the original infection or were infected a second time.

More COVID-19 money for NIH

FUNDING | The U.S. National Institutes of Health (NIH) received $1.8 billion last week in the most recent massive stimulus package approved by Congress. That brings the agency's total to $3.6 billion in three recent bills aimed at fighting the coronavirus pandemic and offsetting its economic impact. Legislators hope the new money will speed development and distribution of two kinds of tests: one for quick and easy detection of the virus, and the other for antibodies that presumably confer some protection for those who have recovered from COVID-19. As in the two previous packages, NIH officials were given some flexibility in deciding what kinds of research to support with the new money as well as who can apply for it.

Internet giants track outbreaks

DISEASE MONITORING | Facebook and Google have teamed up with Carnegie Mellon University to map local COVID-19 outbreaks across the United States, the university announced last week. The project's maps, online at covidcast.cmu.edu, are meant to provide fine-grained information about the spread of infections to help state and local policymakers adjust social distancing restrictions, says

PHOTO: ANDREW HARNIK/AP PHOTO

Roni Rosenfeld, a computational epidemiologist at the university. The work could also supplement data from tests for SARS-CoV-2 or antibodies to the virus, he says. Each map plots data from one of five sources: two online surveys conducted by Facebook and Google, anonymized data about Google searches related to COVID-19, influenza testing statistics from test manufacturer Quidel (a proxy for respiratory illness), and nationally reported figures on visits to doctors' offices. This "now-cast" is just a first step, Rosenfeld says: Using machine learning, researchers hope to forecast 4 weeks in advance the demand for intensive care and ventilators for COVID-19 patients.

Chloroquine warning from FDA

DRUG REGULATION | A global debate about the merits of using of two antimalarial drugs touted by President Donald Trump as potential COVID-19 treatments reached a new pitch last week. The U.S. Food and Drug Administration, which last month authorized the emergency use of chloroquine and hydroxychloroquine in COVID-19 patients, advised doctors on 24 April not to prescribe the drugs outside of hospitals or clinical trials, and to monitor patients closely for side effects. The drugs have not yet proved effective against the virus in large clinical trials, and in some patients increase the risk of a heart arrhythmia that can lead to cardiac arrest. Also last week, the Trump administration ousted Rick Bright from his position as director of the Department of Health and Human Services's Biomedical Advanced Research and Development Authority; he said in a statement that he was dismissed for resisting pressure to invest in hydroxychloroquine as a COVID-19 treatment.

Vaccine push makes a billionaire

INNOVATION | Timothy Springer has made some good bets in his life—and his latest windfall will help an institute developing protein therapies. In 1993, the Harvard University molecular biologist turned his research on how white blood cells destroy foreign targets into a biotech company sold 6 years later, earning him a reported $100 million. He invested $5 million in Moderna, a biotech company focused on messenger RNA that went public in 2018, netting Springer a nearly 100-fold return on his investment. Now, the COVID-19 virus has pushed his wealth even higher. Moderna scientists devised a messenger RNA vaccine that prompts cells to make pieces of viral proteins that aim to train immune sentries to recognize the invader. The U.S. Biomedical Advanced Research and Development Authority recently awarded the company nearly $500 million to conduct clinical tests of the vaccine. That has helped the company's stock price more than double during the past 2 months, enough to elevate Springer's worth to more than $1 billion, according to the Bloomberg Billionaires Index. Springer has said he plans to donate most of his money to the Institute for Protein Innovation, an open source hub that he and colleague Andrew Kruse founded in 2017 to design antibodies and other proteins as cures for intractable diseases.

PHOTO: NATIONAL BOBBLEHEAD HALL OF FAME AND MUSEUM

POPULAR CULTURE

Fauci inspires collectors' items

Anthony Fauci's burgeoning fame as a voice for science within White House corridors and beyond reached new heights in April with the release of a raft of merchandise in his honor, including a bobblehead. The for-profit National Bobblehead Hall of Fame and Museum is selling the plastic figurine of Fauci, longtime director of the U.S. National Institute of Allergy and Infectious Diseases, as a fundraiser for COVID-19 masks. Even though Fauci has not attended some recent White House briefings on coronavirus, the Hall of Fame says his bobblehead remains its best-selling ever. Other vendors are selling socks, shirts, prayer candles, and beer emblazoned with Fauci's name and face. "That's nice if people want to do [it]," Fauci said of the blitz during a *Fox & Friends* interview, but "I have other things to worry about." The Hall of Fame is also selling a bobblehead of Deborah Birx, the White House's coronavirus response coordinator.

BY THE NUMBERS

29% Americans staying at home

The 24 April figure marked a downward slide from 35% in mid-March—a sign of fatigue with social distancing requirements, say researchers at the Maryland Transportation Institute at the University of Maryland, College Park. They defined staying at home as no trips more than 1.5 kilometers away from home. The figure is likely to dip further as some states this week began to allow selected businesses to reopen. The Maryland researchers have been using anonymized, aggregated location data from mobile devices and other sources to track travel metrics that include distance and trips per person to quantify the extent of social distancing. The figures, at https://data.covid.umd.edu, are updated daily for each state.

NIH pulls viral origins grant

FUNDING | The U.S. National Institutes of Health (NIH) on 24 April abruptly terminated a long-standing grant to the EcoHealth Alliance (EA), a New York City nonprofit, which has supported research—including by scientists in China—on how viruses spread from bats and other wildlife to humans. The move, first reported by *Politico*, came after the grant was criticized by conservative politicians and media figures who have suggested, without evidence, that the current pandemic was caused by a virus that escaped from the Wuhan Institute of Virology. The institute collaborated with EA on past projects, but EA said it had not given the lab money this year. NIH's order barring the alliance from spending some $370,000 remaining on the grant for 2020 drew criticism from some researchers, who fear it was motivated by political, not scientific, concerns. The pandemic, some noted, has only highlighted the need to better understand how wildlife pathogens can spill into human populations. As *Science* went to press, NIH refused to explain the cancellation, saying policy prevented it from doing so.

SCIENCEMAG.ORG/TAGS/CORONAVIRUS
Read additional *Science* coverage of the pandemic.

PALEONTOLOGY

Society wants ban on Myanmar papers

Paleontologists should not apply their expertise to any amber fossils that have recently emerged from Myanmar, the Society of Vertebrate Paleontology (SVP) said last week. In a 21 April letter, SVP called on journal editors and publishers to stop publishing papers that involve amber specimens purchased since 2017 from sources in Myanmar. That is when the country's military seized control of mining operations in a region that has yielded stunning fossils of 100-million-year-old insects, snakes, birds, and dinosaurs (*Science*, 24 May 2019, p. 722). The military's takeover, in part spurred by the amber riches, killed and displaced thousands of people in what the United Nations has condemned as a crime against humanity, SVP leaders wrote. In the same letter, the society also reminds journals that papers should only describe fossils permanently deposited in a public repository. Even long-term loans of specimens held by private collectors—a common situation with amber specimens—are not enough to guarantee their availability for future research, SVP wrote.

Groundwater gets protections

LEGAL AFFAIRS | The U.S. Supreme Court gave hydrologic science top billing in a closely watched ruling last week affirming that the federal Clean Water Act covers groundwater pollution. In a six-to-three decision, Justice Stephen Breyer wrote for the majority that pollution starting in groundwater could be subject to federal regulations if it drains into protected rivers, lakes, or oceans in a way that is the "functional equivalent" of being poured directly into surface waters. The case revolved around a sewage treatment plant on Maui in Hawaii that pumped treated wastewater into wells, much of which flowed underground into a nearby ocean reef. Maui county and the Trump administration argued the law didn't apply to groundwater. During oral arguments in November 2019, Breyer signaled his confidence in using science to track polluted groundwater, noting that a brief filed by scientists "really convinced me they're geniuses and they can trace all kinds of things."

IN FOCUS An image of a tardigrade, a microscopic animal known as a "water bear," won the Olympus Image of the Year Global Life Science Light Microscopy Award, Americas division. Tardigrades are mostly colorless, so Tagide deCarvalho of the University of Maryland, Baltimore County, used fluorescent dyes to highlight its organs and stomach filled with food.

PHOTO: TAGIDE DECARVALHO/OLYMPUS

In memoriam: Donald Kennedy

LEADERSHIP | Don Kennedy would have blushed at a colleague's tribute as "very close to being a Renaissance man." But it's fitting for a person whose resume included being president of Stanford University, leading the U.S. Food and Drug Administration (FDA), and serving as editor-in-chief of *Science* magazine. "He could talk on any level to people about science, without condescending to them," says Tom Grumbly, a Washington, D.C., operative who first worked with Kennedy at FDA. "And he could stand toe to toe with the best scientists in the world." The neurobiologist died 21 April of COVID-19 at the age of 88. His 2008 advice to his successor at *Science* also stands as an epitaph: "Be as fair as you can, sympathize with anger, confess institutional error when appropriate, and be firm."

SpaceX plans satellite 'Sun visor'

ASTRONOMY | SpaceX said last week it is adapting internet satellites to be launched this year to diminish their brightness in orbit, which the company hopes will reduce their interference with astronomical observations. The company launches the satellites in batches of 60, and some are blamed for creating light tracks in images taken by ground-based telescopes. Last year, astronomical societies asked the company for remedies. SpaceX CEO Elon Musk tweeted last week about adding "a special dark foam that's extremely radio transparent" and does not block the satellites' phased array antennas. "Looks a lot like a car sun visor," he wrote. The company will also try a separate darkening measure, changing the alignment of the satellites' solar panels relative to Earth while they are moving into their orbits, *Space News* reported. The launch of the upgraded satellites has not been scheduled, but would come after another launch planned for May. SpaceX aims for an initial constellation of about 1600 to bring internet service worldwide, but has applied for authorization to loft as many as 42,000.

A pulse oximeter on a COVID-19 patient's finger measures blood oxygenation.

PHOTO: MARCO BERTORELLO/AFP VIA GETTY IMAGES

IN DEPTH

COVID-19

The mystery of the pandemic's 'happy hypoxia'

Doctors debate how to treat patients with low blood oxygen but without trouble breathing

By **Jennifer Couzin-Frankel**

Among the many surprises of the new coronavirus is one that seems to defy basic biology: infected patients with extraordinarily low blood-oxygen levels, or hypoxia, scrolling on their phones, chatting with doctors, and generally describing themselves as comfortable. Clinicians call them happy hypoxics.

"There is a mismatch [between] what we see on the monitor and what the patient looks like in front of us," says Reuben Strayer, an emergency physician at Maimonides Medical Center in New York City. Speaking from home while recovering from COVID-19 himself, Strayer says he was first struck by the phenomenon in March as patients streamed into his emergency room. He and other doctors are keen to understand this hypoxia, and when and how to treat it.

A normal blood-oxygen saturation is at least 95%. In most lung diseases, such as pneumonia, falling saturations accompany other changes, including stiff or fluid-filled lungs, or rising levels of carbon dioxide because the lungs can't expel it efficiently. It's these features that leave us feeling short of breath—not, counterintuitively, low oxygen saturation itself, says Paul Davenport, a respiratory physiologist at the University of Florida. "The brain is tuned to monitoring the carbon dioxide with various sensors," Davenport explains. "We don't sense our oxygen levels."

In serious cases of COVID-19, patients struggle to breathe with damaged lungs, but early in the disease, low saturation isn't always coupled with obvious respiratory difficulties. Carbon dioxide levels can be normal, and breathing deeply is comfortable—"the lung is inflating so they feel OK," says Elnara Marcia Negri, a pulmonologist at Hospital Sírio-Libanês in São Paulo. But oxygen saturation, measured by a device clipped to a finger and in many cases confirmed with blood tests, can be in the 70s, 60s, or 50s. Or even lower. Although mountain climbers can have similar readings, here the slide downward, some doctors believe, is potentially "ominous," says Nicholas Caputo, an emergency physician at New York City Health + Hospitals/Lincoln.

Hypotheses about what causes it are emerging. Many doctors now recognize clotting as a major feature of severe COVID-19 (*Science*, 24 April, p. 356). Negri thinks subtle clotting might begin early in the lungs, perhaps thanks to an inflammatory reaction in their fine web of blood vessels, which could set off a cascade of proteins that prompts blood to clot and prevents it from getting properly oxygenated.

Negri developed this idea after treating a woman whose breathing troubles coincided with circulatory problems in her toes. Negri's team gave the woman heparin, a common blood thinner, and not only her toes but her breathing recovered. Negri wondered whether heparin could boost patients' low oxygen levels regardless of whether they were struggling to breathe. On 20 April, she posted a preprint detailing her hospital's experience with 27 COVID-19 patients. Patients with hypoxia received heparin, and the dose was increased if they had elevated levels of D-dimer, a blood marker of excess clotting.

One of the 27 was lost to follow-up after transferring to another hospital. But 24 others are recovering—including six of eight who needed mechanical ventilation, a better rate of positive outcomes than has been reported elsewhere. Two remain critically ill. Negri is now planning to follow more patients. And several clinical trials elsewhere will test whether blood thinners can prevent or treat complications of severe COVID-19, including respiratory problems.

Strayer finds it reasonable to imagine that hypoxia emerges because "small blood vessels of the lung are being showered with clots." His own hospital and others are beginning to test many admitted COVID-19 patients for markers of excess clotting and treat those who show it with blood thinners. But "It is simply not known" whether clotting causes

Science's COVID-19 coverage is supported by the Pulitzer Center.

happy hypoxia, Strayer says. There are other possibilities. Recent imaging of a hypoxic patient showed "almost waxy-looking film all around the lungs," Caputo says. "I don't know what is actually going on pathophysiologically down there."

Caputo says this hypoxia is likely stressing a body already straining to battle the virus. What to do about it is prompting debate. An emerging view is that doctors should avoid aggressive treatment they've been trained to offer in other settings. Luciano Gattinoni, a guest professor in intensive care at the University of Göttingen Medical Center, is wary of what he calls a "Pavlovian response" to COVID-19 hypoxia, in which doctors may swoop in to inflate lungs with ventilators or high-pressure oxygen even when patients seem comfortable. Those measures, Gattinoni wrote online in *JAMA* on 24 April, could harm lungs that are inflating on their own but may be needed if patients aren't helped by noninvasive treatment.

Simpler interventions, he and others say, are important. Strayer, Caputo, and their collaborator Richard Levitan, a physician at Littleton Regional Healthcare in New Hampshire, who spent time treating COVID-19 patients in a New York City emergency room, offered patients supplemental oxygen and also flipped them on their belly, an approach traditionally used for people on ventilators, which can open the lower lungs. Last month in *Academic Emergency Medicine*, they reported that among 50 patients with low oxygen saturation, switching to a prone position raised average saturation significantly. However, 13 of the patients weren't helped for long and needed intubation within 24 hours.

Doctors are uncertain about the value of detecting low oxygen saturation early using inexpensive devices called pulse oximeters at home. Is home monitoring "going to prevent all bad outcomes in COVID? Absolutely not," says Levitan, who wrote a 20 April op-ed in *The New York Times* arguing that early hypoxia can rapidly progress to pneumonia and death. "If we were able to detect them when they were less sick, they'd do better." Negri tells her patients to monitor their oxygen saturation and visit the hospital if it drops to 93% or below. At that point, she considers blood thinners and other therapy.

No one, however, has studied whether early detection of hypoxia might head off bad outcomes. Some physicians believe pulse oximeters are best used with a doctor's guidance, perhaps through telemedicine. With many COVID-19 patients frightened to visit a hospital and arriving only when their symptoms have dangerously advanced, doctors also wonder whether home monitoring could hasten treatment—and whether, for some, that could make all the difference. ■

Sinovac Biotech has created a vaccine by growing the novel coronavirus in Vero monkey cells and inactivating it.

PHOTO: XINHUA/ALAMY STOCK PHOTO

BIOMEDICINE

COVID-19 shot protects monkeys

Vaccine from Chinese firm uses old-fashioned "killed" virus

By **Jon Cohen**

For the first time, one of the many COVID-19 vaccines in development has protected an animal, rhesus macaques, from the new coronavirus. The vaccine, an old-fashioned formulation consisting of a chemically inactivated version of the virus, produced no obvious side effects in the monkeys; human trials began on 16 April. And encouraging monkey results for other vaccines are close behind.

Researchers from Sinovac Biotech, a privately held Beijing-based company, gave two different doses of their COVID-19 vaccine to a total of eight rhesus macaques. Three weeks later, the group introduced SARS-CoV-2, the virus that causes COVID-19, into the monkeys' lungs. None developed a full-blown infection, and the monkeys given the highest dose of vaccine had the best response: Seven days after the animals received the virus, researchers could not detect it in their pharynx or lungs. Some of the lower dosed animals had a "viral blip" but also appeared to have controlled the infection, the Sinovac team reports in a paper published on 19 April on the preprint server bioRxiv.

In contrast, four control animals developed high levels of viral RNA and severe pneumonia. The results "give us a lot of confidence" that the vaccine will work in humans, says Meng Weining, Sinovac's senior director for overseas regulatory affairs.

"This is old school but it might work. What I like most is that many vaccine producers, also in lower–middle-income countries, could make such a vaccine," says Florian Krammer, a virologist at the Icahn School of Medicine at Mount Sinai.

But Douglas Reed of the University of Pittsburgh, who is developing and testing COVID-19 vaccines in monkeys, says the number of animals was too small to yield statistically significant results. In a manuscript in preparation, his team also raises concerns about the way the Sinovac team grew the stock of novel coronavirus used to challenge the animals, which may have evolved differences from the strains that infect humans. What's more, the monkeys are not a perfect model for COVID-19 as they don't develop some symptoms that kill many humans.

The study did address worries that partial protection by a vaccine could be dangerous. Earlier animal experiments with vaccines against the related coronaviruses that cause severe acute respiratory syndrome and Middle East respiratory syndrome had found that low antibody levels could lead to aberrant immune responses, enhancing the infection and damaging their lungs. But the Sinovac team did not find any evidence of lung damage in vaccinated animals that produced relatively low levels of antibodies, which "lessens the

concern about vaccine enhancement," Reed says. "More work needs to be done, though."

To check the possibility that SARS-CoV-2 variants might thwart a vaccine, the Sinovac researchers mixed antibodies taken from monkeys, rats, and mice given their vaccine with strains of the virus isolated from patients in China, Italy, Switzerland, Spain, and the United Kingdom. The antibodies potently "neutralized" all the strains, which are "widely scattered on the phylogenic tree," the researchers noted.

"This provides strong evidence that the virus is not mutating in a way that would make it resistant to a #COVID19 vaccine," tweeted immunologist Mark Slifka of Oregon Health & Science University. "Good to know."

An experimental vaccine made by the University of Oxford has also shown promise, although the data have not yet been published. Vincent Munster and his team at the Rocky Mountain Laboratories gave six monkeys the vaccine, which contains a gene for the surface protein of SARS-CoV-2 stitched into a harmless adenovirus that infects chimpanzees. Four weeks later, the researchers challenged the vaccinated animals and six controls. Seven days later, the vaccinated animals had a much stronger reduction of virus in their lower respiratory tracts than the controls. "The preliminary results look promising," Munster says. "People just have to be patient."

Sinovac recently started phase I human trials of its vaccine in Jiangsu province, north of Shanghai, which aim to gauge safety and immune responses in 144 volunteers. The company hopes to start phase II studies by mid-May that will assess the same endpoints but will enroll more than 1000 people.

If all goes well, Meng says, Sinovac will launch phase III efficacy trials that compare the vaccine with a placebo in thousands of people. Because of the low level of transmission now occurring in China, the company may run additional trials in harder hit countries. "We can't put all our eggs in one basket," Meng says. Sinovac may also ask regulatory agencies in China and elsewhere for emergency authorization to give the vaccine to those at high risk of becoming infected, such as customs agents and police officers.

According to the World Health Organization, the Oxford vaccine and five others had entered human trials as of 26 April, and 82 candidates were in development. Most use versions of the SARS-CoV-2 surface protein, rather than whole, killed virus. Meng says how a vaccine is made will not ultimately matter. "In this pandemic situation, the most important thing is to make a vaccine, no matter what kind of vaccine it is, that's safe and effective as soon as possible." ■

SCIENTIFIC COMMUNITY

Scientists discover upsides of virtual meetings

As the COVID-19 pandemic pushes conferences online, audiences grow

By **Michael Price**

Biochemist Kathleen Prosser wasn't planning to present her research at a conference this spring. But when COVID-19 caused organizers to cancel a series of local chemistry meetings across Canada—called Inorganic Discussion Weekends—and offer a virtual alternative, she signed up to give a talk. Prosser, a Canadian citizen who is a postdoc at the University of California (UC), San Diego, figured she'd be talking mostly to fellow Canadians. But by going virtual, she gained an international audience. The day after her talk she heard from a chemist in Australia, asking for more details and hinting at a future collaboration. "The time zone difference would not have allowed them to see it live, but they watched it [afterward]," she says.

As the novel coronavirus outbreak shutters businesses and disrupts everyday life for billions around the globe, massive annual conferences and small society meetings alike have moved online. The new format poses numerous technical and organizational challenges, but it also offers opportunities—for reaching wider audiences, reducing the carbon footprint of meeting travel, and improving diversity and equity. For some meetings, the shift may be permanent.

The scientific community is "making lemonade out of lemons," Prosser says. "It's taking [a situation] that's really quite horrible and providing people a way to connect in spite of it all."

In many ways, virtual conferences offer a better experience, says Russ Altman, associate director of the Stanford Institute for Human-Centered Artificial Intelligence (AI). Altman's institute had planned an inperson conference in April, but COVID-19 forced organizers to scuttle it. In its place, they threw together a virtual conference to discuss how AI can help scientists fight the ongoing pandemic. The event was a smashing success, Altman says. The original conference—meant to focus on how AI intersects with neuroscience and psychology—would have drawn a few hundred attendees, but 30,000 people tuned in to the online version.

Altman says the virtual environment allowed moderators to better control the flow of discussion and questions from the audience. By privately messaging one another behind the scenes, they were able to discuss how a session was going and make adjustments in real time. "For example, we had one panelist who we thought was contributing a little bit too much," he says. The moderators responded by using private messages to encourage others to speak, and they made a mutual decision to ask questions designed to draw comment from other, less vocal pan-

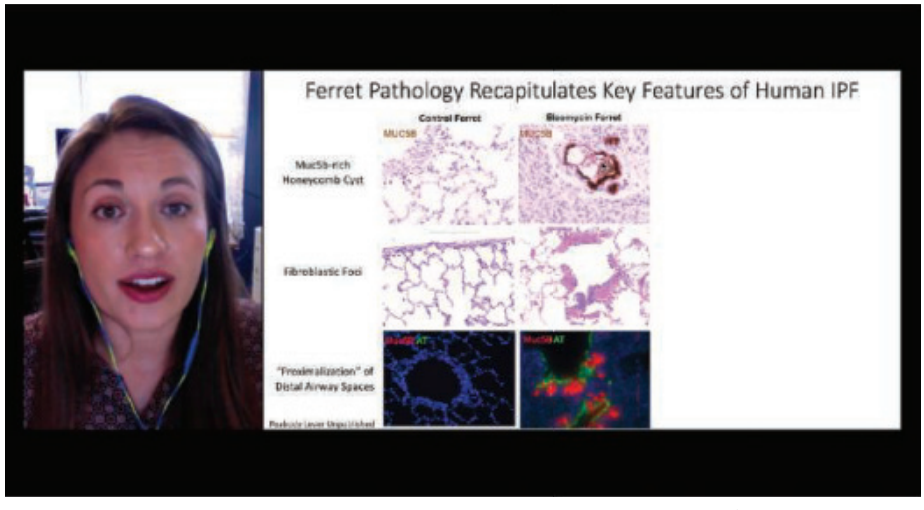

Jacelyn Peabody Lever of the University of Alabama goes virtual for the American Physician Scientists Association.

PHOTO: AMERICAN PHYSICIAN SCIENTISTS ASSOCIATION/YOUTUBE/CC-BY/JACELYN PEABODY LEVER/LABORATORY OF STEVEN ROWE AT UAB

elists. "That's hard to do in person because everyone is up [on stage] and you can't have a backchannel conversation."

During the audience question period, the moderators didn't open up the virtual floor for anyone to speak. Instead, they asked audience members to type their questions, and "a little army of people reading chat windows" prioritized the most insightful inquiries. "It's not just one person who ran up to the microphone after a talk and takes up all the airtime," Altman says.

Prosser had a similar experience with her chemistry talk, noting that because moderators could screen questions from the audience, she didn't face the "nonquestion questions you sometimes see at meetings."

Scientists acknowledge that virtual conferences can't entirely replicate the conference experience, which normally involves impromptu meetings in hallways and other social get-togethers. "Humans are a social species," notes Jennifer Kwan, a clinical fellow at the Yale School of Medicine. "We're used to being able to see body language, being able to interface with someone in person." So virtual meetings might lose some of their appeal once stay-at-home requirements loosen, she says.

Even so, Kwan sees growing support for online opportunities. She organized a virtual session in April for the annual meeting of the American Physician Scientists Association, one of the first large conferences to go virtual. Close to 500 attendees tuned in to her session, which featured Francis Collins—director of the U.S. National Institutes of Health—as a guest speaker and focused on ways to support early-career scientists amid the turmoil of the coronavirus outbreak. Kwan says the success of her society's meeting "has spurred the discussion of [hosting] additional virtual sessions in the future."

For some societies, the COVID-19 crisis hasn't so much started discussions about virtual conferences as accelerated them. Last fall, the Cognitive Neuroscience Society's governing board began to ponder how to make future meetings more accessible, affordable, and environmentally friendly. "A lot of our membership had started to ask about our carbon footprint," says George Mangun, a cognitive neuroscientist at UC Davis who sits on the society's governing board. Originally, board members discussed holding a portion of the 2021 meeting virtually. But when the pandemic hit, they adjusted their strategy and now plan to hold the entire 2020 meeting online in May. If the conference succeeds this year, Mangun notes, it will further solidify the society's march toward virtual meetings.

Altman agrees. "Whether we like it or not, the scientific community is going to very quickly come to expect this." ■

REGULATORY SCIENCE

Critics say EPA's 'transparency' rules would favor industry

Agency could consider studies available only by cumbersome Freedom of Information Act requests

By **Jeffrey Mervis**

What is a public document? That question is the latest battleground in a long war over a U.S. Environmental Protection Agency (EPA) proposal to change the kinds of studies and data the agency will consider as it shapes its regulations.

The proposal, which EPA says is meant to promote transparency and "sound science," would generally bar the agency from using data that are not publicly available (*Science*, 13 March, p. 1180). Critics already worry the policy would allow EPA to ignore studies that have been key to developing tighter health and safety rules, such as air pollution standards, but rest on difficult-to-release information, such as confidential patient records. Now, they have a new worry: EPA has proposed a definition of "publicly available" that could allow the agency to exclude those studies but continue to use others—often from industry—even if their data are effectively hidden.

> **"To say that something is FOIA-able is actually admitting that it is not publicly available."**
> **Steven Aftergood**, Federation of American Scientists

The definition, spelled out in a 3 March EPA notice seeking additional comments on the broader transparency proposal, says information available through "disclosures to the general public that are required to be made by federal, state, or local law" is fair game for regulators. In practice, that means the agency can use data and documents that outsiders can obtain only through requests made under the federal Freedom of Information Act (FOIA).

The transparency proposal is open for public comments until 18 May, but critics are already weighing in. "To say that something is FOIA-able is actually admitting that it is not publicly available," says Steven Aftergood, who directs the Project on Government Secrecy at the Federation of American Scientists. "If it were, a FOIA request would be redundant."

The FOIA process, he and others say, can be costly, cumbersome, and slow. EPA often takes months or years to fully respond to a FOIA request, says Jennifer Sass of the Natural Resources Defense Council (NRDC), one of many groups that routinely files requests. And because the law gives federal agencies substantial leeway in deciding what information they must release (it allows agencies to withhold personal data and trade secrets, for example), Sass notes that her group and others often have to go to federal court to force agencies to cough up documents.

Environmental groups fear that although the policy could bar the use of academic studies that are published in the open literature, it could allow EPA to continue to use industry data that might justify more relaxed regulations. For example, EPA routinely requires companies to submit unpublished studies and data when assessing and regulating chemicals. That information can end up "behind a FOIA wall that is … largely impenetrable to the general public," Sass says.

As a result, outsiders are often left in the dark about what data EPA is using to shape rules, says NRDC's Lucas Rhoads, who tracks pesticide regulation. "Without the documents," he says, "it's hard to make substantive comments on what EPA has proposed."

Letting EPA decide what to disclose is fine with Steven Malloy, a Washington, D.C.–based lobbyist and libertarian political commentator who has advocated for EPA's transparency proposal. "That's how FOIA works," he says. Malloy doubts EPA would use the law to deny requests for research data. "If you just want the raw environmental data, I can't think of a reason that the government wouldn't give it to you," he says.

Aftergood and Rhoads, however, suggest a much better way for EPA to meet its transparency goal would be to create a searchable, online library of all documents and data it uses in its work. Aftergood even proposes a simple test for deciding whether EPA is being transparent: "If I look it up, I'll find it." ■

At a Kansas site where plants now have less nutrients, this two-striped grasshopper is in decline.

PHOTO: DAVE RINTOUL

ECOLOGY

Carbon dioxide increase may promote 'insect apocalypse'

Study links low-nutrient plants to fewer grasshoppers

By **Elizabeth Pennisi**

Empty calories may be grasshoppers' downfall. Many insect populations are declining, and a provocative new hypothesis suggests one problem is that rising levels of atmospheric carbon dioxide (CO_2) are making plants less nutritious. That could spell trouble not just for insects, but for plant eaters of all sizes.

Over the past 5 years, several studies have documented dwindling insect populations, prompting "insect apocalypse" headlines and calls for increased conservation efforts (*Science*, 12 May 2017, p. 576). Not everyone was convinced; insect populations can have booms and busts, and the trends might vary depending on the species. Just last week, for example, a meta-analysis of 166 insect populations found that although terrestrial species are indeed declining overall, aquatic insects seem to be doing fine (*Science*, 24 April, p. 417). But a study on the Kansas prairie has convinced Michael Kaspari, an ecologist at the University of Oklahoma, that the decline is real—and that "nutrient dilution" in plants could be a major problem.

"The insect decline papers thus far haven't been testing particular mechanisms for the declines they purport to show, so this proposed mechanism with concrete data is extremely powerful," says Chelse Prather, a conservation biologist at the University of Dayton. Nutrient dilution "could be a global problem," adds Roel van Klink, an entomologist at the German Centre for Integrative Biodiversity Research, whose team did last week's analysis of insect trends.

Ellen Welti, Kaspari's postdoc, had been analyzing data on 44 species of grasshoppers at the Konza Prairie Biological Station, a 3487-hectare native tallgrass preserve in northeastern Kansas that is the site of a long-term ecological research (LTER) program. She tracked population trends in two surveys of grasshopper abundance, one done in undisturbed habitats from 1996 to 2017 and another done from 2002 to 2017 where bison grazed. Population booms and busts coincided with major climatic events, such as El Niño, a Pacific Ocean disturbance that alters temperature and rainfall. But when Welti factored out those events, it became clear to her and Kaspari that over the long term, the grasshoppers were declining, by 30% over 2 decades. "I was actually quite surprised," Welti recalls.

She and other researchers have assumed that habitat loss and pesticides underlie most of the reported drops in insect numbers. But those factors are not thought to be in play on the Konza Prairie.

Kaspari and Welti wondered whether another global trend could be responsible. Increasing CO_2 concentrations in the air speed plant growth. But as Harvard University planetary health scientist Samuel Myers and his colleagues demonstrated in 2014, plants including wheat, maize, rice, and other major crops grown under expected future CO_2 levels accumulate less nitrogen, phosphorous, sodium, zinc, and other nutrients than they do under current CO_2 levels. The thinking is that roots cannot keep up with the growth stimulated by the extra carbon and therefore don't provide adequate supplies of other elements.

Since then, most of the concern about nutrient dilution has focused on human health. Given the predicted rises in CO_2, "diluted" plants could increase the number of people worldwide who are not getting enough nutrients in their diet—already 1 billion or so—by hundreds of millions, Myers says.

But he and others have wondered about the broader ecological impact. It "is an enormously important question," Myers says. "As humans we have a lot of choices about what we eat, but there are a lot of animals that just eat what they eat."

At the Kansas LTER, other researchers had collected and stored samples of the various grass species each year. So, Welti determined concentrations of 30 elements in those samples. The biomass of the grasses doubled over the past 30 years, but the plants' nitrogen content declined about 42%, phosphorous by 58%, potassium by 54%, and sodium by 90%, Kaspari's team reported recently in the *Proceedings of the National Academy of Sciences*. "This paper is a good red flag for the scientific community," says biologist Arianne Cease at Arizona State University, Tempe.

Sebastian Seibold, a conservation biologist at the Technical University of Munich who has been studying insect declines for the past 10 years, cautions that the idea needs to be tested in different ecosystems. "We cannot derive general conclusions from it," he says. "In German landscapes, there is no evidence for nutrient shortage," adds Wolfgang Wägele, a taxonomist at the Zoological Research Museum Alexander Koenig.

Yet others suspect the work signals a sea change. "The study nicely demonstrates how climate change adds to the global problem of insect decline, even in presumably undisturbed areas," says Lars Krogmann, a systematic entomologist at the University of Hohenheim.

Kaspari predicts that as investigators analyze the data sets van Klink pulled together for last week's study, they will find that plant eaters are among the species most devastated in this decline. At the Konza Prairie, Welti hopes to bolster the hypothesis by looking for a decline in nutrients in the grasshoppers' own tissues. Larger plant eaters, such as elephants, pandas, and elk, may also be at risk, Prather says. "If nutrient dilution is widespread, this has enormous implications for herbivorous organisms all over." ■

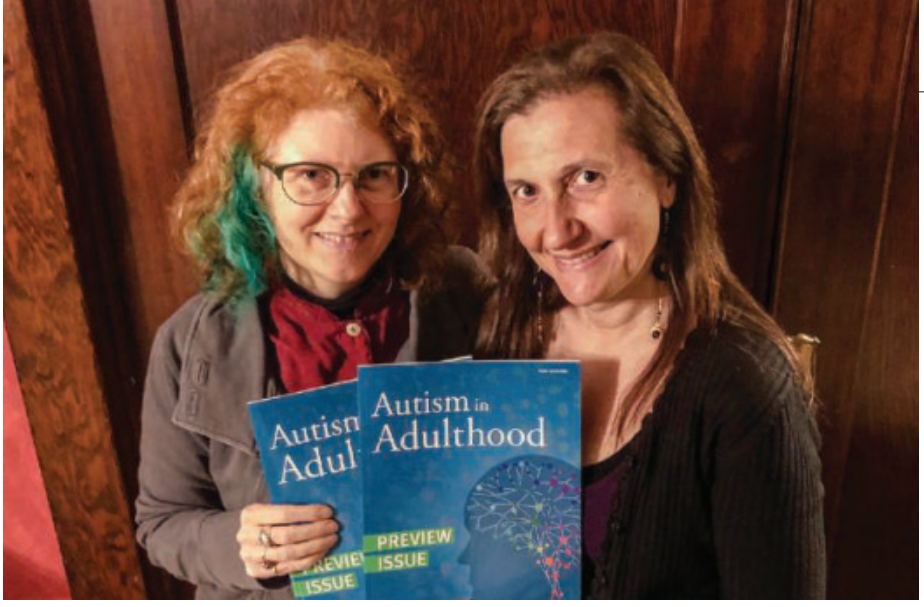

Dora Raymaker (left) and Christina Nicolaidis edit the new journal *Autism in Adulthood*.

PHOTO: BEN JACKLET

SOCIAL SCIENCE

Autistic people take the helm of studies

Trend brings new focus on well-being of autistic adults

By **Emily Willingham**

Professional burnout is all too familiar: Go at something too hard for too long, and the motivational tank empties. But burnout for an autistic person isn't always about overwork, Dora Raymaker, an autistic systems scientist at Portland State University (PSU), found in a study of autistic workers. Instead, the need to mask autistic behaviors through a workday with nonautistic people can cause chronic exhaustion, reduced ability to tolerate stimuli like light or sound, and loss of skills, the study showed through interviews and a survey of social media comments.

The work, which Raymaker's team published last month, highlights a new trend in autism research. Raymaker and colleagues are part of a small but growing number of research teams with autistic members. These groups are shifting the focus in autism research from cause and cure to practical steps, including ones that help autistic people in settings such as the workplace. And they're publishing some of their findings in a new journal, *Autism in Adulthood*, which is dedicated to including the perspectives of autistic people in what it publishes.

Interest in those perspectives is "skyrocketing," says Christina Nicolaidis, a co-author on the burnout study. Nicolaidis, a professor in the School of Social Work at PSU, has an adult son who is autistic. Although much research on autism has focused on children, autistic adults who came of age in the 1990s and early 2000s are joining the field and bringing a focus on their own experience. One member of that cohort is TC Waisman, a doctoral candidate at the University of Calgary studying how faculty and staff can improve autistic students' college experiences. Waisman says she sees researchers increasingly "respecting us as our own self-determined culture and foregrounding our needs in studies."

Before the burnout study, Raymaker says, "There was literally no research … even though it's been talked about in the community forever." In interviews with dozens of autistic people, Raymaker and colleagues found that having an autism-friendly workplace requires not expecting workers to mask autistic traits and come across as neurotypical. Too often, says Raymaker, who uses they/them pronouns, "The burden gets put on the autistic person to fix the problem." Instead, they say in their *Autism in Adulthood* paper, workplaces should make accommodations, such as accepting autistic people for who they are and providing flexible work arrangements.

Medically oriented studies of autism still dominate the field and draw most of the millions in research funding. Such studies usually involve searching for autism-associated genes or trying to recapitulate behaviors of autism in mouse models. Yet many researchers who do such work "have never even seen the condition," says Connie Kasari, a psychologist at the University of California, Los Angeles, who notes that she has autistic people on her research team. "They don't understand that social development in a mouse doesn't look like social development in a human of any sort."

Many of the new studies grow out of social science practices established for other marginalized populations. Still, the shift toward including autistic people's perspectives has not been painless. Some scientists worry about introducing bias when someone with the condition under investigation is on the research team. But Nicolaidis says, "You are not more biased by being autistic than by being nonautistic."

To address another concern, that including autistic people in research could decrease its rigor, Nicolaidis points to work she's done using survey instruments that autistic people helped her modify. Among the adjustments was using fewer percentages in response options, such as "I do this activity _____ percent of the time." Autistic people often have co-occurring intellectual disability, she says, and can be uncomfortable with percentages. Nicolaidis's team substituted images of cylinders shaded to reflect percent values.

Had she surveyed autistic people with an instrument for a general population, she argues, she would have wound up with unreliable results. Failing to get input from autistic adults would have been "like doing research in Spanish and not having anybody who's Latino on your team."

A similar philosophy underlies *Autism in Adulthood*. The peer-reviewed journal released a preview issue in spring 2018 and started to publish quarterly last year. Nicolaidis is editor-in-chief and Raymaker is one of several self-identified autistic members of the editorial team.

Researchers can be surprised by some of *Autism in Adulthood*'s policies, including using the identity-first phrase "autistic person," which the journal favors over "person with autism." Language that is medical in nature is verboten, for instance calling autism an "impairment." And every submission gets at least one autistic reviewer. Autistic reviewers often comment on manuscripts' language, including whether information is understandable. "I don't think most authors are used to getting a review from an autistic community member, but for the most part they have responded very positively," Nicolaidis says.

For Waisman, it's about time. "Autistic voices should be heard and acknowledged first and foremost," she says. Autistic adults, she adds, "have the right, and perhaps the duty, to speak for ourselves." ■

Emily Willingham is a science journalist in the San Francisco Bay Area who has an autistic adult family member.

BIOMEDICINE

Cancer DNA blood test gets real-world trial

Early detection test spots tumors in 26 women, but also produces false positives

By **Jocelyn Kaiser**

Detecting many kinds of cancers early, with a simple blood test for DNA shed by tumor cells, is a seductive prospect. Such tests, often called liquid biopsies, are now stepping out of the lab. This week, a pioneering real-world study confirms some of their promise—and highlights a potential drawback that may soon confront physicians, regulators, and the public: a small but not insignificant number of alarming but false detections.

In the first trial of such a test in a large, general population, instead of in groups with known tumors or at high risk of cancer, researchers screened nearly 10,000 women with CancerSEEK, an assay for circulating tumor DNA developed at Johns Hopkins University. It detected 26 previously unknown tumors, they reported online in *Science* this week and at a virtual session of an American Association for Cancer Research meeting on 28 April.

Observers say the results are promising, but leave key questions unanswered. "I'm very impressed with this paper. They did all the right things. But it does not mean the assay should be put on the market and sold," says breast cancer researcher Daniel Hayes of the University of Michigan, Ann Arbor. It's not yet clear that the early warnings saved the women's lives. And 101 of the women who had a positive test and received follow-up imaging turned out not to have cancer; 22 of them underwent fruitless invasive tests such as an endoscopy.

The earlier cancer is detected, the better—but not always, as some tumors may never grow enough to need any treatment. And false alarms can lead to needless anxiety and unnecessary procedures. Such concerns fuel debates over the frequency and worth of existing screening methods such as mammograms and colonoscopies, and the concerns are amplified for cancer blood tests because they promise to make it easy to screen millions of healthy people.

To explore those issues with an early version of CancerSEEK, the Geisinger Health System in Pennsylvania recruited women between the ages of 65 and 75 who had no known cancer history. CancerSEEK pulls circulating DNA from a blood sample and looks for mutations in 16 genes known to drive the growth of various cancers. It combines this information with established protein biomarkers for some cancers. If a woman's test was positive, an expert panel decided whether she should get a second blood test to confirm the initial finding and rule out molecular changes in her blood that might have fooled the first test. If the positive test appeared real, the woman was invited to undergo full-body imaging.

Mixed signals

One-year follow-up results of the DETECT-A study of nearly 10,000 women, ages 65 to 75.

	WOMEN
Initial blood test	9911
Cancers detected with blood test	26
Cancers detected with standard screening	24
Cancers detected with neither approach	46
Total cancers detected	96
Imaging based on false blood test	101
Invasive diagnostics after false blood test	22

During participants' first year in the study, dubbed DETECT-A, the Hopkins test picked up 10 types of cancer in 26 women, roughly double the number found with conventional screening. Seven of the cancers, such as ovarian, have no approved screening test and are often deadly because they are rarely found early. Seventeen of the 26 women had early-stage cancers that had not spread far, beyond nearby muscle and lymph nodes. Most of the 26 had surgery or are undergoing treatment and 12 are in remission, suggesting they did benefit from the test.

The DETECT-A study "makes great strides in its approach," says ovarian cancer researcher David Huntsman of the University of British Columbia, Vancouver. But more data attesting to an overall survival benefit from testing are needed, he and others stress, before the blood test should be approved for widespread use.

The 101 false positives is a modest number given the scale of the study, Huntsman and Hayes say. But the test also had false negatives. Conventional screening over the DETECT-A study's first year of follow-up found breast, lung, and colon cancers in 24 women whose CancerSEEK test was negative. Tumors in 46 more women became apparent through symptoms or other reasons. The Hopkins team views its test, which it has continued to improve, as "additive and complementary" to standard screening, says Nickolas Papadopoulos, who led the study with Kenneth Kinzler and Bert Vogelstein.

Some public health experts have worried that if a blood test were available, people might shun these other, proven screens. But participating in the study didn't deter the women from continuing mammograms. And in a follow-up survey completed by nearly 6900 women, only 0.3% said they regretted participating in the study, including only one of 120 with a false positive or negative result. The DETECT-A study "suggests that multicancer blood-based screening is safe and feasible," says oncologist Minetta Liu of the Mayo Clinic.

Liu is part of an academic group running studies of another blood test, developed by the biotech Grail, which looks at patterns of methyl groups on cell-free DNA to detect cancers. In a March paper in the *Annals of Oncology* and at the virtual cancer meeting, Grail shared the latest results from a study that enrolled 15,000 people, some with newly diagnosed cancer and others with no evidence of the disease. Its test for 50 cancers had a detection rate of 44% for early- to midstage cancer and also determined the site of the known cancer in 93% of cases, which could reduce the need for full-body imaging. In December 2019, the company launched PATHFINDER, a prospective study of 6200 people—all older than 50 and 70% at elevated risk for cancer. "This is an important next step toward the commercialization of our test," says Grail spokesperson Kelsey Grossman.

As for when CancerSEEK might reach the clinic, a startup company called Thrive owns the rights to further develop the test. It raised $110 million last year and is planning a large follow-up trial designed to earn regulatory approval. Questions persist about how officials and expert groups that set screening guidelines, such as the U.S. Preventive Services Taskforce, will weigh early cancer detection tests. Will decade-plus studies that show survival benefits be required, for example, as they were for other screening methods such as mammograms and lung scans for smokers? Or can proxies, such as data showing the tests find more early cancers than existing screening methods, satisfy the various groups? "That is what everybody in the field is grappling with now," Papadopoulos says. ■

DATA: LENNON *ET AL*., *SCIENCE*, 28 APRIL. DOI: 10.1126/SCIENCE.ABB9601

THE CORONAVIRUS CZAR

The COVID-19 pandemic has made German virologist Christian Drosten an unlikely cult figure

By **Kai Kupferschmidt**, *in Berlin*

PHOTO: VOLKER LANNERT

Christian Drosten admits the pandemic surprised him, despite having worked on coronaviruses for 17 years.

On a recent Monday morning, Christian Drosten said goodbye to his wife and 2-year-old son in front of his apartment block and got on his bicycle for his daily commute to Charité University Hospital here.

It looked like a scene from normal daily life. But of course it wasn't. His wife was going for a walk with their child instead of bringing him to the day care center, which was closed. The Berlin streets Drosten traversed were eerily quiet, most shops were closed, and some people on the sidewalks wore masks. Charité's Institute of Virology, which Drosten heads, was studying exotic viruses, as always, but now one of those pathogens was killing patients in a hospital a few blocks away.

And instead of teaching virology to a few hundred students, Drosten now addresses hundreds of thousands of anxious Germans. Twice a week around 10 a.m., he sets a blue microphone on his desk, puts on headphones, and waits for a science journalist from German radio station NDR Info to call him. For the next 40 minutes, he answers questions about vaccines, respiratory droplets, school closures, or masks. The podcast, simply titled Coronavirus Update, has made Drosten the face, or rather the voice, of the pandemic in Germany. More than 1 million people regularly download what has become the country's most popular podcast.

Drosten is one of the world's foremost experts on coronaviruses; his career has closely tracked their emergence as a global threat. Now, he is also a popular—if nerdy—hero. In one widely shared meme, his face, with a pair of horn-rimmed glasses photoshopped on it, sits next to three movie stills of actor Jeff Goldblum, to whom he bears a passing resemblance. "He has fought dinosaurs, body snatchers, and aliens," the caption reads, "so I'll trust him with this virus too." Drosten's cult status reminds Holger Wormer, a journalism professor at the Technical University of Dortmund, of Stephen Hawking's: "Many people may not understand everything he says. But it is comforting to listen to someone explaining what is going on."

His calm, considered communication has earned Drosten widespread appreciation. "It's a stroke of luck that we have someone here in Germany who is recognized worldwide as an expert on coronaviruses and who is willing and able to communicate so well," says Volker Stollorz, head of the German Science Media Center. On 20 April, the German Research Foundation announced it was awarding Drosten a one-off prize for "outstanding science communication during the COVID-19 pandemic."

Drosten also explains coronaviruses to politicians. He has advised German Chancellor Angela Merkel—they chatted by phone for about an hour recently, he says—and Minister of Health Jens Spahn. He has been called Germany's "coronavirus-explainer-in-chief" and "the coronavirus pope," the German equivalent of a "coronavirus czar."

Yet colleagues describe Drosten, 47, as an unlikely character for his new role. "He is not someone who seeks out this kind of attention," says Isabella Eckerle, a former lab member who now runs a laboratory for emerging viral diseases at the University of Geneva. Drosten says he wouldn't have stepped into the limelight if SARS-CoV-2 weren't exactly the kind of virus he has spent most of his life studying. "If this were influenza, for instance, I would not be doing this," he says.

Science's COVID-19 coverage is supported by the Pulitzer Center.

DROSTEN'S CORONAVIRUS CAREER effectively began on Saturday, 15 March 2003, when a 32-year-old doctor from Singapore named Leong Hoe Nam was taken off a plane in Frankfurt, Germany, and taken to the city's university clinic. Leong had treated patients in Singapore before attending an infectious diseases course in New York City, and had developed symptoms consistent with an alarming new respiratory disease that was rapidly spreading in Asia. That same day, the World Health Organization (WHO) had christened the new disease "severe acute respiratory syndrome," or SARS.

> **"Many people may not understand everything he says. But it is comforting to listen to someone explaining what is going on."**
>
> **Holger Wormer**, Technical University of Dortmund

At the time, Drosten was building up a lab for molecular diagnostics at the Bernhard Nocht Institute for Tropical Medicine in Hamburg, Germany. The Frankfurt virologists sent Leong's blood and other samples to Drosten, hoping he could help identify what was believed to be a new virus. But tests for everything from adenoviruses to paramyxoviruses came back negative.

About 1 week later, however, when Drosten was in Frankfurt to defend his doctoral thesis, the same virologists told him they had managed to grow the virus in a petri dish. Drosten realized this would allow him to use a new catch-all method he had developed for identifying unknown viruses, which amplified viral genetic material so it could be sequenced and checked against online databases. Drosten picked up a sample, then drove the 5 hours back to Hamburg in his old Opel and went straight to his lab. After a few days with little sleep, he had a small part of the new virus' genome. The closest match was a cattle coronavirus that doesn't infect people. "My first thought was, maybe it is some kind of contamination from the FCS," the fetal calf serum used to grow cells in the lab, Drosten recalls.

But he and his colleague Stephan

Microbes and man

Christian Drosten's career paralleled the emergence of coronaviruses as a serious human threat. He worked on severe acute respiratory syndrome (SARS) and Middle East respiratory syndrome (MERS) and in January, his lab developed the first test for SARS-CoV-2, the new pandemic virus.

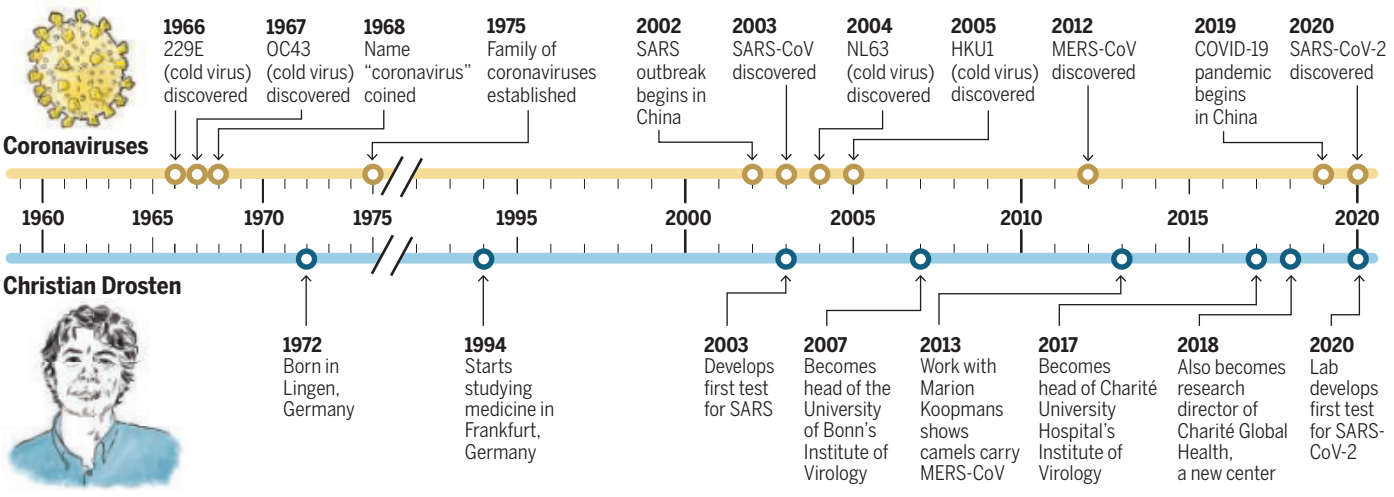
Coronaviruses
1966 229E (cold virus) discovered
1967 OC43 (cold virus) discovered
1968 Name "coronavirus" coined
1975 Family of coronaviruses established
2002 SARS outbreak begins in China
2003 SARS-CoV discovered
2004 NL63 (cold virus) discovered
2005 HKU1 (cold virus) discovered
2012 MERS-CoV discovered
2019 COVID-19 pandemic begins in China
2020 SARS-CoV-2 discovered
1960
1965
1970
1975
1995
2000
2005
2010
2015
2020
Christian Drosten
1972 Born in Lingen, Germany
1994 Starts studying medicine in Frankfurt, Germany
2003 Develops first test for SARS
2007 Becomes head of the University of Bonn's Institute of Virology
2013 Work with Marion Koopmans shows camels carry MERS-CoV
2017 Becomes head of Charité University Hospital's Institute of Virology
2018 Also becomes research director of Charité Global Health, a new center
2020 Lab develops first test for SARS-CoV-2

Günther quickly realized they were seeing a deadly new member of the family. "At the time, medical students learned hardly anything about coronaviruses," Drosten says. The only two known to cause disease in humans, named OC43 and 229E, accounted for a small percentage of human colds every winter. This new virus was a very different beast. SARS killed 10% of the almost 8000 people it infected in nearly 30 countries before it was contained.

Researchers at the U.S. Centers for Disease Control and Prevention and the University of Hong Kong realized the culprit was a coronavirus around the same time. But Drosten was the first to develop a diagnostic test, and he distributed the protocol freely on the internet. It earned him international recognition as well as the Federal Cross of Merit, an important German award. (Leong survived his bout with SARS and is now treating COVID-19 patients himself. He says he has not met Drosten, but reads every paper coming from his lab. "Truly, he is an incredible scientist, with out-of-the-box thinking," Leong wrote in an email.)

DROSTEN GREW UP on a pig farm in northern Germany. He studied medicine in Frankfurt, the first person in his family to go to university, and rose quickly in German academia. After his stint in Hamburg, he became a full professor at the University of Bonn and, at 35, head of the Institute of Virology. His research interests were ideal preparation for COVID-19. He established a system for probing the function of the SARS virus' genes and started to study viral evolution, looking for close relatives of human viruses in animals. In one such study, his team discovered that mumps, which like measles is caused by a paramyxovirus, had jumped to humans from bats. They also showed that Nipah, another bat-borne virus, originated in Africa, even though it was discovered in Malaysia after hundreds of pig farmers there developed encephalitis in 1999.

Scientists discovered two new coronaviruses in the years after the SARS outbreak, both of which caused the common cold. Then in 2012, researchers isolated a new coronavirus that spelled greater danger. It came from a 60-year-old man in Saudi Arabia who had developed pneumonia. Intrigued, Drosten geared his research to the new agent, which was soon called the Middle East respiratory syndrome (MERS) virus. In 2013, he reported on a wealthy 73-year-old patient from Abu Dhabi, United Arab Emirates, who was treated for MERS in Germany and died. Relatives said the patient had cared for a sick racing camel before falling ill—the first sign that camels might be involved.

Saudi Arabia, which had the most MERS cases and a multimillion-dollar camel racing industry, initially scoffed at the link. "We don't think camels are involved," then–Deputy Minister of Health Ziad Memish said. But work from Drosten's group and others soon confirmed the suspicion. Memish and Drosten teamed up to study the new disease, and Drosten's Bonn lab became a leading MERS hub. It developed a test to detect the virus' RNA and then an antibody assay that helped show the virus had likely been infecting people in the region for decades.

The research yielded some unexpected insights. While looking for coronaviruses in camels, the scientists found pathogens closely related to 229E, one of the common cold coronaviruses, suggesting that virus, too, originated in camels. It was a warning sign, Drosten said at the time, that MERS could follow the same course as SARS, which had originated in bats, and evolve to become a true human disease. Animal coronaviruses, it seemed, posed a particular threat of sparking a pandemic.

WHEN ANOTHER severe respiratory syndrome emerged this year, Drosten—who moved to the prestigious Charité University Hospital in 2017—was prepared. After seeing the first rumors about a coronavirus in China online, Victor Corman, who leads the lab's virus diagnostics group, began to scour existing sequences of SARS-related coronaviruses, isolated from bats, for regions that were the same across different viruses. He was trying to guess what parts of a new SARS-like coronavirus might look like, in order to create a test. Based on those sequences, he designed and ordered 20 pairs of so-called primers, little snippets of DNA, that pair with a pathogen's genome, so that it can be amplified and detected.

When Chinese researchers finally published the genome of the new virus from Wuhan on 10 January, Corman used the primers that best matched the viral sequence and prepared the diagnostic test almost immediately. WHO posted Corman's protocol on its website on 13 January, allowing countries around the world to produce a test themselves and detect imported cases of the new virus. Drosten predicted the test would also help scientists understand whether the virus was able to spread from human to human.

It was.

Three and a half months later, SARS-CoV-2, as it is now known, has traveled to all corners of the world, infecting millions of people and

GRAPHIC: N. DESAI/*SCIENCE*

killing well over 200,000. It has forced countries from Austria to Zambia to shut down their economies and societies, causing immense suffering and igniting heated debates about the right way to deal with the threat.

Drosten concedes it has surprised him, despite his 17 years of work on coronaviruses and his knowledge of the threat they pose. "I didn't think that SARS would come back like this," he says—as a virus that is both deadly and much more transmissible. It is adept at infecting cells of the upper respiratory tract, from which a cough can expel it, and unlike SARS—but like the flu—it can spread before symptoms emerge. "That's pretty astonishing," Drosten says.

Drosten says a key reason for SARS-CoV-2's success may be a tiny part of the "spike," the protein that sits on the virus' surface and makes it look like a crown when seen through a microscope. The spike protein attaches to a receptor on human cells called angiotensin-converting enzyme 2. Before the virus can enter the cell, however, a part of the protein has to be cleaved. The SARS-CoV-2 spike protein cleaves more readily than equivalent proteins in other coronaviruses, because it has evolved something called a polybasic cleavage site, which Drosten likens to the perforations on a notepad that make it easier to rip off a page. That feature may explain the virus' rapid spread from cell to cell, he says.

Drosten started to warn of the new virus' potential in TV interviews in January, but quickly grew exasperated. After long interviews, journalists often used one short quote that failed to convey the immense threat, he says. "I actually called up some of them afterwards and told them: 'You are missing the boat on this.'" So when a producer from NDR asked Drosten in February whether he was willing to answer a few questions every day, his answer was swift: "Traveling at the moment, like the idea, we can start Monday." (Drosten recently reduced the frequency to twice a week.)

The show's conversation is easygoing, and Drosten occasionally offers advice. In March, he told listeners to avoid beer from the tap, because glasses might not be cleaned thoroughly. "When I go to a bar, I always order beer in a bottle, for many years now," he said. If Drosten is himself emotionally shaken by the pandemic and the way it is changing the world, he doesn't show it.

Drosten also seems unfazed by his newfound fame, but he gets annoyed when the focus drifts away from the science. He chided political journalists who asked whether important soccer matches and Germany's sacred Oktoberfest would need to be canceled, saying that was not his expertise. He bristles at stories describing his "sensual lips" and tousled hair. "I talk about science," he says. "I don't want to read about my haircut." Wormer says Drosten is doing a great job talking about the science, but is a tad naïve about what interests the media. "For some people going to the stadium is important and you just have to accept that," he says. For a public figure, a bit of mockery comes with the territory as well, he says.

Drosten has balked at suggestions that he has become a political player. He seemed genuinely angry after a spate of stories suggesting virologists had taken the reins of German government. "If that doesn't change, we are reaching the point where science has to start an orderly retreat," he said on the podcast. His role as a political adviser is small, he told *Science*. "It's not like I'm in and out of ministries all day." When a German newspaper ran his photo under the headline "Is this our new chancellor?" he bristled at the idea.

Christian Drosten (center) at a March press conference with German Minister of Health Jens Spahn (right) and Petra Gastmeier, director of the Charité Institute of Hygiene and Environmental Medicine (left).

PHOTO: EMMANUELE CONTINI/NURPHOTO VIA GETTY IMAGES

DROSTEN FEELS most at home concentrating on his research. Virologist Marion Koopmans of Erasmus Medical Center in the Netherlands recalls seeing him during a technical planning meeting of a large research consortium, huddled at the back of the room with two or three others. "Probably writing a *Nature* paper," she says. "He doesn't like the blah blah blah."

But Drosten wants his research to save lives. Large cardboard boxes in his office hold supplies of two medicines waiting to be tried in the clinic. One is camostat mesylate, a pancreatitis drug approved in Japan that Drosten and others found can prevent both SARS-CoV and SARS-CoV-2 from entering cells. The other drug is niclosamide, used to treat tapeworms and other parasites. In a paper posted on the preprint server bioRxiv this month, Drosten's colleague Marcel Müller showed that SARS-CoV-2 interferes with the cellular recycling process called autophagy. It's unclear how exactly that benefits the virus, but niclosamide counters the interference. Treatment with the compound reduced SARS-CoV-2's growth in cell culture by 70%, the authors write. Drosten hopes to start to enroll patients soon in a trial to test a combination of the two drugs.

For the moment, Drosten is learning what he can from sequencing virus samples and probing the pathogen in the biosafety level 3 lab in the institute's basement. He is also interested in how SARS-CoV-2 made its way from animals to humans. He's fascinated by the role livestock appear to play as a bridge between bats, which are coronaviruses' natural hosts, and humans. 229E and MERS came from camels, OC43 from cattle. SARS infected civets and also raccoon dogs, raised by the millions in China's fur industry. SARS-CoV-2's origin is unclear, but Drosten wonders whether raccoon dogs could be an intermediate host. "I would love to take samples from 20 of these farms," he says.

FOUR MONTHS after the emergence of the pandemic, Germany is widely seen as a success story in Europe. The country tests widely for the virus—thanks in part to that first assay, developed in Drosten's lab—and has managed to keep case numbers low. Now, as in many countries, pressure is building to reopen shopping malls, bars, and restaurants. Drosten is worried some German states are moving too fast, which could lead to an explosive resurgence of the virus.

That concern has led him to depart from his science-only strategy. "In this situation, for once, I have to express my opinion a little bit here in this podcast," he said on 22 April. Discussing press reports of shopping malls full of people, he said, "It's sad to see that we may be in the process here in Germany of completely gambling away the advantage we have had."

With COVID-19 drugs and vaccines unavailable, such words may be the most powerful tool to curb the spread of the virus. And whether or not he likes it, Drosten's podcast has given him real influence, says Marcel Fratzscher, head of DIW Berlin, an economic research institute. "At this point, if Drosten says it is too early, that carries as much weight as Merkel saying it." ■

ASTRONOMY

What future awaits the Sun?

Stellar data question the notion that the Sun is stemming its magnetic activity cycle

By **Ângela R. G. Santos**[1] *and* **Savita Mathur**[2,3]

The Sun and other similar (solar-like) stars have an internal magnetic field that can emerge on the surface, forming features such as dark spots, which drive the so-called magnetic activity. For both the Sun and solar-like stars, magnetic activity varies with time and strongly correlates with photometric (brightness) variability. In the solar and stellar scientific communities, a debate rages about how the magnetic activity of the Sun compares with that of similar stars and whether the Sun will reach very high activity levels or is in a period of transition to a state of reduced magnetic activity. On page 518 of this issue, Reinhold *et al*. (*1*) compare the Sun's photometric variability with that of solar-like stars and find the latter to be more active.

The appearance and disappearance of magnetic features on the Sun's surface cycle over an 11-year period called the solar cycle (*2*). As the magnetic fields emerge, they form sunspots at mid- to low latitudes, which appear darker than the surrounding quiet surface. The number of sunspots varies over the activity cycle: Near activity maximum, the Sun exhibits hundreds of sunspots, and during an activity minimum, sunspots are almost absent. The number of sunspots on the Sun's surface is the most regularly used solar-activity proxy. When the magnetic field lines are disturbed or during an activity maximum, solar flares might occur. Coronal mass ejections—release of magnetized solar plasma—often follow the flares and represent what is commonly called a solar storm.

The detailed mechanisms that control solar magnetic activity are not yet fully understood. Studying stars that roughly share properties with the Sun (similar temperature, mass, age, rotation period, and chemical composition) allows scientists to place the Sun in the context of other stars, investigate changes in the Sun over time, and predict its future. Such comparisons often place the Sun in a special category: an outlier in the context of other stars.

Contrary to sunspots, which can be observed with the naked eye, starspots on the surface of distant stars cannot be resolved in this way. Instead, scientists seek to detect the indirect effects of starspots on, for example, stellar brightness. The advent of planet-hunting missions in space (that is, avoiding Earth's atmosphere), particularly that of the Kepler space telescope, has yielded unprecedented, high-precision, long-term observations of stellar light. Such information is exceptional not only for exoplanet research but also for stellar physics. Because stars rotate, dark spots move in and out of view and modulate the observed stellar light (see the figure). Whereas the periodicity of the stellar light modulation is related to surface rotation (*3*), the amplitude is related to the percentage of stellar surface covered by spots, thus representing a proxy for stellar magnetic activity (*4*).

The Kepler space telescope observed a small patch of the sky in the Cygnus and Lyra constellations for almost four continuous years. Kepler's long-term and high-quality observations are ideal to characterize stellar activity. Combining Kepler data with the

There is debate on whether the Sun is in transition to a less active state.

PHOTO: GREG PIEPOL/SCIENCE SOURCE

[1]Space Science Institute, 4765 Walnut Street, Suite B, Boulder, CO 80301, USA. [2]Instituto de Astrofísica de Canarias, Santa Cruz de Tenerife, Spain. [3]Department of Astrophysics, Universidad de La Laguna, Santa Cruz de Tenerife, Spain. Email: asantos@spacescience.org

Star light, star bright

Dark magnetic spots are a manifestation of stellar activity. As the star rotates, spots modulate stellar brightness, revealing stellar rotation and magnetic properties. The amplitude of spot modulation is proportional to the area of the Sun or star covered by spots. Data from the VIRGO instrument and Kepler satellite show that stars with solar-like properties are typically more active than the Sun.

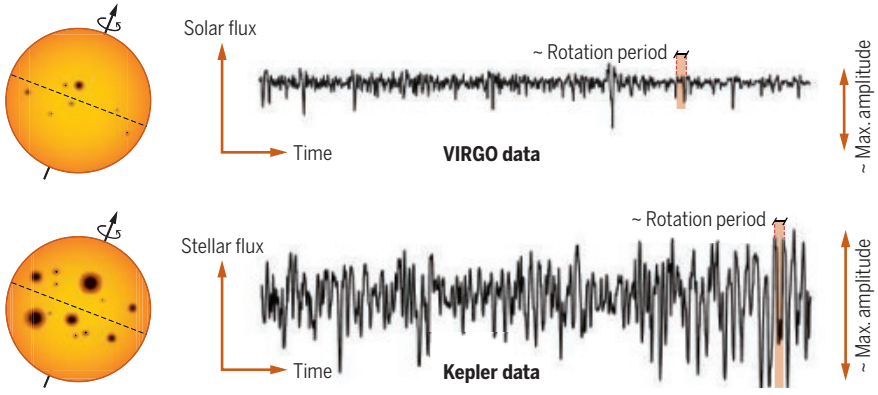

recent data released from the Gaia mission to map the Milky Way Galaxy, Reinhold *et al.* meticulously selected solar-like stars with reliable periods and measured their photometric variability. This sample of stars represents the largest number of solar-like stars with the closest properties to those of the Sun identified to date. For the Sun, the authors used data from the VIRGO (Variability of Solar Irradiance and Gravity Oscillations) experiment. The authors established that the magnetic activity level of the Sun, based on photometric variability, is lower than that of the solar-like stars. But why does the Sun seem to differ so much from other stars that appear to be the most similar to it? Are the data telling us that the Sun can reach higher activity levels?

The notion that the Sun might reach higher solar activity levels is quite unpleasant news for technological societies. The Sun's strong activity and the associated solar storms not only produce the beautiful northern and southern lights but also might compromise satellites and power lines, threaten the lives of astronauts in space, and affect Earth's climate. High stellar activity also has a non-negligible impact on the habitability of planets found around active stars because their atmospheres might be swept out into deep space by such high magnetic activity. Thus, characterizing stellar magnetic properties is also extremely important for exoplanet research.

These results also question the theory of a transitioning Sun. Astronomers thought that, as stars evolve, they gradually slow down (the rotation period grows longer) and become less active (*5*). Recent studies have suggested, however, that at a given point in its lifetime, the star faces a dramatic midlife crisis: Its activity cycle shuts down, and the star's rotation stops slowing down (*6*, *7*). According to this scenario, the Sun is approaching that time of its life. Can the Sun already be transitioning, while the solar-like stars observed with Kepler in the new study continue to progress in their steady evolution?

The future of our Sun remains uncertain. The Kepler mission unexpectedly revolutionized stellar physics and, with new discoveries, challenged what we thought we knew. Six years after the conclusion of its main mission, the legacy of Kepler data continues to yield noteworthy information, as shown by Reinhold *et al.* The current TESS (Transiting Exoplanet Survey Satellite) and future PLATO (Planetary Transits and Oscillations of stars) space missions, while searching the full sky for exoplanets, will collect data for an extraordinary number of stars. However, these missions are planned to obtain short-term observations, which will hamper a proper characterization of stellar magnetic activity.

On the bright side, these missions will observe brighter stars than Kepler did. This will allow astronomers to do ground-based follow-up observations, which will provide independent constraints on stellar activity. This was not possible for most Kepler targets, which are faint. Future research will certainly provide answers to some of the open questions on rotation and magnetic evolution and, in turn, stellar evolution itself. ■

REFERENCES AND NOTES

1. T. Reinhold *et al.*, *Science* **368**, 518 (2020).
2. D. H. Hathaway, *Living Rev. Sol. Phys.* **12**, 4 (2015).
3. A. R. G. Santos *et al.*, *Astrophys. J. Suppl. Ser.* **244**, 21 (2019).
4. S. Mathur *et al.*, *Astron. Astrophys.* **562**, A124 (2014).
5. A. Skumanich, *Astrophys. J.* **171**, 565 (1972).
6. J. L. van Saders *et al.*, *Nature* **529**, 181 (2016).
7. T. S. Metcalfe *et al.*, *Astrophys. J.* **826**, L2 (2016).

ACKNOWLEDGMENTS

The authors are supported by grants from NASA (NNX17AF27G) and the Spanish Ministry (RYC-2015-17697).

10.1126/science.abb9208

GRAPHIC: KELLIE HOLOSKI/*SCIENCE*

CANCER

Profiling prostate biology

Prostate luminal secretory cells can function as facultative stem cells

By **Kathleen Kelly**

Molecular profiling of heterogeneous cell populations at the single-cell level using single-cell RNA sequencing (scRNA-seq) has provided refined cell type–specific gene expression signatures and allowed the discovery of rare cell types. Applying such an approach in the context of anatomy and pathology informs disease mechanisms. A requirement for androgen is a cardinal feature in the development and maintenance of normal prostate and for the maintenance of prostate adenocarcinoma (*1*). On page 497 of this issue, Karthaus *et al.* (*2*) provide an in-depth characterization of prostatic cellular heterogeneity and address mechanisms of androgen independence in regenerating mouse prostates. They identify an adaptive stemlike phenotype in a large population of secretory epithelial cells undergoing androgen-dependent regeneration, uncovering an unappreciated plasticity in these differentiated cells, which has implications for prostate cancer therapy.

Prostate epithelium consists of three primary cell types: luminal cells, an underlying layer of basal cells, and rare neuropeptide-secreting neuroendocrine cells. Luminal cells express the androgen receptor (AR) transcription factor and are thought to be the main cell of origin for prostate cancer (*3*). To better understand the potential of luminal cells as targets of genetic alteration and transformation, much attention has focused on their self-renewal characteristics.

In rodents, androgen withdrawal by castration results in the death of ~90% of luminal cells, and androgen readministration fully regenerates the prostate within a month. Similarly, normal human prostates regress in size and cellularity after androgen deprivation. Using lineage tracing, whereby selected cells and their progeny can be specifically visualized, luminal cells in adult mice were shown to derive from luminal progenitor

Laboratory of Genitourinary Cancer Pathogenesis, Center for Cancer Research, National Cancer Institute, National Institutes of Health, Bethesda, MD, USA.
Email: kellyka@mail.nih.gov

Prostate luminal cell responses to androgen

In the mouse prostate, secretory (L1) and nonsecretory (L2) luminal cell populations respond differently to the presence and absence of androgen through androgen receptor (AR)–mediated transcription. After castration, L1 and L2 populations demonstrate converging gene expression profiles. On androgen reintroduction, both L1 and L2 populations proliferate and regain their differentiated identities.

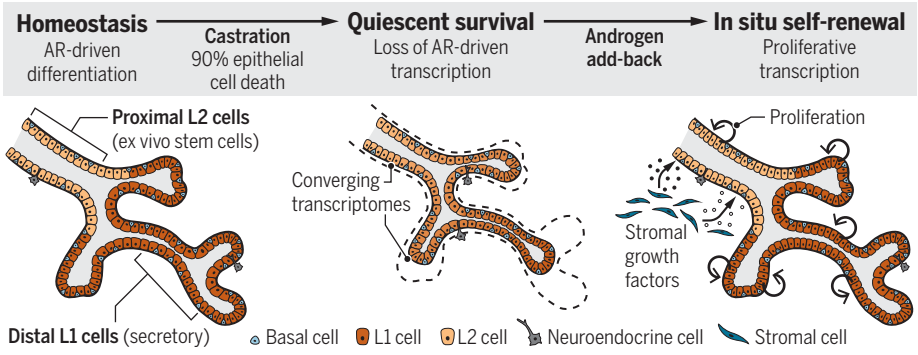

cells but not basal cells, which are the stem cells during embryonic development (*4*). A critical question is whether there are specialized committed luminal progenitors or facultative (that is, adaptive) cells that repopulate the prostate on regeneration.

Karthaus *et al.* carried out scRNA-seq in mouse prostate, which revealed several cell types, including three AR-positive luminal epithelial populations—L1, L2, and L3—and AR-positive mesenchymal populations. L1 cells, the largest population, are secretory cells located in the distal prostate of mice. As shown by scRNA-seq, L1-like cells are similarly enriched in the peripheral zone of human prostates, the location of most adenocarcinomas, which express many of the phenotypic properties of human L1 cells (*5*). L2 cells represent a population that has been identified and isolated on the basis of the expression of a variety of markers (*6*–*8*). Prior studies have shown that L2 cells are located in the proximal prostate (adjacent to the urethra) and have the highest ex vivo and transplantable self-renewal activity, lack secretory proteins, and survive androgen withdrawal at a higher frequency than L1 cells. These properties suggest that L2 cells act as luminal stem or progenitor cells.

In the human prostate, a population of cells with transcriptomes approximating L2 cells has been identified in the proximal prostate (called the transition zone in humans) (*5*). L2 gene expression profiles overlap with those of pulmonary luminal epithelial club cells, which line the trachea (windpipe) and are self-renewing progenitors of differentiated secretory cells (*9*). Karthaus *et al.* also identified a rare L3 population in mouse prostate on the basis of a segregating gene expression profile similar to that of pulmonary ionocytes, which regulate ion and fluid balance in lung secretions (*9*).

To evaluate the numbers of individual regenerating luminal progenitors in the mouse prostate, Karthaus *et al.* used genetically engineered (confetti) mice to demonstrate the clonality of small clusters of repopulating luminal cells distributed throughout the prostate. Although prior work has suggested that a relatively large proportion of cells in the distal prostate that survive castration subsequently proliferate on androgen addition (*10*, *11*), the clonal origins of proliferating cells were not addressed. These findings establish that most surviving luminal cells divide in situ on average two to three times and that regeneration is not due to a limited number of highly migratory repopulating clones.

A question of great interest has been whether the cells that survive castration display distinct molecular characteristics. Karthaus *et al.* found that there was no distinct signature that identified a preexisting stem or progenitor cell population among L1, L2, and L3 cells immediately surviving castration. However, adaptive transcriptional changes were observed among the remaining luminal cells. Under castrated conditions, the gene expression profiles of the surviving L1 secretory population approximated those of the less castration-sensitive L2 population, although each population also maintained distinct markers. On androgen add-back, the L1 and L2 populations expressed proliferative programs as well as their characteristic transcription profiles. Loss of AR-mediated gene regulation was a major mechanism of the transcriptional changes observed in L1 cells. Defining the transcriptional networks that cross-regulate AR-mediated differentiated functions with survival and self-renewal programs is an important next step (see the figure).

What are the mechanisms that determine castration resistance in normal luminal cells? The prevailing evidence suggests that AR activity in mesenchyme, rather than luminal epithelium, may be responsible for androgen-dependent regeneration in the normal prostate (*12*, *13*). Perhaps luminal cell survival and regrowth are determined by the heterogeneity of microenvironmental niches, which can vary in soluble ligand expression (*14*) and mechanical properties. Karthaus *et al.* identified, in mesenchyme populations within regenerating prostates, induced RNAs encoding growth factors that functionally enhanced the growth of ex vivo luminal epithelial cells in organoid culture. Further work to validate the in vivo role of specific mesenchymal growth factors will be important to define signaling mechanisms associated with regenerative growth.

In men, L1 populations are anatomically associated with prostate cancer and L2 populations with a common hyperproliferative disease, benign prostate hypertrophy. It is possible that the intrinsic properties of L1 and L2 cells, as well as their niches, contribute to these distinct disease outcomes. Does the potential of L1 cells to express a less differentiated "stemlike" state in the context of the distal microenvironment predispose to malignant transformation? Conversely, do factors enriched in the proximal microenvironment, such as transforming growth factor–β (TGF-β) (*14*), suppress transformation? It is unclear what physiological conditions (e.g., inflammation) might lead to L1 cell dedifferentiation.

These findings have implications for prostate cancer treatment. Prostate adenocarcinomas are autonomously dependent on AR activity, and inhibiting AR signaling is a mainstay of treating high-risk primary and metastatic prostate cancer (*1*). Acute survival mechanisms in response to AR signaling inhibition of adenocarcinoma may include signaling pathways normally initiated by mesenchymal paracrine growth factors used by normal luminal cells. Targeting such pathways in combination with AR inhibitors may prove to be one approach to increasing treatment efficacy for advanced prostate cancer. ■

REFERENCES AND NOTES

1. P. A. Watson *et al.*, *Nat. Rev. Cancer* **15**, 701 (2015).
2. W. R. Karthaus *et al.*, *Science* **368**, 497 (2020).
3. J. J. Li *et al.*, *Cold Spring Harb. Perspect. Med.* **9**, a030395 (2019).
4. N. Choi *et al.*, *Cancer Cell* **21**, 253 (2012).
5. G. H. Henry *et al.*, *Cell Rep.* **25**, 3530 (2018).
6. A. Tsujimura *et al.*, *J. Cell Biol.* **157**, 1257 (2002).
7. O. J. Kwon, L. Zhang, L. Xin, *Stem Cells* **34**, 191 (2016).
8. Y. A. Yoo *et al.*, *J. Natl. Cancer Inst.* **111**, 311 (2019).
9. D. T. Montoro *et al.*, *Nature* **560**, 319 (2018).
10. J. Liu *et al.*, *Mol. Endocrinol.* **25**, 1849 (2011).
11. J. C. Pignon *et al.*, *PLOS ONE* **10**, e0128489 (2015).
12. G. R. Cunha, B. Lung, *J. Exp. Zool.* **205**, 181 (1978).
13. Q. Xie *et al.*, *Nat. Commun.* **8**, 14284 (2017).
14. X. Wei *et al.*, *Cell Stem Cell* **24**, 753 (2019).

ACKNOWLEDGMENTS

K.K. is funded by the intramural program, Center for Cancer Research, National Cancer Institute, NIH.

10.1126/science.abb7052

GRAPHIC: A. KITTERMAN/*SCIENCE*

NUCLEAR PHYSICS

π^0 decay precision-tests the chiral anomaly

More precise neutral pion lifetime measurements probe quantum symmetry breaking

By **Harvey B. Meyer**

Most subatomic particles are strongly interacting composites called hadrons. Most hadrons are unstable and decay on extremely short time scales (10^{-22} s) to lighter hadrons. The electrically neutral pion, π^0, is the lightest hadron and decays on a time scale of 10^{-16} s in 98.8% of cases into two photons, $\gamma\gamma$, through the electromagnetic interaction. Historically, understanding this time scale presented a major challenge to theoreticians. On page 506 of this issue, Larin *et al.* (*1*) report that the measurement of the lifetime of the neutral pion has reached a precision of 1.5% through the combined results of the PrimEx-I and -II experiments. Its dominant decay to two photons proceeds mainly through the chiral anomaly, and calculating its decay time represents an important test of quantum chromodynamics in its low-energy, nonperturbative regime.

In the 1960s, it was realized that the multitude of hadron species could be understood economically in terms of more elementary degrees of freedom: the quarks. This simpler and deeper description is similar in nature to the understanding of the properties of the chemical elements in terms of the electronic structure of atoms. In the early 1970s, it became understood that the force that binds quarks into hadrons is mediated by a set of gauge fields. Quantum chromodynamics is the fundamental quantum field theory that describes this type of interaction.

The underlying cause of the short π^0 lifetime was found in 1969 with the discovery of the so-called chiral anomaly (*2*, *3*). Up to that point, it was assumed that a symmetry of the classical Lagrangian would protect π^0 from decaying in the limit of massless up and down quarks and lead to a longer lifetime. However, it turns out to be impossible to regularize quantum chromodynamics without breaking that symmetry. Therefore, the latter is not respected by the quantum fluctuations of the quantum chromodynamics fields and does not protect π^0 from decaying.

The quantum origin of the symmetry breaking leads to an exact prediction for the strength of π^0 coupling to $\gamma\gamma$ and hence the π^0 lifetime in the limit of massless up and down quarks. The product of the π^0 lifetime and the charged pion π^+ lifetime, which decays through the weak interaction, depends on no hadronic quantity other than the pion masses (see the figure). The matrix element of the divergence of the axial current, $\partial \cdot j_A$, between the vacuum and a $\gamma\gamma$ state can be calculated exactly and depends only on the fine-structure constant and the photon momenta. However, the matrix element is saturated by the exchange of a π^0, which the axial current j_A creates proportionally to the amplitude for the π^+ decay into the charged muon μ^+ and the muon neutrino ν_μ. Thus, in order for the two evaluations of the matrix element to be consistent, the coupling of π^0 to $\gamma\gamma$ must be inversely proportional to the π^+ decay amplitude.

A major objective of the measurement of the neutral pion lifetime by the PrimEx collaboration was to test its prediction at the percent level. With an overall precision of 1.5%, this goal has been reached. At this precision level, refinements must be applied to the prediction. They have been worked out by several groups and found to be on the order of +4.5 ± 1.0% (*4*). One of the most sophisticated theory predictions (*5*) obtains 8.04 (±0.11) × 10^{-17} s for the π^0 lifetime. Adding statistical and systematic errors in quadrature, this amounts to a tension of 1.8 standard deviations versus the combined result of the PrimEx-I and -II experiments, 8.34 (±0.13) × 10^{-17} s. Although this difference could be a statistical fluctuation, it provides motivation to revisit the theory prediction. The $\gamma\pi \to \pi\pi$ reaction also has a sharp low-energy prediction based on the chiral anomaly (*6*, *7*) and is being investigated by the COMPASS experiment (*8*).

The $\gamma\gamma$ decay width of π^0 has recently been evaluated from first principles using lattice quantum chromodynamics simulations (*9*). This numerical result is in agreement with the experimental measurement, but with its full uncertainty of 7%, it does not yet have the precision to clarify the above-mentioned tension between theory and experiment. Still, lattice quantum chromodynamics calculations have the potential to improve in the near future. The π^0-$\gamma\gamma$ coupling allows the two photons to scatter off each other through formation of the π^0 resonance. "Scattering of light by light" is one of the virtual processes that cause the magnetic dipole moment g of the muon to deviate from 2. This process is one of the leading sources of uncertainty in the predicting $(g-2)_\mu$, whose measurement serves as a precision test of the standard model of particle physics (*10*). Therefore, the new precision measurement of the pion lifetime by Larin *et al.* contributes to consolidating the standard model prediction of this important quantity. ■

Limits on a lifetime

The neutral pion π^0 lifetime measured by Larin *et al.* can be compared to the calculated lifetime, which depends on the matrix element illustrated below.

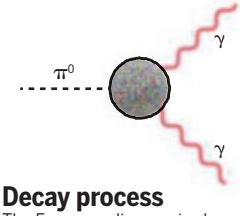

Decay process
The Feynman diagram is shown for the decay amplitude of π^0 into two photons γ.

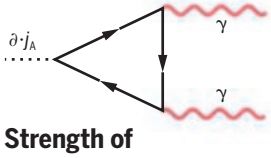

Strength of π^0-$\gamma\gamma$ coupling
The matrix element of the divergence of the axial current, $\partial \cdot j_A$, between the vacuum and a $\gamma\gamma$ state can be calculated exactly from this triangle diagram.

Institute for Nuclear Physics, University of Mainz, 55099 Mainz, Germany. Email: meyerh@uni-mainz.de

GRAPHIC: A. KITTERMAN/*SCIENCE*

REFERENCES AND NOTES

1. I. Larin *et al.*, *Science* **368**, 506 (2020).
2. S. L. Adler, *Phys. Rev.* **177**, 2426 (1969).
3. J. Bell, R. Jackiw, *Nuovo Cim. A* **60**, 47 (1969).
4. A. M. Bernstein, B. R. Holstein, *Rev. Mod. Phys.* **85**, 49 (2013).
5. K. Kampf, B. Moussallam, *Phys. Rev. D* **79**, 076005 (2009).
6. J. Wess, B. Zumino, *Phys. Lett. B* **37**, 95 (1971).
7. E. Witten, *Nucl. Phys. B* **223**, 422 (1983).
8. COMPASS Collaboration, J. M. Friedrich, *EPJ Web Conf.* **199**, 01016 (2019).
9. A. Gérardin, H. B. Meyer, A. Nyffeler, *Phys. Rev. D* **100**, 3034520 (2019).
10. F. Jegerlehner, *The Anomalous Magnetic Moment of the Muon* (Springer, 2017).

ACKNOWLEDGMENTS

H.B.M.'s work is supported by the European Research Council (ERC) under the European Union's Horizon 2020 research and innovation program through grant agreement 771971-SIMDAMA.

10.1126/science.aba8063

METABOLISM

Exercised cytokines promote endurance

Muscle tissue secretory response to exercise promotes beneficial metabolism

By **Jorge C. Correia** *and* **Jorge L. Ruas**

Exercise is important for human health. Many of the beneficial effects of exercise come from the activation of metabolism to drive muscle contraction, which mobilizes and utilizes fuel stores and promotes healthy systemic energy homeostasis. Conversely, sedentary behaviors are linked to higher incidence of diseases such as diabetes and cardiovascular disorders, but also neurodegeneration and certain types of cancer (*1*). For these reasons, identifying the molecular mediators of the benefits of exercise could provide new therapeutic tools to fight many chronic diseases. On page 488 of this issue, Knudsen *et al.* (*2*) report that the cytokine interleukin-13 (IL-13) is produced in mouse skeletal muscle tissue and increases with exercise. This cytokine is necessary for the metabolic adaptation to exercise and enhances endurance and systemic metabolism in mice.

Molecular and Cellular Exercise Physiology, Department of Physiology and Pharmacology, Biomedicum, Karolinska Institutet, 171 77 Stockholm, Sweden. Email: jorge.ruas@ki.se

The complexity of skeletal muscle is often overlooked. In addition to muscle fibers, skeletal muscle has many other resident cells such as muscle stem cells (satellite cells), myoblasts, fibroblasts, fibro-adipogenic precursors (a specialized mesenchymal cell), endothelial cells, and immune cells. Adaptation to exercise training depends on proficient communication between them, often through secreted factors or "exerkines". To date, most efforts to identify exerkines have focused on factors secreted by muscle fibers, called myokines. These can have autocrine, paracrine, and/or endocrine actions and affect muscle size and strength, systemic energy expenditure, immunity, and mental health, among others (*3, 4*). The findings of Knudsen *et al.* establish that IL-13, potentially secreted by type 2 innate lymphoid cells (ILC2s) within the skeletal muscle, elicits metabolic reprograming in skeletal muscle fibers. ILC2s are a type of immune cell mainly associated with immune responses to allergens and helminth infections. Identified only a decade ago, ILC2s are emerging as key regulators of metabolic homeostasis, tissue regeneration, and fibrosis (*5*). These findings further implicate these cells at the interface between immunity and muscle metabolism.

Muscle contraction requires high amounts of energy, mainly provided by oxidation of glucose and fatty acids. These fuels can be stored in muscle fibers or mobilized from liver and adipose tissue. The choice of which fuel to oxidize during endurance exercise depends on factors such as exercise duration and intensity, and the training state of the individual (*6*). This is the case for both rodents and humans. For example, in individuals who exercise at mild to moderate intensities, muscle fibers use fatty acid oxidation almost exclusively. Prioritizing fatty acid utilization until the supply and transport to skeletal muscle becomes limiting conserves glucose stores (as glycogen) for later stages of performance. Exercise training not only delays the switch to glucose oxidation but also makes it more energy efficient (*6*, *7*).

Knudsen *et al.* show that IL-13 in skeletal muscle is important for this metabolic flexibility. Indeed, mice in which the *Il13* gene was deleted preferentially used mus-

PHOTO: KLEIN AND HUBERT/MINDEN PICTURES

Enduring prolonged activity takes regular exercise and the release of "exerkines" from muscles.

cle glycogen stores and showed reduced performance in endurance exercise. Even after several weeks of training, they were unable to up-regulate the expression of genes necessary for muscle oxidative metabolism and to improve performance. Delivering IL-13 to mouse skeletal muscle in vivo conferred an endurance training–like effect, which translated into increased exercise performance and a mild improvement in the ability of muscle to take up glucose from circulation. It remains to be determined how the IL-13–mediated break on glycolysis is removed to allow exercise at higher intensity.

Mechanistically, Knudsen *et al.* demonstrate that signal transducer and activator of transcription 3 (STAT3) is essential for the effects of IL-13 on skeletal muscle metabolism and performance. STAT3 is a ubiquitously expressed transcription factor that activates gene programs associated with cell survival, proliferation, and growth in response to a variety of cytokines and growth factors, most notably IL-6. STAT3 has important regulatory functions in a plethora of physiological and pathophysiological processes, including embryonic development, wound healing, cancer, and immunity (*8*). In skeletal muscle, the effects of STAT3 activation are complex and context dependent. Heightened STAT3 activation has been implicated in the development of cancer cachexia (muscle wasting in cancer patients) and in the pathophysiology of various muscular diseases (*9*). Activation of STAT3 in fibro-adipogenic progenitors contributes to mouse skeletal muscle atrophy and fibrosis induced by experimental denervation (*10*), whereas transient pharmacological inhibition of STAT3 improves muscle regeneration in old and dystrophic mice by expanding the pool of satellite cells (*11*). Thus, STAT3 inhibition (widely pursued in clinical trials as a therapy for various types of cancer) has emerged as a potential therapeutic approach for muscular diseases.

Despite its negative effects on skeletal muscle function, STAT3 is transiently activated in muscle fibers by resistance exercise, suggesting a potential role for STAT3 signaling in the physiological adaptation to exercise. Furthermore, Knudsen *et al.* showed that, in mice, STAT3 is activated by endurance exercise and that STAT3 signaling in skeletal muscle fibers is necessary for the beneficial effects of IL-13 on exercise performance and glucose homeostasis. These findings change the view of STAT3, which to date was mostly considered deleterious to skeletal muscle function. This positive role of STAT3 in muscle metabolism should be taken into consideration when devising potential therapies that inhibit STAT3 signaling in skeletal muscle.

In the quest for health-promoting strategies, exercise training and maintaining muscle metabolic fitness are some of the best tools available. The identification of IL-13 as an exerkine that promotes muscle oxidative metabolism could be the foundation for future therapies to help patients with metabolic dysregulation. It will be interesting to follow how the biological effects of IL-13 fit within the larger picture of systemic adaptations to exercise. ■

REFERENCES AND NOTES

1. C. Handschin, B. M. Spiegelman, *Nature* **454**, 463 (2008).
2. N. Knudsen *et al.*, *Science* **368**, eaat3987 (2020).
3. R. Piccirillo, *Front. Physiol.* **10**, 287 (2019).
4. I. Cervenka, L. Z. Agudelo, J. L. Ruas, *Science* **357**, eaaf9794 (2017).
5. M. Messing, S. C. Jan-Abu, K. McNagny, *Int. J. Mol. Sci.* **21**, E1350 (2020).
6. J. Hawley, *Aust. J. Nutr. Diet* **58**, S19 (2001).
7. L. Z. Agudelo *et al.*, *Nat. Commun.* **10**, 2767 (2019).
8. A. C. Guanizo *et al.*, *Growth Factors* **36**, 1 (2018).
9. E. Guadagnin, D. Mázala, Y. W. Chen, *Int. J. Mol. Sci.* **19**, E2265 (2018).
10. L. Madaro *et al.*, *Nat. Cell Biol.* **20**, 917 (2018).
11. M. T. Tierney *et al.*, *Nat. Med.* **20**, 1182 (2014).

10.1126/science.abb4116

NEUROSCIENCE

Dampening light sensitivity

An inhibitory signal from the retina limits the response to light

By **Jennifer Ding** *and* **Wei Wei**

In the eyes of vertebrates, the retina detects incoming photons of visible light and transforms them through intricate neural circuits into multiple channels of visual information that are then conveyed to the brain. Each channel is represented by the spiking activity of a specific type of retinal ganglion cell (RGC) whose axons project to one or more brain regions to support a multitude of visual functions (*1*). Like many other long-range projection neurons in the brain, RGCs provide excitatory inputs to their targets in the brain using the neurotransmitter glutamate (*2*). On page 527 of this issue, Sonoda *et al.* (*3*) describe an inhibitory channel from the eye to the brain by way of a subset of intrinsically photosensitive RGCs (ipRGCs) that release γ-aminobutyric acid (GABA) in mice. The authors report that the inhibitory inputs from these GABAergic ipRGCs are involved in curbing the sensitivity of certain non–image-forming behaviors and renders them resilient to minor perturbations in light level.

The excitatory glutamatergic signaling of RGCs is unequivocally established by anatomical, physiological, and molecular characterizations of the retina and retinorecipient structures in the brain, such as the dorsal lateral geniculate nucleus (dLGN) and the superior colliculus (SC) (*4*–*6*). Curiously, earlier immunohistochemical studies indicated that a small number of RGCs in several mammalian species express markers of GABAergic neurotransmission, such as GABA and the GABA synthesis enzyme glutamate decarboxylase (GAD) (*7*–*9*). However, the function of these apparent GABAergic RGCs is unknown.

Sonoda *et al.* revisit this puzzle in the mouse by leveraging the powerful toolset of circuit analysis available for this model organism. Using a transgenic mouse line in which GABAergic neurons are selectively labeled, they found that GAD-expressing cells are a small subset of ipRGCs (~10%)

Department of Neurobiology, University of Chicago, Chicago, IL, USA. Email: weiw@uchicago.edu

and project to the expected brain targets of ipRGCs such as the suprachiasmatic nucleus (SCN), the circadian pacemaker that regulates the body clock, and the olivary pretectal nucleus (OPN), a structure involved in pupillary light reflex. Furthermore, by optogenetically activating these GAD-expressing ipRGCs, the authors show that these cells make functional GABAergic synapses with neurons in the SCN. Among SCN neurons showing postsynaptic responses to activated GAD-expressing RGC axons, ~30% received GABAergic inhibitory inputs.

These findings allude to a previously unknown level of complexity in ipRGCs, which are distinct among RGCs for their intrinsic photosensitivity. Unlike other RGCs that solely rely on rod and cone photoreceptors in the outer retina for light detection, ipRGCs express the photopigment melanopsin and thereby can be activated by light even in the absence of rod and cone photoreceptor inputs (*10*, *11*). There are at least six different types of ipRGCs in the mouse retina (*12*, *13*). Future characterization of the morphology and physiology of these GABAergic ipRGCs in the retina will clarify whether these inhibitory minorities belong to the existing type(s) or form a new type in the ipRGC family. Notably, Sonoda *et al.* found that most of the SCN neurons that received optogenetically activated GABAergic retinal inputs also received simultaneous glutamatergic retinal inputs, raising the intriguing possibility that GABAergic ipRGCs may corelease glutamate and GABA from their axonal terminals; this awaits further testing.

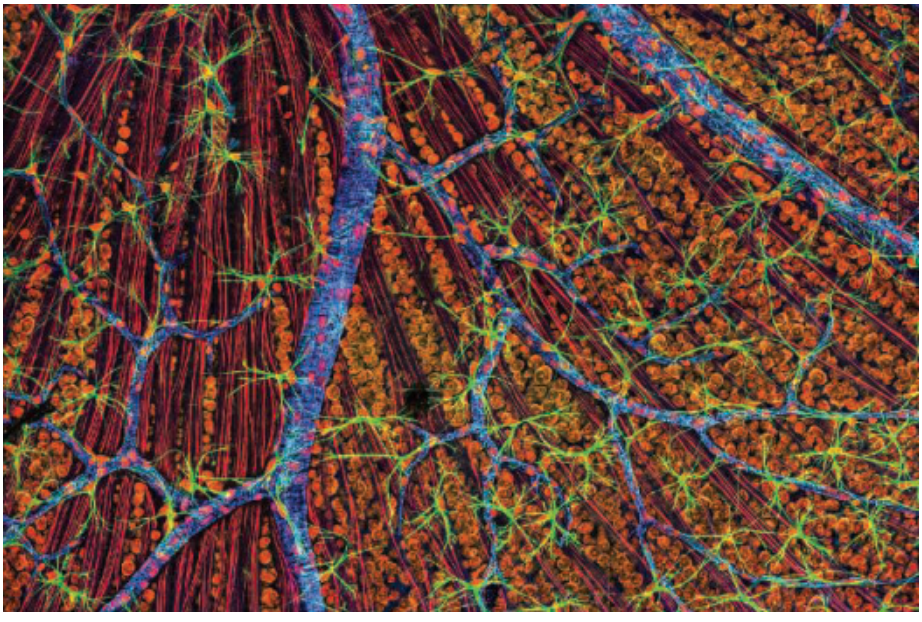

The retina is connected to the brain by retinal ganglion cells (orange) and their optic nerve fibers (red).

Given the prominent axonal projections of GABAergic ipRGCs in the SCN and the OPN, Sonoda *et al.* examined the effect of GABAergic signaling from these ipRGCs on two non–image-forming behaviors mediated by these nuclei: respectively, circadian photoentrainment and pupillary light reflex. Circadian photoentrainment is the synchronization of the body's internal clock with the solar cycle. Pupillary light reflex assists the adaptation of vision to different light levels by controlling the diameter of the pupil to light intensity. Glutamatergic ipRGC inputs to the SCN and OPN inform these brain nuclei about ambient light level of the visual environment (*14*). The retinal inputs interact with the rest of the brain circuitries to synchronize internal circadian rhythm with the solar cycle and adjust pupil diameter. When Sonoda *et al.* disrupted the GABAergic output channel from the retina by genetically deleting *Gad* in ipRGCs, they found that the mutant mice were able to perform circadian photoentrainment more effectively at lower light levels and had a more sensitive pupillary light reflex in dim light compared with that of control animals. Thus, the authors propose that the GABAergic ipRGC inputs dampen the sensitivity of SCN and OPN circuits that are driven by the more common glutamatergic ipRGC inputs so that the non–image-forming behaviors are more resilient to smaller fluctuations in brightness.

How do GABAergic ipRGC inputs feed into the circuits of non–image-forming brain structures? Sonoda *et al.* have begun exploring the wiring specificity of GABAergic ipRGCs to SCN neuronal subpopulations. They observed a similar proportion of GABAergic retinal inputs to vasoactive intestinal peptide (VIP)–positive and VIP-negative SCN neurons, whereas glutamatergic retinal inputs are more frequently detected in the VIP-positive group. Interpreting these results would require a more comprehensive understanding of SCN circuitry than is currently available. Notably, a recent study in mice that combined genetic labeling and a state-of-the-art imaging technique called correlated light and electron microscopy reveals exceptional diversity in ipRGC axonal morphology and presynaptic bouton connectivity with target neurons in the SCN and the OPN (*15*).

In the SCN, ipRGC axonal terminals preferentially target distal dendrites and are enriched in a population of putative GABAergic neurons that make dendro-dendritic synapses with each other (*15*). Future efforts in determining the precise axonal targeting patterns of GABAergic ipRGC axons in the SCN and the OPN will provide insights into how the opposing retinal signals from GABAergic and glutamatergic ipRGCs are integrated to set the sensitivity of non–image-forming behaviors at the circuit level. Furthermore, Sonoda *et al.* also showed evidence for GABAergic ipRGC projections to image-forming regions such as the medial posterior superior colliculus and the shell of the dorsal lateral geniculate nucleus. Assessing how this inhibitory retinal channel can dually influence conscious visual behavior would also be of future interest. Overall, the work of Sonoda *et al.* has opened the door for the study of functional GABAergic ipRGC circuits in higher-order visual centers and offers new and exciting hypotheses for future exploration. ■

REFERENCES AND NOTES

1. J. R. Sanes, R. H. Masland, *Annu. Rev. Neurosci.* **38**, 221 (2015).
2. S. C. Massey, in Progress in Retinal Research, N. N. Osborne, G. Chader, Eds. (Pergamon, 1990), vol. 9, pp. 399–425.
3. T. Sonoda *et al.*, *Science* **368**, 527 (2020).
4. J. R. Wilson, M. J. Friedlander, S. M. Sherman, *Proc. R. Soc.* **8221**, 411 (1984).
5. T. Sakurai, T. Miyamoto, Y. Okada, *Neurosci. Lett.* **109**, 299 (1990).
6. R. R. Mize, G. D. Butler, *J. Comp. Neurol.* **371**, 633 (1996).
7. B.-C. Yu, C. B. Watt, D. M. K. Lam, K. R. Fry, *Brain Res.* **439**, 376 (1988).
8. N. Lugo-García, R. E. Blanco, *Brain Res.* **564**, 19 (1991).
9. P. C. Rogers, D. V. Pow, *Vis. Neurosci.* **12**, 1143 (1995).
10. D. M. Berson, F. A. Dunn, M. Takao, *Science* **295**, 1070 (2002).
11. S. Hattar *et al.*, *Science* **295**, 1065 (2002).
12. L. Lazzerini Ospri *et al.*, *Annu. Rev. Neurosci.* **40**, 539 (2017).
13. L. E. Quattrochi *et al.*, *J. Comp. Neurol.* **527**, 297 (2019).
14. C. S. Colwell, *Nat. Rev. Neurosci.* **12**, 553 (2011).
15. K.-Y. Kim *et al.*, *Cell Rep.* **29**, 628 (2019).

ACKNOWLEDGMENTS

This work was supported by NIH 1R01NS109990 and NSF GRFP DGE-1746045 (J.D.).

10.1126/science.abb7529

PHOTO: NCMIR/TOM DEERINCK/SCIENCE SOURCE

QQ group: 970508760

Cytokine release syndrome in severe COVID-19

Lessons from arthritis and cell therapy in cancer patients point to therapy for severe disease

By **John B. Moore**[1] *and* **Carl H. June**[2]

In December 2019, a new strain of coronavirus, severe acute respiratory syndrome–coronavirus 2 (SARS-CoV-2), was recognized to have emerged in Wuhan, China. Along with SARS-CoV and Middle East respiratory syndrome–coronavirus (MERS-CoV), SARS-CoV-2 is the third coronavirus to cause severe respiratory illness in humans, called coronavirus disease 2019 (COVID-19). This was recognized as a pandemic by the World Health Organization (WHO) in March 2020 and has had considerable global economic and health impacts. Although the situation is rapidly evolving, severe disease manifested by fever and pneumonia, leading to acute respiratory distress syndrome (ARDS), has been described in up to 20% of COVID-19 cases. This is reminiscent of cytokine release syndrome (CRS)–induced ARDS and secondary hemophagocytic lymphohistiocytosis (sHLH) observed in patients with SARS-CoV and MERS-CoV as well as in leukemia patients receiving engineered T cell therapy. Given this experience, urgently needed therapeutics based on suppressing CRS, such as tocilizumab, have entered clinical trials to treat COVID-19.

SARS-CoV-2 is a betacoronavirus that is most closely related to SARS-CoV. Both viruses use the angiotensin-converting enzyme–related carboxypeptidase (ACE2) receptor to gain entry to cells. This receptor is widely expressed in cardiopulmonary tissues but also in some hematopoietic cells, including monocytes and macrophages. A key feature of COVID-19 infection is lymphopenia (low blood lymphocyte count), which correlates with clinical severity (*1*). SARS-CoV efficiently infects primary human monocytes and dendritic cells, whereas MERS-CoV infects monocytes and T cells via dipeptidyl peptidase 4 (DPP4) (*2*, *3*). It is possible that SARS-CoV-2 also infects dendritic cells. T cell apoptosis and exhaustion resulting from defective activation due to dendritic cell dysfunction might contribute to the immunopathology of COVID-19 (*2*, *4*). However, lymphopenia as a biomarker of poor prognosis for COVID-19 is not specific because it was also a biomarker that correlated with fatality in the 2009 influenza A (H1N1) pandemic (*5*).

CRS was found to be the major cause of morbidity in patients infected with SARS-CoV and MERS-CoV (*6*). Elevated serum concentrations of the cytokine interleukin-6 (IL-6) and other inflammatory cytokines are hallmarks of severe MERS-CoV infections (*7*). CRS is common in patients with COVID-19, and elevated serum IL-6 correlates with respiratory failure, ARDS, and adverse clinical outcomes (*8*, *9*). Elevated serum C-reactive protein (CRP), a protein whose expression is driven by IL-6, is also a biomarker of severe betacoronavirus infection.

Betacoronavirus infection of monocytes, macrophages, and dendritic cells results in their activation and secretion of IL-6 and other inflammatory cytokines. IL-6 has prominent proinflammatory properties (see the figure). IL-6 can signal through two main pathways referred to as classic cis signaling or trans signaling (*10*). In cis signaling, IL-6 binds to membrane-bound IL-6 receptor (mIL-6R) in a complex with gp130; downstream signal transduction is mediated by JAKs (Janus kinases) and STAT3 (signal transducer and activator of transcription 3). Membrane-bound gp130 is ubiquitously expressed, whereas mIL-6R expression is restricted largely to immune cells. Activation of cis signaling results in pleiotropic effects on the acquired immune system (B and T cells) as well as the innate immune system [neutrophils, macrophages, and natural killer (NK) cells], which can contribute to CRS (*10*).

In trans signaling, high circulating concentrations of IL-6 bind to the soluble form of IL-6R (sIL-6R), forming a complex with a gp130 dimer on potentially all cell surfaces. The resultant IL-6–sIL-6R–JAK-STAT3 signaling is then activated in cells that do not express mIL-6R, such as endothelial cells. This results in a systemic "cytokine storm" involving secretion of vascular endothelial growth factor (VEGF), monocyte chemoattractant protein–1 (MCP-1), IL-8, and additional IL-6, as well as reduced E-cadherin expression on endothelial cells (*11*). VEGF and reduced E-cadherin expression contribute to vascular permeability and leakage, which participate in the pathophysiology of hypotension and pulmonary dysfunction in ARDS.

sHLH is a hyperinflammatory syndrome characterized by CRS, cytopenias (low blood cell counts), and multiorgan failure (including the liver) (*12*). In adults, sHLH is most commonly triggered by severe viral infections but also occurs in leukemia patients receiving engineered T cell therapy. In addition to elevated serum cytokines, high concentrations of ferritin are characteristic of sHLH. CD163-expressing macrophages are implicated as the source of ferritin given their role in reticuloendothelial iron signaling, hence sHLH is alternatively known as macrophage activation syndrome. A retrospective study of COVID-19 patients found that elevated serum ferritin and IL-6 correlated with nonsurvivors (*9*).

Patients receiving chimeric antigen receptor (CAR) T cell therapy can also develop CRS and sHLH. This therapy involves engineering patient T cells to express CAR molecules that recognize antigens on tumor cells. When transplanted back into the patient, these engineered T cells target tumor cells, thereby activating immune clearance. Emily Whitehead, the first patient to receive CD19-targeted CAR T cells to treat pediatric B cell acute lymphoblastic leukemia in 2012, developed severe CRS and sHLH, leading to ARDS with multiorgan failure and hypotension that was refractory to standard treatment with steroids (*13*). Because of greatly elevated serum IL-6 in this patient, she was treated empirically with tocilizumab, an IL-6R antagonist approved at the time to treat rheumatic conditions such as juvenile idiopathic arthritis. She received a single dose of tocilizumab on day 7 after CAR T cell administration, with rapid resolution of fever within hours followed by weaning from vasopressors (which treat hypotension) and from ventilator support as ARDS resolved. Tocilizumab is now approved by the U.S. Food and Drug Administration (FDA) for the treatment of CAR T cell–induced CRS, with confirmed efficacy and minimal side effects in hundreds of patients.

The efficacy of IL-6–IL-6R antagonists for the treatment of CRS as well as sHLH underscores the central role of IL-6 signaling in the pathophysiology of cytokine-driven hyperinflammatory syndromes (*10*). Severe COVID-19 cases may benefit from IL-6 pathway inhibition given the associated CRS- and sHLH-like serum cytokine elevations. Indeed, preliminary results from an open-label study in 21 patients with COVID-19 treated with tocilizumab in China are encouraging (*14*). Fever subsided

[1]Department of Hematology-Oncology, Walter Reed National Military Medical Center, Bethesda, MD, USA. [2]Center for Cellular Immunotherapies, University of Pennsylvania, Philadelphia, PA, USA. Email: john.b.moore74.mil@mail.mil; cjune@upenn.edu

Pathways leading to cytokine release syndrome

Coronavirus infection results in monocyte, macrophage, and dendritic cell activation. IL-6 release then instigates an amplification cascade that results in cis signaling with T_H17 differentiation, among other lymphocytic changes, and trans signaling in many cell types, such as endothelial cells. The resulting increased systemic cytokine production contributes to the pathophysiology of severe COVID-19, including hypotension and acute respiratory distress syndrome (ARDS), which might be treated with IL-6 antagonists such as tocilizumab, sarilumab, and siltuximab.

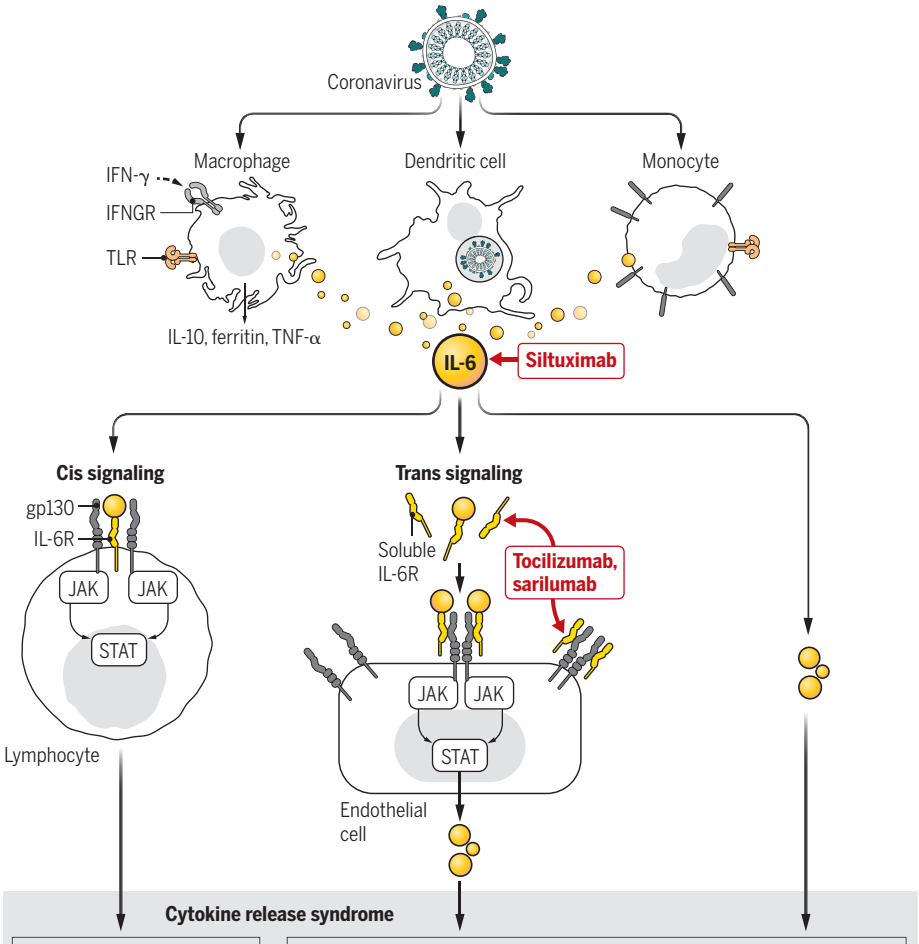

C3, complement 3; CRP, C reactive protein; IFN-γ, interferon-γ; IFNGR, IFN-γ receptor; IL, interleukin; IL-6R, IL-6 receptor; JAK, Janus kinase; MCP-1, monocyte chemoattractant protein–1; STAT3, signal transducer and activator of transcription 3; T_{FH}, T follicular helper cell; T_H17, T helper 17 cell; TNF-α, tumor necrosis factor–α; TLR, Toll-like receptor; TPO, thrombopoietin; T_{reg}, T regulatory cell; VEGF, vascular endothelial growth factor.

in all patients within the first day of receiving tocilizumab. Oxygen requirements were reduced in 75% of the patients (*14*).

Controlled clinical trials are under way worldwide to test IL-6 and IL-6R antagonists for the management of COVID-19 patients with severe respiratory complications. One issue to resolve is whether there will be differential effectiveness between IL-6 antagonists and IL-6R antagonists. Relevant to this is that IL-6R inhibitors can suppress both cis and trans signaling as well as trans presentation, a recently described third mode of signaling. Trans presentation involves IL-6 binding to mIL-6R expressed on an immune cell, which forms a complex with gp130 on T helper 17 (TH17) cells, leading to downstream T cell signaling that may be involved in ARDS (*10*, *11*, *15*). However, IL-6 inhibitors can suppress only cis and trans signaling. The immediate goal of IL-6 antagonism is to ameliorate severe COVID-19 cases so that requirements for advanced care are minimized. The long-term goal should include a focus on the development of antivirals and vaccines that prevent or ameliorate the infection.

There are a number of caveats to consider, given the global urgency of mitigating the COVID-19 pandemic. In sepsis-associated ARDS, corticosteroids are often administered. However, corticosteroid use in SARS and MERS patients did not improve mortality and resulted in delayed viral clearance (*6*). As a result, the expert consensus from infectious disease authorities and the WHO is to avoid systemic corticosteroids in COVID-19 patients at present. A theoretical possibility is that the suppression of inflammation by IL-6 antagonism might delay viral clearance. However, IL-6 blockade also results in rapid reduction of serum IL-10, an immunosuppressive cytokine secreted by macrophages, which may mitigate concerns about prolonging viral clearance (*11*). Moreover, one or two doses of an IL-6 antagonist are unlikely to result in complications, such as fungal infections or osteonecrosis of the jaw, which occur in patients dosed monthly on these drugs for chronic conditions such as rheumatoid arthritis. It is notable that tocilizumab was first approved for rheumatic conditions, then for CRS in patients receiving CAR T cell therapy, and is now being further repurposed for the COVID-19 pandemic. It is possible that IL-6 directed therapies will be used in future pandemics involving other viruses such as influenza and Ebola (*5*, *11*). ■

REFERENCES AND NOTES

1. X. Yang *et al.*, *Lancet Respir. Med.* 10.1016/S2213-2600(20)30079-5 (2020).
2. H. Chu *et al.*, *J. Infect. Dis.* **213**, 904 (2016).
3. H. K. Law *et al.*, *Blood* **106**, 2366 (2005).
4. M. Zheng *et al.*, *Cell. Mol. Immunol.* 10.1038/s41423-020-0402-2 (2020).
5. R. Perez-Padilla *et al.*, *N. Engl. J. Med.* **361**, 680 (2009).
6. R. Channappanavar, S. Perlman, *Semin. Immunopathol.* **39**, 529 (2017).
7. A. R. Fehr, R. Channappanavar, S. Perlman, *Annu. Rev. Med.* **68**, 387 (2017).
8. G. Chen *et al.*, *J. Clin. Invest.* 137244 (2020).
9. Q. Ruan, K. Yang, W. Wang, L. Jiang, J. Song, *Intensive Care Med.* 10.1007/s00134-020-05991-x (2020).
10. S. Kang, T. Tanaka, M. Narazaki, T. Kishimoto, *Immunity* **50**, 1007 (2019).
11. T. Tanaka, M. Narazaki, T. Kishimoto, *Immunotherapy* **8**, 959 (2016).
12. C. B. Crayne, S. Albeituni, K. E. Nichols, R. Q. Cron, *Front. Immunol.* **10**, 119 (2019).
13. S. A. Grupp *et al.*, *N. Engl. J. Med.* **368**, 1509 (2013).
14. X. Xu *et al.*, *ChinaXiv* 202003 (5 March 2020).
15. S. Heink *et al.*, *Nat. Immunol.* **18**, 74 (2017).

ACKNOWLEDGMENTS

This work was funded by NIH grant 2R01CA120409 (C.H.J.) and a sponsored research grant from the Parker Institute for Cancer Immunotherapy. J.B.M. is an employee of the U.S. Government. This work was prepared as part of his official duties. The views expressed in this article are those of the authors and do not necessarily reflect the official policy or position of the Department of the Navy, the Department of Defense, or the U.S. Government. The therapeutics discussed in this Perspective are undergoing clinical testing and are not currently approved for the treatment of COVID-19.

Published online 17 April 2020
10.1126/science.abb8925

GRAPHIC: V. ALTOUNIAN/*SCIENCE*

RETROSPECTIVE

Philip W. Anderson (1923–2020)

Intellectual giant of condensed matter physics

By **Patrick A. Lee**[1] *and* **N. Phuan Ong**[2]

Philip Anderson, groundbreaking physicist, died on 29 March at the age of 96. During his prolific career, Anderson launched many major branches of condensed matter physics. He excelled in extracting deep, foundational principles from raw experimental data and designed models that elegantly captured the essence of seemingly intractable quantum phenomena.

Anderson was born on 13 December 1923 in Indianapolis, Indiana. After obtaining his Ph.D. in physics from Harvard University in 1949 under the guidance of John H. Van Vleck, Anderson joined Bell Labs (where P.A.L. met him). In 1975, he joined the faculty at Princeton University (where he met N.P.O.) and remained there until his retirement in 1996.

Anderson had an uncanny ability to sniff out the deep questions raised by experimental data. In the late 1950s, experiments on silicon had found that the diffusion of a spin wave packet became anomalously slow at a temperature of 4 K. Anderson theorized that this "localization" (which he initially called "cisport," a wordplay on "transport") resulted from coherent interference of multiple reflections of the wave packet in a disordered crystalline environment. This 1958 prediction, dubbed "Anderson localization," was cited in his 1977 Nobel Prize. In the 1980s, Anderson localization blossomed into a major experimental industry, and it has since been applied to optics, astronomy, ultracold atoms, and tumor detection in mammography.

Anderson's work in the 1950s also laid the foundation for the modern theory of magnetism by explaining how electron spins form local magnetic moments. This is an example of broken symmetry, where a system has less symmetry than suggested by basic physical laws. In a 1972 article in *Science* titled "More is different," Anderson expanded on this concept, emphasizing that knowing the laws of physics at the microscopic level is not sufficient for understanding nature on a macroscopic scale. Anderson resolved another fundamental problem soon after physicists John Bardeen, Leon Cooper, and John Robert Schrieffer published the theory of superconductivity in 1957. The symmetry breaking that was identified was expected to lead to a zero-mass mode, which was not seen in a superconductor. Anderson resolved this puzzle by pointing out that, in a superconductor, the wave function is coupled to the electromagnetic field, which merges with the zero-mass mode to become the familiar plasma oscillations. The photon has acquired a mass inside the superconductor. Anderson recognized that this mechanism solved the important problem of unwanted massless particles in theories hotly pursued at the time to unify quantum electrodynamics and weak interactions. Physicist Peter Higgs and others carried out the fully relativistic formulation, but Higgs gave Anderson credit in his paper and Nobel lecture. The Anderson-Higgs mechanism is now a cornerstone of particle and condensed matter physics.

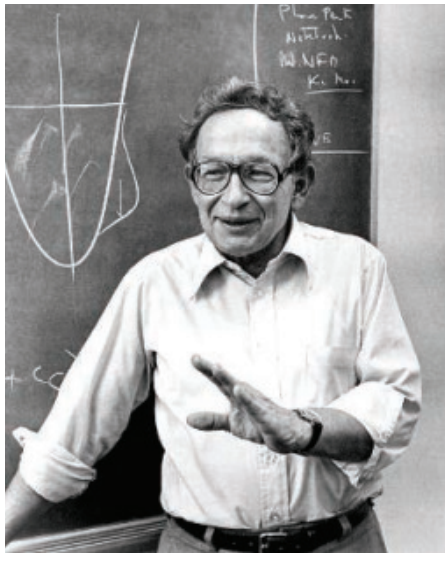

PHOTO: EMILIO SEGRE VISUAL ARCHIVES/AMERICAN INSTITUTE OF PHYSICS/SCIENCE SOURCE

Shortly after the discovery in 1986 of high-temperature (high-T_c) superconductivity in cuprates, Anderson proposed a radical theory. He suggested that the parent state of the high-T_c superconductor is a magnetic insulator driven by strong electron repulsion. Removing some of the electrons by chemical substitution allows the vacancies ("holes") to move freely and conduct current. Anderson's identification of the parent state is now universally accepted. To explain why the mobile holes pair up to realize superconductivity, Anderson invoked the physics of spin liquids, which he pioneered in 1973. In a spin liquid, spins fail to attain the antiferromagnetic state because of conflicting lattice constraints and quantum fluctuations. Anderson called this the resonating valence bond (RVB) state. He proposed that when carriers are introduced into this state, it becomes a superconductor. These revolutionary ideas encountered considerable resistance. Today, although Anderson's specific mechanism remains controversial, many of the ideas in his 1987 paper, such as superconductivity arising from strong repulsion, have gained wide acceptance. The RVB state is the archetypal example of a quantum spin liquid, currently a topic of intense interest. Another idea of great importance is that the excitations of the spin liquid behave as electrons that have lost their charge but retain their spin. This early example of the notion of fractionalization is supported by exactly soluble models as well as by recent experiments. In time, Anderson's spin liquid RVB theory may well be remembered as his most profound and prescient.

Despite being a self-professed curmudgeon, Anderson was compassionate and amazingly loyal to friends and colleagues. Former students who had hit a rough patch often moved back to Princeton to work with him until they regained their footing. After learning that a collaborator had suffered a stroke, Anderson flew to stay with him for a week. He had a puckish sense of humor. During dinners that he and his wife, Joyce, regularly hosted, Anderson, offering coffee, would ask each guest "caffeine or non?" He would then prepare a single pot mixed with the correct proportions of each. To our amusement, he and Joyce took great pleasure in belting out songs by Tom Lehrer (a friend from college). Both held strong antiestablishment convictions. At the height of the Vietnam War, Anderson was once detained by security for posting "Stop the Bombing" pamphlets at Bell Labs. He was a vocal opponent of the Strategic Defense Initiative. Well into his 90s, Anderson retained a vibrant curiosity. He wanted to know who Dr. Dre was (a frequent clue in the *New York Times* crossword puzzle) and wanted to hear "Desolation Row" after Bob Dylan's Nobel Prize win.

Anderson's expansive intellect, his passion, and the special insights he brought to everything he touched will be sorely missed. His passing marks the loss of the last of the intellectual giants who shaped the field of quantum matter. ■

[1]Department of Physics, Massachusetts Institute of Technology, Cambridge, MA, USA. [2]Department of Physics, Princeton University, Princeton, NJ, USA. Email: palee@mit.edu; npo@princeton.edu

10.1126/science.abc1042

POLICY FORUM

RESEARCH ETHICS: COVID-19

Against pandemic research exceptionalism

Crises are no excuse for lowering scientific standards

By **Alex John London**[1] *and* **Jonathan Kimmelman**[2]

The global outbreak of coronavirus disease 2019 (COVID-19) has seen a deluge of clinical studies, with hundreds registered on clinicaltrials.gov. But a palpable sense of urgency and a lingering concern that "in critical situations, large randomized controlled trials are not always feasible or ethical" (*1*) perpetuate the perception that, when it comes to the rigors of science, crisis situations demand exceptions to high standards for quality. Early phase studies have been launched before completion of investigations that would normally be required to warrant further development of the intervention (*2*), and treatment trials have used research strategies that are easy to implement but unlikely to yield unbiased effect estimates. Numerous trials investigating similar hypotheses risk duplication of effort, and droves of research papers have been rushed to preprint servers, essentially outsourcing peer review to practicing physicians and journalists. Although crises present major logistical and practical challenges, the moral mission of research remains the same: to reduce uncertainty and enable caregivers, health systems, and policy-makers to better address individual and public health. Rather than generating permission to carry out low-quality investigations, the urgency and scarcity of pandemics heighten the responsibility of key actors in the research enterprise to coordinate their activities to uphold the standards necessary to advance this mission.

Rigorous research practices can't eliminate all uncertainty from medicine, but they represent the most efficient way to clarify the causal relationships clinicians hope to exploit in decisions with momentous consequences for patients and health systems. Nevertheless, fastidious research standards may seem a luxury that pandemics can ill accommodate. Commenting on a study using suboptimal design, one group of scientists stated, "Given the urgency of the situation, some limitations…may be acceptable, including the small sample size, use of an unvalidated surrogate end point, and lack of randomization or blinding" (*1*). The perception that core methodological components of high-quality research are dispensable is underpinned by three problematic assumptions. The first is that some evidence now, even if flawed, seems preferable to expending greater resources on more-demanding studies whose benefits only materialize later. Because the window for learning in pandemics is often short, the need to "balance scientific rigor against speed" seems inevitable (*3*).

The problem with this view is that challenges that rigorous methods address do not disappear in the face of urgent need. Small studies that build on basic science and preclinical research in early phases of drug development routinely generate signals of promise that are not confirmed in subsequent trials. Even when new drugs are established to be safe and effective, rarely are their benefits so massive that they can be detected in small, open-label, nonrandomized trials. The proliferation of small studies that are not part of an orchestrated trajectory of development is a recipe for generating false leads that threaten to divert already scarce resources toward ineffective practices, slow the uptake of effective interventions because of an inability to reliably detect smaller but clinically meaningful benefits, and engender treatment preferences that make patients and clinicians reluctant to participate in randomized trials. These problems are amplified by published reports of compassionate use, which was designed as an alternative pathway to access interventions outside of research, not to support systematic evaluation.

The second underpinning of research exceptionalism is the view that key features of rigorous research, like randomization or placebo comparators, conflict with clinicians' care obligations. However, when studies begin in, and are designed to disturb a state of, clinical equipoise (meaning that it's uncertain whether a particular treatment is better than the alternatives), they ensure that no study participant receives a standard of care known to be inferior to any available alternative (*4*). Under this condition, randomized trials with appropriate comparators configure medical practice in a way that allows patients to access investigational interventions under conditions designed to eliminate ineffective strategies and exploit effective alternatives.

The third underpinning of research exceptionalism derives from the expectation that researchers and sponsors are generally free to exercise broad discretion over the organization and design of research. However, that discretion never operates in a vacuum. Even under normal conditions, the goal of research ethics and policy is to use regulations, reporting guidelines, and other social controls to align research conduct with the public interest. Crucially, the information that research produces is a public good on which caregivers, health systems, and policy-makers rely to efficiently discharge important moral responsibilities. As recent international guidelines for ethical research emphasize, the justification for research is its social and scientific value, understood as its ability to produce the information that multiple actors need to make decisions that implicate health, welfare, and the use of scarce resources (*5*).

To enable stakeholders to fulfill their social responsibilities, research should embody five conditions of informativeness and social value (*6*). The first is importance. Trials should address key evidence gaps. Interventions selected for testing should capture the most promising therapeutic and prophylactic alternatives as judged from reviews of existing evidence and trials. They should aim to detect effects that are realistic but clinically meaningful. As of this writing, more than 18 clinical trials enrolling more than 75,000 patients have been registered in North America for testing various hydroxychloroquine regimens for COVID-19. This massive commitment concentrates resources on nearly identical clinical hypotheses, creates competition for recruitment, and neglects opportunities to test other clinical hypotheses. Testing different regimens derived from a common clinical hypothesis in uncoordinated protocols increases the probability of false-positive findings due to chance (*7*). This also frustrates cross-comparisons and squanders opportunities to evaluate regimens side by side (*8*).

The second component is rigorous design. Trials should be designed to detect clinically meaningful effects so that both positive and negative results serve the informational needs of clinicians and health systems. Studies designed to detect massive effects often eschew randomization or use surrogate end points. Although easily launched, such studies are at high risk for producing inconclusive findings that sow confusion and necessitate further

[1]Center for Ethics and Policy, Carnegie Mellon University, Pittsburgh, PA, USA. [2]Studies of Translation, Ethics, and Medicine (STREAM), Biomedical Ethics Unit, McGill University, Montreal, QC, Canada. Email: jonathan.kimmelman@mcgill.ca

evaluation. The decision to forgo a dummy comparator and use a nonvalidated surrogate end point, absenteeism, in a study testing use of a tuberculosis vaccine to prevent coronavirus infection jeopardizes the study's ability to clarify the merits of this intervention (*9*).

The third component is analytical integrity. Designs should be prespecified in protocols, prospectively registered, and analyzed in accordance with prespecification. A recent study of hydroxychloroquine reported a beneficial effect on clinical primary outcomes in a preprint, whereas registration documents revealed a different study design and a polymerase chain reaction –based primary end point. The glaring discrepancy, a well-known source of bias in trials, was not flagged in some reporting on the trial (*10*).

Fourth, trials should be reported completely, promptly, and consistently with prespecified analyses. One reporting challenge present in the best of times, and likely to reemerge during pandemics, is the deposition of positive findings in preprint servers earlier than nonpositive studies. Another challenge is quality control. Qualified peer reviewers are a scarce resource, and the proliferation of low-quality papers saps the ability of scientists to place findings into context before they are publicized (*11*). Some recent trials garnering press coverage did not adhere to well-established reporting standards.

The fifth component is feasibility: Studies must have a credible prospect of reaching their recruitment target and being completed within a time frame where the evidence is still actionable. This condition is in tension with the others because their resource demands under conditions of scarcity create the prospect that research might never be completed. However, making research feasible by relaxing the other four standards contradicts the social justification for research. The system of incentives normally used to align research actors with the public good is imperfect in noncrisis situations and likely to be ineffective in the context of a pandemic. Therefore, to meet the requirement of feasibility, investigators, sponsors, health systems, and regulators have responsibilities to make exceptional efforts to cooperate and collaborate in a way that concentrates resources on a portfolio of studies that satisfy the above conditions.

Sponsors, research consortia, and health agencies should prioritize research approaches that test multiple interventions, foster modularity, and permit timely adaptation (*12*). Master protocols enable multiple interventions to be trialed under a common statistical framework, facilitating cross-comparisons and promoting multicenter collaboration (*13*). Adaptive designs allow flagging interventions to be dropped quickly and promising alternatives to be added with fewer delays than would be incurred from the design and approval of new studies. Seamless trial designs reduce transition time between trial phases and can extend into the provision of care to large numbers of patients.

Individual clinicians should avoid off-label use of unvalidated interventions that might interfere with trial recruitment and resist the urge to carry out uncontrolled, open-label studies. They should instead seek out opportunities to join larger, carefully orchestrated protocols to increase the prospect that high-quality studies will be completed quickly and generate the information needed to advance individual and public health. Academic medical centers can facilitate such coordination by surveying the landscape of ongoing studies and establishing mechanisms for "prioritization review" to triage studies (*14*). The goal would be to incentivize participation in efforts that uphold the criteria outlined here and to foster robust participation in multicenter studies so that data can be generated from different institutions before their capacity to meet fastidious research requirements is overwhelmed by surging medical demand.

Regulatory agencies and public health authorities should play a leading role in identifying studies that meet these standards and fostering collaboration among a sufficient number of centers to ensure adequate recruitment and timely results. They should also avoid making public recommendations or granting emergency use authorization for interventions whose clinical merits remain to be established and, instead, present clinical trials as a mechanism for addressing uncertainty without compromising patient interests. At public briefings, health authorities can point stakeholders to trials being pursued within their catchment and report recruitment milestones to elevate the profile and progress of high-quality studies.

Greater coordination of research effort, such as this coronavirus disease 2019 (COVID-19) vaccine trial, can help maintain exacting standards during a crisis.

PHOTO: TED S. WARREN/AP PHOTO

In a report on the ethics and science of research conducted during the 2014–2015 Ebola outbreak (during which ethical and practical concerns about using standard research methodologies, like randomization and placebo comparators, yielded a body of inconclusive findings), a U.S. National Academy of Medicine committee argued that clinical research is an integral part of outbreak response and that "despite [the] sense of urgency, research during an epidemic is still subject to the same core scientific and ethical requirements that govern all research on human subjects" (*15*). One lesson of the current outbreak is that expeditious research in a crisis situation is feasible. Absent robust leadership from regulators, health authorities, and major funding bodies, however, the responsibility for coordinating research activities falls to the wide range of stakeholders who might normally pursue research on a more independent basis. Although many of these parties face powerful, parochial incentives to conduct research that is feasible with the resources that are locally available, the exigencies of crisis situations like global pandemics require exceptional steps to combine efforts, divide labor, and triage out low-value and duplicative research. ■

REFERENCES AND NOTES

1. A. H. J. Kim *et al*., *Ann. Intern. Med*. 10.7326/M20-1223(2020).
2. E. Broodman, "Researchers rush to test coronavirus vaccine in people without knowing how well it works in animals," *Stat*, 11 March 2020; www.statnews.com/2020/03/11/researchers-rush-to-start-moderna-coronavirus-vaccine-trial-without-usual-animal-testing/.
3. K. Kupferschmidt, J. Cohen, "WHO launches global megatrial of the four most promising coronavirus treatments," *Science*, eabb8497, 22 March 2020; www.sciencemag.org/news/2020/03/who-launches-global-megatrial-four-most-promising-coronavirus-treatments.
4. A. J. London, *Bioethics* **33**, 326 (2019).
5. Council for International Organizations of Medical Sciences (CIOMS), "International ethical guidelines for health-related research involving humans, fourth edition" (CIOMS, Geneva, 2016), pp. 1–2.
6. D. A. Zarin *et al*., *JAMA* **322**, 813 (2019).
7. A. J. London, J. Kimmelman, *Hastings Cent. Rep*. **49**, 31 (2019).
8. L. E. Dodd *et al*., *Sci. Transl. Med*. **11**, eaaw1049 (2019).
9. J. de Vrieze, *Science*, eaab8297, 23 March 2020; www.sciencemag.org/news/2020/03/can-century-old-tb-vaccine-steel-immune-system-against-new-coronavirus.
10. D. Grady, "Malaria drug helps virus patients improve, in small study," New York Times, 1 April 2020; www.nytimes.com/2020/04/01/health/hydroxychloroquine-coronavirus-malaria.html.
11. A. Marcus, I. Oransky, "The science of this pandemic is moving at dangerous speeds," Wired, 28 March 2020; www.wired.com/story/the-science-of-this-pandemic-is-moving-at-dangerous-speeds/.
12. D. C. Angus *et al*., *Nat. Rev. Drug Discov*. **18**, 797 (2019).
13. N. E. Dean *et al*., *N. Engl. J. Med*. **382**, 1366 (2020).
14. L. Gelinas *et al*., *J. Med. Ethics* **43**, 803 (2017).
15. National Academies of Sciences, Engineering, and Medicine, "Integrating clinical research into epidemic response: The Ebola experience" (The National Academies Press, Washington, DC, 2017).

Published online 23 April 2020
10.1126/science.abc1731

BOOKS *et al.*

History and literature can provide tinctures against existential terror.

PHOTO: CULTURA CREATIVE (RF)/ALAMY STOCK PHOTO

HISTORY OF SCIENCE

Tinctures of time and Schrödinger's virus

Literature and science converge in a pandemic

By **Luis Campos**

"Tedious were it to recount, how citizen avoided citizen, how among neighbours was scarce found any that shewed fellow-feeling for another, how kinsfolk held aloof, and never met," wrote Giovanni Boccaccio in the *Decameron* ca. 1349, having retreated to a villa outside of Florence amid the "great dying" of the bubonic plague (*1*). More than three centuries later, Daniel Defoe recounted similarly trying times in *A Journal of the Plague Year*: "When every one's private Safety lay so near them, that they had no Room to pity the Distresses of others…The Danger of immediate Death to ourselves, took away all Bonds of Love, all Concern for one another" (*2*).

Our lives are overturned by such "emergent occasions," as John Donne reported in 1624 in *Devotions upon Emergent Occasions*: "We study *Health*, and we deliberate upon our *meats*, and *drink*, and *ayre*, and *exercises*, and we hew, and we polish every stone, that goes to that building; and so our *Health* is a long and a regular work; But in a minute a Canon batters all, overthrowes all, demolishes all; a *Sicknes* unprevented for all our diligence, unsuspected for all our curiositie…summons us, seizes us, possesses us, destroyes us in an instant" (*3*).

What written consolations might we turn to in this time of COVID-19? For those searching for meaning in the midst of plague, history and literature have long offered tinctures against terror.

A body is burdened with a sickness, as Susan Sontag well understood, but it is the body politic that suffers in a pandemic, as our social life changes irrevocably. "Well, everybody is worried about everybody now," she wrote in a work of fiction in the *New Yorker* in 1986, during the burgeoning AIDS crisis. "[T]hat seems to be the way we live, the way we live now…the end of bravado, the end of folly, the end of trusting life, the end of taking life for granted" (*4*).

Even echoes of an earlier generation's atomic anxieties and apocalypses register differently when read in this moment. Nevil Shute's 1957 postapocalyptic novel *On the Beach*, for example, now seems to eerily presage our own tallying of 2-week quarantines in cities not yet abandoned but already rewilding: "'It's horrible,' she said vehemently. 'Everything shut up, and dirty, and stinking. It's as if the end of the world had come already.' 'It's pretty close, you know,' he said… 'How far off is it, Peter?' 'About a fortnight,' he said. 'It doesn't happen with a click, you know. People start getting ill, but not all on the same day. Some people are more resistant than others.'…'But everybody gets it, don't they?' she asked in a low tone. 'I mean, in the end.' He nodded. 'Everybody gets it, in the end.'…'It's possible to get it slightly and get over it,' he said. 'But then you get it again ten days or a fortnight later.'…He nodded. 'That's the way it is. We've just got to take it as it comes. After all, it's what we've always had to face, only we've never faced it, because we're young'" (*5*).

In an effort to understand our present predicament, we turn not only to earlier fears but also to speculative futures, whether in the form of scientific models or science fiction novels. Although it was terrestrial microbes that ended H. G. Wells's 1898 novel

The reviewer is secretary of the History of Science Society and regents' lecturer in the Department of History, University of New Mexico, Albuquerque, NM 87131, USA. Email: luiscampos@unm.edu

The War of the Worlds, fictional fears of cosmic pandemics—like those Michael Crichton described in *The Andromeda Strain* in 1969—are not new to the world of science. On the day after the famed 1975 Asilomar Conference addressing the potential biohazards of recombinant DNA research, the *Boston Globe* trumpeted on its front page: "Scientists to Resume Risky Work on Genes: Danger of 'Andromeda Strain' Posed" (*6*). And in the years that followed, narratives about alien-induced pandemics repeatedly intruded into conversations on Capitol Hill about appropriate laboratory biocontainment strategies for newly engineered organisms.

While many might (and did) deride such references to intergalactic fiction as mere sensationalism, these sorts of invocations—framing legislative responses within not only the language of science but also that of science fiction—suggest that we would do well to seek to understand the unexpected and sometimes unruly cultural narratives in which science is always situated.

"Plague came to Whileaway in P.C. 17 (Preceding Catastrophe) and ended in A.C. 03, with half the population dead," wrote Joanna Russ in 1975 in *The Female Man*, a brilliant feminist novel that deploys plague and tinctures of time as part of a larger critique of gender essentialism (*7*). The plague "started so slowly that no one knew about it until it was too late. It attacked males only." But what need is there of such fictions of plague when the future itself is terrifying enough?

Climate change will bring about new plagues, asserted David Wallace-Wells in 2019 in *The Uninhabitable Earth*. "[T]here are the plagues that climate change will confront us with for the very first time—a whole new universe of diseases humans have never before known to even worry about. 'New universe' is not hyperbole. Scientists guess the planet could harbor more than a million yet-to-be-discovered viruses" (*8*). The effects of even one of these viruses run amok could be dire, he envisioned (as we are now experiencing). In the face of climate change, Wallace-Wells predicts "the global halving of economic resources would be permanent…a brutally cruel normal against which we might measure tiny burps of decimal-point growth as the breath of a new prosperity…in economic terms, a Great Dying." Another great dying, except this time, a villa in Tuscany offers no refuge.

As unprotected heroes head into hospitals and supermarkets, many of the rest of us pass unending challenging days at home, echoing the weary, entrapped, plague-addled world of Samuel Delany's 1975 novel *Dhalgren*: "You do *know* how terrible it is to live inside here…with everything slipping away?…This has got to stop, you know! Management must be having all sorts of difficulty while we're going through this crisis. I understand that. I make allowances. But it's not as though a bomb had fallen, or anything. If a bomb had fallen, we'd be dead. This is something perfectly natural. And we have to make do, don't we, until the situation is rectified?" (*9*).

"The existential inconvenience of coronavirus," as Geoff Dyer described our moment in the *New Yorker* in March (*10*), alludes to Jean-Paul Sartre's truth that in a time of existential crisis, "hell is other people" (*11*). But our ability to physically distance while remaining socially connected through social media has also brought forth playful parallels offering poignant critique: "We all have Schrödinger's virus now," wrote one Mat Krahn, now enjoying his 15 minutes of Facebook fame. "Because we cannot get tested, we can't know whether we have the virus or not. We have to act as if we have the virus so that we don't spread it to others. We have to act as if we've never had the virus because if we didn't have it, we're not immune. Therefore, we both have and don't have the virus. Thus, Schrödinger's virus" (*12*).

Historians tell us that there is a rhythm to life and death, not only for individuals but also for societies. "Epidemics start at a moment in time, proceed on a stage limited in space and duration, follow a plot line of increasing and revelatory tension, move to a crisis of individual and collective character, then drift toward closure," the historian of medicine Charles Rosenberg has written (*13*). As laboratory workers pursue promising leads, and the battle between "freedom from" and "freedom to" plays out in countries around the world, we might even turn to Emily Dickinson, who—in the tiniest tincture of all—queries whether our political leaders will finally recognize the urgencies of the moment: "Faith is a fine invention / For Gentlemen who *see*! / But Microscopes are prudent / In an Emergency!" (*14*). ■

REFERENCES AND NOTES

1. G. Boccaccio, *Decameron* (ca. 1349).
2. D. Defoe, *A Journal of the Plague Year* (1722).
3. J. Donne, *Devotions upon Emergent Occasions* (1624).
4. S. Sontag, "The way we live now," *New Yorker*, 24 November 1986.
5. N. Shute, *On the Beach* (Heinemann, 1957).
6. *Boston Globe*, 28 February 1975, p. 1.
7. J. Russ, *The Female Man* (Bantam Books, 1975).
8. D. Wallace-Wells, *The Uninhabitable Earth* (Tim Duggan Books, 2019).
9. S. Delany, *Dhalgren* (Bantam Books, 1975).
10. G. Dyer, "The existential inconvenience of coronavirus," *New Yorker*, 23 March 2020.
11. J.-P. Sartre, *No Exit (Huis Clos)* (1944).
12. Mat Krahn, Facebook, 30 March 2020; www.facebook.com/mat.krahn/posts/3076953808995462.
13. C. Rosenberg, *Daedalus* **118**, 1 (1989).
14. E. Dickinson, *The Complete Poems of Emily Dickinson* (Little, Brown, 1924).

10.1126/science.abc1732

THE GOLDEN GOOSE AWARD

Congratulations to the 2019 Winners

David Sachar
The Frog Skin that Saved 50 Million Lives

Noel Rose and Ernest Witebsky
Advancing Autoimmunity

Jack Levin and Frederik Bang
The Blood of the Horseshoe Crab

The Golden Goose Award honors federally funded researchers whose work may have seemed odd or obscure when it was conducted but which led to major breakthroughs and significant societal benefit.

Nominations are now being accepted.

www.goldengooseaward.org

AAAS
AMERICAN ASSOCIATION FOR THE ADVANCEMENT OF SCIENCE

PSYCHOLOGY

The other public health crisis

Social connection is critical, but many struggle to form and maintain meaningful relationships

By **Joanna Schug**

As a fledgling physician, Vivek Murthy considered social issues such as loneliness to be outside the domain of doctoring. That all changed when he met a patient named James, whose health concerns appeared to stem from social isolation that started after winning the lottery. In restructuring his life to his new economic standing, James had inadvertently cut himself off from his existing support network, sending his health into a downward spiral. In his book *Together*, Murthy—who served as the 19th surgeon general of the United States—draws from decades of scientific research and his own experiences with patients like James to show just how damaging loneliness can be.

The timing of the book's release coincides with a global public health crisis, as people around the world adapt to the ongoing COVID-19 pandemic. Murthy's account of the factors driving loneliness and his suggestions to combat isolation are particularly poignant now, as many abide by recommendations to stay home and avoid social contact with others.

The reviewer is at the Department of Psychological Sciences, College of William and Mary, Williamsburg, VA 23185, USA. Email: jschug@wm.edu

The link between loneliness and health is rooted in the evolutionary history of humankind. As a social species, early humans depended on their communities for food, shelter, and safety. Survival required building and maintaining relationships with others, and exclusion from these relationships was deadly. Given this history, it is no wonder that the drive to connect with others—and the pain experienced when disconnected from others—emerged as a very important survival instinct.

Just as experiencing physical pain signals our body to move away from the pain source, the pain we feel when separated or excluded from social relationships can serve as a signal to reconnect with our friends, family, and community. When forming or maintaining these important social bonds proves difficult, our mental and physical health suffers.

Whereas early humans would have lived in tight-knit communities where social connections were guaranteed, advances in mobility and technology in modern society make sustaining social relationships both effortful and difficult. Many of us live far away from our families and friends, and hectic careers quickly absorb the time needed to cultivate relationships. Many of our social interactions now take place through screens rather than in person, and increasingly individualistic cultures cause us to put less priority on our relationships.

Together: The Healing Power of Human Connection in a Sometimes Lonely World
Vivek H. Murthy
Harper Wave, 2020. 352 pp.

Murthy describes how many such cultural and technological factors can have both positive and negative impacts on our relationships. Social media, for example, can help us keep in touch with friends and family across long distances and enable us to reconnect with loved ones from whom we have grown apart. At the same time, technology can prevent us from investing in our relationships with those closest to us, leading to greater disconnect.

Collectivistic communities—those that emphasize the needs of the group over the needs of individuals—can foster connectedness by providing social institutions that bind people together. But oppressive social norms inherent in many such communities can cause undue stress, and those who do not conform to these norms can be ostracized and left even more isolated than those from individualistic communities. Understanding the profound necessity of connectedness and how we can protect ourselves from isolation in modern society can help us to take deliberate action to cultivate our relationships with others.

For those who are fortunate, the practice of social distancing during the COVID-19 pandemic may provide valuable opportunities to reconnect with family and loved ones quarantined at home. For many others, the situation will be dire. Those living alone will experience increased isolation, and those most at risk, such as the elderly and ill, may be kept in isolation from their loved ones. On a societal level, the public health implications of this widespread disconnect may be severe.

By showcasing research on the impact of loneliness and its social and environmental antecedents, Murthy presents a road map of the various pathways that lead to connection or isolation. Although the path to connectedness may be long and arduous, particularly while social distancing, the direction in which we must head is clear. ■

Technology can help us connect with others, but it can also prevent us from investing deeply in relationships.

PHOTO: ISTOCK.COM/TOLGART

10.1126/science.abb3582

Invasive sun corals threaten Brazil's native reefs.

PHOTO: LEO FRANCINI/ALAMY STOCK PHOTO

Edited by **Jennifer Sills**

Brazil policy invites marine invasive species

Invasive species threaten biodiversity and ecosystem function and can affect human well-being and services (*1*). In November 2019, Brazil's Tourism Ministry launched a plan to sink 1200 scrapped ships, trains, and airplanes, most of them inside marine protected areas (MPAs) (*2*), supposedly to promote diving tourism business. Artificial reefs, such as those that would be created by sinking these vehicles, are used by invading species as stepping-stones to natural reefs, causing ecological, social, and economic deterioration (*3*). This plan, if implemented, would undermine efforts to attain Convention on Biological Diversity (*4*) and National Environmental Policy Act targets (*5*).

Among the most likely invaders are sun corals (*Tubastraea* spp.), which were first reported in Brazil on oil platforms in the 1980s (*6*). These noxious corals spread along 3000 km of coastline, aided by transfer on the oil industry's platforms and drill ships as well as shipwrecks (*3*). On natural reefs, sun corals kill native corals, change reef communities and processes (*3*, *7*), and modify seascapes (*8*), causing loss of income and requiring management (*9*).

In February 2020, ships sunk by the government between 2009 and 2017 were found to be covered in sun corals near the largest coastal reefs in Brazil, the Costa dos Corais MPA (*10*). The government plans to sink scrap in other sensitive areas, such as the World Heritage–listed Fernando de Noronha Marine National Park (*11*). Brazil has a National Plan for the prevention of sun corals that highlights suppression of pathways of dispersion to protect native species and ecosystems (*5*), so the Tourism Ministry appears to be both ignoring its own government's advice and violating international conservation principles. The plan is controversial given that natural reefs and wrecks in Brazil are not overused by divers, and SCUBA is an expensive sport available to few people (*12*). Instead of moving forward with the plan to sink more ships, Brazil should encourage better use of natural reefs and historical shipwrecks and support monitoring and management of reefs.

Ricardo J. Miranda[1]*, José A. C. C. Nunes[2], Joel C. Creed[3], Francisco Barros[4], Raphael M. Macieira[5], Robson G Santos[1], Gislaine V. Lima[6], Antônio V. F. Pontes[6], Luís G. F. C. Silva[6], Ralf T. Cordeiro[7,8], Cláudio L. S. Sampaio[9], Taciana K. Pinto[9], Ana C. M. Malhado[1], Richard Ladle[1], Pedro HC Pereira[6]

[1]Universidade Federal de Alagoas, 57072-900, Maceió, Alagoas, Brazil. [2]Grupo de Ecologia Recifal, 40155-010, Salvador, Bahia, Brazil. [3]Universidade do Estado do Rio de Janeiro, 20550-900, Rio de Janeiro, Brazil. [4]Universidade Federal da Bahia, 40170-290, Salvador, Bahia, Brazil. [5]Universidade Federal do Espírito Santo, 29075-910, Vitória, Brazil. [6]Projeto Conservação Recifal, 51021-010, Recife, Pernambuco, Brazil. [7]Universidade Federal Rural de Pernambuco, 52171-900, Recife, Pernambuco, Brazil. [8]Department of Invertebrate Zoology, National Museum of Natural History, Smithsonian Institution, Washington, DC, 20013, USA. [9]Universidade Federal de Alagoas, 57000-200, Penedo, Alagoas, Brazil.
*Corresponding author.
Email: ricardojdemiranda@gmail.com

REFERENCES AND NOTES

1. L. Pejchar, H. A. Mooney, *Trends Ecol. Evol.* **24**, 497 (2009).
2. Ministério do Turismo, "Embratur anuncia programa de afundamento de navios para fomentar o turismo náutico," *Embratur* (2019) [in Portuguese].
3. J. C. Creed *et al.*, *Biol. Invasions* **19**, 283 (2017).
4. U.N. Convention on Biological Diversity, "Strategic Plan for Biodiversity 2011–2020 and the Aichi Targets" (2010).
5. Ministério do Meio Ambiente/Instituto Brasileiro do Meio Ambiente e dos Recursos Naturais Renováveis, "Plano Nacional de Prevenção, Controle e Monitoramento do coral-sol (*Tubastraea* spp.) no Brasil" (2018) [in Portuguese].
6. C. B. Castro, D. O. Pires, *Bull. Mar. Sci.* **69**, 357 (2001).
7. R. J. Miranda *et al.*, *Mar. Environ. Res.* **138**, 19 (2018).
8. K. C. C. Capel *et al.*, *Bull. Mar. Sci.* **96**, 217 (2020).
9. S. Rodrigues, "Empresas terão que adotar medidas contra coral-sol," *O Eco* (2017) [in Portuguese].
10. L. Markman, "Espécie de coral vira praga no litoral de Pernambuco e ameaça biodiversidade" *TV Globo* (2020) [in Portuguese].
11. A. Borges, "Sem regra ambiental, plano de Bolsonaro é fazer 73 naufrágios artificiais no litoral" *O Estado de S. Paulo* (2020) [in Portuguese].
12. R. Y. G. Rowe, G. E. O. Santos, *Cad. Virtual Tur.* **16**, 61 (2016).

COMPETING INTERESTS

R.J.M. receives funding from Coordenação de Aperfeiçoamento de Pessoal de Nível Superior, Conselho Nacional de Desenvolvimento Científico e Tecnológico, and Fundação de Amparo à Pesquisa do Estado de Alagoas.

10.1126/science.abb7255

Brazil threatens Indigenous lands

Brazil's President Jair Bolsonaro has adopted anti-environmental measures for the Amazon since taking office in January 2019 (*1*), and deforestation pressures are increasing with plans for expanding plantations of soy and other

export crops (including biofuels) and for building new roads, dams, and mines (*1*, *2*). On 6 February, Bolsonaro submitted a bill to Brazil's National Congress that would open Indigenous lands for mining, extraction of oil and gas, and construction of hydroelectric dams, cattle ranches, and mechanized monocultures such as soy (*3*). Indigenous leaders would be allowed to rent tribal land to non-Indigenous agribusiness entrepreneurs (*3*). The bill would allow mining in Indigenous lands without authorization from their Indigenous inhabitants (*3*). This bill, if passed, would violate the rights of Indigenous peoples and threaten the environment.

The Brazilian Society for the Progress of Science (SBPC) organized a public seminar at the National Institute of Amazonian Research (INPA) to discuss the risks the bill poses to Amazonia (*4*), and the organizers drafted an open letter alerting civil society and decision makers to the bill's violation of Brazilian legislation and ILO Convention 169, which require free, prior, and informed consultation of Indigenous peoples affected by actions such as this (*5*). The right to consultation has been routinely ignored by large enterprises in the Amazon, putting many traditional peoples at risk (*6*).

Bolsonaro's desire to open Indigenous lands to agribusiness and mining has often been expressed in his extemporaneous remarks and social media posts. Early in his term of office, a visit by his ministers of agriculture and environment to an illegal soy plantation in an Indigenous land signaled impunity for violations of current legal restrictions (*1*). The proposed law now makes the threat imminent. The administration's discourse is credited with invasions of Indigenous lands and killings of Indigenous leaders reaching record levels in 2019 (*7*). The impact of illegal gold miners (garimpeiros)—a constant threat to Indigenous lands—will now be even greater thanks to the proposed law and to the risk of spreading coronavirus disease 2019 (COVID-19). Bolsonaro has repeatedly expressed support for these invaders (*1*). On 14 April, his environment minister dismissed one of the directors of the environmental agency as punishment for having ordered the removal of garimpeiros from an Indigenous land (*8*).

Demarcated Indigenous lands represent 24% of Brazil's Amazon biome, thus protecting more than the 14% that is in federal "conservation units" (protected areas for biodiversity) (*9*). Indigenous lands act as shields protecting traditional peoples, biodiversity, carbon stocks, and ecosystem services. Destruction of these forested areas poses a risk to the entire planet, as it affects one of the world's largest carbon stocks (*10*). We urge the president of Brazil's Chamber of Deputies not to put this bill to a vote, and we encourage Brazil's Supreme Court to act quickly to protect the country's Indigenous peoples.

Lucas Ferrante[1]* and Philip M. Fearnside[2]
[1]Ecology Graduate Program, National Institute of Amazonian Research (INPA), Manaus, Amazonas, Brazil. [2]Department of Environmental Dynamics, INPA, Manaus, Amazonas, Brazil.
*Corresponding author.
E-mail: lucasferrante@hotmail.com

REFERENCES AND NOTES

1. L. Ferrante, P. M. Fearnside, *Environ. Conserv.* **46**, 261 (2019).
2. E. J. A. L. Pereira *et al.*, *Land Use Pol.*, 10.1016/j.landusepol.2020.104491 (2020).
3. Senado Notícias, "Chega ao Congresso projeto que permite mineração em terras indígenas" (2020); https://www12.senado.leg.br/noticias/materias/2020/02/06/chega-ao-congresso-projeto-que-permite-mineracao-em-terras-indigenas [in Portuguese].
4. SBPC, "SBPC-AM promove evento para discutir a Mineração na Amazônia" (2020); http://portal.sbpcnet.org.br/noticias/sbpc-am-promove-evento-para-discutir-a-mineracao-na-amazonia/ [in Portuguese].
5. SBPC, INPA, "Nota contra o Projeto de Lei 191/2020 e em defesa da Amazônia" (2020); www.jornaldaciencia.org.br/wp-content/uploads/2020/03/Nota_Oficial_SBPC_INPA.pdf [in Portuguese].
6. L. Ferrante, M. Gomes, P. M. Fearnside, *Land Use Pol.*, 10.1016/j.landusepol.2020.104548 (2020).
7. Human Rights Watch (HRW), *Rainforest Mafias: How Violence and Impunity Fuel Deforestation in Brazil's Amazon* (HRW, 2019); www.hrw.org/sites/default/files/report_pdf/brazil0919_web.pdf.
8. Jornal Nacional, "Ministro do Meio Ambiente exonera o diretor de Proteção Ambiental do Ibama" (2020); https://g1.globo.com/jornal-nacional/noticia/2020/04/14/ministro-do-meio-ambiente-exonera-o-diretor-de-protecao-ambiental-do-ibama.ghtml [in Portuguese].
9. E. M. Nogueira *et al.*, *Reg. Environ. Chang.* **18**, 261 (2018).
10. S. S. Saatchi *et al.*, *Proc. Natl. Acad. Sci. U.S.A.* **108**, 9899 (2011).

10.1126/science.abb6327

Call for transparency of COVID-19 models

A hallmark of science is the open exchange of knowledge. At this time of crisis, it is more important than ever for scientists around the world to openly share their knowledge, expertise, tools, and technology. Scientific models are critical tools for anticipating, predicting, and responding to complex biological, social, and environmental crises, including pandemics. They are essential for guiding regional and national governments in designing health, social, and economic policies to manage the spread of disease and lessen its impacts. However, presenting modeling results alone is not enough. Scientists must also openly share their model code so that the results can be replicated and evaluated.

Given the necessity for rapid response to the coronavirus pandemic, we need many eyes to review and collectively vet model assumptions, parameterizations, and algorithms to ensure the most accurate modeling possible. Transparency engenders public trust and is the best defense against misunderstanding, misuse, and deliberate misinformation about models and their results. We need to engage as many experts as possible for improving the ability of models to represent epidemiological, social, and economic dynamics so that we can best respond to the crisis and plan effectively to mitigate its wider impacts.

We strongly urge all scientists modeling the coronavirus disease 2019 (COVID-19) pandemic and its consequences for health and society to rapidly and openly publish their code (along with specifying the type of data required, model parameterizations, and any available documentation) so that it is accessible to all scientists around the world. We offer sincere thanks to the many teams that are already sharing their models openly. Proprietary black boxes and code withheld for competitive

NEXTGEN VOICES: SUBMIT NOW

Imagining a post-pandemic world

Add your voice to *Science*! Our new NextGen Voices survey is now open:
What do you hope or fear will be the long-term effects of the coronavirus disease 2019 (COVID-19) pandemic? To answer this question, imagine that you are a science writer in the year 2040. Write a science news story about an event, milestone, or debate taking place in 2040 and how it relates to the COVID-19 pandemic.

To submit, go to www.sciencemag.org/nextgen-voices
Deadline for submissions is 15 May. A selection of the best responses will be published in the 3 July issue of *Science*. Submissions should be 200 words or less. Anonymous submissions will not be considered.

motivations have no place in the global crisis we face today. As soon as possible, please place your code in a trusted digital repository (*1*) so that it is findable, accessible, interoperable, and reusable (*2*).

C. Michael Barton[1]*, Marina Alberti[2], Daniel Ames[3], Jo-An Atkinson[4], Jerad Bales[5], Edmund Burke[6], Min Chen[7], Saikou Y Diallo[8], David J. D. Earn[9], Brian Fath[10], Zhilan Feng[9], Christopher Gibbons[11], Ross Hammond[12], Jane Heffernan[9], Heather Houser[13], Peter S. Hovmand[14], Birgit Kopainsky[15], Patricia L. Mabry[16], Christina Mair[17], Petra Meier[18], Rebecca Niles[19], Brian Nosek[20], Nathaniel Osgood[21,22], Suzanne Pierce[23], J. Gareth Polhill[24], Lisa Prosser[25], Erin Robinson[26], Cynthia Rosenzweig[27], Shankar Sankaran[28], Kurt Stange[29], Gregory Tucker[30]

[1]Director, Network for Computational Modeling in Social and Ecological Sciences, Tempe, AZ, USA. [2]Director, Urban Eco-Evolutionary Research Network, Seattle, WA, USA. [3]President, International Environmental Modelling and Software Society, Manno, Ticino, Switzerland. [4]Managing Director, Computer Simulation and Advanced Research Technologies, Sidney, NSW, Australia. [5]Executive Director, Consortium of Universities for the Advancement of Hydrologic Science Inc., Cambridge, MA, USA. [6]President, Operational Research Society, Birmingham, West Midlands, UK. [7]Director, Open Geographic Modeling and Simulation at Nanjing Normal University, Nanjing, Jiangsu, China. [8]President, Society for Modeling and Simulation International, Suffolk, VA, USA. [9]Governing Committee, Mathematical Epidemiology Subgroup of the Society for Mathematical Biology, West Lafayette, IN, USA. [10]Secretary-General, International Society for Ecological Modeling, Severna Park, MD, USA. [11]Director, Business Intelligence Team of the City of Sheffield, Sheffield, South Yorkshire, UK. [12]Director, Center on Social Dynamics and Policy at the Brookings Institution, Washington, DC, USA. [13]Chair, Planet Texas 2050 Bridging Barriers Program at the University of Texas, Austin, TX, USA. [14]Director, Social System Design Lab of Washington University, St. Louis, MO, USA. [15]Director, System Dynamics Group at the University of Bergen, Bergen, Norway. [16]Research Investigator, HealthPartners Institute, Minneapolis, MN, USA. [17]Director, Center for Social Dynamics and Community Health of the University of Pittsburgh, Pittsburgh, PA, USA. [18]Director, Systems Science in Public Health and Health Economics Research Consortium, Sheffield, South Yorkshire, UK. [19]Executive Director, System Dynamics Society, Albany, NY, USA. [20]Director, Center for Open Science, Charlottesville, VA, USA. [21]Director, Computational Epidemiology and Public Health Informatics at the University of Saskatchewan, Saskatoon, SK, Canada. [22]Founder, System Science in Health, Saskatoon, SK, Canada. [23]Director, Intelligent Systems and Geosciences Research Coordination Network, Austin, TX, USA. [24]President, European Social Simulation Association, Zürich, Zürich, Switzerland. [25]President, Society for Medical Decision Making, Bridgewater, NJ, USA. [26]Executive Director, Earth Science Information Partners, Boulder, CO, USA. [27]Co-Leader, Agricultural Model Intercomparison and Improvement Project, New York, NY, USA. [28]President, International Society for the Systems Sciences, Ashland, KY, USA. [29]Director, Center for Community Health Integration at Case Western Reserve University, Cleveland, OH, USA. [30]Executive Director, Community Surface Dynamics Modeling System, Boulder, CO, USA.
*Corresponding author.
Email: michael.barton@asu.edu

REFERENCES AND NOTES

1. CoMSES Network, Trusted Digital Repositories (www.comses.net/resources/trusted-digital-repositories/).
2. M. D. Wilkinson *et al.*, *Sci. Data* **3**, 160018 (2016).

COMPETING INTERESTS

All authors have signed on behalf of the listed organizations only. J.-A.A. is the head of the Systems Modeling and Simulation, Brain and Mind Centre at the University of Sydney in Australia but does not represent that institution here. B.F. is affiliated with the Advanced Systems Analysis Program at the International Institute for Applied Systems Analysis in Austria but does not represent that organization.

10.1126/science.abb8637

ERRATA

Erratum for the Report "Design of an in vitro biocatalytic cascade for the manufacture of islatravir" by M. A. Huffman *et al.*, *Science* 368, eabc1954 (2020). Published online 17 April 2020; 10.1126/science.abc1954

Erratum for the Report "Mutual control of coherent spin waves and magnetic domain walls in a magnonic device" by J. Han *et al.*, *Science* 368, eabc1767 (2020). Published online 17 April 2020; 10.1126/science.abc1767

Science Webinars help you keep pace with emerging scientific fields!

Stay informed about scientific breakthroughs and discoveries.
Gain insights into current research from top scientists.
Take the opportunity to ask questions during live broadcasts.
Get alerts about upcoming free webinars.

Sign up at: webinar.sciencemag.org/stayinformed

RESEARCH

IN *SCIENCE* JOURNALS

Edited by **Michael Funk**

NANOPHOTONICS

Nanowire-based THz detection

Terahertz (THz) radiation is an interesting region of the electromagnetic spectrum lying between microwaves and infrared. Non-ionizing and transparent to most fabrics, it is finding application in security screening and imaging but is also being developed for communication and chemical sensing. To date, most THz detectors have focused just on signal intensity, an effort that discards half the signal in terms of the full optical state, including polarization. Peng *et al*. developed a THz detector based on crossed nanowires (arranged in a hash structure) that is capable of resolving the full state of the THz light. The approach provides a nanophotonic platform for the further development of THz-based technologies. —ISO *Science*, this issue p. 510

A detector made from crossed nanowires resolves the full polarization state of terahertz radiation.

CORONAVIRUS

Antiviral error catastrophe

The development of broad-spectrum antiviral drugs is desirable, particularly in the context of emerging zoonotic infections for which specific interventions do not yet exist. Sheahan *et al*. tested the potential of a ribonucleoside analog, β-D-N^4-hydroxycytidine, which was previously shown to be active against RNA viruses such as influenza and Ebola virus, to inhibit coronaviruses. This drug was effective in cell lines and primary human airway epithelial cultures against multiple coronaviruses, including severe acute respiratory syndrome–coronavirus 2 (SARS-CoV-2). Mouse models of two other coronaviruses demonstrated that early treatment reduced viral replication and damage to the lungs. Mechanistically, this drug is incorporated into the viral RNA, inducing mutations and eventually leading to error catastrophe in the virus. —LP

Sci. Transl. Med. **12**, eabb5883 (2020).

APPLIED ECOLOGY

New roads threaten Asian tigers

The development of road networks in Asia, specifically China's Belt and Road Initiative, is expanding at an unprecedented rate and eating up previously protected areas meant for endangered tigers. Carter *et al*. found that ~43% of the area where tiger breeding occurs and ~57% of tiger conservation landscapes have fallen prey to proliferating road networks. According to this analysis, more than 20% of tiger and prey abundance could decrease by the year 2050. Sustainable road development is thus an urgent priority to prevent further decreases in endangered tiger species. —SN

Sci. Adv. 10.1126/sciadv.aaz9619 (2020).

CORONAVIRUS

Tracing infection from mobility data

What sort of measures are required to contain the spread of severe acute respiratory syndrome–coronavirus 2 (SARS-CoV-2), which causes coronavirus disease 2019 (COVID-19)? The rich data from the Open COVID-19 Data Working Group include the dates when people first reported symptoms, not just a positive test date. Using these data and real-time travel data from the internet services company Baidu, Kraemer *et al*. found that mobility statistics offered a precise record of the spread of SARS-CoV-2 among the cities of China at the start of 2020. The frequency of introductions from Wuhan were predictive of the size of the epidemic sparked in other provinces. However, once the virus had escaped Wuhan, strict local control measures such as social isolation and hygiene, rather than

IMAGE: PENG *ET AL.*

long-distance travel restrictions, played the largest part in controlling SARS-CoV-2 spread. —CA

Science, this issue p. 493

CATALYSIS

A water boost for methanol synthesis

Model catalysts based on metals and metal oxides can dissociate methane (CH_4) at room temperature, converting it directly to methanol (CH_3OH). Liu *et al*. show that for one of these catalysts, an "inverted" CeO_x-Cu_2O oxide on Cu(111), water tunes the selectivity from forming CO and CO_2 to forming surface CH_3O groups, as revealed by ambient-pressure x-ray photoelectron spectroscopy. Theoretical modeling showed that adsorbed water blocks O_2 dissociation and O_2 instead oxidizes the reduced catalyst. Hydroxyl groups from water generate the CH_3O species from dissociated CH_4, and water then goes on to form and displace CH_3OH to the gas phase. —PDS

Science, this issue p. 513

CERAMICS

Speedy ceramic sintering

Synthesizing ceramics can require heating for long times at high temperatures, making the screening of high-throughput materials challenging. C. Wang *et al*. developed a new ceramic-sintering technique that uses resistive heating of thin carbon strips to ramp up and ramp down temperature quickly. This method allows for the quick synthesis of a wide variety of ceramics while mitigating the loss of volatile elements. Ultrafast sintering is ideal for synthesizing many compositions to screen for ideal properties for a variety of applications, including the development of new solid-state electrolytes. —BG

Science, this issue p. 521

A complex silicon oxycarbide structure fabricated by ultrafast high-temperature sintering

CREDITS (FROM LEFT): WANG *ET AL*.; JOSE CALVO/SCIENCE SOURCE

TISSUE REGENERATION

Equal opportunity tissue regeneration

Tissue regeneration is thought to be driven primarily by rare stem cells with distinctive properties. Single-cell RNA sequencing allows rigorous testing of this hypothesis. Karthaus *et al*. examined the regeneration of normal prostate tissue in mice after androgen ablation, a common treatment for prostate cancer (see the Perspective by Kelly). Unexpectedly, they found that in addition to rare stem cells, a large population of differentiated cells was a major contributor to prostate regeneration, a result that they confirmed in a study of human prostate tissue. Investigation of the molecular mechanism by which the differentiated cells acquired regenerative potential yielded insights that could potentially lead to improved therapies for prostate cancer. —PAK

Science, this issue p. 497; see also p. 467

SUPERCONDUCTIVITY

An unexpected order

The phase diagram of cuprate superconductors, in addition to superconductivity, contains many ordered states such as antiferromagnetism, charge density waves, and nematicity. Sarkar *et al*. show that ferromagnetism should be added to this list. Studying thin films of $La_{2-x}Ce_xCuO_4$ at high dopings, past the point at which superconductivity disappears, the researchers found signatures of ferromagnetism in both the transport and optical properties of the films. —JS

Science, this issue p. 532

IN OTHER JOURNALS

Edited by **Caroline Ash** *and* **Jesse Smith**

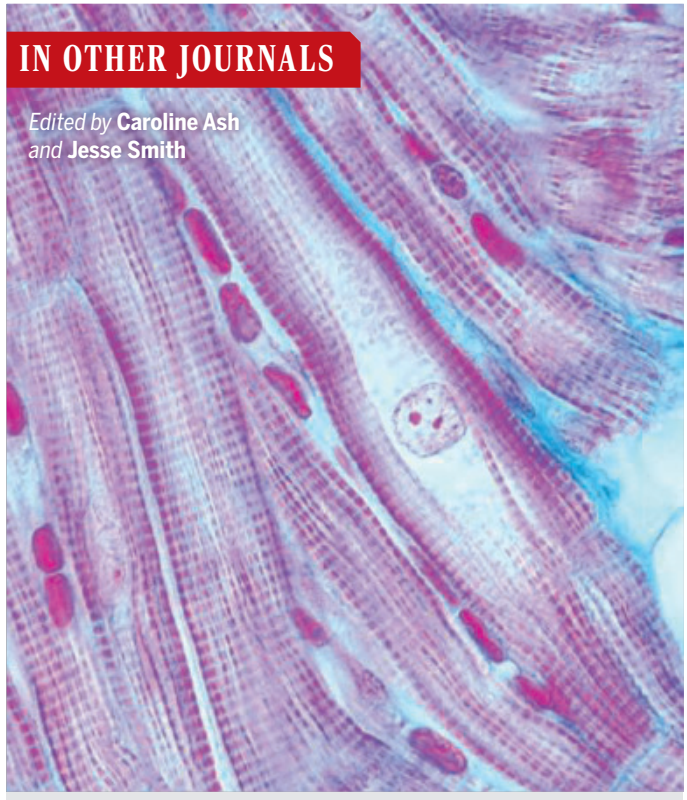

REGENERATION

Mending broken hearts

Adult heart muscle cells (cardiomyocytes) cannot regenerate after ischemic injury. However, neonatal cardiomyocytes do regenerate. Cui *et al*. undertook single-nucleus RNA sequencing of cardiomyocytes to find out how mice of various ages respond to heart injury. The gene expression profiles showed that several subsets of cardiomyocytes enter the cell cycle after injury, but these become depleted as mice age, and thus heart regeneration capacity declines. The authors identified two transcription factors involved in driving these responses to injury. Retrovirus-mediated expression of these factors in cardiomyocytes in mature mice helped to protect heart tissue from ischemic injury. These findings might inform new therapeutic strategies to treat patients with ischemic heart disease. —GKA

Dev. Cell **53**, 102 (2020).

Cardiac muscle cells, shown in this light micrograph, can regain some capacity to regenerate on treatment with transcription factors present in neonatal cells.

PHYSICS

A pseudo-real combination

Straining graphene can generate pseudomagnetic fields, which lead to some of the same effects as real magnetic fields. One of those effects is the formation of the so-called Landau energy levels, which can be probed through scanning tunneling spectroscopy. Li *et al*. used this technique to study the energy spectra along a nanoscale ripple in graphene. The nonuniform pseudomagnetic field generated on the ripple, in combination with a real applied magnetic field, caused a spatially

TOXINS

A poisonous relationship

Many animal species harbor microbes that provide specialized services, such as the production of poisonous molecules that the animals can accumulate to protect them from predation. Vaelli *et al.* studied the skin microbiome of rough-skinned newts, which are known to have population-level variations in their propensity to accumulate the ion channel blocker tetrodotoxin (TTX). They found that newts with high levels of TTX harbored a very different set of bacterial species, including those capable of producing this toxin. They also identified three mutations within newt ion channels that confer TTX resistance in vitro. An important question raised by these results is whether newts can manipulate their microbiome to cultivate the bacteria that produce TTX. —MAF

eLife **9**, e53898 (2020).

Rough-skinned newts (*Taricha granulosa*) with high levels of the poison tetrododoxin host a distinct set of bacteria that produce the toxin.

dependent splitting of Landau levels. The authors interpreted this splitting in terms of valley polarization, suggesting that the findings may contribute to the control of the valley degree of freedom in the emerging field of valleytronics. —JS

Phys. Rev. Lett. **124**, 106802 (2020).

EPIDEMIOLOGY

SARS-CoV-2 in Iceland

Like so many countries, Iceland, with its population of 364,000 inhabitants, has been stricken by severe acute respiratory syndrome coronavirus 2 (SARS-CoV-2). From 13 January through 4 April 2020, 13.3% of 9199 persons chosen for testing because they had symptoms or had traveled from places of high risk were found to be positive. Voluntary testing of 13,080 people from the general population revealed that 0.8% were positive for SARS-CoV-2. Using contact tracing, Gudbjartsson *et al*. revealed that the source of infection shifted over time, from travel to family contact. Viral sequencing data confirmed how imported viral strains spread to others in Iceland. The data from late March indicate a stable infection rate, showing the effect of the social distancing measures that Iceland put in place. —PJH

N. Engl. J. Med. 10.1056/NEJMoa2006100 (2020).

NEUROSCIENCE

Circuit promotes overeating

Compulsive eating can be induced in rodents by stimulation of γ-aminobutyric acid (GABA) neurons in the lateral hypothalamus. In mice, this promotes rapid approach to food and causes eating even if the animal has just finished a meal and is fully sated. Marino *et al*. investigated the brain circuitry involved in such paradoxical behavior. Stimulation failed to drive eating through interaction with GABA or dopamine neurons in the ventral tegmental area. Instead, the authors found that eating was elicited by stimulation of lateral hypothalamic neurons. The behavior was mediated by a projection that passes through the ventral tegmental area and terminates in a brainstem structure next to the locus coeruleus. These results may contribute to our understanding of obesity because this circuit initiates compulsive eating in the absence of any physiological hunger stimulus. —PRS

Proc. Natl. Acad. Sci. U.S.A. **117**, 8611 (2020).

BIOMEDICINE

The tuberculous tickle

Tuberculosis is caused by *Mycobacterium tuberculosis* (Mtb) and often manifests with a persistent cough. This cough is concerning not only for the patient but also because it provides a mechanism for onward transmission. Coughing often results from the activation of nociceptive neurons in the lungs. Ruhl *et al*. wanted to know how Mtb infection induces cough in patients. They isolated extracts from the bacterium and applied them to nociceptive neurons in vitro. A specific glycolipid, sulfolipid-1 (SL-1), activated the neurons and induced cough in guinea pigs, but Mtb mutants that did not synthesize SL-1 failed to induce cough in these animals. Thus, this bacterial molecule appears to specifically enhance transmissibility of Mtb. —SMH

Cell **181**, 293 (2020).

AUTOCATALYSIS

Charting the course of the Soai reaction

The Soai reaction is unusual in its capacity to produce just one of two mirror-image products by amplifying miniscule asymmetries at the outset. The reaction adds an isopropyl group from organozinc to a specific pyrimidine-substituted aldehyde. The product alcohol then appears to coordinate isopropylzinc in a tetrameric arrangement to catalyze subsequent additions. Athavale *et al*. report kinetic, spectroscopic, and modeling studies with a simplified substrate (pyridine in place of pyrimidine) that still manifests autocatalysis. They conclude that amplification stems from better substrate accommodation by the less stable homochiral tetramer. —JSY

Nat. Chem. **12**, 412 (2020).

PHOTO: GERRY ELLIS/MINDEN PICTURES

REVIEW SUMMARY

ANTIMICROBIAL PEPTIDES

Antimicrobial peptides: Application informed by evolution

Brian P. Lazzaro, Michael Zasloff, Jens Rolff*

BACKGROUND: Antimicrobial peptides (AMPs) are small proteins with potent antibacterial, antiviral, and antifungal activity. AMPs are ubiquitous among multicellular eukaryotes, with most plant and animal species expressing dozens of distinct AMP genes in epithelial tissues and in response to infection. The diversity and potency of AMPs make them attractive candidates for translational application, and several are already in clinical trials. However, if AMPs are to be used effectively and sustainably, it will be imperative to understand their natural biology and evolution in order to lessen the risk of collateral harm and avoid the resistance crisis currently facing conventional antibiotics.

ADVANCES: For most of the past 25 years, the prevailing wisdom has been that AMPs are generally nonspecific and functionally redundant—largely interchangeable provided that they were produced quickly enough to a threshold that could contain infection. Support for this model was drawn from molecular evolutionary observations that AMP genes are rapidly duplicated and pseudogenized within and between species, often with little evolution at the level of the primary amino acid sequence. Furthermore, it was believed that the biochemical simplicity of AMPs reflected fundamentally irresistible modes of action, including permeabilization of the cell envelope through the formation of open pores, which was assumed to largely prevent bacterial evolution of resistance.

New evidence within the past 5 years, however, has begun to overturn that model. We now know that AMPs can exhibit remarkable levels of specificity and that some of the evolutionary degradation of AMP gene families may be adaptive. We are learning that genetic variability in AMPs, even at the level of single amino acids, can dramatically alter resistance to infection. There are now multiple documentations of convergent evolution of identical amino acid variants between species and of shared allelic diversity between species. It is increasingly clear that AMPs are highly functionally diversified and that they play roles in varied biological processes, including the regulation of symbiotic communities. It is also becoming apparent that bacteria can evolve resistance to AMPs, although the pharmacodynamics and mechanisms of killing of AMPs are much more favorable than those of conventional antibiotics for the prevention of resistance evolution.

ON OUR WEBSITE

Read the full article at https://dx.doi.org/10.1126/science.aau5480

OUTLOOK: AMPs hold considerable promise for translational applications, but developing their potential will require more sophisticated foundational understanding. AMPs function synergistically in vivo, and emerging evidence indicates that their activities in biological contexts may not be fully captured with classical in vitro assays. Further development of mathematical approaches to study synergies will be required, especially for higher-order interactions, in order to rationally develop cocktails that have high efficacy at low concentrations. Synergies between AMPs and conventional antibiotics should be exploited to rescue drugs that are currently lost to resistance. AMPs should be mined from all domains of life: Although more than 3100 naturally occurring AMPs have been described from taxa representing the breadth of life on earth, almost 40% of AMPs under clinical trial are of human origin. This is potentially risky because any evolved resistance to those AMPs may result in collateral resistance to endogenous human immunity. The biochemical properties and pharmacodynamics of AMPs make them far more refractory to resistance evolution than conventional antibiotics, but care should still be taken to deploy them responsibly. Translational use of AMPs in clinical and other applied settings will be greatly enhanced by understanding how specific AMPs function in their natural contexts and how their evolutionary history may predict their future utility. If we combine the insights from the evolutionary diversification of the AMPs, their activity in the context of synergistic cocktails, and our growing understanding of how to limit resistance evolution, we may avoid repeating the mistakes that have resulted in the current crisis of antibiotic resistance. ■

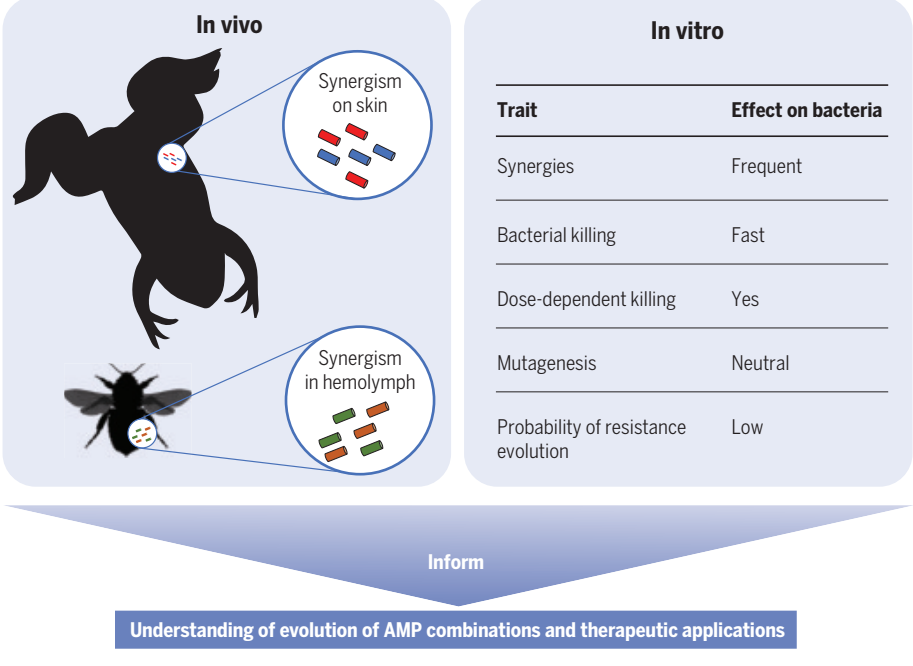

The combined insight from studying AMPs across the tree of life and the adaptive evolution of AMPs will inform their application and the understanding of AMPs in their natural context. In nature, AMPs are highly diverse, with most AMPs (more than 1000) described in Amphibia. They are released as synergistic cocktails in vivo. In vitro studies found that synergies are frequent and that other traits of AMPs result in a low probability of resistance evolution compared with conventional antibiotics.

CREDIT: BEE ILLUSTRATION BY MELISSA BROUSSARD/PHYLOPIC/CC

The list of author affiliations is available in the full article online.
*Corresponding author. Email: jens.rolff@fu-berlin.de
Cite this article as B. P. Lazzaro *et al.*, *Science* **368**, eaau5480 (2020). DOI: 10.1126/science.aau5480

RESEARCH ARTICLE SUMMARY

IMMUNOMETABOLISM

Interleukin-13 drives metabolic conditioning of muscle to endurance exercise

Nelson H. Knudsen, Kristopher J. Stanya, Alexander L. Hyde, Mayer M. Chalom, Ryan K. Alexander, Yae-Huei Liou, Kyle A. Starost, Matthew R. Gangl, David Jacobi, Sihao Liu, Danesh H. Sopariwala, Diogo Fonseca-Pereira, Jun Li, Frank B. Hu, Wendy S. Garrett, Vihang A. Narkar, Eric A. Ortlund, Jonathan H. Kim, Chad M. Paton, Jamie A. Cooper, Chih-Hao Lee*

INTRODUCTION: Exercise provides a vast array of health benefits. The increased metabolic activity of contracting skeletal muscle elicits an integrated response involving multiple tissues and signaling pathways to cope with increased energy and oxygen demands. A coordinated effort to promote endurance is mediated by a switch from glycolytic to oxidative metabolism favoring fatty acids as the energy source. This metabolic fueling strategy is met with specialized muscle fibers that exhibit distinct energy substrate preferences and mitochondrial oxidative capacity. These adaptive changes—such as increased cardiorespiratory capacity, enhanced muscle oxidative metabolism, and improved whole-body glucose homeostasis—promote metabolic fitness. However, the mechanisms that mediate these adaptive responses remain unclear.

RATIONALE: In the early 1960s, labile blood and lymph factors were found to mediate some of the metabolic effects of exercise. Recent studies further support the notion that communication between resident immune cells and their host tissues is important for regulating the metabolic setpoint and thereby maintaining tissue function. We found that endurance exercise increased circulating levels of the cytokine interleukin-13 (IL-13) in mice and humans. Endurance exercise also led to the expansion of type 2 innate lymphoid cells (ILC2s), one of the primary IL-13–producing cell types within mouse muscle. This implicated a role for IL-13 in the control of the adaptive responses elicited by exercise. We used several molecular and bioenergetic assays and generated three genetic models to determine the role of IL-13 signaling in the metabolic reprogramming of skeletal muscle in response to endurance exercise training.

RESULTS: Relative to wild-type control animals, *Il13*-deficient mice showed reduced running capacity on a treadmill. RNA sequencing of skeletal muscle from control and *Il13*-deficient mice was performed to examine the role of IL-13 in exercise physiology. IL-13 did not have an appreciable effect on metabolic gene expression in resting muscles. However, endurance training increased a network of mitochondrial and fatty acid oxidation genes in muscle of control animals, which was lost in mice lacking *Il13*. *Il13*-deficient muscle showed defective fatty acid utilization after a single bout of exercise and failed to increase mitochondrial biogenesis after endurance training. Furthermore, endurance training in control animals led to increased numbers of muscle oxidative fibers and improvements in mitochondrial respiration, endurance capacity, and glucose tolerance. All of these metabolic benefits of exercise training required intact IL-13 signaling.

We found that IL-13 acts directly on skeletal muscle through its receptor IL-13Rα1, leading to the activation of Stat3. Stat3 phosphorylation was elevated in muscle after both a single session and endurance training—an effect lost in *Il13*-deficient mice. In C2C12 myotubes, IL-13 treatment increased mitochondrial respiration that was dependent on *Il13ra1* and *Stat3*. The IL-13–Stat3 axis controlled the metabolic program elicited by exercise training partly through a coordinated transcriptional regulation with two nuclear receptors and mitochondrial regulators, ERRα and ERRγ. Mice specifically lacking *Il13ra1* or *Stat3* in skeletal muscle displayed reductions in muscle fatty acid oxidation and endurance capacity. By contrast, increasing levels of IL-13 in skeletal muscle recapitulated the metabolic reprogramming induced by endurance exercise in a Stat3-dependent manner, leading to improvements in systemic glucose homeostasis and running capacity.

ON OUR WEBSITE

Read the full article at https://dx.doi.org/10.1126/science.aat3987

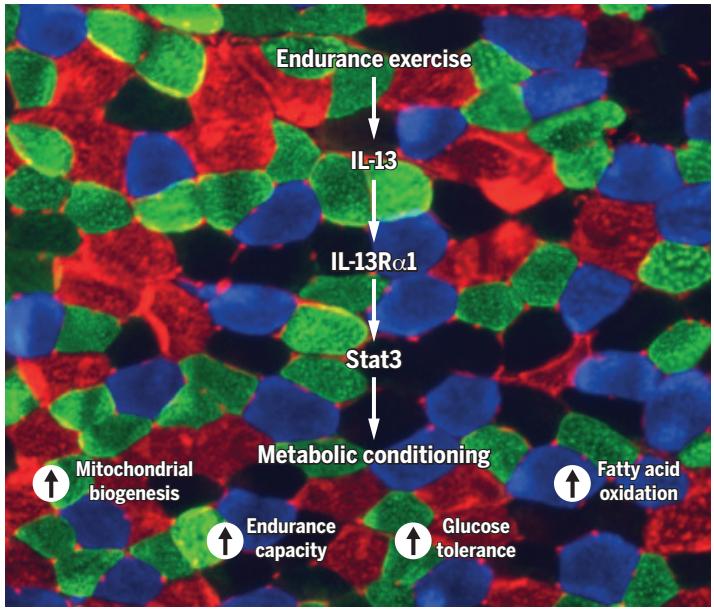

IL-13 mediates muscle metabolic programming to support endurance exercise via IL-13Rα1 and Stat3. Image shows gastrocnemius muscle cross section stained for myosin heavy chain (MyHC) isoforms to determine muscle fiber type composition. Blue, green, and red indicate MyHC I-, IIa-, and IIb-positive muscle fibers, respectively. Type I and type IIa muscles contain more oxidative fibers and are characterized by high endurance, whereas type IIb muscle fibers are glycolytic and prone to fatigue.

CONCLUSION: IL-13 signaling appears to be activated immediately after exercise and stabilized by endurance training, with the effects of modulating substrate utilization and mediating mitochondrial biogenesis, respectively. As such, it fits the criteria of a humoral factor that regulates exercise-induced metabolic effects. IL-13 exerts direct effects on skeletal muscle to increase transcriptional programs encoding fatty acid oxidation and mitochondrial electron transport chain complexes through IL-13Rα1 and the downstream effector Stat3. This adaptive response, an interplay of the immune and metabolic pathways, primes muscle for sustained physical activity. These observations highlight the importance of immune signaling in the maintenance of tissue metabolic fitness. ■

The list of author affiliations is available in the full article online.
*Corresponding author. Email: clee@hsph.harvard.edu
Cite this article as N. H. Knudsen *et al.*, *Science* **368**, eaat3987 (2020). DOI: 10.1126/science.aat3987

RESEARCH ARTICLES

CORONAVIRUS

QQ群: 970508760

Substantial undocumented infection facilitates the rapid dissemination of novel coronavirus (SARS-CoV-2)

Ruiyun Li[1]*, Sen Pei[2]*†, Bin Chen[3]*, Yimeng Song[4], Tao Zhang[5], Wan Yang[6], Jeffrey Shaman[2]†

Estimation of the prevalence and contagiousness of undocumented novel coronavirus [severe acute respiratory syndrome–coronavirus 2 (SARS-CoV-2)] infections is critical for understanding the overall prevalence and pandemic potential of this disease. Here, we use observations of reported infection within China, in conjunction with mobility data, a networked dynamic metapopulation model, and Bayesian inference, to infer critical epidemiological characteristics associated with SARS-CoV-2, including the fraction of undocumented infections and their contagiousness. We estimate that 86% of all infections were undocumented [95% credible interval (CI): 82–90%] before the 23 January 2020 travel restrictions. The transmission rate of undocumented infections per person was 55% the transmission rate of documented infections (95% CI: 46–62%), yet, because of their greater numbers, undocumented infections were the source of 79% of the documented cases. These findings explain the rapid geographic spread of SARS-CoV-2 and indicate that containment of this virus will be particularly challenging.

The novel coronavirus that emerged in Wuhan, China, at the end of 2019, severe acute respiratory syndrome–coronavirus 2 (SARS-CoV-2), quickly spread to all Chinese provinces and, as of 1 March 2020, to 58 other countries (*1*, *2*). Efforts to contain the virus are ongoing; however, given the many uncertainties regarding pathogen transmissibility and virulence, the effectiveness of these efforts is unknown.

The fraction of undocumented but infectious cases is a critical epidemiological characteristic that modulates the pandemic potential of an emergent respiratory virus (*3*–*6*). These undocumented infections often go unrecognized owing to mild, limited, or lack of symptoms and thus, depending on their contagiousness and numbers, can expose a far greater portion of the population to the virus than would otherwise occur. Here, to assess the full epidemic potential of SARS-CoV-2, we use a model-inference framework to estimate the contagiousness and proportion of undocumented infections in China during the weeks before and after the shutdown of travel in and out of Wuhan.

We developed a mathematical model that simulates the spatiotemporal dynamics of infections among 375 Chinese cities (see supplementary materials). In the model, we divided infections into two classes: (i) documented infected individuals with symptoms severe enough to be confirmed, i.e., observed infections; and (ii) undocumented infected individuals. These two classes of infection have separate rates of transmission: β, the transmission rate due to documented infected individuals; and μβ, the transmission rate due to undocumented individuals, which is β reduced by a factor μ.

Spatial spread of SARS-CoV-2 across cities is captured by the daily number of people traveling from city j to city i and a multiplicative factor. Specifically, daily numbers of travelers between 375 Chinese cities during the Spring Festival period ("Chunyun") were derived from human mobility data collected by the Tencent location-based service during the 2018 Chunyun period (1 February–12 March 2018) (*7*). Chunyun is a period of 40 days—15 days before and 25 days after the Lunar New Year—during which there are high rates of travel within China. To estimate human mobility during the 2020 Chunyun period, which began 10 January, we aligned the 2018 Tencent data on the basis of relative timing to the Spring Festival. For example, we used mobility data from 1 February 2018 to represent human movement on 10 January 2020, as these days were similarly distant from the Lunar New Year. During the 2018 Chunyun, 1.73 billion travel events were captured in the Tencent data, whereas 2.97 billion trips were reported by the Ministry of Transport of the People's Republic of China (*7*). To compensate for underreporting and reconcile these two numbers, a travel multiplicative factor, θ, which is greater than 1, is included (see supplementary materials).

To infer SARS-CoV-2 transmission dynamics during the early stage of the outbreak, we simulated observations during 10–23 January 2020 (i.e., the period before the initiation of travel restrictions) (fig. S1) using an iterated filter-ensemble adjustment Kalman filter framework (*8*–*10*). With this combined model-inference system, we estimated the trajectories of four model state variables (S_i, E_i, I_i^r, and I_i^u: the susceptible, exposed, documented infected, and undocumented infected subpopulations in city i, respectively) for each of the 375 cities, while simultaneously inferring six model parameters (Z, D, μ, β, α, and θ: the average latency period, the average duration of infection, the transmission reduction factor for undocumented infections, the transmission rate for documented infections, the fraction of documented infections, and the travel multiplicative factor, respectively).

Details of model initialization, including the initial seeding of exposed and undocumented infections, are provided in the supplementary materials. To account for delays in infection confirmation, we also defined a time-to-event observation model using a gamma distribution (see supplementary materials). Specifically, for each new case in group I_i^r, a reporting delay t_d (in days) was generated from a gamma distribution with a mean value of T_d. In fitting both synthetic and the observed outbreaks, we performed simulations with the model-inference system using different fixed values of T_d (6 days ≤ T_d ≤ 10 days) and different maximum seeding, $Seed_{max}$ (1500 ≤ $Seed_{max}$ ≤ 2500) (see supplementary materials) (fig. S2). The best-fitting model-inference posterior was identified by log likelihood.

Validation of the model-inference framework

We first tested the model-inference framework versus alternate model forms and using synthetic outbreaks generated by the model in free simulation. These tests verified the ability of the model-inference framework to accurately estimate all six target model parameters simultaneously (see supplementary methods and figs. S3 to S14). The system could identify a variety of parameter combinations and distinguish outbreaks generated with high α and low μ from those generated with low α and high μ. This parameter identifiability is facilitated by the assimilation of observed case data from multiple (375) cities into the model-inference system and the incorporation of human movement into the mathematical model structure (see supplementary methods and figs. S15 and S16).

[1]MRC Centre for Global Infectious Disease Analysis, Department of Infectious Disease Epidemiology, School of Public Health, Faculty of Medicine, Imperial College London, London W2 1PG, UK. [2]Department of Environmental Health Sciences, Mailman School of Public Health, Columbia University, New York, NY 10032, USA. [3]Department of Land, Air and Water Resources, University of California, Davis, Davis, CA 95616, USA. [4]Department of Urban Planning and Design, The University of Hong Kong, Hong Kong. [5]Ministry of Education Key Laboratory for Earth System Modeling, Department of Earth System Science, Tsinghua University, Beijing 10084, P. R. China. [6]Department of Epidemiology, Mailman School of Public Health, Columbia University, New York, NY 10032, USA.
*These authors contributed equally to this work.
†Corresponding author. Email: sp3449@cumc.columbia.edu (S.P.); jls106@cumc.columbia.edu (J.S.)

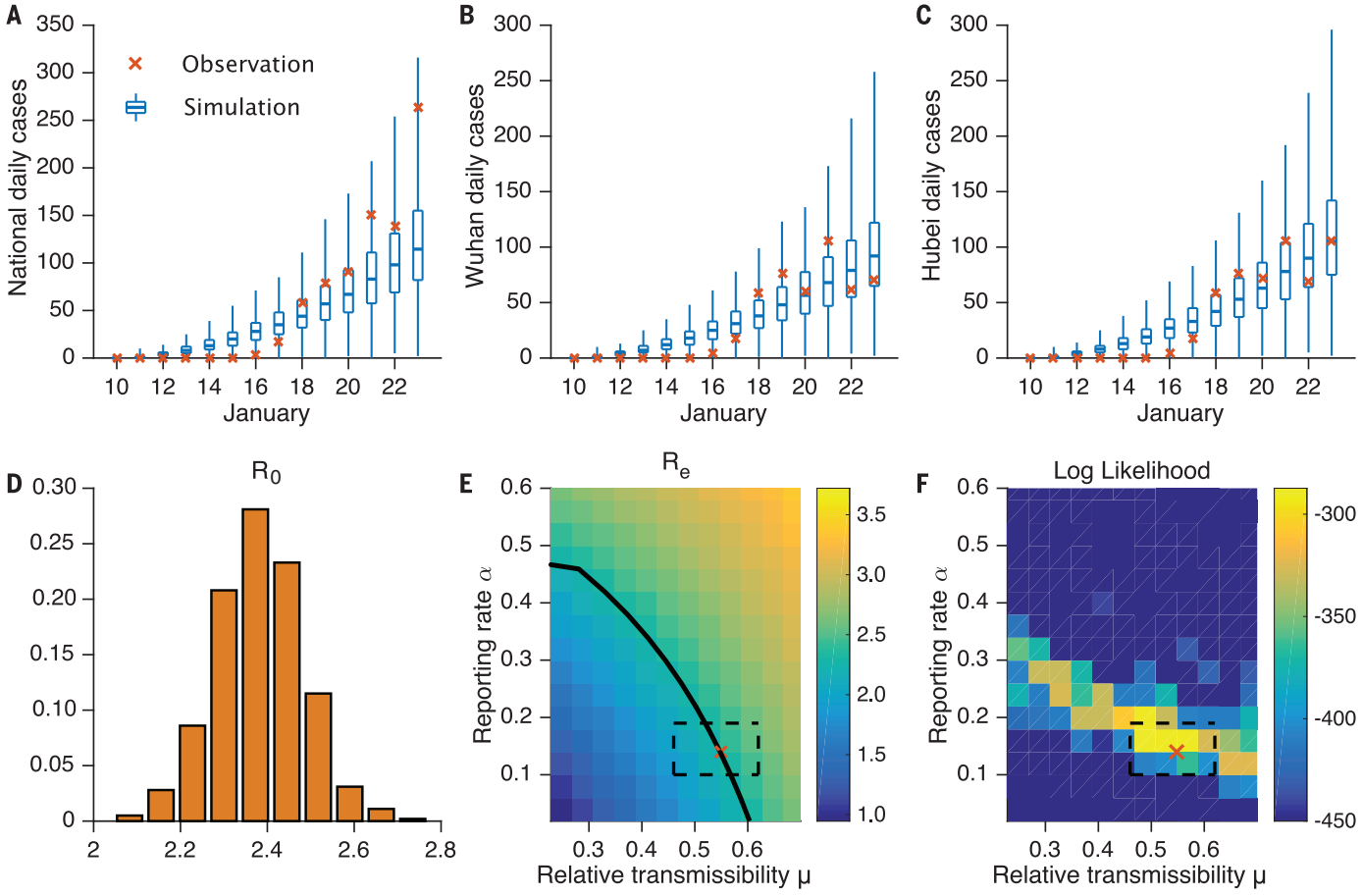

Fig. 1. Best-fit model and sensitivity analysis. Simulation of daily reported cases in all cities (**A**), Wuhan city (**B**), and Hubei province (**C**). The blue box and whiskers show the median, interquartile range, and 95% CIs derived from 300 simulations using the best-fit model (Table 1). The red x's are daily reported cases. (**D**) The distribution of estimated R_e. (**E**) The impact of varying α and μ on R_e with all other parameters held constant at Table 1 mean values. The black solid line indicates parameter combinations of (α,μ) yielding R_e = 2.38. The estimated parameter combination α = 0.14 and μ = 0.55 is indicated by the red x; the dashed box indicates the 95% credible interval of that estimate. (**F**) Log likelihood for simulations with combinations of (α,μ) and all other parameters held constant at Table 1 mean values. For each parameter combination, 300 simulations were performed. The best-fit estimated parameter combination α = 0.14 and μ = 0.55 is indicated by the red x (the x is plotted at the lower-left corner of its respective heat map pixel, i.e., the pixel with the highest log likelihood); the dashed box indicates the 95% CI of that estimate.

Epidemiological characteristics during 10–23 January 2020

We next applied the model-inference framework to the observed outbreak before the travel restrictions imposed on 23 January 2020—a total of 801 documented cases throughout China, as reported by 8 February (*1*). Figure 1, A to C, shows simulations of reported cases generated using the best-fitting model parameter estimates. The distribution of these stochastic simulations captures the range of observed cases well. In addition, the best-fitting model captures the spread of infections with the novel coronavirus disease 2019 (COVID-19) to other cities in China (fig. S17). Our median estimate of the effective reproductive number, R_e—equivalent to the basic reproductive number, R_0, at the beginning of the epidemic—is 2.38 [95% credible interval (CI): 2.03–2.77], indicating that COVID-19 has a high capacity for sustained transmission (Table 1 and Fig. 1D). This finding aligns with other recent estimates of the reproductive number for this time period (*6*, *11*–*15*). In addition, the median estimates for the latency and infectious periods are ~3.69 and 3.47 days, respectively. We also find that, during 10–23 January, only 14% (95% CI: 10–18%) of total infections in China were reported. This estimate reveals a very high rate of undocumented infections: 86%. This finding is independently corroborated by the infection rate among foreign nationals evacuated from Wuhan (see supplementary materials). These undocumented infections are estimated to have been half as contagious per individual as reported infections (μ = 0.55;

Table 1. Best-fit model posterior estimates of key epidemiological parameters for simulation with the full metapopulation model during 10–23 January 2020. $Seed_{max}$ = 2000, T_d = 9 days.

Parameter	Median (95% CIs)
Transmission rate (β, days^{-1})	1.12 (1.06, 1.19)
Relative transmission rate (μ)	0.55 (0.46, 0.62)
Latency period (*Z*, days)	3.69 (3.30, 3.96)
Infectious period (*D*, days)	3.47 (3.15, 3.73)
Reporting rate (α)	0.14 (0.10, 0.18)
Basic reproductive number (R_e)	2.38 (2.03, 2.77)
Mobility factor (θ)	1.36 (1.27, 1.45)

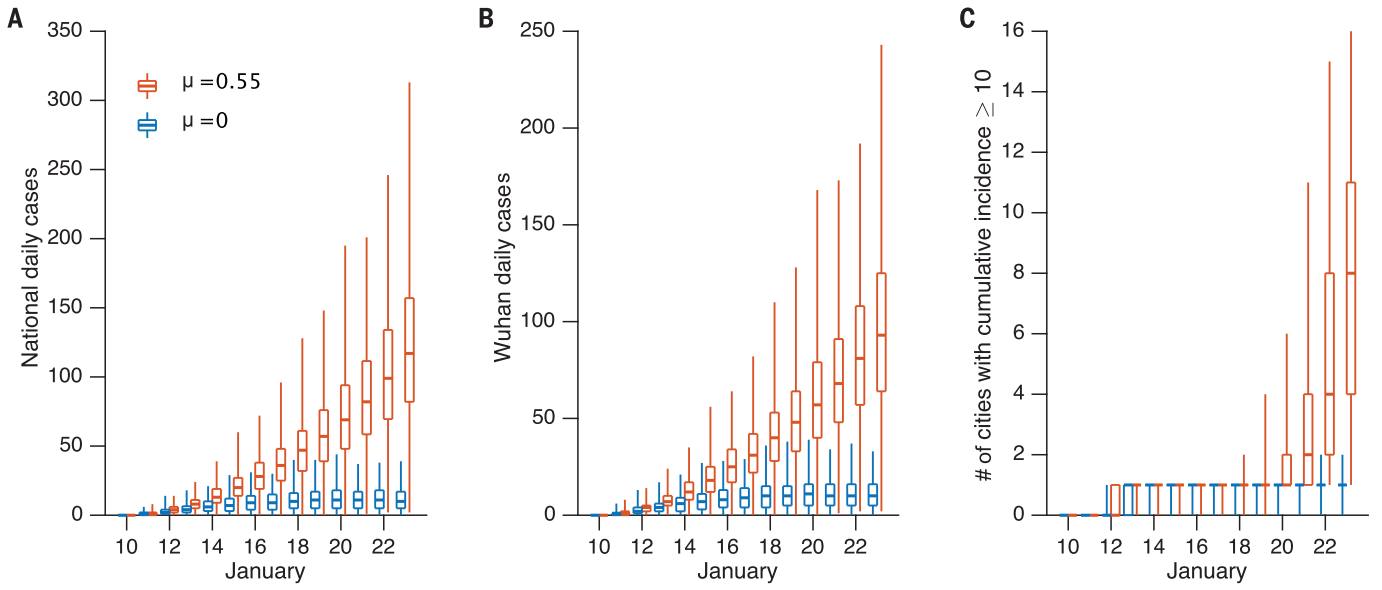

Fig. 2. Impact of undocumented infections on the transmission of SARS-CoV-2. Simulations generated using the parameters reported in Table 1 with μ = 0.55 (red) and μ = 0 (blue) showing daily documented cases in all cities (**A**), daily documented cases in Wuhan city (**B**), and the number of cities with ≥10 cumulative documented cases (**C**). The box and whiskers show the median, interquartile range, and 95% CIs derived from 300 simulations.

Table 2. Best-fit model posterior estimates of key epidemiological parameters for simulation of the model during 24 January–3 February and 24 January–8 February. $Seed_{max}$ = 2000 on 10 January, T_d = 9 days before 24 January, and T_d = 6 days between 24 January and 8 February. Travel to and from Wuhan is reduced by 98%, and other intercity travel is reduced by 80%.

Parameter	24 January–3 February [Median (95% CIs)]	24 January–8 February [Median (95% CIs)]
Transmission rate (β, days^{-1})	0.52 (0.42, 0.72)	0.35 (0.28, 0.45)
Relative transmission rate (μ)	0.50 (0.37, 0.69)	0.43 (0.31, 0.61)
Latency period (Z, days)	3.60 (3.41, 3.84)	3.42 (3.30, 3.65)
Infectious period (D, days)	3.14 (2.71, 3.72)	3.31 (2.96, 3.88)
Reporting rate (α)	0.65 (0.60, 0.69)	0.69 (0.65, 0.72)
Effective reproductive number (R_e)	1.34 (1.10, 1.67)	0.98 (0.83, 1.16)

95% CI: 0.46–0.62). Other model fittings made using alternate values of T_d and $Seed_{max}$ or different distributional assumptions produced similar parameter estimates (figs. S18 to S22), as did estimations made using an alternate model structure with separate average infectious periods for undocumented and documented infections (see supplementary methods, table S1). Further sensitivity testing indicated that α and μ are uniquely identifiable given the model structure and abundance of observations used (see supplementary methods and Fig. 1, E and F). In particular, Fig. 1F shows that the highest log-likelihood fittings are centered in the 95% CI estimates for α and μ and drop off with distance from the best-fitting solution (α = 0.14 and μ = 0.55).

Using the best-fitting model (Table 1 and Fig. 1), we estimated 13,118 (95% CI: 2974–23,435) new COVID-19 infections (documented and undocumented combined) during 10–23 January in Wuhan city. Further, 86.2% (95% CI: 81.5–89.8%) of all infections originated from undocumented cases. Nationwide, the number of infections during 10–23 January was 16,829 (95% CI: 3797–30,271), with 86.2% (95% CI: 81.6–89.8%) originating from undocumented cases. To further examine the impact of contagious, undocumented COVID-19 infections on overall transmission and reported case counts, we generated a set of hypothetical outbreaks using the best-fitting parameter estimates but with μ = 0, i.e., the undocumented infections are no longer contagious (Fig. 2). We find that without transmission from undocumented cases, reported infections during 10–23 January are reduced by 78.8% across all of China and by 66.1% in Wuhan. Further, there are fewer cities with more than 10 cumulative documented cases: only one city with more than 10 documented cases versus the 10 observed by 23 January (Fig. 2C). This finding indicates that contagious, undocumented infections facilitated the geographic spread of SARS-CoV-2 within China.

Epidemiological characteristics after 23 January 2020

We also modeled the transmission of COVID-19 in China after 23 January, when greater control measures were effected. These control measures included travel restrictions imposed between major cities and Wuhan, self-quarantine and contact precautions advocated by the government, and more available rapid testing for infection confirmation (*11*, *12*). These measures, along with changes in medical care–seeking behavior due to increased awareness of the virus and increased personal protective behavior (e.g., wearing of face masks, social distancing, self-isolation when sick), likely altered the epidemiological characteristics

of the outbreak after 23 January. To quantify these differences, we reestimated the system parameters using the model-inference framework and city-level daily cases reported between 24 January and 8 February. Given that intercity mobility was restricted after 23 January, we tested two altered travel scenarios: (i) scenario 1: a 98% reduction of travel in and out of Wuhan and an 80% reduction in travel between all other cities, as indicated by changes in the Baidu mobility index (*16*) (table S2); and (ii) scenario 2: a complete stoppage of intercity travel (i.e., θ to 0) (see supplementary methods for more details).

The results of inference for the 24 January–8 February period are presented in Table 2, figs. S23 to S26, and table S3. As control measures have continually shifted, we present estimates for both 24 January–3 February (period 1) and 24 January–8 February (period 2). For both periods, the best-fitting model for scenario 1 had a reduced reporting delay, T_d, of 6 days (versus 9 days before 23 January), consistent with more rapid confirmation of infections. Estimates of both the latency and infectious periods were similar to those made for 10–23 January; however, α, β, and R_e all shifted considerably. The transmission rate of documented cases, β, dropped to 0.52 (95% CI: 0.42–0.72) during period 1 and to 0.35 (95% CI: 0.28–0.45) during period 2, less than half the estimated transmission rate prior to travel restrictions (Table 2). The fraction of all infections that were documented, α, was estimated to be 0.65 (95% CI: 0.60–0.69), i.e., 65% of infections were documented during period 1, up from 14% before travel restrictions, and remained nearly the same for period 2. The reproductive number was 1.34 (95% CI: 1.10–1.67) during period 1 and 0.98 (95% CI: 0.83–1.16) during period 2, down from 2.38 prior to travel restrictions. While the estimate for the relative transmission rate, μ, is lower than before 23 January, the contagiousness of undocumented infections, represented by μβ, was substantially reduced, possibly reflecting that only very mild, less contagious infections remain undocumented or that individual protective behavior and contact precautions have proven effective. Similar parameter estimates are derived under scenario 2 (no travel at all) (table S3). These inference results for both periods 1 and 2 should be interpreted with caution, as care-seeking behavior and control measures were continually in flux at these times.

Outlook

Overall, our findings indicate that a large proportion of COVID-19 infections were undocumented prior to the implementation of travel restrictions and other heightened control measures in China on 23 January and that a large proportion of the total force of infection was mediated through these undocumented infections (Table 1). This high proportion of undocumented infections, many of which were likely not severely symptomatic, appears to have facilitated the rapid spread of the virus throughout China. Indeed, suppression of the infectiousness of these undocumented cases in model simulations reduces the total number of documented cases and the overall spread of SARS-CoV-2 (Fig. 2). In addition, the best-fitting model has a reporting delay of 9 days from initial infectiousness to confirmation; in contrast, line-list data for the same 10–23 January period indicates an average 6.6-day delay from initial manifestation of symptoms to confirmation (*17*). This discrepancy suggests that presymptomatic shedding may be typical among documented infections. The relative timing of onset and peak of viremia and shedding versus onset and peak of symptoms has been shown to potentially affect outbreak control success (*18*).

Our findings also indicate that a radical increase in the identification and isolation of currently undocumented infections would be needed to fully control SARS-CoV-2. Increased news coverage and awareness of the virus in the general population have likely already prompted increased rates of seeking medical care for respiratory symptoms. In addition, awareness among health care providers and public health officials and the availability of viral identification assays suggest that capacity for identifying previously missed infections has increased. Further, general population and government response efforts have increased the use of face masks, restricted travel, delayed school reopening, and isolated suspected persons, all of which could additionally slow the spread of SARS-CoV-2.

Combined, these measures are expected to increase reporting rates, reduce the proportion of undocumented infections, and decrease the growth and spread of infection. Indeed, estimation of the epidemiological characteristics of the outbreak after 23 January in China indicates that government control efforts and population awareness have reduced the rate of virus spread (i.e., lower β, μβ, R_e), increased the reporting rate, and lessened the burden on already overextended health care systems.

The situation on the ground in China is changing day to day. New travel restrictions and control measures are being imposed on populations in different cities, and these rapidly varying effects make certain estimation of the epidemiological characteristics for the outbreak difficult. Further, reporting inaccuracies and changing care-seeking behavior add another level of uncertainty to our estimations. Although the data and findings presented here indicate that travel restrictions and control measures have reduced SARS-CoV-2 transmission considerably, whether these controls are sufficient for reducing R_e below 1 for the length of time needed to eliminate the disease locally and prevent a rebound outbreak once control measures are relaxed is unclear. Moreover, similar control measures and travel restrictions would have to be implemented outside China to prevent reintroduction of the virus.

The results for 10–23 January 2020 delineate the characteristics of SARS-CoV-2 moving through a developed country, China, without major restrictions or control. These findings provide a baseline assessment of the fraction of undocumented infections and their relative infectiousness for such an environment. However, differences in control activity, viral surveillance and testing, and case definition and reporting would likely affect rates of infection documentation. Thus, the key findings, that 86% of infections went undocumented and that, per person, these undocumented infections were 55% as contagious as documented infections, could shift in other countries with different control, surveillance, and reporting practices.

Our findings underscore the seriousness of SARS-CoV-2. The 2009 H1N1 pandemic influenza virus also caused many mild cases, quickly spread globally, and eventually became endemic. Presently, there are four endemic coronavirus strains circulating in human populations (229E, HKU1, NL63, and OC43). If the novel coronavirus follows the pattern of 2009 H1N1 pandemic influenza, it will also spread globally and become a fifth endemic coronavirus within the human population.

REFERENCES AND NOTES

1. National Health Commission of the People's Republic of China, Update on the novel coronavirus pneumonia outbreak; www.nhc.gov.cn/xcs/yqtb/list_gzbd.shtml.
2. World Health Organization, Coronavirus disease (COVID-2019) situation reports; www.who.int/emergencies/diseases/novel-coronavirus-2019/situation-reports/.
3. J. F. Chan *et al*., *Lancet* **395**, 514–523 (2020).
4. P. Wu *et al*., *Euro Surveill.* **25**, 2000044 (2020).
5. V. J. Munster, M. Koopmans, N. van Doremalen, D. van Riel, E. de Wit, *N. Engl. J. Med.* **382**, 692–694 (2020).
6. Z. Du *et al*., *Emerg. Infect. Dis.* **26**, (2020).
7. X. Qiao, "2018 Chunyun ended, 74.8% surveyed travelers felt satisfied" [in Chinese], *People's Daily*, 15 March 2018; http://society.people.com.cn/n1/2018/0315/c1008-29869526.html.
8. E. L. Ionides, C. Bretó, A. A. King, *Proc. Natl. Acad. Sci. U.S.A.* **103**, 18438–18443 (2006).
9. A. A. King, E. L. Ionides, M. Pascual, M. J. Bouma, *Nature* **454**, 877–880 (2008).
10. S. Pei, F. Morone, F. Liljeros, H. Makse, J. L. Shaman, *eLife* **7**, e40977 (2018).
11. Health Commission of Hubei Province, The 8th Press Conference on the Prevention and Control of COVID-19; wjw.hubei.gov.cn/fbjd/dtyw/202001/t20200130_2016544.shtml.
12. Health Commission of Hubei Province, The 9th Press Conference on the Prevention and Control of COVID-19; wjw.hubei.gov.cn/fbjd/dtyw/202001/t20200131_2017018.shtml.
13. J. T. Wu, K. Leung, G. M. Leung, *Lancet* **395**, 689–697 (2020).
14. J. Riou, C. L. Althaus, *Euro Surveill.* **25**, 2000058 (2020).
15. N. Imai *et al*., Report 2: Estimating the potential total number of novel Coronavirus cases in Wuhan City, China (Imperial College London, 2020); http://hdl.handle.net/10044/1/77150.
16. Baidu Migration; https://qianxi.baidu.com/.
17. M. Kramer *et al*., Epidemiological data from the nCoV-2019 Outbreak: Early Descriptions from Publicly Available Data;

http://virological.org/t/epidemiological-data-from-the-ncov-2019-outbreak-early-descriptions-from-publicly-available-data/337.
18. C. Fraser, S. Riley, R. M. Anderson, N. M. Ferguson, *Proc. Natl. Acad. Sci. U.S.A.* **101**, 6146–6151 (2004).
19. S. Pei, SenPei-CU/COVID-19: COVID-19, Version 1, Zenodo (2020); http://doi.org/10.5281/zenodo.3699624.

ACKNOWLEDGMENTS

Funding: This work was supported by U.S. National Institutes of Health (NIH) grants GM110748 and AI145883. The content is solely the responsibility of the authors and does not necessarily represent the official views of the National Institute of General Medical Sciences, the National Institute of Allergy and Infectious Diseases, or the NIH. **Author contributions:** R.L., S.P., B.C., W.Y., and J.S. conceived of the study. R.L., B.C., Y.S., and T.Z. curated the data. S.P. performed the analysis. R.L., S.P., W.Y., and J.S. wrote the first draft of the manuscript. B.C., Y.S., and T.Z. reviewed and edited the manuscript. **Competing interests:** J.S. and Columbia University disclose partial ownership of SK Analytics. J.S. also reports receiving consulting fees from Merck and BNI. All other authors declare no competing interests. **Data and materials availability:** All code and data are available in the supplementary materials and posted online at https://github.com/SenPei-CU/COVID-19 and (*19*). This work is licensed under a Creative Commons Attribution 4.0 International (CC BY 4.0) license, which permits unrestricted use, distribution, and reproduction in any medium, provided the original work is properly cited. To view a copy of this license, visit https://creativecommons.org/licenses/by/4.0/. This license does not apply to figures/photos/artwork or other content included in the article that is credited to a third party; obtain authorization from the rights holder before using such material.

SUPPLEMENTARY MATERIALS

science.sciencemag.org/content/368/6490/489/suppl/DC1
Materials and Methods
Figs. S1 to S26
Tables S1 to S3
References (*20*–*37*)
MDAR Reproducibility Checklist
Data S1

15 February 2020; accepted 12 March 2020
Published online 16 March 2020
10.1126/science.abb3221

QQ群: 970508760

CORONAVIRUS

The effect of human mobility and control measures on the COVID-19 epidemic in China

Moritz U. G. Kraemer[1,2,3]*, Chia-Hung Yang[4], Bernardo Gutierrez[1,5], Chieh-Hsi Wu[6], Brennan Klein[4], David M. Pigott[7], Open COVID-19 Data Working Group†, Louis du Plessis[1], Nuno R. Faria[1], Ruoran Li[8], William P. Hanage[8], John S. Brownstein[2,3], Maylis Layan[9,10], Alessandro Vespignani[4,11], Huaiyu Tian[12], Christopher Dye[1], Oliver G. Pybus[1,13]*, Samuel V. Scarpino[4]*

The ongoing coronavirus disease 2019 (COVID-19) outbreak expanded rapidly throughout China. Major behavioral, clinical, and state interventions were undertaken to mitigate the epidemic and prevent the persistence of the virus in human populations in China and worldwide. It remains unclear how these unprecedented interventions, including travel restrictions, affected COVID-19 spread in China. We used real-time mobility data from Wuhan and detailed case data including travel history to elucidate the role of case importation in transmission in cities across China and to ascertain the impact of control measures. Early on, the spatial distribution of COVID-19 cases in China was explained well by human mobility data. After the implementation of control measures, this correlation dropped and growth rates became negative in most locations, although shifts in the demographics of reported cases were still indicative of local chains of transmission outside of Wuhan. This study shows that the drastic control measures implemented in China substantially mitigated the spread of COVID-19.

The outbreak of coronavirus disease 2019 (COVID-19) spread rapidly from its origin in Wuhan, Hubei Province, China (*1*). A range of interventions were implemented after the detection in late December 2019 of a cluster of pneumonia cases of unknown etiology and identification of the causative virus, severe acute respiratory syndrome–coronavirus 2 (SARS-CoV-2), in early January 2020 (*2*). Interventions include improved rates of diagnostic testing; clinical management; rapid isolation of suspected cases, confirmed cases, and contacts; and, most notably, restrictions on mobility (hereafter called cordon sanitaire) imposed on Wuhan city on 23 January 2020. Travel restrictions were subsequently imposed on 14 other cities across Hubei Province, and partial movement restrictions were enacted in many cities across China. Initial analysis suggests that the Wuhan cordon sanitaire resulted in an average 3-day delay of COVID-19 spread to other cities (*3*), but the full extent of the effect of the mobility restrictions and other types of interventions on transmission has not been examined quantitatively (*4*–*6*). Questions remain over how these interventions affected the spread of SARS-CoV-2 to locations outside of Wuhan. Here, we used real-time mobility data, crowdsourced line list data of cases with reported travel history, and timelines of reporting changes to identify early shifts in the epidemiological dynamics of the COVID-19 epidemic in China, from an epidemic driven by frequent importations to local transmission.

[1]Department of Zoology, University of Oxford, Oxford, UK. [2]Harvard Medical School, Harvard University, Boston, MA, USA. [3]Boston Children's Hospital, Boston, MA, USA. [4]Network Science Institute, Northeastern University, Boston, MA, USA. [5]School of Biological and Environmental Sciences, Universidad San Francisco de Quito USFQ, Quito, Ecuador. [6]Mathematical Sciences, University of Southampton, Southampton, UK. [7]Institute for Health Metrics and Evaluation, Department of Health Metrics, University of Washington, Seattle, WA, USA. [8]Harvard T.H. Chan School of Public Health, Boston, MA, USA. [9]Mathematical Modelling of Infectious Diseases Unit, Institut Pasteur, UMR2000, CNRS, Paris, France. [10]Sorbonne Université, Paris, France. [11]ISI Foundation, Turin, Italy. [12]State Key Laboratory of Remote Sensing Science, College of Global Change and Earth System Science, Beijing Normal University, Beijing, China. [13]Department of Pathobiology and Population Sciences, The Royal Veterinary College, London, UK.
***Corresponding author. Email: s.scarpino@northeastern.edu (S.V.S.); oliver.pybus@zoo.ox.ac.uk (O.G.P.); moritz.kraemer@zoo.ox.ac.uk (M.U.G.K.)** †Members of the Open COVID-19 Data Working Group are listed in the supplementary materials.

Human mobility predicts the spread and size of epidemics in China

As of 1 March 2020, 79,986 cases of COVID-19 were confirmed in China (Fig. 1A) (*7*). Reports of cases in China were mostly restricted to Hubei until 23 January 2020 (81% of all cases), after which most provinces reported rapid increases in cases (Fig. 1A). We built a line list dataset from reported cases in China with information on travel history and demographic characteristics (*8*). We note that the majority of early cases (before 23 January 2020; see the materials and methods) reported outside of Wuhan had known travel history to Wuhan (57%) and were distributed across China (Fig. 1B), highlighting the importance of Wuhan as a major source of early cases. However, initial testing was focused mainly on travelers from Wuhan, potentially biasing estimates of travel-related infections upward (see the materials and methods). Among cases known to have traveled from Wuhan before 23 January 2020, the time from symptom onset to confirmation was 6.5 days (SD = 4.2 days; fig. S2), providing opportunity for onward transmission at the destination. More active surveillance reduced this interval to 4.8 days (SD = 3.03 days; fig. S2) for those who traveled after 23 January 2020.

To identify accurately a time frame for evaluating early shifts in SARS-CoV-2 transmission in China, we first estimated from case data the average incubation period of COVID-19 infection [i.e., the duration between time of infection and symptom onset (*9*, *10*)]. Because infection events are typically not observed directly, we estimated the incubation period from the span of exposure during which infection likely occurred. Using detailed information on 38 cases for whom both the dates of entry to and exit from Wuhan were known, we estimated the mean incubation period to be 5.1 days (SD = 3.0 days; fig. S1), similar to previous estimates from other data (*11*, *12*). In subsequent analyses, we added an upper estimate of one incubation period (mean + 1 SD = 8 days) to the date of Wuhan shutdown to delineate

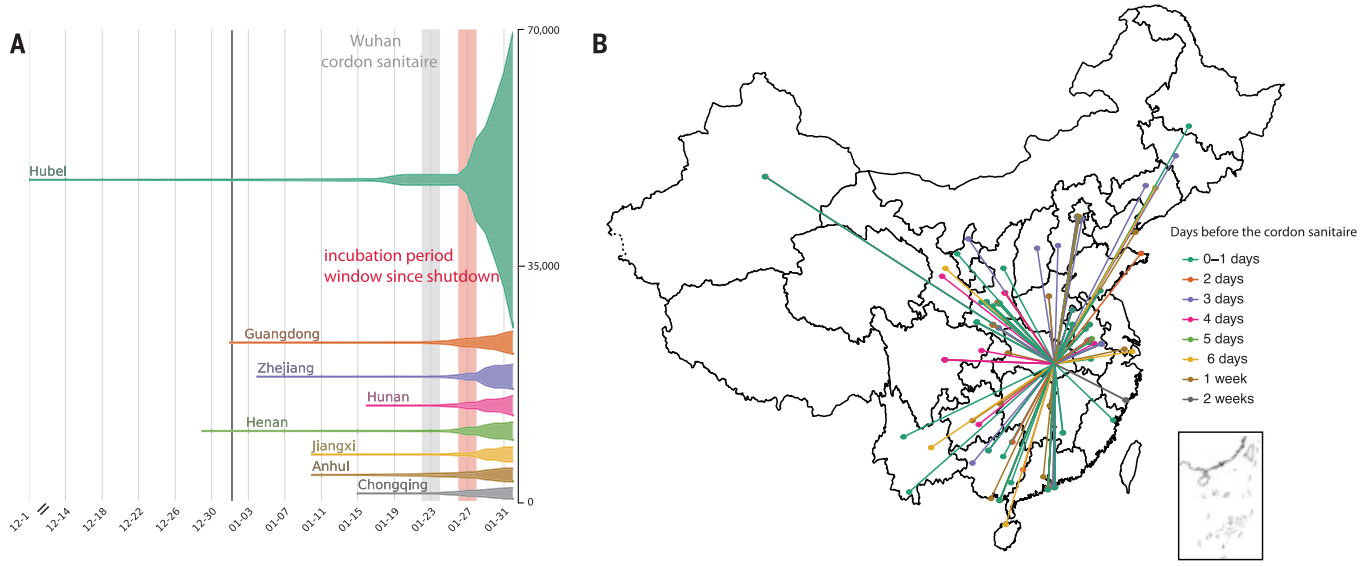

Fig. 1. Number of cases and key dates during the epidemic. (**A**) Epidemic curve of the COVID-19 outbreak in provinces in China. Bars indicate key dates: implementation of the cordon sanitaire of Wuhan (gray) and the end of the first incubation period after the travel restrictions (red). The black line represents the closure of the Wuhan seafood market on 1 January 2020. The width of each horizontal tube represents the number of reported cases in that province. (**B**) Map of COVID-19 confirmed cases (n = 554) that had reported travel history from Wuhan before travel restrictions were implemented on 23 January 2020. Colors of the lines indicate date of travel relative to the date of travel restrictions.

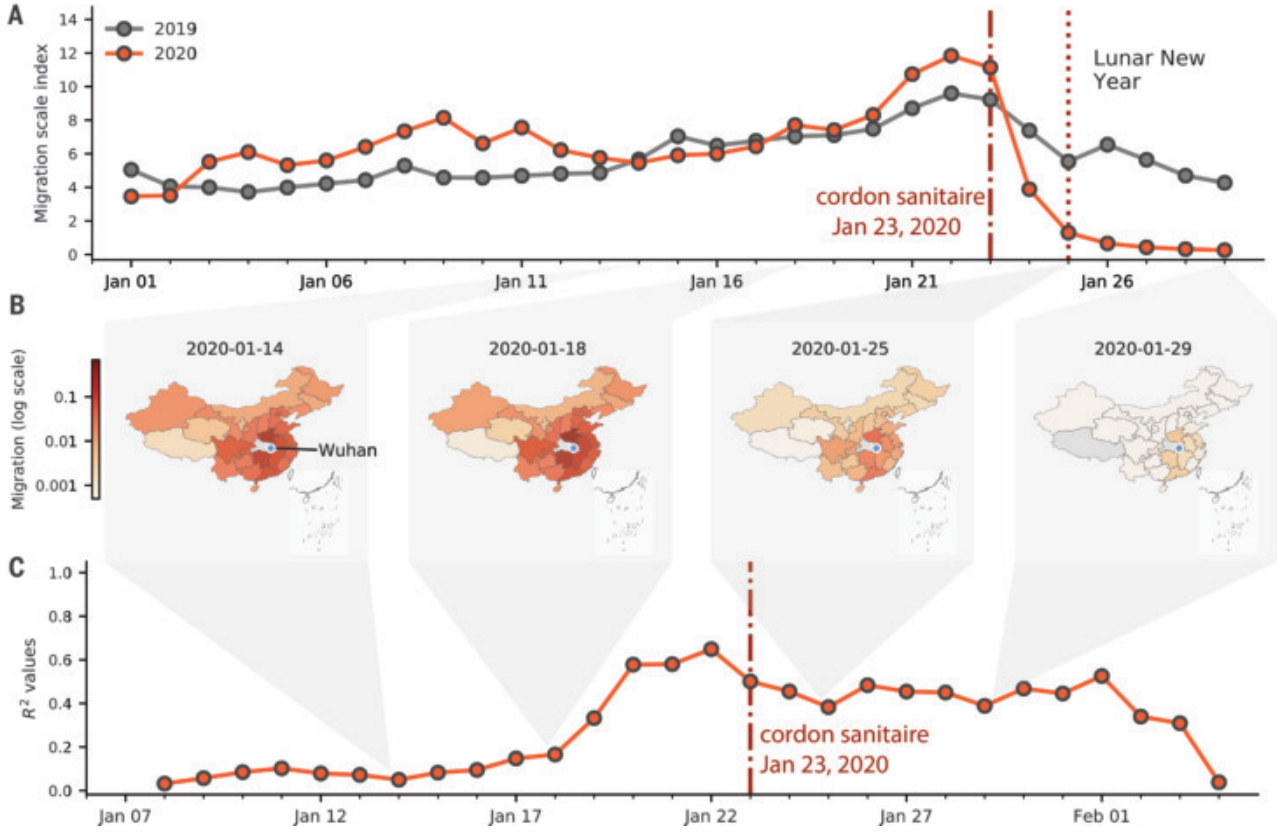

Fig. 2. Human mobility, spread, and synchrony of the COVID-19 outbreak in China. (**A**) Human mobility data extracted in real time from Baidu Inc. Travel restrictions from Wuhan and large-scale control measures started on 23 January 2020. Gray and red lines represent fluxes of human movements for 2019 and 2020, respectively. (**B**) Relative movements from Wuhan to other provinces in China. (**C**) Timeline of the correlation between daily incidence in Wuhan and incidence in all other provinces, weighted by human mobility.

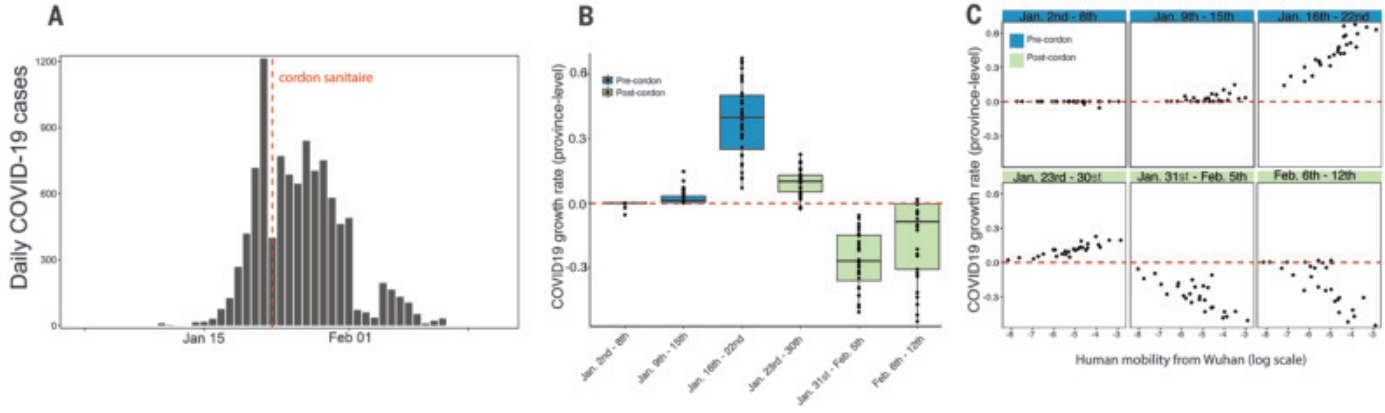

Fig. 3. Human mobility explains the early epidemic growth rate in China. (**A**) Daily counts of cases in China. (**B**) Time series of province-level growth rates of the COVID-19 epidemic in China. Estimates of the growth rate were obtained by performing a time-series analysis using a mixed-effects model of lagged, log linear daily case counts in each province (see the materials and methods). Above the red line are positive growth rates and below are negative rates. Blue indicates dates before the implementation of the cordon sanitaire and green after. (**C**) Relationship between growth rate and human mobility at different times of the epidemic. Blue indicates before the implementation of the cordon sanitaire and green after.

the date before which cases recorded in other provinces might represent infections acquired in Hubei (i.e., 1 February 2020; Fig. 1A).

To understand whether the volume of travel within China could predict the epidemic outside of Wuhan, we analyzed real-time human mobility data from Baidu Inc., together with epidemiological data from each province (see the materials and methods). We investigated spatiotemporal disease spread to elucidate the relative contribution of Wuhan to transmission elsewhere and to evaluate how the cordon sanitaire may have affected it.

Among cases reported outside of Hubei province in our dataset, we observed 515 cases with known travel history to Wuhan and a symptom onset date before 31 January 2020, compared with only 39 cases after 31 January 2020, illustrating the effect of travel restrictions (Figs. 1B and 2A and fig. S3). We confirmed the expected decline of importation with real-time human mobility data from Baidu Inc. Movements of individuals out of Wuhan increased in the days before the Lunar New Year and the establishment of the cordon sanitaire, before rapidly decreasing to almost no movement (Fig. 2, A and B). The travel ban appears to have prevented travel into and out of Wuhan around the time of the Lunar New Year celebration (Fig. 2A) and likely reduced further dissemination of SARS-CoV-2 from Wuhan.

To test the contribution of the epidemic in Wuhan to seeding epidemics elsewhere in China, we built a naïve COVID-19 "generalized" linear model [GLM (*13*)] of daily case counts (see the materials and methods). We estimated the epidemic doubling time outside of Hubei to be 4.0 days (range across provinces, 3.6 to 5.0 days) and estimated the epidemic doubling time within Hubei to be 7.2 days, consistent with previous reports (*5*, *12*, *14*, *15*). Our model predicted daily case counts across all provinces with relatively high accuracy (as measured with a pseudo-R^2 from a negative binomial GLM) throughout early February 2020 and when accounting for human mobility (Fig. 2C and tables S1 and S2), consistent with an exploratory analysis (*6*).

We found that the magnitude of the early epidemic (total number of cases until 10 February 2020) outside of Wuhan was very well predicted by the volume of human movement out of Wuhan alone (R^2 = 0.89 from a log-linear regression using cumulative cases; fig. S8). Therefore, cases exported from Wuhan before the cordon sanitaire appear to have contributed to initiating local chains of transmission, both in neighboring provinces (e.g., Henan) and in more distant provinces (e.g., Guangdong and Zhejiang) (Figs. 1A and 2B). Further, the frequency of introductions from Wuhan were also predictive of the size of the early epidemic in other provinces (controlling for population size) and thus the probability of large outbreaks (fig. S8).

After 1 February 2020 (corresponding to one mean + one SD incubation period after the cordon sanitaire and other interventions were implemented), the correlation of daily case counts and human mobility from Wuhan decreased (Fig. 2C), indicating that variability among locations in daily case counts was better explained by factors unrelated to human mobility, such as local public health response. This suggests that whereas travel restrictions may have reduced the flow of case importations from Wuhan, other local mitigation strategies aimed at halting local transmission increased in importance later.

We also estimated the growth rates of the epidemic in all other provinces (see the materials and methods). We found that all provinces outside of Hubei experienced faster growth rates between 9 January and 22 January 2020 (Fig. 3, A and B, and fig. S4b), which was the time before travel restrictions and substantial control measures were implemented (Fig. 3C and fig. S6); this was also apparent from the case counts by province (fig. S6). In the same period, variation in the growth rates is almost entirely explained by human movements from Wuhan (Fig. 3C and fig. S9), consistent with the theory of infectious disease spread in highly coupled metapopulations (*16*, *17*). After the implementation of drastic control measures across the country, growth rates became negative (Fig. 3B), indicating that transmission was successfully mitigated. The correlation of growth rates and human mobility from Wuhan became negative; that is, provinces with larger mobility from Wuhan before the cordon sanitaire (but also larger number of cases overall) had more rapidly declining growth rates of daily case counts. This could be due partly to travel restrictions but also to the fact that control measures may have been more drastic in locations with larger outbreaks driven by local transmission (for more details, see "Current role of imported cases in Chinese provinces" section).

The travel ban coincided with increased testing capacity across provinces in China. Therefore, an alternative hypothesis is that the observed epidemiological patterns outside of Wuhan were the result of increased testing capacity. We tested this hypothesis by including differences in testing capacity before and after the rollout of large-scale testing in China on 20 January 2020 [the date that COVID-19 became a class B notifiable disease (*18*, *19*)] and determined the impact of this binary variable on the predictability of daily cases (see the materials and methods). We plotted the relative improvement in the prediction of our model (on the basis of normalized residual error) of (i) a model that includes daily mobility from Wuhan and (ii) a model that includes testing availability (for more details,

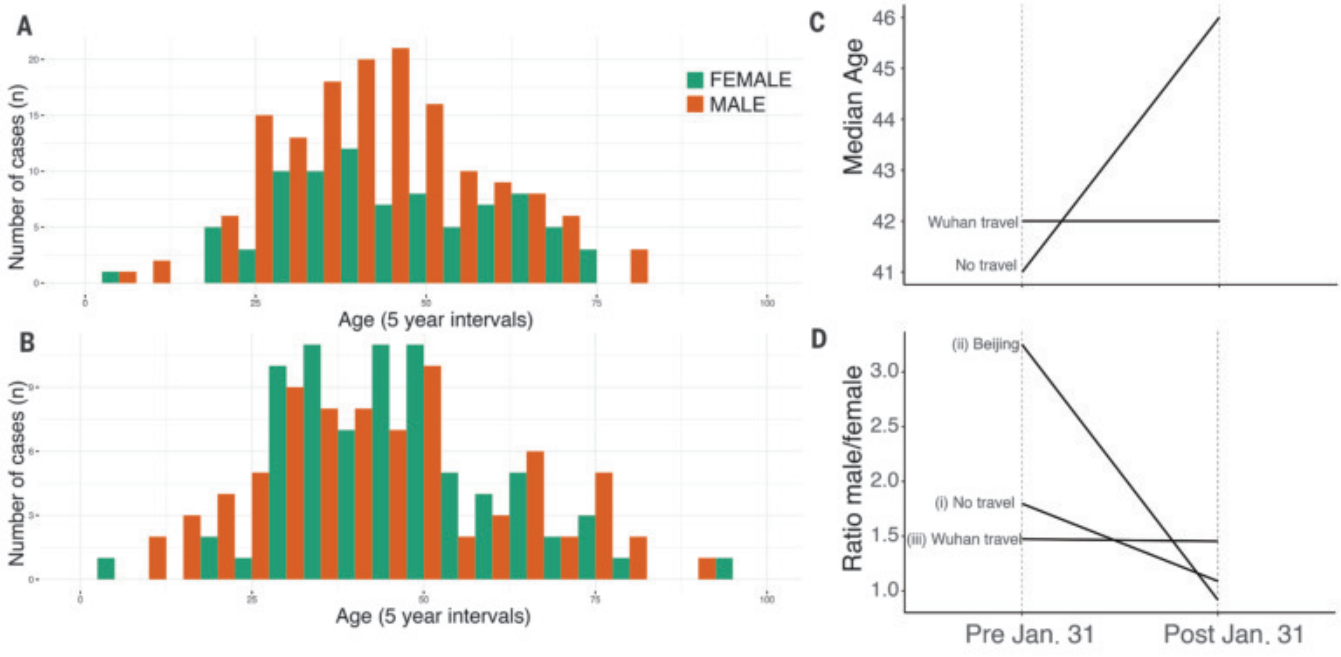

Fig. 4. Shifting age and sex distributions through time. (**A**) Age and sex distributions of confirmed cases with known travel history to Wuhan. (**B**) Age and sex distributions of confirmed cases that had no travel history to Wuhan. (**C**) Median age for cases reported early (before 1 February) and those reported later (between 1 and 10 February). Full distributions are shown in fig. S7. (**D**) Change through time in the sex ratio of (i) all reported cases in China with no reported travel history, (ii) cases reported in Beijing without travel history, and (iii) cases known to have traveled from Wuhan.

see the materials and methods). Overall, the inclusion of mobility data from Wuhan produced an improvement in the model's prediction [delta-Bayesian information criterion > 250 (*20*)] over a naïve model that considers only autochthonous transmission with a doubling time of 2 to 8 days (Fig. 3B). Of the 27 provinces in China reporting cases through 6 February 2020, we found that the largest improvements in prediction for 12 provinces could be achieved using mobility only (fig. S5). In 10 provinces, both testing and mobility improved the model's prediction, and in only one province (Hunan) was testing the most important factor improving model prediction (fig. S5). We conclude that laboratory testing during the early phase of the epidemic was critical; however, mobility out of Wuhan remained the main driver of spread before the cordon sanitaire. Large-scale molecular and serological data will be important to investigate further the exact magnitude of the impact of human mobility compared with other factors.

Current role of imported cases in Chinese provinces

Because case counts outside of Wuhan have decreased (Fig. 3B), we can further investigate the current contribution of imported cases to local epidemics outside of Wuhan by investigating case characteristics. Age and sex distributions can reflect heterogeneities in the risk of infection within affected populations. To investigate meaningful shifts in the epidemiology of the COVID-19 outbreak through time, we examined age and sex data for cases from different periods of the outbreak and from individuals with and without travel from Wuhan. However, details of travel history exist for only a fraction of confirmed cases, and this information was particularly scant for some provinces (e.g., Zhejiang and Guangdong). Therefore, we grouped confirmed cases into four categories: (I) early cases (i.e., reported before 1 February 2020) with travel history, (II) early cases without travel history, (III) later cases (i.e., reported between 1 February and 10 February 2020) with travel history, and (IV) later cases without travel history.

Using crowdsourced case data, we found that cases with travel history (categories I and III) had similar median ages and sex ratios in both the early and later phases of the outbreak (age 41 versus 42 years; 50% interquartile interval: 32.75 versus 30.75 and 54.25 versus 53.5 years, respectively; P value > 0.1, 1.47 versus 1.45 males per female, respectively; Fig. 4D and fig. S7). Early cases with no information on travel history (category II) had a median age and sex ratio similar to those with known travel history (age 42 years; 50% interquartile interval: 30.5 to 49.5, P value > 0.1; 1.80 males per female; Fig. 4D). However, the sex ratio of later cases without reported travel history (category IV) shifted to ~1:1 (57 male versus 62 female, X^2 test, P value < 0.01), as expected under a null hypothesis of equal transmission risk [Fig. 4, A, B, and D; see also (*21*, *22*) and the materials and methods], and the median age in this group increased to 46 (50% interquartile interval: 34.25 to 58, t test: P value < 0.01; Fig. 4, A to C, and fig. S7). We hypothesize that many of the cases with no known travel history in the early phase were indeed travelers who contributed to disseminating SARS-CoV-2 outside of Wuhan. The shift toward more equal sex ratios and older ages in nontravelers after 31 January 2020 confirms the finding that epidemics outside of Wuhan were then driven by local transmission dynamics. The case definition changed to include cases without travel history to Wuhan after 23 January 2020 (see the materials and methods).

Discussion

Containment of respiratory infections is particularly difficult if they are characterized by relatively mild symptoms or transmission before the onset of symptoms (*23*, *24*). Intensive control measures, including travel restrictions, have been implemented to limit the spread of COVID-19 in China. Here, we show that travel restrictions are particularly useful in the early stage of an outbreak when it is confined to a certain area that acts as a major source. However, travel restrictions may be less effective once the outbreak is more widespread. The combination of interventions implemented in China was clearly successful in mitigating spread and reducing local transmission of

COVID-19, although in this work it was not possible to definitively determine the impact of each intervention. Much further work is required to determine how to balance optimally the expected positive effect on public health with the negative impact on freedom of movement, the economy, and society at large.

REFERENCES AND NOTES

1. S. Chen, J. Yang, W. Yang, C. Wang, T. Bärnighausen, *Lancet* **395**, 764–766 (2020).
2. N. Zhu *et al*., *N. Engl. J. Med.* **382**, 727–733 (2020).
3. H. Tian *et al*., *Science* 10.1126/science.abb6105 (2020).
4. Z. Du *et al*., *Emerg. Infect. Dis.* **26** (2020).
5. J. T. Wu, K. Leung, G. M. Leung, *Lancet* **395**, 689–697 (2020).
6. S. Zhao *et al*., *J. Travel Med.* 10.1093/jtm/taaa022 (2020).
7. World Health Organization (WHO), *Coronavirus Disease 2019 (COVID-19) Situation Report – 27* (2020); https://www.who.int/docs/default-source/coronaviruse/situation-reports/20200216-sitrep-27-covid-19.pdf?sfvrsn=78c0eb78_2.
8. B. Xu *et al*., *Sci. Data* **7**, 106 (2020).
9. S. Cauchemez *et al*., *Lancet Infect. Dis.* **14**, 50–56 (2014).
10. J. Lessler *et al*., *Lancet Infect. Dis.* **9**, 291–300 (2009).
11. J. A. Backer, D. Klinkenberg, J. Wallinga, *Euro Surveill.* **25**, 20–28 (2020).
12. Q. Li *et al*., *N. Engl. J. Med.* NEJMoa2001316 (2020).
13. T. J. Hastie, D. Pregibon, "Generalized linear models" in *Statistical Models in S*, J. M. Chambers, T. J. Hastie, Eds. (Wadsworth & Brooks/Cole, 1992), pp. 195–246.
14. J. Riou, C. L. Althaus, *Euro Surveill.* **25**, 1–5 (2020).
15. A. R. Tuite, D. N. Fisman, *Ann. Intern. Med.* (2020).
16. M. J. Keeling, O. N. Bjørnstad, B. T. Grenfell, "Metapopulation dynamics of infectious diseases" in *Ecology, Genetics and Evolution of Metapopulations*, I. Hanski, O. E. Gaggiotti, Eds. (Elsevier, 2004), pp. 415–445.
17. D. J. Watts, R. Muhamad, D. C. Medina, P. S. Dodds, *Proc. Natl. Acad. Sci. U.S.A.* **102**, 11157–11162 (2005).
18. World Health Organization, *Report of the WHO-China Joint Mission on Coronavirus Disease 2019 (COVID-19)* (WHO, 2020); https://www.who.int/docs/default-source/coronaviruse/who-china-joint-mission-on-covid-19-final-report.pdf.
19. Z. Wu, J. M. McGoogan, *JAMA* **2019**, 17–20 (2020).
20. K. P. Burnham, D. R. Anderson, *Sociol. Methods Res.* **33**, 261–304 (2004).
21. Novel Coronavirus Pneumonia Emergency Response Epidemiology Team, *Zhonghua Liu Xing Bing Xue Za Zhi* **41**, 145–151 (2020).
22. E. Goldstein, V. E. Pitzer, J. J. O'Hagan, M. Lipsitch, *Epidemiology* **28**, 136–144 (2017).
23. C. Fraser, S. Riley, R. M. Anderson, N. M. Ferguson, *Proc. Natl. Acad. Sci. U.S.A.* **101**, 6146–6151 (2004).
24. R. Li *et al*., *Science* 10.1126/science.aba9757 (2020).
25. M. U. G. Kraemer *et al*., Open COVID-19 Data Working Group, L. du Plessis *et al*., Code for: The effect of human mobility and control measures on the COVID-19 epidemic in China. Zenodo (2020); https://doi.org/10.5281/zenodo.3714914.

ACKNOWLEDGMENTS

We thank all individuals who are collecting epidemiological data of the COVID-19 outbreak around the world. **Funding:** H.T., O.G.P., and M.U.G.K. acknowledge support from the Oxford Martin School. M.U.G.K. is supported by a Branco Weiss Fellowship. B.G. is supported by a Universities of Academic Excellence Scholarship Program of the Secretariat for Higher Education, Science, Technology, and Innovation of the Republic of Ecuador (grant no. ARSEQ-BEC-003163-2017). N.R.F. is supported by a Sir Henry Dale Fellowship. W.P.H. is supported by the National Institute of General Medical Sciences (grant no. U54GM088558). The funders had no role in study design, data collection and analysis, decision to publish, or preparation of the manuscript. **Author contributions:** M.U.G.K., O.G.P., and S.V.S. developed the idea and research. M.U.G.K. and S.V.S. wrote the first draft of the manuscript, and all other authors discussed results and edited the manuscript. M.U.G.K., B.G., S.V.S., D.M.P., and the Open COVID-19 Data Working Group collected and validated epidemiological data. R.L. and M.U.G.K. collected intervention data. C.-H.Y., B.K., and S.V.S. collected and processed human mobility data. **Competing interests:** S.V.S. is on the advisory board for BioFire Diagnostics Trend Surveillance, which includes paid consulting. A.V. reports past grants and personal fees from Metabiota Inc. outside of the submitted work. The remaining authors declare no competing interests. **Data and materials availability:** Code and data are available on the following GitHub repository: https://github.com/Emergent-Epidemics/covid19_cordon and permanently on Zenodo (*25*).

SUPPLEMENTARY MATERIALS

science.sciencemag.org/content/368/6490/493/suppl/DC1
Materials and Methods
Supplementary Text
Figs. S1 to S9
Tables S1 and S2
List of Members of the Open COVID-19 Data Working Group
References (*26*–*39*)

3 March 2020; accepted 23 March 2020
Published online 25 March 2020
10.1126/science.abb4218

TISSUE REGENERATION

Regenerative potential of prostate luminal cells revealed by single-cell analysis

Wouter R. Karthaus[1]*, Matan Hofree[2]*, Danielle Choi[1], Eliot L. Linton[1], Mesruh Turkekul[7], Alborz Bejnood[2], Brett Carver[1], Anuradha Gopalan[1], Wassim Abida[1], Vincent Laudone[1], Moshe Biton[2], Ojasvi Chaudhary[3], Tianhao Xu[3], Ignas Masilionis[3], Katia Manova[7], Linas Mazutis[3], Dana Pe'er[3,6], Aviv Regev[2,4,5]†, Charles L. Sawyers[1,4]†

Androgen deprivation is the cornerstone of prostate cancer treatment. It results in involution of the normal gland to ~90% of its original size because of the loss of luminal cells. The prostate regenerates when androgen is restored, a process postulated to involve stem cells. Using single-cell RNA sequencing, we identified a rare luminal population in the mouse prostate that expresses stemlike genes (*Sca1*$^+$ and *Psca*$^+$) and a large population of differentiated cells (*Nkx3.1*$^+$, *Pbsn*$^+$). In organoids and in mice, both populations contribute equally to prostate regeneration, partly through androgen-driven expression of growth factors (Nrg2, Rspo3) by mesenchymal cells acting in a paracrine fashion on luminal cells. Analysis of human prostate tissue revealed similar differentiated and stemlike luminal subpopulations that likewise acquire enhanced regenerative potential after androgen ablation. We propose that prostate regeneration is driven by nearly all persisting luminal cells, not just by rare stem cells.

Epithelial tissue homeostasis, at steady state or in response to injury, depends on replenishment of cells by stem cell populations. Whether such stem cells are rare cells with multilineage and self-renewal potential or if they are recruited from lineage-committed cells (facultative stem cells) varies across different tissues (*1*). The normal prostate gland includes luminal epithelial cells, basal epithelial cells, and rare neuroendocrine cells surrounded by stroma and vasculature (*2*, *3*). After surgical or pharmacological castration (a common treatment for advanced prostate cancer), the prostate involutes to ~90% of its original size, mainly because of the loss of luminal epithelial cells (*3*, *4*). Upon exogenous addition of testosterone, the mouse prostate fully regenerates within 4 weeks, which has sparked efforts to identify an underlying stem cell population (*4*–*6*). To provide further insights into this matter, we used single-cell RNA seq (scRNA-seq) to characterize cell types in the murine and human prostate and track their gene expression programs during castration and, in mouse, during regeneration.

Results

To characterize the different cell populations of the prostate, we collected droplet-based scRNA-seq profiles from 13,398 cells from the mouse prostate (concentrating initially on the anterior lobe) without fluorescence-activated cell sorting (FACS). We identified 15 distinct cell subsets by unsupervised graph clustering (Fig. 1A and fig. S1, a and b), with further partitioning to 22 subsets, spanning 6 epithelial and 16 nonepithelial subsets (figs. S1, d to f, and S2). To ensure adequate representation of all epithelial cells, we also profiled Epcam-positive and -negative cells isolated by FACS, but found a substantial reduction in quality and near-complete loss of two luminal populations (fig. S1c). We therefore conducted all subsequent experiments using

[1]Human Oncology and Pathogenesis Program, Memorial Sloan Kettering Cancer Center, New York, NY 10065, USA. [2]Klarman Cell Observatory, Broad Institute of Massachusetts Institute of Technology and Harvard University, Cambridge, MA 02142, USA. [3]Program for Computational and Systems Biology, Sloan Kettering Institute, Memorial Sloan Kettering Cancer Center, New York, NY 10065, USA. [4]Howard Hughes Medical Institute, Chevy Chase, MD 20815, USA. [5]Koch Institute of Integrative Cancer Research, Department of Biology, Massachusetts Institute of Technology, Cambridge, MA 02139, USA. [6]Parker Institute for Cancer Immunotherapy, Memorial Sloan Kettering Cancer Center, New York, NY 10065, USA. [7]Molecular Cytology, Memorial Sloan Kettering Cancer Center, New York, NY 10065, USA.
*These authors contributed equally to this work.
†Corresponding author. Email: aregev@broadinstitute.org (A.R.); sawyersc@mskcc.org (C.L.S)

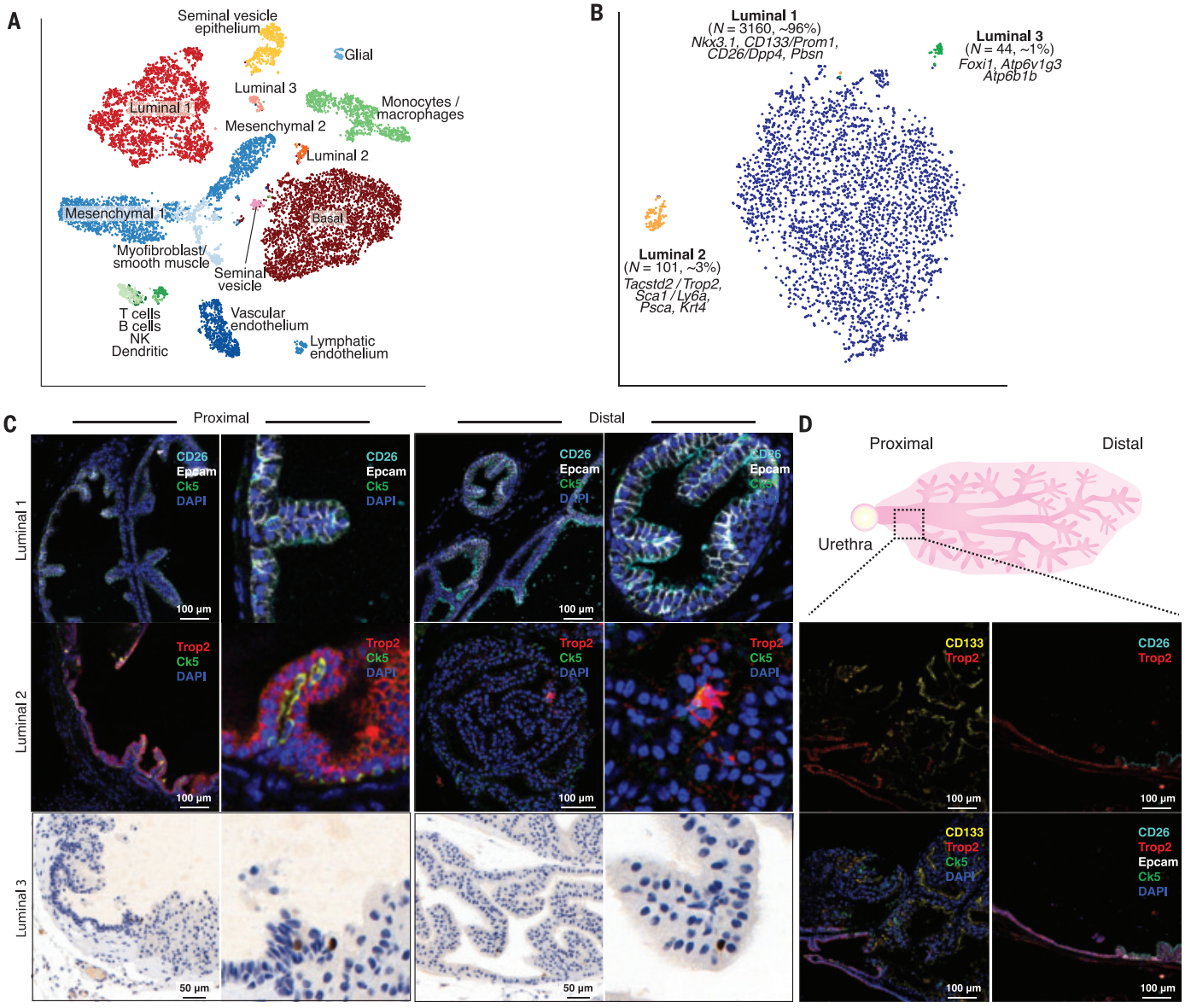

Fig. 1. Three subsets of luminal cells identified by scRNA-seq of the intact mouse prostate. (**A**) Single-cell census of the intact prostate. Shown is tSNE of scRNA-seq profiles colored by unsupervised clustering of 15 subsets and labeled post hoc. (**B**) Prostatic luminal subtypes. Shown is tSNE of scRNA-seq profiles only from the luminal clusters in (A). (**C**) Validation of luminal subset markers in situ. Shown is immunofluorescence (IF) staining of L1 (CD26/Dpp4, cyan, top) and L2 (Tacstd2/Trop2, red, middle) markers in the proximal and distal anterior lobe, along with Epcam (for epithelial cells, white), Ck5 (basal cells, green), and DAPI (nuclei). Also shown is IHC staining of Foxi1 in the proximal and distal anterior lobe (bottom). (**D**) Sharp transition from L2 to L1 cells. Shown is IF staining of L1 (CD133/Prom1 or CD26/Dpp4) and L2 (Tacst2/Trop2) markers, along with Epcam (for epithelial cells), Ck5 (basal cells), and DAPI (nuclei). A distinct border can be observed between proximal and distal prostatic regions. Scale bars, 100 or 50 μm as labeled.

whole mouse prostate anterior lobe without enrichment.

We annotated each of the six epithelial subsets by the expression of marker genes, revealing three seminal vesicle (SV) subsets, a basal subset, and three luminal subsets. The SV subsets (fig. S1e) were defined by two small clusters with high expression of *Pax2*, *Pate4*, and *Calml3*, known epididymal genes that were likely carried over during surgical dissection because of the anatomical proximity of the SV to the prostate lobes. One large subset consisted of basal cells marked by expression of the canonical genes *Trp63*, *Krt5*, and *Krt14* (fig. S1f). Finally, there were three subsets of luminal cells: a large population and two smaller subsets, all three expressing the canonical luminal markers *CD24a*, *Krt8*, and *Krt18* (fig. S1f), labeled as luminal 1 (L1), L2, and L3 cells, respectively.

The nonepithelial subsets revealed a previously unknown complexity in the stromal compartment, specifically the identification of two mesenchymal subpopulations (designated M1 and M2), myofibroblasts and smooth muscle cells. The mesenchymal populations were distinguished by the expression of ligands and/or receptors known to be associated with epithelial growth and differentiation such as *Wnt2*, *Wnt6*, *Wnt10a*, and *RorB* in M1 cells and *Rspo1*, *Fgf10*, and *Sult1e1* in M2 cells (fig. S2b). In addition to M1 and M2, we identified myofibroblasts and smooth muscle populations on the basis of the expression of canonical contractile genes such as *Acta2* and *MyH11*. These cells separately expressed *Rspo3* or *Notch3*

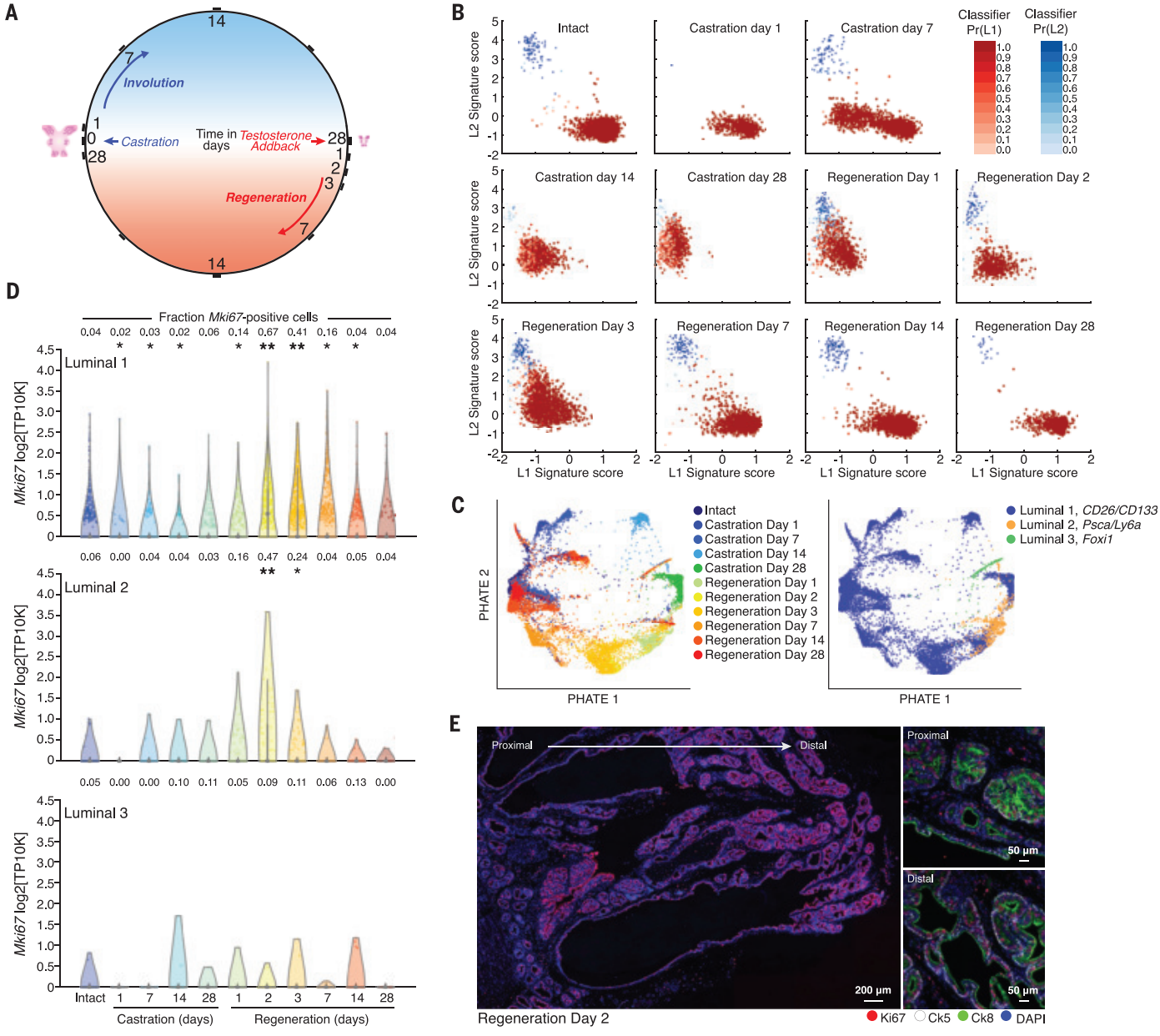

Fig. 2. Transcriptomic changes in murine luminal subpopulations during castration and organ regeneration. (**A**) Schematic overview of the C/R cycle with experimental time points. (**B**) Scatterplots of the L1 (*x* axis) and L2 (*y* axis) intact signature score (*z* score) for each cell (dot) assigned to L1 (red) or L2 (blue) at each time point (panel). Dot color intensity is scaled by the strength of classifier assignment probability for the dot's assigned class (color bar). (**C**) Similar transcriptional states of L1 and L2 during castration. PHATE graph of scRNA-seq profiles from luminal cells, colored by time point (left panel) or L1, L2, and L3 based on expression profiles in T0 (right panel). L1 cells undergo the most substantial transcriptional changes. On castration day 28 (dark green, left panel) and regeneration day 1 (light green, left panel) L1 are coembedded with L2 cells (orange, right panel). (**D**) Rapid entry of L1 and L2 cells into the cell cycle during regeneration. Each plot shows the distribution of *Mki67* mRNA expression (*y* axis) throughout the C/R cycle (*x* axis) for L1, L2, and L3 cells. Fraction of cells with *Mki67* expression detected is noted on top. *Expression is significantly different from intact (T0) (Bonferroni-corrected $P < 0.05$, one-sided Wilcoxon rank-sum test). **Fold change of 1.5 or greater and area under the curve of 0.65. (**E**) IF staining of Ki67 in the anterior lobe at regeneration day 2. (Left) Low-magnification image showing proximal and distal regions. (Right) representative higher magnification (20×) of proximal and distal regions. Shown are Ki67 (red), Ck8 (Green), Ck5 (white), and DAPI (purple). Scale bars, 200 or 50 µm as labeled.

(fig. S2e), revealing a level of complexity greater than that suggested previously (*7*). All of these populations expressed the gene encoding the androgen receptor, suggestive of hormone-driven communication with epithelial cells (discussed below). We also identified multiple immune populations, such as B and T lymphocytes, natural killer (NK) cells, dendritic cells (*Xcr1*), and four subpopulations of monocytes and macrophages (*CD14*, *IBA1*). Other cell types included vascular endothelial cells (*CD31*), lymphatic endothelial cells (*CD31*, *Prox1*), and glial cells (*Sox10*) (fig. S2, b and c). We did not observe a distinct neuroendocrine cluster, most likely because of the rarity of neuroendocrine cells (fig. S2d).

Of the three luminal subpopulations, L1 cells were predominant (~96% of profiled luminal

cells) and expressed high levels of canonical androgen receptor target genes such as *Pbsn* and *Nkx3.1*, as well as *CD26/Dpp4*, *CD59a*, and *CD133/Prom1* (Fig. 1B and fig. S3, a and b). Although L1 cells form a single subset using unsupervised graph clustering (t-distributed stochastic neighbor embedding, tSNE), there is variation within the subset as revealed by hierarchical clustering of differentially expressed genes (fig S3d). By contrast, L2 (~3%) and L3 (1%) are distinct minority luminal populations. L2 cells express *Sca1/Ly6a*, *Tacstd2/Trop2*, and *Psca*, all of which have been previously associated with stem cell–like activity, as well as *Krt4* and Claudin10 (Fig. 1B and fig. S3, a, b, and h). L3 cells are defined by expression of the transcription factor *Foxi1*, a master regulator of subunits of the vacuolar ATPase proton pump such as *Atp6v1g3* and *Atp6b1b* (*8*), both of which are strongly expressed in these cells (Fig. 1B and fig. S3, a and b). We and others have recently identified Foxi1$^+$ pulmonary ionocytes with features similar to those of cells in the gills of freshwater fish that regulate ion transport. Pulmonary ionocytes regulate salt balance in airway secretions and may be implicated in the pathophysiology of cystic fibrosis (*9*, *10*). We also detected *Foxi1*-expressing cells among the *Pax2*$^+$ SV population (fig. S3a). Male *Foxi1*-null mice are infertile because of a failure to properly acidify the epididymal fluid (*11*).

In situ analysis revealed that L1 cells (CD26/Dpp4$^+$CD133/Prom1$^+$) are almost exclusively found in the distal prostate ducts, whereas L2 cells (Trop2$^+$) are predominantly located in the proximal prostate (Fig. 1C and fig. S3, e to h), a pattern consistent with prior studies of Psca$^+$ or Sca1/Ly6a$^+$ cells (*12*, *13*). The spatial transition from L2 to L1 cells is abrupt when moving distally along a proximal duct (Fig. 1D), suggesting that anatomically localized inductive signals have a role in defining L1 versus L2 cell fates. By contrast, ionocyte-like L3 cells are interspersed in both proximal and distal locations (Fig. 1C). The in situ pattern for L1, L2, and L3 cells was similar in the dorsolateral prostate but not in the ventral prostate, where we observed an expanded number of Trop2$^+$ and Claudin10$^+$ L2 cells, indicative of variability in the relative percentage of L1 and L2 cells in different lobes (fig. S4).

Gene expression changes in the mouse prostate across a castration/regeneration cycle

Because the murine prostate gland can fully regenerate after castration-induced involution, there has been considerable interest in defining potential stem cells underlying this regeneration. Although a fraction of luminal cells is known to persist after castration (*14*, *15*), little is known about their transcriptional features relative to those in hormonally intact mice. The small fraction of L2 cells (~3%) relative to L1 cells, together with prior data implicating the L2-expressed genes *Sca1/Ly6a*, *Psca*, and *Tacstd2/Trop2* as prostate stem cell markers (*13*, *16*), prompted us to investigate whether L2 cells function as stem cells in regeneration.

To this end, we collected scRNA-seq profiles of the mouse prostate throughout a complete castration/regeneration (C/R) cycle (Fig. 2A and fig. S5, a and b). We first compared the relative frequency of L1 and L2 cells in castrated mice using FACS with cell surface markers that distinguish between L1 (CD26/Dpp4 or CD133/Prom1) and L2 (Sca1/Ly6a) cells. L2 cells were two- to threefold enriched in castrated versus intact mice, consistent with a potential stem cell role (*12*); however, the majority (>50%) of persistent luminal cells (CD24$^+$; CD49f$^-$) were L1 (CD26/Dpp4$^+$; CD133/Prom1$^+$) (fig. S5, c to e). Computational analysis of transcriptomes across the C/R cycle revealed, on the basis of scatterplots of L1 versus L2 signature scores, that L1 cells gain features very similar to L2 cells after castration (day 28) but revert back to baseline during regeneration (Fig. 2B and fig. S6c). This result was seen using both raw and scaled classification scores (fig. S6d) and was further supported by pairwise correlation of L1 and L2 expression profiles, which peaked on day 28 after castration and then declined during regeneration (fig. S6b). In addition, hierarchical clustering based on program genes showed that L1 and L2 cells co-cluster 28 days after castration and 1 day into regeneration but not at other time points (fig. S7). By contrast, L3 cells remained distinct from L1 and L2 throughout this cycle despite robust androgen receptor expression ($P < 0.05$, Wilcoxon rank-sum test) (fig. S6, b to d). Finally, when visualized by PHATE (*17*), a graph diffusion–based 2D embedding approach that preserves global distance relationships, transcriptional profiles of L1 and L2 cells were closely embedded on day 28 after castration but separated by day 28 after regeneration (Fig. 2C and fig. S6a). Similar co-embedding was also observed with other dimensionality reduction methods (fig. S5b). One reason for the similarity in transcriptional features of L1 and L2 cells after castration is loss of androgen receptor–regulated transcription, which contributes substantially to the distinction between these two populations in the presence of androgen. For example, there is a substantial decline in the expression of *CD59a* and *Nkx3.1* in L1 cells and of *Psca* in L2 cells. Conversely, genes whose transcription is not dependent on the androgen receptor, such as *CD26/Dpp4* and *Sca1/Ly6a*, maintain L1- and L2-specific expression (fig. S8b), indicating that the two populations remain distinct.

Enhanced regenerative potential of luminal cells in mouse organoid culture

In light of the overlapping transcriptomic features of L1 and L2 cells after castration, we explored the relative contribution of each to regeneration, starting with an analysis of their recruitment into the cell cycle after androgen (testosterone) addback. Sixty-eight percent of L1 cells and 45% of L2 cells had a surge in *Ki67* transcript expression (a marker of proliferating cells) just 2 days after implantation of testosterone pellets; in addition, there was increased expression of G_1/S and G_2/M cell cycle gene sets ($P < 0.05$, Wilcoxon rank-sum test) (Fig. 2D and fig. S5, f and g). These findings were confirmed in situ, on the basis of robust Ki67 staining throughout the prostate, 2 to 3 days after androgen addback, particularly in the distal gland where L1 cells reside (Fig. 2E and fig. S9). L3 cells and basal epithelial cells also showed increased *Mki67* expression but at more modest levels (11 and 15%, respectively; $P < 0.05$, Wilcoxon rank-sum test) (Fig. 2D and fig. S5h).

The fact that so many luminal cells rapidly enter the cell cycle during the C/R cycle suggested to us that a larger number of persisting cells might contribute to regeneration than would be predicted from a conventional stem cell model. As a first test of this hypothesis, we measured the organoid regeneration potential of a pan-luminal epithelial cell population (CD24$^+$, CD49f$^-$) from castrated mice and from mice after 1, 2, or 3 days of androgen addback. We observed an increase in the efficiency of organoid formation from ~5 to >20% within 2 days (fig. S10a). To dissect the relative roles of L1 and L2 cells in this regeneration, we isolated L1 cells (CD26/Dpp4$^+$ or CD133/Prom1$^+$) and L2 cells (Sca1/Ly6a$^+$) at different time points along the C/R cycle and compared their organoid formation potential. L2 cells from intact mice showed superior organoid formation (9 to 10%) compared with L1 cells (~4%) ($P < 0.05$, t test) (Fig. 3A), as expected from prior studies of Sca1/Ly6a$^+$ cells (*12*). However, L1 cells generated twofold more organoids in the castration setting (~9%; $P < 0.05$, t test), with a further doubling (~20%) 2 days into regeneration ($P < 0.05$, t test) (Fig. 3, A and B, and fig. S10, b and c). L2 cells also generated more organoids 2 days after regeneration (Fig. 3B) but the change after castration was not significant (Fig. 3A). In addition, both L1- and L2-derived organoids gave rise to Ck5$^+$ basal cells (Fig. 3C and fig. S10d), indicative of their bilineage potential. L1-derived organoids also displayed more polarized morphology and thicker walls, consistent with their more differentiated gene expression profile in hormonally intact glands (Fig. 3C and fig. S10d). Regeneration potential was not influenced by dihydrotestosterone (DHT) in the organoid culture medium

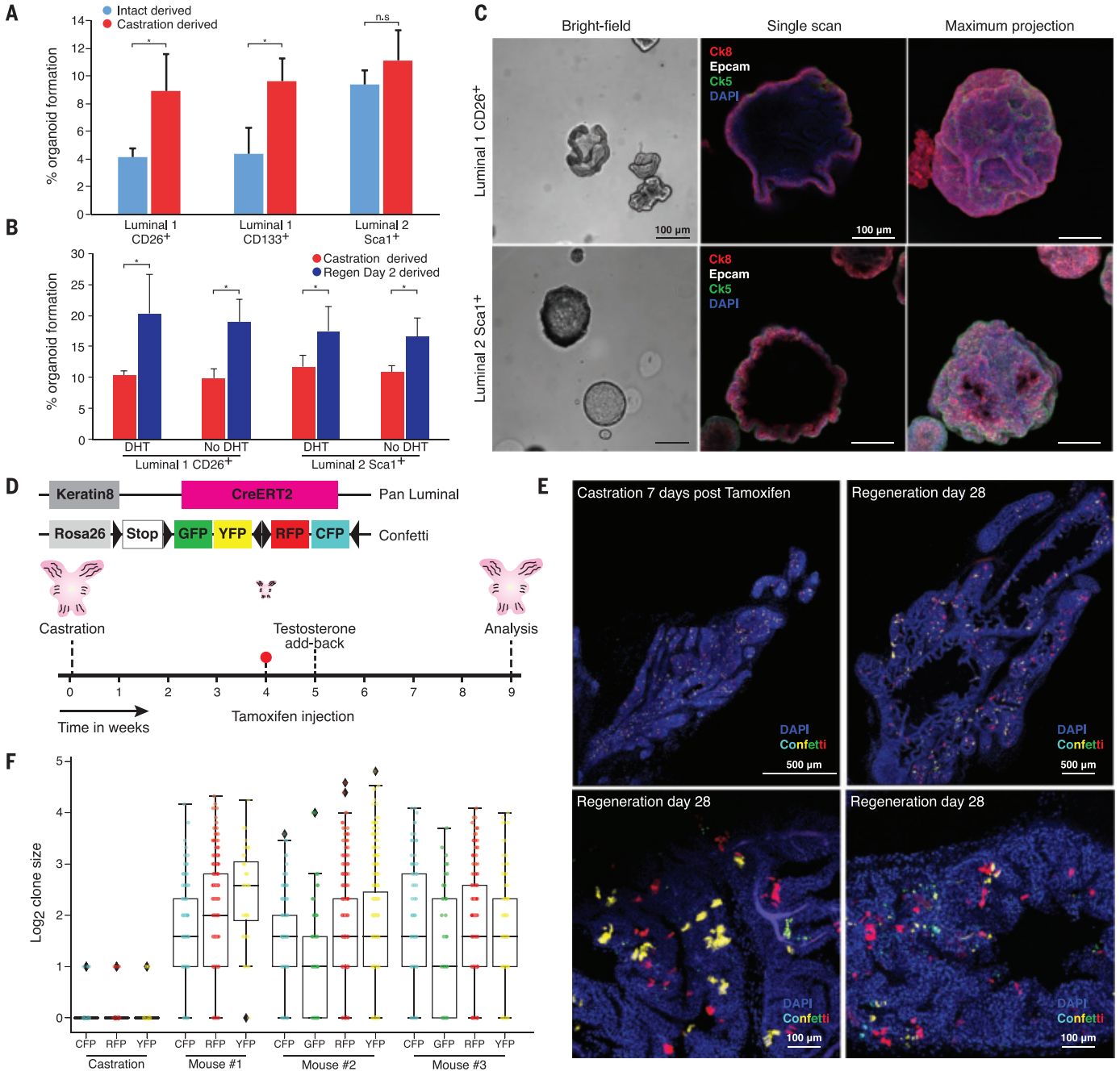

Fig. 3. Enhanced regenerative potential of murine luminal cells after castration in organoid culture and in vivo. (**A** to **C**) Enhanced organoid formation of L1 and L2 cells isolated after castration or during regeneration. (A) Relative organoid formation (%, *y* axis; mean ± SD) in the presence of 1 nM DHT in cultures initiated by L1 or L2 cells isolated by CD26/Dpp4 (L1), CD133/Prom1 (L1), or Sca1/Ly6a (L2) expression from hormonally intact prostate (blue) or prostate 28 days after castration (red). The number of organoids was quantified 7 days after seeding 200 cells ($N = 3$; $^*P < 0.05$, *t* test). (B) Relative organoid formation (%, *y* axis; mean ± SD) from L1 or L2 cells isolated by CD26/Dpp4 or Sca1/Ly6a expression, respectively, from a prostate 28 days after castration (red) or a prostate 2 days into regeneration (blue) in the presence or absence of 1 nM DHT. The number of organoids was quantified 7 days after seeding 200 cells ($N = 3$; $^*P < 0.05$, *t* test). (C) Representative images of organoids derived from CD26/Dpp4$^+$ L1 cells (top) or Sca1$^+$ L2 cells (bottom). (Left) Bright-field images. (Right) Confocal images (single *Z* and maximum projection) stained with Ck8 (red) or Ck5 (green), Epcam (white), or DAPI (purple) 7 days after establishment. Scale bars, 100 µm. (**D**) Lineage-tracing strategy. (**E** and **F**) Contribution of multiple clones to prostate gland regeneration. (E) (Top) Maximum projection of a castrated prostate 7 days after tamoxifen injection (left) and 4 weeks after regeneration (right). Only red fluorescence protein (RFP) and yellow fluorescence protein (YFP) are shown. Scale bars, 500 µm. (E) (Bottom) Higher magnification of lineage-traced prostates showing contribution of multiple clones to gland regeneration. Scale bars, 100 µm. (F) Distribution of size of different color clones. Log_2 clone size (*y* axis) is plotted from three independent mice compared with control (castrated 7 days after tamoxifen) (*x* axis). Raw data are shown in table S2. As observed previously, GFP$^+$ clones are infrequent in the prostate (*34*).

($P > 0.05$, t test) (Fig. 3B) despite robust androgen receptor expression in L1 and L2 cells. This result suggests that the effect of in vivo testosterone supplementation on luminal cell regeneration is indirect, which we address further below.

Lineage tracing of luminal cells during murine prostate regeneration

To determine the contribution of persisting luminal cells to prostate regeneration in vivo, we conducted a lineage-tracing experiment by crossing the Rosa26/four-color Confetti allele (*18*) with the luminal-specific *Krt8* Cre^{ERT2} driver (*19*) (Fig. 3D). In contrast to prior lineage-tracing experiments using a prostate-specific antigen Cre driver (*20*), *Krt8* expression was robust in luminal cells after castration, as shown by successful marking of single luminal cells throughout the prostate (~6%) 1 week after injecting mice with tamoxifen (Fig. 3E, fig. S11a, and tables S1 and S2a). We were unable to identify any labeled basal cells (3 mice, $n = 1204$ cells), indicative of the specificity of the K8-Cre driver for luminal cells (table S1a and fig. S11b). To determine the relative contribution of labeled cells to regeneration, we examined fully reconstituted prostate glands 4 weeks after androgen addback. Analysis of ~450 clones from each of three independent mice revealed an average clone size of ~4.5 cells (4.40 ± 0.39, 95% confidence intervals), indicative of two to three doublings per cell. The different clones were distributed throughout the proximal and distal regions of individual prostate ducts, suggesting that they each arose locally rather than by migration from proximal "stemlike" cells (Fig. 3, E and F; fig. S11, c to e; and table S2). Moreover, the number of labeled luminal cells

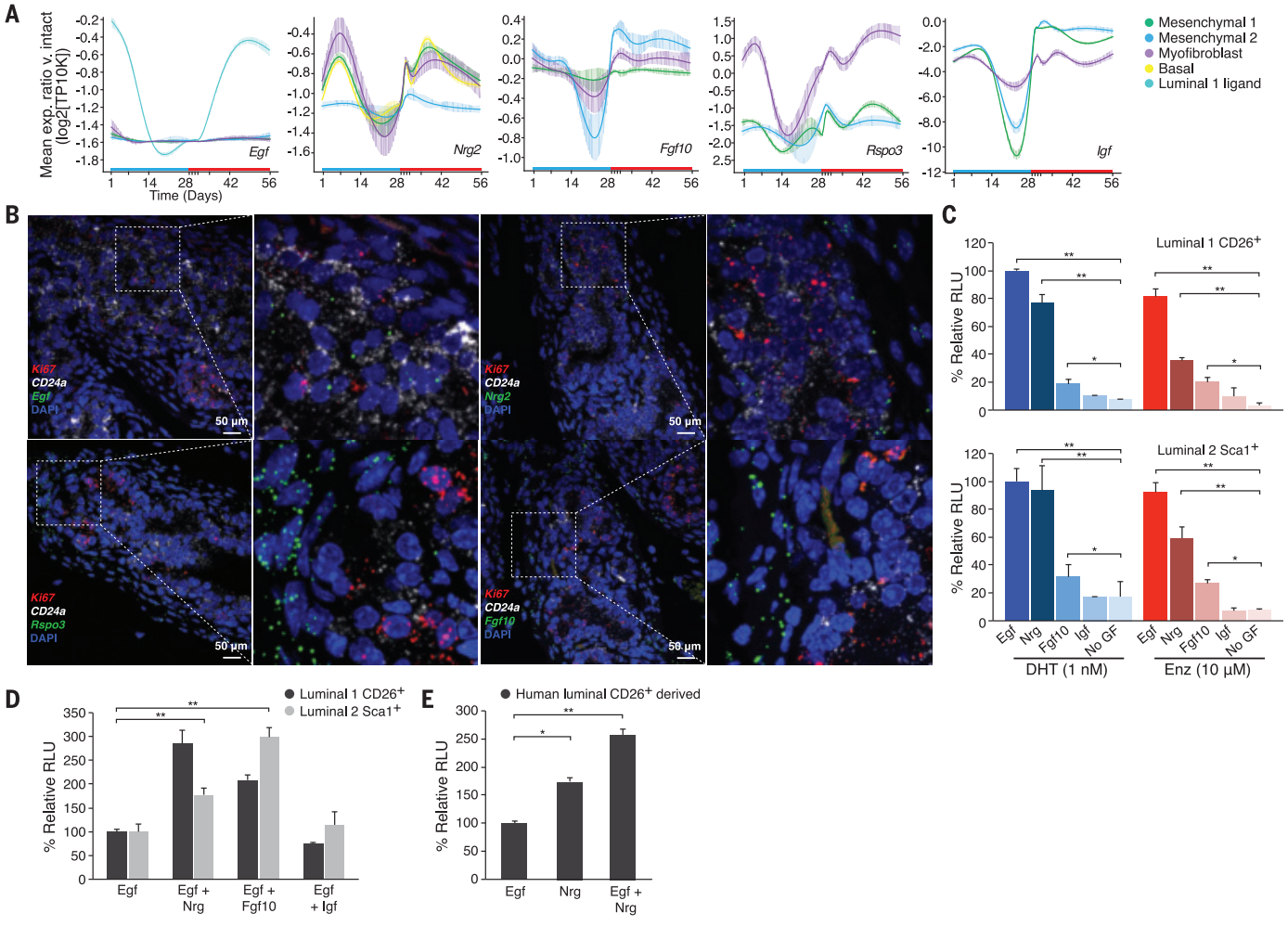

Fig. 4. Androgen receptor–mediated induction of neuregulin in mesenchymal cells is a potential driver of luminal regeneration. (**A**) Changes in expression of key stromal ligands over the C/R time course. Shown is the smoothed mean expression relative to intact prostate (T0) (*y* axis) of ligands in different subsets of stromal and epithelial cells (per color code). (**B**) In situ validation of growth factor expression by RNA-FISH of prostate tissue isolated on regeneration day 2. Representative growth factors (*Egf*, *Nrg2*, *Rspo3*, and *Fgf10*; green), luminal cells (*CD24a*; white), and proliferating cells (*Mki67*; red) are shown. Scale bar, 25 µm. (**C** to **E**) Nrg promotes luminal regeneration in mouse and human organoids. (C) Relative proliferation of murine L1 cells ($CD26/Dpp4^+$; top) and L2 cells ($Sca1/Ly6a^+$; bottom) in the presence of Egf, Nrg, Fgf10, Igf, or no growth factor in the presence of DHT (1 nM) or enzalutamide (10 µM). The data are displayed as average growth ± SD (*y* axis) of 5000 cells measured by CellTiter-Glo at 7 days. Base organoid medium contains noggin, R-spondin, A83-001, and Y-27632. $N = 3$. $^*P < 0.05$, $^{**}P < 0.01$, t test. (D) Relative proliferation of murine L1 and L2 cells measured as in (C) in the presence of EGF alone or EGR in combination with Nrg, Ffg10, or Igf, all in the presence of DHT (1 nM) (*x* axis). $N = 3$. $^*P < 0.05$, $^{**}P < 0.01$, t test. (E) Relative proliferation of human prostate luminal cells ($CD26/DPP4^+$) measured as in (C) in the presence of EGF, NRG, or ERG plus NRG in base human organoid medium (NOGGIN, R-SPONDIN1, FGF2, FGF10, PGE2, A83-001, NICOTINAMID, SB202190, DHT, and Y-27632). $N = 3$. $^*P < 0.05$, $^{**}P < 0.01$, t test. Human organoids for this panel were derived from normal prostate tissue isolated during cystectomy surgery.

remained constant (~6%) after 28 days (table S6a), suggesting that they contribute uniformly to the regenerated gland. Proximal clones were slightly smaller (3.47 ± 0.21 cells) than the overall clone size (4.4 ± 0.35 cells; $P < 0.05$, Welch's t test) (table S5b). In situ analysis using L1 (CD26/Dpp4)– and L2 (Tacstd2/Trop2)–specific markers revealed that most clones (located distally) were composed of L1 cells, whereas proximal clones were composed exclusively of L2 cells. Rare Ck5$^+$ basal cells were detected in some clones (<1% tracing

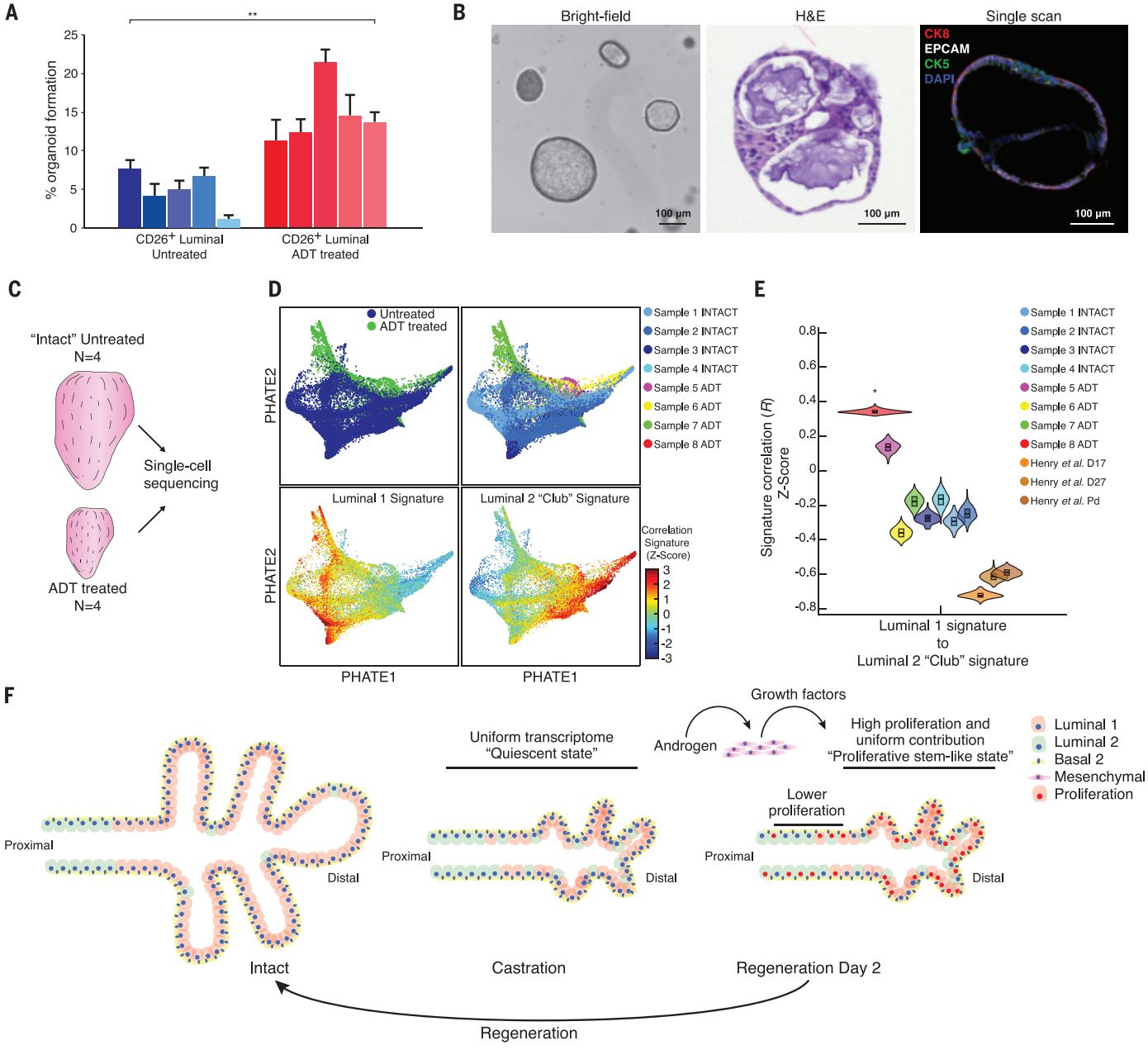

Fig. 5. Androgen deprivation enhances the regenerative potential of human prostate luminal cells. (**A**) Enhanced organoid formation by human luminal cells obtained after castration. (Left) Relative organoid formation (mean ± SD) of CD26/DPP4$^+$ luminal cells isolated from prostates obtained by radical prostatectomy from hormonally intact patients (N = 5, blue) or patients treated with androgen deprivation therapy (N = 5, red). Organoids were quantified 14 days after seeding of 200 cells. N = 4. **P < 0.01, Welch's t test. (**B**) Representative bright-field image (right), H&E-stained image (middle), and confocal image (right) of a human organoid derived a patient treated with ADT as in (A). For the confocal image: CK8 (red), CK5 (green), EPCAM (white), and DAPI (purple). Scale bar, 100 µm. (**C**) Schematic of human prostate processing for scRNA-seq. (**D**) (Top) PHATE map of luminal cells from all samples stratified by treatment (left) and by sample (right). (Bottom) PHATE maps colored by correlation to RNA signatures derived from Henry *et. al.* (*30*). Shown are L1 cells (left) and L2 "Club" cells (right). (**E**) Pairwise correlation of signature scores for L1 and L2 "Club" cells (*30*) per patient after CNA filtering. Signatures were generated using previously published human prostate luminal cell data (*30*). *Significant change of the median correlation (P < 0.05, Welch's t test, one-sided test). (**F**) Model of prostate regeneration. The prostate gland shrinks ~90% after androgen deprivation (castration) because of the loss of luminal epithelial cells. During this process, the transcriptome of L1 cells closely resembles that of more stemlike L2 cells. Androgen addback stimulates production of growth factors by distinct populations of mesenchymal cells, which rapidly recruit nearly all persisting luminal cells into the cell cycle. Each of these proliferating luminal cells collectively contributes to the regeneration of the prostate gland, rather than a rare stem cell population.

events) (table S1c), indicating that luminal cells retain bilineage potential during regeneration (fig. S11c).

Mesenchymal-derived growth factors support luminal cell growth in organoid culture

To explain the discrepancy between the effects of androgen addback in vivo (which greatly enhanced the clonogenicity of L1 cells in organoid culture) versus androgen supplementation in vitro (which had no effect), we postulated that the effect of in vivo androgen addback is indirect despite robust androgen receptor expression in L1 cells. Indeed, early work using renal capsule tissue recombination assays reported an essential role of androgen receptor in mesenchymal cells in prostate regeneration, demonstrating the importance of androgen-regulated mesenchymal growth factors (*21*). More recent studies of conditional *Ar* deletion have shown that the androgen receptor is dispensable for luminal regeneration after castration but is required for certain functions such as proliferation of castration-resistant, Nkx3.1-expressing luminal cells (*22*).

To address this discrepancy, we examined the effect of in vivo androgen addback on non-epithelial cells and observed profound transcriptional changes in M1 and M2 mesenchymal subpopulations during the C/R cycle (fig. S12, a and b), which were similar in extent to the changes seen in luminal cells (Fig. 2C) and basal cells (fig. S12b). We reasoned that reciprocal changes in the levels of ligands and/or cognate receptors may provide clues to cell-cell circuits that drive prostate regeneration. We thus searched for changes in androgen-dependent expression of previously annotated ligand-receptor pairs (*23*) across the complete C/R cycle in all cells in the prostate. Between every pair of cell subtypes (e.g., L1 and M2), we tested the enrichment of ligand-receptor pairs that were differentially expressed across the subtypes (table S3). Among the most substantial changes in ligand expression at the mRNA level were neuregulin 2 (*Nrg2*) (M1 and smooth muscle 1), insulin-like growth factor 1 (*Igf1*) (M1 and M2), fibroblast growth factor 10 (*Fgf10*) (M2), and r-spondin 3 (*Rspo3*) (smooth muscle 1) (Fig. 4A and fig. S12c), with corresponding changes in fibroblast growth factor receptor 2 (*Fgfr2*) and leucine-rich repeat containing G protein–coupled receptor 4 (*Lgr4*) expression, primarily in L1 cells. All of these signaling pathways are implicated in prostate development (*24*–*27*). We also observed a modest increase in epidermal growth factor (*Egf*) ligand expression by L1 cells within 24 hours of androgen addback that peaked after full reconstitution. This is noteworthy because EGF is a key component of epithelial organoid culture media (Fig. 4A and fig. S12c). We confirmed the spatiotemporal expression of these growth factors in situ during the C/R cycle using RNA fluorescence in situ hybridization (RNA-FISH) (Fig. 4B and fig. S13).

To test the functional impact of these mRNA expression changes, we compared the organoid generation potential of L1 and L2 cells isolated from castrated mice in standard medium (with EGF, Noggin, R-spondin, and A83) with new media conditions guided by the growth factor expression changes identified by single-cell analysis (Fig. 4C and fig. S14a). Nrg stimulated growth 10-fold in L1 cells and fivefold in L2 cells, even when androgen receptor signaling was pharmacologically inhibited by enzalutamide. Histologically, Nrg-treated organoids had larger lumens with more polarized luminal cells, a phenotype that was inhibited by enzalutamide (figs. S12e and S14b). Fgf10 had a more modest effect on growth (twofold over background), whereas Igf1 was inactive (Fig. 4C and figs. S12e and S14a). Combinations of Erg$^+$Nrg or Egf$^+$Fgf10 stimulated growth and lumen size even more potently, at levels two- to threefold above those seen with Egf alone (Fig. 4D and figs. S12f and S14c). These growth factors were similarly active in promoting the growth of normal human prostate organoids, indicative of cross-species conservation (Fig. 4E and figs. S12, g and h, and S14, d and e).

Luminal subpopulations are present in human prostate, with enhanced regenerative properties after androgen ablation

To determine whether the castration-induced changes in the regenerative potential of murine luminal cells extends to human prostate, we isolated luminal populations from prostate samples derived from men who were treated for prostate cancer by radical prostatectomy after receiving androgen deprivation therapy (ADT) (fig. S15a). We focused specifically on histologically normal regions to minimize contamination with tumor cells. As controls, we isolated luminal cells samples from five hormonally intact prostate cancer patients treated with radical prostatectomy. CD26/DPP4$^+$ cells isolated from ADT-treated patients displayed a threefold increase in organoid formation (14.6 ± 3.9%) compared with those from the hormonally intact patients (4.9 ± 2.5%) ($P < 0.05$, Welch's t test) (Fig. 5A and fig. S15b), consistent with our findings in mice. Moreover, these CD26/DPP4$^+$ cells could give rise to PSCA$^+$ luminal cells and CK5$^+$ basal cells, indicative of their multipotency in vitro (Fig. 5B and fig. S15c).

To determine the effect of androgen withdrawal on RNA expression in the human prostate, we generated scRNA-seq profiles from the histologically normal regions of eight of these samples (four hormonally intact and four ADT treated) (Fig. 5C). To ensure that our analysis was restricted to normal cells (and not tumor cells), we inferred single-cell DNA copy number alteration (CNA) profiles on the basis of expression of genes from large genomic regions (*28*). CNAs typical of those seen in primary prostate cancer, such as 3p14, 8p, 8q, 13q, and 16q (*29*), were faithfully identified by inferCNV in luminal cells from samples with histologically confirmed tumor cells (e.g., intact sample 2 and ADT sample 3) (figs. S16 and S17). However, cells with predicted CNAs consistent with known prostate cancer alterations were also detected in histologically normal regions at frequencies ranging from 17 to 50% of luminal cells in the hormonally intact patients. Although some of these cells clustered by their expression profiles with their copy-neutral counterparts (fig. S18) and therefore may be false positives, we conservatively filtered all CNA-predicted cells from all subsequent analyses to ensure that we focused on normal prostate cells.

Unsupervised clustering defined 20 cell subsets in the hormonally intact prostate. Reminiscent of the murine prostate, B cell, T cell, NK cell, macrophage, and dendritic cell populations were present in all samples (fig. S19a). The stromal compartment contained vascular and lymphatic endothelium, glia, and two distinct smooth muscle and mesenchymal populations expressing *WNT2*, *FGF10*, or *RSPO3* (fig. S20). We identified four distinct epithelial clusters (two basal and two luminal) and one small neuroendocrine cluster (fig. S19, b to d). The two basal cell clusters share expression of the canonical basal markers *KRT5*$^+$and *TP63*$^+$ and are primarily distinguished by the expression of *KRT13*$^+$. Basal cells expressing *KRT13*$^+$ have previously been observed in the lung trachea in specific histological structures called "hillocks" (*9*, *30*). The larger luminal population shares features with L1 cells in the mouse, such as expression of secretory and AR-regulated genes (*CD26/DPP4*^{high}, *KLK3/PSA*^{high}, and *PLA2G2A*$^+$). The smaller luminal population is more stem like (*PSCA*$^+$ and *KRT4*$^+$), reminiscent of L2 cells in the mouse, and is primarily distinguished by expression of the secretoglobulin family gene *SCGB1A1*$^+$. Murine *Scgb1a1* is a marker of club cells, a subpopulation in the lung with long-term repopulating activity (*31*, *32*) (Fig. 5D and figs. S19b, S21, and S22). Luminal cells expressing both L1 (*PLA2G2A*^{low}) and L2 (*PSCA*) markers were detected in some samples (figs. S19b and S21). These are unlikely to be doublets from coencapsulation or incomplete digestion because of their relatively high abundance and the fact that L1 and L2 cells are spatially distinct. Their presence thus suggests the possibility of bipotent progenitor cells or cells in transition, which we label luminal intermediates (fig. S21). Although we did not identify a distinct human luminal 3 (ionocyte) cluster by scRNA-seq, we observed rare FOXI1$^+$ cells

interspersed throughout the gland using immunohistochemistry (IHC) (fig. S19d). To determine whether the human counterparts of mouse L1 and L2 cells also share transcriptional features after androgen withdrawal, we compared their expression profiles in hormonally intact and ADT samples. Signatures of human L1 and L2 cells from two of the ADT samples (samples 5 and 8) showed evidence of coembedding in either tSNE or a PHATE map and had a higher correlation of L1 and L2 profiles compared with intact samples (Fig. 5, D and E, and figs. S23, a to c, and S24). One of the ADT samples where L1 and L2 cells did not show this enhancement in shared features had significant tumor content (~50% by histology, Gleason grade 9) despite our attempts at filtering by inferred CNA profiles (fig. S23, d to f).

Discussion

Our study has uncovered a previously unknown complexity of cell subtypes within the prostate. In addition, we found that after castration, most persisting luminal cells (rather than a rare population of stem cells) contribute to the proliferative response, akin to the regenerative process observed after liver injury (*33*). In hormonally intact mice, the prostate gland contains three primary luminal subtypes, the most predominant of which are the secretory epithelial cells lining the distal branching ducts, which we call L1 or secretory luminal cells. Murine L2 cells (*Sca1/Ly6a*$^+$, *Psca*$^+$, and *Tacstd2/Trop2*$^+$) have been described previously in independent reports examining the expression of each of these markers, but our work now consolidates this into a single subtype. Anatomically, L2 cells line the proximal duct with a very sharp transition to L1 cells in distal branching ducts, suggestive of a hierarchical relationship during prostate development. In humans, the L2 counterpart is primarily defined by the club cell marker *SCGB1A1*$^+$; in the lung, cells with this marker are responsible for airway maintenance (*31*). L3 cells have not been previously identified but they resemble pulmonary ionocytes, which have been implicated in the regulation of salt balance within airways (*9*, *10*). Analogous luminal subpopulations are present in humans, with the caveat that L3 cells were detected by IHC only.

An important question is what is the mechanism by which persisting luminal cells acquire enhanced self-renewal, particularly because L1 cells are well-differentiated secretory cells at baseline. The fact that L1 and L2 cells acquire stemlike transcriptional features in response to castration suggests a reprogramming event or cell state change. This hypothesis is further supported by androgen-regulated expression of known stem cell niche factors (Nrg, Fgf10, and Rspo3) in mesenchymal cells. Although we cannot rule out the possibility that a subset of cells with preexisting self-renewal properties is present within the hormonally intact gland, our transcriptomic analysis failed to define a distinct subpopulation matching that of persistent L1 cells (fig. S6e).

Although we have not yet directly explored the implications of these luminal cell subtypes in cancer, it is noteworthy that mice with *Nkx3.1*- and *CD133/Prom1*-specific Cre expression (each of which is L1 restricted) develop prostate cancers when crossed with various floxed cancer driver alleles (*34*, *35*). Thus, L1 cells can clearly serve as cells of origin for prostate cancer. It will be of interest to explore this question with L2-specific Cre drivers (e.g., *Psca*), as well as in L3 cells. Another question is whether the persistence of large numbers of luminal cells after castration has clinical relevance, particularly for the use of ADT in prostate cancer patients. A precise molecular understanding of how differentiated normal luminal cells acquire stemlike regenerative properties could provide insight into ways to interfere with this process in malignant prostate cells. Our work suggests that microenvironmental niche factors such as NRG and FGF10 may play a role. Because cancer cells often exploit the stemlike niches used by normal cells, these insights could suggest new prostate cancer therapies that might be useful in combination with AR blockade.

REFERENCES AND NOTES

1. H. Clevers, F. M. Watt, *Annu. Rev. Biochem.* **87**, 1015–1027 (2018).
2. J. E. McNeal, *Am. J. Surg. Pathol.* **12**, 619–633 (1988).
3. H. F. English, N. Kyprianou, J. T. Isaacs, *Prostate* **15**, 233–250 (1989).
4. X. Wang *et al.*, *Nature* **461**, 495–500 (2009).
5. N. Choi, B. Zhang, L. Zhang, M. Ittmann, L. Xin, *Cancer Cell* **21**, 253–265 (2012).
6. M. Ousset *et al.*, *Nat. Cell Biol.* **14**, 1131–1138 (2012).
7. O. J. Kwon *et al.*, *iScience* **13**, 328–338 (2019).
8. H. Vidarsson *et al.*, *PLOS ONE* **4**, e4471 (2009).
9. D. T. Montoro *et al.*, *Nature* **560**, 319–324 (2018).
10. L. W. Plasschaert *et al.*, *Nature* **560**, 377–381 (2018).
11. S. R. Blomqvist, H. Vidarsson, O. Söder, S. Enerbäck, *EMBO J.* **25**, 4131–4141 (2006).
12. O. J. Kwon, L. Zhang, L. Xin, *Stem Cells* **34**, 191–202 (2016).
13. S. Ross, S. D. Spencer, L. A. Lasky, H. Koeppen, *Am. J. Pathol.* **158**, 809–816 (2001).
14. H. F. English, R. J. Santen, J. T. Lsaacs, *Prostate* **11**, 229–242 (1987).
15. G. S. Evans, J. A. Chandler, *Prostate* **11**, 339–351 (1987).
16. A. S. Goldstein *et al.*, *Proc. Natl. Acad. Sci. U.S.A.* **105**, 20882–20887 (2008).
17. K. R. Moon *et al.*, *Nat. Biotechnol.* **37**, 1482–1492 (2019).
18. H. J. Snippert *et al.*, *Cell* **143**, 134–144 (2010).
19. A. Van Keymeulen *et al.*, *Nature* **479**, 189–193 (2011).
20. J. Liu *et al.*, *Mol. Endocrinol.* **25**, 1849–1857 (2011).
21. G. R. Cunha, B. Lung, *J. Exp. Zool.* **205**, 181–193 (1978).
22. Q. Xie *et al.*, *Nat. Commun.* **8**, 14284 (2017).
23. J. A. Ramilowski *et al.*, *Nat. Commun.* **6**, 7866 (2015).
24. P. C. Marker, A. A. Donjacour, R. Dahiya, G. R. Cunha, *Dev. Biol.* **253**, 165–174 (2003).
25. A. A. Donjacour, A. A. Thomson, G. R. Cunha, *Dev. Biol.* **261**, 39–54 (2003).
26. W. Luo *et al.*, *Stem Cells* **31**, 2492–2505 (2013).
27. V. Mehta *et al.*, *Dev. Dyn.* **240**, 2548–2560 (2011).
28. I. Tirosh *et al.*, *Science* **352**, 189–196 (2016).
29. B. S. Taylor *et al.*, *Cancer Cell* **18**, 11–22 (2010).
30. G. H. Henry *et al.*, *Cell Rep.* **25**, 3530–3542.e5 (2018).
31. E. L. Rawlins *et al.*, *Cell Stem Cell* **4**, 525–534 (2009).
32. K. U. Hong, S. D. Reynolds, A. Giangreco, C. M. Hurley, B. R. Stripp, *Am. J. Respir. Cell Mol. Biol.* **24**, 671–681 (2001).
33. J. R. Schaub, Y. Malato, C. Gormond, H. Willenbring, *Cell Rep.* **8**, 933–939 (2014).
34. Z. A. Wang *et al.*, *Nat. Cell Biol.* **15**, 274–283 (2013).
35. L. Zhu *et al.*, *Cell* **166**, 1132–1146.e7 (2016).

ACKNOWLEDGMENTS

We thank members of the Regev and Sawyers laboratories for valuable critiques and discussions; the Molecular Cytology Core Facility at MSKCC for help with confocal microscopy and IHC; and the Flow Cytometry Core Facility at MSKCC for help with FACS experiments. **Funding:** C.L.S. is supported by HHMI; National Institutes of Health grants CA193837, CA092629, CA224079, CA155169, and CA008748; and Starr Cancer Consortium grant I12-0007. A.R. is an HHMI Investigator and is supported by the Klarman Cell Observatory, NCI grants 1U24CA180922 and R33-CA202820, Koch Institute NCI Support (core) grant P30-CA14051, and the Ludwig Center at MIT (AR). W.R.K. is supported by a fellowship from the Dutch Cancer Foundation and a Prostate Cancer Foundation Young Investigator Award. **Author contributions:** W.R.K. and C.L.S. conceived the project. W.R.K. designed the experiments. W.R.K. performed staining and confocal microscopy. W.R.K., M.H., A.R., and C.L.S. wrote the manuscript. W.R.K, D.C., and E.L.L. performed all mouse work. W.R.K. performed all organoid work. M.H. and A.B. performed bioinformatics analyses. W.K., M.H., A.R., and C.L.S. interpreted the data. M.T. performed IHC and RNA FISH. B.C., A.G., and W.A. provided human prostate samples. M.B., O.C., I.M., O.C., and T.X. performed single-cell sequencing. L.M. and D.P. oversaw the single-cell–sequencing experiments. A.R. and C.L.S. oversaw the project. **Competing interests:** C.L.S. is on the board of directors of Novartis, is a cofounder of ORIC Pharmaceuticals, and is a coinventor of the prostate cancer drugs enzalutamide and apalutamide, covered by U.S. patents 7,709,517, 8,183,274, 9,126,941, 8,445,507, 8,802,689, and 9,388,159 filed by the University of California. C.L.S. is on the scientific advisory boards of the following biotechnology companies: Agios, Beigene, Blueprint, Column Group, Foghorn, Housey Pharma, Nextech, KSQ Therapeutics, Petra Pharma, and PMV Pharma, and is a cofounder of Seragon Pharmaceuticals, purchased by Genentech/Roche in 2014. A.R. is a cofounder of and equity holder of Celsius Therapeutics, equity holder of Immuntias, and is on the scientific advisory boards of Syros Pharmaceuticals, Neogene Therapeutics, ASIMOV Biotechnology, and ThermoFisher Scientific. W.R.K. is a coinventor on patent WO2012168930A2 filed by Koninklijke Nederlandse Akademie Van Wetenschappen that covers organoid technology. **Data and materials availability:** Mouse gene expression data are available at the Gene Expression Omnibus repository https://www.ncbi.nlm.nih.gov/geo/ (accession no. GSE146811). Human raw data are available at the Data Use and Oversight System controlled access repository: https://duos.broadinstitute.org/ (accession no. DUOS-000115). Processed expression data can be downloaded and explored at: https://singlecell.broadinstitute.org/single_cell/study/SCP859 (mouse data) and https://singlecell.broadinstitute.org/single_cell/study/SCP864 (human data).

SUPPLEMENTARY MATERIALS

science.sciencemag.org/content/368/6490/497/suppl/DC1
Materials and Methods
Figs. S1 to S24
Tables S1 to S9
References (*36*–*49*)

15 May 2019; accepted 14 March 2020
10.1126/science.aay0267

REPORTS

NUCLEAR PHYSICS

Precision measurement of the neutral pion lifetime

I. Larin[1,2], Y. Zhang[3,4], A. Gasparian[5]*, L. Gan[6], R. Miskimen[2], M. Khandaker[7], D. Dale[8], S. Danagoulian[5], E. Pasyuk[9], H. Gao[3,4], A. Ahmidouch[5], P. Ambrozewicz[5], V. Baturin[9], V. Burkert[9], E. Clinton[2], A. Deur[9], A. Dolgolenko[1], D. Dutta[10], G. Fedotov[11,12], J. Feng[6], S. Gevorkyan[13], A. Glamazdin[14], L. Guo[15], E. Isupov[11], M. M. Ito[9], F. Klein[16], S. Kowalski[17], A. Kubarovsky[9], V. Kubarovsky[9], D. Lawrence[9], H. Lu[18], L. Ma[19], V. Matveev[1], B. Morrison[20], A. Micherdzinska[21], I. Nakagawa[22], K. Park[9], R. Pedroni[5], W. Phelps[23], D. Protopopescu[24], D. Rimal[15], D. Romanov[25], C. Salgado[7], A. Shahinyan[26], D. Sober[16], S. Stepanyan[9], V. V. Tarasov[1], S. Taylor[9], A. Vasiliev[27], M. Wood[2], L. Ye[10], B. Zihlmann[9], PrimEx-II Collaboration†

The explicit breaking of the axial symmetry by quantum fluctuations gives rise to the so-called axial anomaly. This phenomenon is solely responsible for the decay of the neutral pion π^0 into two photons ($\gamma\gamma$), leading to its unusually short lifetime. We precisely measured the decay width Γ of the $\pi^0 \rightarrow \gamma\gamma$ process. The differential cross sections for π^0 photoproduction at forward angles were measured on two targets, carbon-12 and silicon-28, yielding $\Gamma(\pi^0 \rightarrow \gamma\gamma) = 7.798 \pm 0.056(\text{stat.}) \pm 0.109(\text{syst.})$ eV, where stat. denotes the statistical uncertainty and syst. the systematic uncertainty. We combined the results of this and an earlier experiment to generate a weighted average of $\Gamma(\pi^0 \rightarrow \gamma\gamma) = 7.802 \pm 0.052(\text{stat.}) \pm 0.105(\text{syst.})$ eV. Our final result has a total uncertainty of 1.50% and confirms the prediction based on the chiral anomaly in quantum chromodynamics.

The basic symmetries of the classical world are at the origin of the most fundamental conservation laws. Classical symmetries are generally respected in the quantum realm, but it was realized several decades ago that there are exceptions to this rule in the form of so-called anomalies. The most famous one is arguably the axial anomaly, which enables a process of decay of a light hadron called the neutral π meson into two photons, denoted as $\pi^0 \rightarrow \gamma\gamma$. π mesons were first proposed by Yukawa (*1*) as the intermediaries of nuclear interactions; they result from a phenomenon central to strong interaction physics described by quantum chromodynamics (QCD), the theory of quarks and gluons. These three pions (π^+, π^-, and π^0) consist of light quark-antiquark pairs coupled by the exchange of gluons. The axial anomaly is represented by graphs in perturbative quantum field theory that do not require renormalization, thereby enabling a purely analytical prediction from QCD: the π^0 lifetime. Generally, QCD can analytically predict only relative features and requires experimental data, models, or numerical inputs on the lattice to anchor these relative predictions. Thus, experimental verification of this phenomenon with the highest accuracy is a test of quantum field theory and of symmetry breaking by pure quantum effects (*2*).

The fact that the three light quarks—u, d, and s—have much smaller masses than the energy scale of QCD gives rise to an approximate chiral flavor symmetry consisting of chiral left-right and axial symmetries. The chiral symmetry is spontaneously broken by the nonperturbative dynamics of QCD, which leads to the condensation of quark pairs, the $\langle\bar{q}q\rangle$ condensate. This phenomenon is responsible for the observed octet of light pseudoscalar mesons in nature, with the π^0 being one of them. The axial symmetry is explicitly broken by the axial (or chiral) anomaly (*3*, *4*), originating from the quantum fluctuations of the quark and gluon fields. The chiral anomaly drives the decay of the π^0 into two photons with the predicted decay width (*5*)

$$\Gamma(\pi^0 \rightarrow \gamma\gamma) = \frac{m_{\pi^0}^3 \alpha^2 N_c^2}{576\pi^3 F_{\pi^0}^2} = 7.750 \pm 0.016 \text{ eV}$$

where α is the fine-structure constant, m_{π^0} is the π^0 mass, $N_c = 3$ is the number of colors in QCD, and F_{π^0} is the pion decay constant. $F_{\pi^0} = 92.277 \pm 0.095$ MeV extracted from the charged pion weak decay (*6*); there are no free parameters.

The study of corrections to the chiral anomaly prediction has been mainly done with chiral perturbation theory (ChPT), with the three light flavors. The dominant corrections are the result of meson state mixing caused by the differences between the quark masses. The π^0 mixes with the η and η' mesons, owing to the isospin symmetry breaking, which is in turn a consequence of $m_u < m_d$; the correction is calculable in a global analysis of the three neutral mesons (*7*). The $\Gamma(\pi^0 \rightarrow \gamma\gamma)$ width was calculated in a combined framework of ChPT and $1/N_c$ expansion up to $\mathcal{O}(p^6)$ and $\mathcal{O}(p^4 \times 1/N_c)$ in the decay amplitude [GBH (Goity-Bernstein-Holstein), next-to-leading order (NLO); $\mathcal{O}$, low-energy expansion order; p, any low-energy quantity, such as momentum] (*7*). Their result, $\Gamma(\pi^0 \rightarrow \gamma\gamma) = 8.10 \pm 0.08$eV with ~1% estimated uncertainty, is ~4.5% higher than the prediction of chiral anomaly. Another NLO calculation in ChPT was performed, resulting in 8.06 ± 0.06 eV [AM (Ananthanarayan-Moussallam), NLO] (*8*). The only next-to-next-to-leading-order (NNLO) calculation for the decay width was subsequently performed (*9*), yielding a similar result: 8.09 ± 0.11 eV. The calculations of the corrections to the chiral anomaly in the framework of QCD using dispersion relations and sum rules in (*10*) resulted in the value of 7.93 ± 0.12 eV, which is ~2% lower than the ChPT predictions. The fact that these calculations performed by different methods differ from the chiral anomaly prediction by a few percent, with an accuracy of ~1%, makes the precision measurement of the $\pi^0 \rightarrow \gamma\gamma$ width a definitive low-energy test of QCD.

In past decades, there have been extensive efforts to measure the π^0 radiative decay width by three experimental methods: the Primakoff, direct, and collider methods. The current

[1]Alikhanov Institute for Theoretical and Experimental Physics, National Research Center (NRC) "Kurchatov Institute," Moscow, 117218, Russia. [2]Department of Physics, University of Massachusetts, Amherst, MA 01003, USA. [3]Department of Physics, Duke University, Durham, NC 27708, USA. [4]Triangle Universities Nuclear Laboratory, Durham, NC 27708, USA. [5]Department of Physics, North Carolina A&T State University, Greensboro, NC 27411, USA. [6]Department of Physics and Physical Oceanography, University of North Carolina Wilmington, Wilmington, NC 28403, USA. [7]Department of Physics, Norfolk State University, Norfolk, VA 23504, USA. [8]Department of Physics and Nuclear Engineering, Idaho State University, Pocatello, ID 83209, USA. [9]Thomas Jefferson National Accelerator Facility, Newport News, VA 23606, USA. [10]Department of Physics and Astronomy, Mississippi State University, Mississippi State, MS 39762, USA. [11]Department of Physics, Moscow State University, Moscow 119991, Russia. [12]B. P. Konstantinov Petersburg Nuclear Physics Institute, NRC "Kurchatov Institute," Gatchina, St. Petersburg, 188300, Russia. [13]Joint Institute for Nuclear Research, Dubna, 141980, Russia. [14]Kharkov Institute of Physics and Technology, Kharkov, 310108, Ukraine. [15]Department of Physics, Florida International University, Miami, FL 33199, USA. [16]Department of Physics, The Catholic University of America, Washington, DC 20064, USA. [17]Department of Physics, Massachusetts Institute of Technology, Cambridge, MA 02139, USA. [18]Department of Physics, Carnegie Mellon University, Pittsburgh, PA 15213, USA. [19]School of Nuclear Science and Technology, Lanzhou University, Lanzhou, 730000, China. [20]Department of Physics, Arizona State University, Tempe, AZ 85281, USA. [21]Department of Physics, George Washington University, Washington, DC 20064, USA. [22]RIKEN Nishina Center for Accelerator-Based Science, Wako, Saitama 351-0198, Japan. [23]Department of Physics, Computer Science and Engineering, Christopher Newport University, Newport News, VA 23606, USA. [24]School of Physics and Astronomy, University of Glasgow, Glasgow G12 8QQ, UK. [25]Department of Physics, Moscow Engineering Physics Institute, Moscow, Russia. [26]Yerevan Physics Institute, Yerevan 0036, Armenia. [27]Institute for High Energy Physics, NRC "Kurchatov Institute," Protvino, 142281, Russia.

***Corresponding author. Email: gasparan@jlab.org**

†The collaboration consists of all listed authors. There are no additional authors or collaborators.

particle data group (PDG) value of the $\pi^0 \rightarrow \gamma\gamma$ decay width is 7.63 ± 0.16 eV (*6*). This value is the average of five measurements: two Primakoff-type measurements, one from Cornell University [Cornell (Prim.), 7.92 ± 0.42 eV (*11*)] and another from the Jefferson Laboratory [JLab, PrimEx-I (Prim.), 7.82 ± 0.14(stat.) ± 0.17(syst.) eV (stat., statistical uncertainty; syst., systematic uncertainty) (*12*)]; a direct measurement from the European Center for Nuclear Research [CERN (Dir.), 7.25 ± 0.18(stat.) ± 0.14(syst.) eV (*13*)]; a collider measurement from the Crystal Ball detector at Deutsches Electronen-Synchrotron [CBAL (Col.), 7.7 ± 0.72 eV (*14*)]; and a measurement from radiative pion beta decay [(PIBETA), 7.74 ± 1.02 eV (*15*)]. The result from the PrimEx-I experiment (*12*) improved the uncertainty on the decay width quoted in the previous PDG (*16*) value by a factor of 2.5 and confirmed the validity of the chiral anomaly at the few-percent level. However, there is a 6% discrepancy between the two most precise experiments included in the PDG average—the CERN direct (*13*) and PrimEx-I Primakoff (*12*) values. Furthermore, the accuracy of the PDG average is still not adequate to test the theory corrections to the prediction of the anomaly. The PrimEx-II experiment was conducted at JLab to address these issues.

To reach 1.5% precision in the extracted $\pi^0 \rightarrow \gamma\gamma$ decay width, we implemented several basic improvements in the experimental technique (schematically shown in Fig. 1) used in the previous Primakoff-type experiments. The existing tagged photon beam facility [Tagger (*17*)] in Hall B at JLab was used, thus allowing critical improvements in the background separation and the determination of the photon flux. Instead of the traditional Pb-glass–based electromagnetic calorimeter from the previous experiments, we developed and constructed a $PbWO_4$ crystal–based multichannel, high-resolution, and large-acceptance electromagnetic calorimeter (HyCal) (*18*). The combination of these two techniques greatly improved the angular resolution of the photoproduced π^0s, which is critical for Primakoff-type measurements, and substantially reduced the systematic uncertainties that were present in previous experiments. In addition, the cross sections of two well-known electromagnetic processes—Compton scattering and positron-electron (e^+e^-) pair production from the same experimental target—were periodically measured during the experiment to validate the extracted π^0 photoproduction cross sections and their estimated systematic uncertainties. Tagged photons with known energy and timing were incident on the production targets located in the entrance of the large-acceptance dipole magnet [8% radiation length (r.l.) ^{12}C and 10% r.l. ^{28}Si solid targets were used]. This magnet had two key roles in the experiment: deflecting all charged particles produced in the target from the HyCal acceptance and detecting e^+e^- pairs produced in the target [pair spectrometer (PS)], allowing continuous measurement of the relative photon-tagging efficiencies during the experiment. The decay photons from the photoproduced π^0s traveled through the vacuum chamber and the helium bag and were detected in the HyCal calorimeter located 7 m downstream from the targets. Two-planes of scintillator counters (veto counters), located in front of HyCal, provided rejection of charged particles and effectively reduced the background in the experiment. A more detailed description of the experimental setup is presented in section 2 of (*19*).

In this experiment, we measured the differential cross sections for the photoproduced π^0 mesons at forward angles on two targets. At these small angles, the π^0s are produced by two different elementary mechanisms: one-photon exchange (the so-called Primakoff process) and hadron exchange (the so-called strong process). The amplitudes of these processes contribute both coherently and incoherently in the π^0 photoproduction cross sections at forward angles (eq. S1). The cross section of the Primakoff process is directly proportional to the $\pi^0 \rightarrow \gamma\gamma$ decay width, allowing its extraction from the measured differential cross sections with high accuracy. A more detailed description of these processes and our fitting procedure to extract the decay width is presented in section 3 of (*19*).

PrimEx-I achieved a total uncertainty of 2.8% in the extracted width $\Gamma(\pi^0 \rightarrow \gamma\gamma)$ (*12*). The PrimEx-II experiment aimed to significantly increase the statistics and improve the systematic uncertainties to reach percent-level accuracy. The following modifications were implemented to increase the statistics by a factor of 6: (i) the accepted energy interval of the tagged photons was increased by 50%; (ii) thicker solid targets were used (8% r.l. ^{12}C and 10% r.l. ^{28}Si; and (iii) data acquisition performance (at both electronics and software levels) was upgraded to increase the data-taking rate by a factor of 5. The systematic uncertainties were also reduced, owing to several improvements: (i) the central part of the HyCal (~400 modules) was equipped with individual time-to-digital converters for better rejection of time accidental events; (ii) the trigger for the experiment was simplified by using only events with a total deposited energy above 2.5 GeV in HyCal; (iii) a new set of 12 horizontal scintillator veto counters was added for better rejection of charged particles in HyCal (Fig. 1); and (iv) the distance between calorimeter and target was reduced to 7 m, which allowed for better geometrical acceptance between 1.0° and 2.0° in the π^0 production angles and improved separation of the nuclear coherent and incoherent production terms from the Primakoff process in the measured cross sections (eq. S1). In addition, the improved running conditions (e.g., beam intensity and position stability) of the JLab accelerator allowed for a substantial reduction of the beam-related systematic uncertainties. Using an intermediate–atomic number target, ^{28}Si, in combination with a low–atomic number target, ^{12}C, allowed more effective control of systematic uncertainties related to the extraction of the Primakoff contribution. Similar to the PrimEx-I experiment (*12*), the combination of the photon tagger, with its well-defined photon energy and timing, and the HyCal calorimeter defined the event selection criteria.

The event yield (the number of elastically produced π^0 events for each angular bin) was extracted by using the kinematic constraints and fitting the experimental two-photon invariant mass spectra ($M_{\gamma\gamma}$) to subtract the background contributions. Two independent analysis methods, the constrained and hybrid mass methods, were used to extract the event yield in this experiment. The two methods (integrated over the angular range of θ_π = 0° to 2.5° and for the incident energies $E\gamma$ = 4.45 to 5.30 GeV) are in agreement. The total integrated statistics was ~83,000 π^0 events on ^{12}C targets

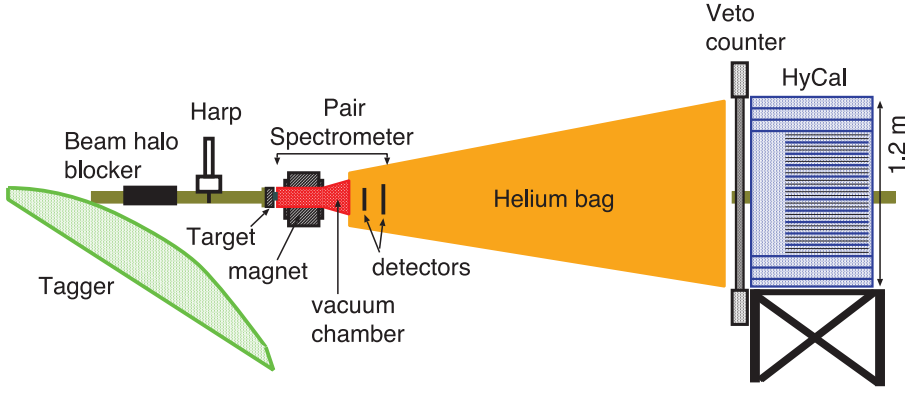

Fig. 1. Experimental setup. Schematic view of the PrimEx-II experimental setup (not to scale; see the text for a description of individual detectors and components).

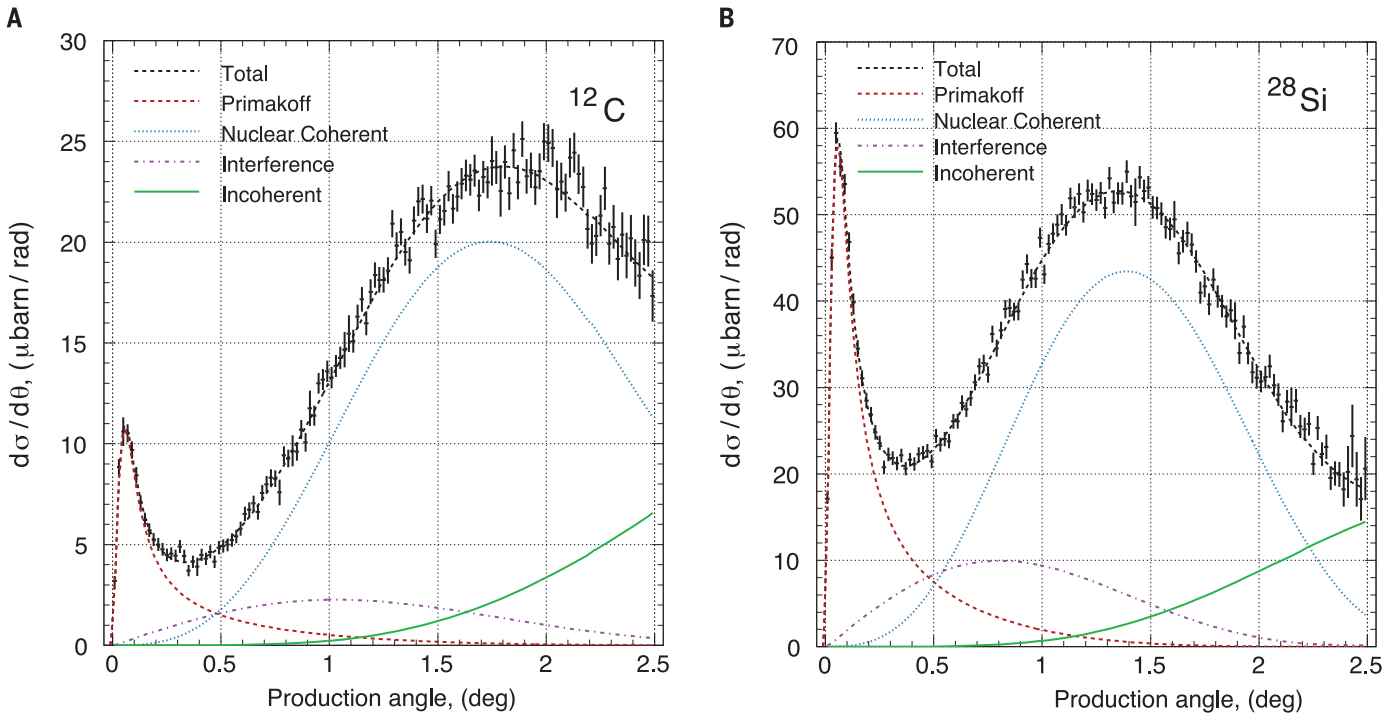

Fig. 2. Experimental cross sections. Experimental differential cross section as a function of the π^0 production angle for ^{12}C (**A**) and ^{28}Si (**B**) together with the fit results for the different physics processes (see text for explanations). Error bars indicate only statistical uncertainties.

and 166,000 events on ^{28}Si targets, a factor-of-6 increase compared with the PrimEx-I values. This result reduced the statistically limited part of the systematic uncertainties in the yield-extraction process. Combining the two analysis methods with the partially independent systematics further reduced the systematic uncertainty to 0.80%. This includes the uncertainty in the physics background subtraction, 0.10%, mostly from ω meson photoproduction.

High-precision monitoring of the photon beam flux during the entire data-taking process is one of the challenging aspects of this type of experiment (*20*). The photon tagger was used for measurements of the photon beam flux, a total absorption counter (TAC) for periodic measurements of the absolute tagging ratios, and a PS for continuous monitoring of the relative tagging ratios and tagger stability (*20*). The stability of the beam parameters (position, width, and frequency of interruptions) was far better than during the PrimEx-I experiment. This, along with more frequent TAC measurements, led to a more accurate measurement of the photon flux (0.80% relative uncertainty was reached in this experiment). Different measurement methods allowed us to achieve subpercent accuracy for the uncertainty in the number of target nuclei per square centimeter: less than 0.10% for ^{12}C targets and 0.35% for ^{28}Si targets (*21*, *22*). The geometrical acceptances and resolutions of the experimental setup have been calculated by a standard nuclear physics Monte Carlo simulation package. The contributed uncertainty in the extracted cross sections from this part is estimated to be 0.55%.

The extracted differential cross sections of π^0 photoproduction on both ^{12}C and ^{28}Si are shown in Fig. 2. They are integrated over the incident photon beam energies of 4.45 to 5.30 GeV (weighted average of 4.90 GeV). The fit results for the four processes that contribute to forward production—Primakoff process, nuclear coherent process, interference between the Primakoff and nuclear coherent amplitudes, and nuclear incoherent process—are also shown.

The $\pi^0 \rightarrow \gamma\gamma$ decay width was extracted by fitting the experimental differential cross sections to the theoretical terms of four contributing processes (eq. S1), convoluted with the angular resolution and experimental acceptances and folded with the measured incident photon energy spectrum. The effect of final state interactions between the outgoing pion and the nuclear target and the photon shadowing effect in nuclear matter must be accurately included in the theoretical cross sections for the precise extraction of the Primakoff term and, therefore, $\Gamma(\pi^0 \rightarrow \gamma\gamma)$ (*23*, *24*). Within our collaboration, two separate groups used different methods to analyze the data. They extracted $\Gamma(\pi^0 \rightarrow \gamma\gamma)$ from their cross sections by using similar fitting procedures (table S1). Thus, for the same target, the statistical and part of the systematic uncertainties from the two analysis groups are correlated. This was accounted for when the two results were combined (*25*). Results for the individual targets were obtained through the weighted average method, yielding: $\Gamma(\pi^0 \rightarrow \gamma\gamma) = 7.763 \pm 0.127(\text{stat.}) \pm 0.117(\text{syst.})$ eV for ^{12}C and $7.806 \pm 0.062(\text{stat.}) \pm 0.109(\text{syst.})$ eV for ^{28}Si. The results from the two different targets were then combined to generate the final result: $\Gamma(\pi^0 \rightarrow \gamma\gamma) = 7.798 \pm 0.056(\text{stat.}) \pm 0.109(\text{syst.})$ eV, with a total uncertainty of 1.57% (Fig. 3).

To check the sensitivity of the extracted decay width to the theory parameters (e.g., nuclear matter density, nuclear radii, photon shadowing parameter, $\pi^0 N$ total cross section), the values of these parameters were changed by several standard deviations and the cross sections were refitted to obtain new decay widths. Using this procedure, we found that the two main contributors to the systematic uncertainties were the nuclear radii and the photon shadowing parameter (*26*, *27*). The nuclear coherent process, which dominates at larger angles for both targets, was determined with high precision (Fig. 2), and this information was used to extract the nuclear radii for the targets. To do so, the radii were varied around the experimental values obtained from electron scattering data (*28*, *29*), known to better than 0.6% uncertainty. Then, the best values for the nuclear radii were defined by minimizing the resulting χ^2 distributions. Our extracted results for the nuclear radii are 2.457 ± 0.047 fm for ^{12}C and 3.073 ± 0.018 fm

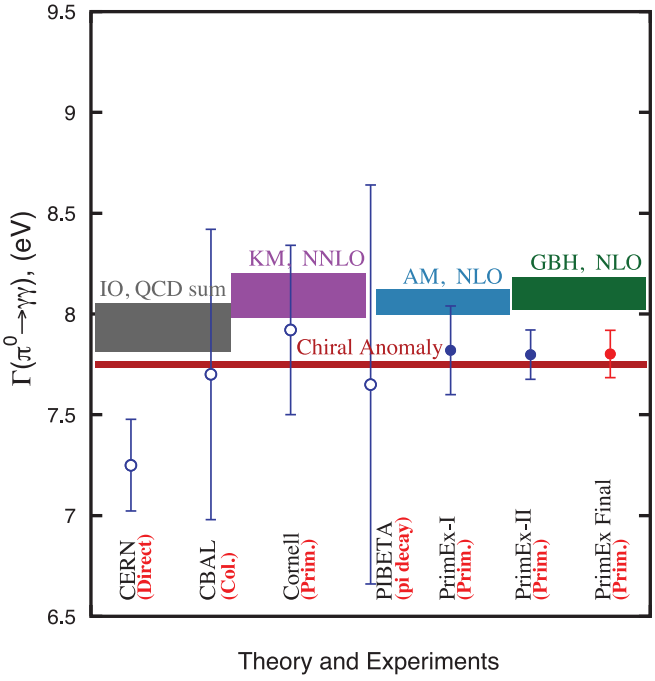

Fig. 3. Theoretical predictions and experimental results of the $\pi^0 \to \gamma\gamma$ decay width. Theory: chiral anomaly (*3*) (red band); IO (Ioffe-Oganesian), QCD sum rule (*10*) (gray band); KM (Kampf-Moussallam), ChPT NNLO (*9*) (purple band); AM, ChPT NLO (*8*) (blue band); and GBH, ChPT NLO (*7*) (green band). Experiments included in the current PDG (*6*): CERN direct (*13*), Crystal Ball (CBAL) collider (*14*), Cornell Primakoff (*11*), PIBETA (*15*), and PrimEx-I (*12*). Our results: PrimEx-II and the PrimEx combined (PrimEx Final). Open circles, experiments before PrimEx; filled circles, PrimEx experiments. Error bars indicate total experimental uncertainties.

for ^{28}Si. These values are consistent with the radii extracted from electron scattering (*28*, *29*). The shadowing parameter was extracted by a similar procedure. The extracted value is $\xi = 0.30 \pm 0.17$, consistent with two previous measurements: [0.25 to 0.50 (*26*) and 0.31 ± 0.12 (*27*)]. Varying this parameter within a 3σ interval generated only a 0.30% uncertainty in the extracted $\Gamma(\pi^0 \to \gamma\gamma)$ (correlated between the two targets). Our systematic uncertainties are described in greater detail in section 3 of (*19*) and are summarized in tables S2 and S3.

For both PrimEx-I and PrimEx-II experiments, the experimental uncertainties have been validated by periodically measuring the Compton cross sections for the same nuclear targets. Our measured Compton cross sections agree with the theoretical simulations of this well-known quantum electrodynamics process to better than 1.7% uncertainty (*30*).

If the results from the two PrimEx experiments are combined, correlations between different systematic uncertainties can be accounted for (*25*). The weighted average final result for the $\pi^0 \to \gamma\gamma$ decay width from the two PrimEx experiments is $7.806 \pm 0.052(\text{stat.}) \pm 0.105(\text{syst.})\text{eV}$ (Fig. 3), defining the new lifetime: $\tau = 8.337 \pm 0.056(\text{stat.}) \pm 0.112(\text{syst.}) \times 10^{-17}$ s. With 1.50% total uncertainty, this is the most precise measurement of the $\Gamma(\pi^0 \to \gamma\gamma)$ decay width and confirms the prediction of the chiral anomaly in QCD at the percent level. As seen from Fig. 3, our result deviates from the theoretical corrections to the anomaly by two standard deviations.

The axial anomaly, which has historically provided strong evidence in favor of the color-charge concept in QCD, continues to teach us about the most fundamental aspects of nature—for example, by strictly constraining physics beyond the Standard Model and presenting an opportunity for measuring the light quark mass ratio. The $\Gamma(\pi^0 \to \gamma\gamma)$ decay width is a critical input for the normalization of the π^0 transition form factor to constrain the hadronic light-by-light scattering contributions to the well-known muon (g-2) anomaly, toward the pursuit of new physics (*31*). The light quark masses are as yet unmeasured, and whether the masses are truly observable is still a matter of debate. Future directions include measuring the anomaly-driven $\eta \to \gamma\gamma$ decay, which provides a normalization to the isospin-violating $\eta \to 3\pi$ decay that leads to a model-independent extraction of the light quark mass ratio (*32*).

REFERENCES AND NOTES

1. H. Yukawa, *Proc. Math. Soc. Jpn.* **17**, 48–57 (1935).
2. S. Weinberg, *The Quantum Theory of Fields*, vol. 2, *Modern Applications* (Cambridge Univ. Press, 1996).
3. J. S. Bell, R. Jackiw, *Nuovo Cim. A* **60**, 47–61 (1969).
4. S. L. Adler, *Phys. Rev.* **177**, 2426–2438 (1969).
5. A. M. Bernstein, B. R. Holstein, *Rev. Mod. Phys.* **85**, 49–77 (2013).
6. M. Tanabashi *et al.*, *Phys. Rev. D* **98**, 030001 (2018).
7. J. L. Goity, A. M. Bernstein, B. R. Holstein, *Phys. Rev. D* **66**, 076014 (2002).
8. B. Ananthanarayan, B. Moussallam, *J. High Energy Phys.* **2002**, 052 (2002).
9. K. Kampf, B. Moussallam, *Phys. Rev. D* **79**, 076005 (2009).
10. B. L. Ioffe, A. G. Oganesian, *Phys. Lett. B* **647**, 389–393 (2007).
11. A. Browman *et al.*, *Phys. Rev. Lett.* **33**, 1400–1403 (1974).
12. I. Larin *et al.*, *Phys. Rev. Lett.* **106**, 162303 (2011).
13. H. W. Atherton *et al.*, *Phys. Lett. B* **158**, 81–84 (1985).
14. D. A. Williams *et al.*, *Phys. Rev. D* **38**, 1365–1376 (1988).
15. M. Bychkov *et al.*, *Phys. Rev. Lett.* **103**, 051802 (2009).
16. C. Amsler *et al.*, *Phys. Lett. B* **667**, 1–6 (2008).
17. D. I. Sober *et al.*, *Nucl. Instrum. Methods A* **440**, 263–284 (2000).
18. A. Gasparian, *Proc. XI Int. Conf. Calorim. Part. Phys.* **1**, 109 (2004).
19. See supplementary materials.
20. A. Teymurazyan *et al.*, *Nucl. Instrum. Methods A* **767**, 300–309 (2014).
21. P. Martel *et al.*, *Nucl. Instrum. Methods A* **612**, 46–49 (2009).
22. C. Harris, R. Miskimen, "Thickness and density measurements for the 10-wafer silicon taget used in PRIMEX II," PrimEx technical notes; www.jlab.org/primex/primex_notes/SiTarget.pdf.
23. S. Gevorkyan, A. Gasparian, L. Gan, I. Larin, M. Khandaker, *Phys. Rev. C* **80**, 055201 (2009).
24. S. Gevorkyan, A. Gasparian, L. Gan, I. Larin, M. Khandaker, *Phys. Part. Nucl. Lett.* **9**, 18–23 (2012).
25. I. Larin, "PrimEx-II $\Gamma(\pi^0 \to \gamma\gamma)$ width: two analyses result and combined Prim-Ex-I and PrimEx-II result," PrimEx technical notes; www.jlab.org/primex/primex_notes/PrimEx_II_uncert.pdf.
26. W. T. Meyer *et al.*, *Phys. Rev. Lett.* **28**, 1344–1347 (1972).
27. A. Boyarski *et al.*, *Phys. Rev. Lett.* **23**, 1343–1347 (1969).
28. H. De Vries, C. W. De Jager, C. De Vries, *At. Data Nucl. Data Tables* **36**, 495–536 (1987).
29. E. A. J. M. Offermann *et al.*, *Phys. Rev. C* **44**, 1096–1117 (1991).
30. P. Ambrozewicz *et al.*, *Phys. Lett. B* **797**, 134884 (2019).
31. M. Hoferichter, B.-L. Hoid, B. Kubis, S. Leupold, S. P. Schneider, *Phys. Rev. Lett.* **121**, 112002 (2018).
32. A. Gasparian *et al.*, "A Precision Measurement of the η Radiative Decay Width via the Primakoff Effect," JLab Proposal E12-10-011 (2009); www.jlab.org/exp_prog/proposals/10/PR12-10-011.pdf.
33. I. Larin, ilyalarin/primex2: Original files, Version 1, Zenodo (2020); https://doi.org/10.5281/zenodo.3731762.

ACKNOWLEDGMENTS

We are grateful to the Accelerator and Physics Divisions at the Jefferson Laboratory, which made these experiments possible. We thank the Hall B engineering and physics staff for their critical contributions during all stages of these experiments. We also thank J. Goity for theoretical support throughout this project. **Funding:** This project was supported in part by the National Science Foundation under a Major Research Instrumentation grant (PHY-0079840) and by the U.S. Department of Energy, including contract no. DE-AC05-06OR23177 under which the Jefferson Science Associates, LLC, operates Thomas Jefferson National Accelerator Facility. **Author contributions:** A.G. is the spokesperson and contact person of the experiment. A.G., R.M., D.D., L.G., and M.K. are the spokespersons of the experiment. A.G. developed the initial concepts of the experiment. A.G., R.M., D.D., L.G., M.M.I., M.K., and I.L. designed, upgraded, and proposed the experiment. The entire PrimEx-II Collaboration constructed the experiment and worked on the data collection. The data acquisition code was developed and built by D.L. The Monte Carlo simulation code was built and validated by I.L., P.A., and M.M.I., with input from other members of the collaboration. Calibrations were carried out by I.L., P.A., Y.Z., J.F., L.M., V.V.T., and L.Y. Analysis software tools were developed by I.L., D.L., M.M.I., Y.Z., J.F., L.M., and V.V.T., with input from all spokespersons. The data analysis was carried out by I.L. and Y.Z., with input from A.G., R.M., D.D., L.G., M.M.I., H.G., D.D., and D.S. All authors reviewed the manuscript. **Competing interests:** The authors declare that they have no competing interests. **Data and materials availability:** The raw data from this experiment, together with all computer codes used for data analysis and simulation, are archived in Jefferson Laboratory's mass storage silo and available at Zenodo (*33*).

SUPPLEMENTARY MATERIALS

science.sciencemag.org/content/368/6490/506/suppl/DC1
Materials and Methods
Supplementary Text
Figs. S1 and S2
Tables S1 to S5
References (*34*–*36*)

11 July 2019; accepted 30 March 2020
10.1126/science.aay6641

NANOPHOTONICS

Three-dimensional cross-nanowire networks recover full terahertz state

Kun Peng[1], Dimitars Jevtics[2], Fanlu Zhang[3], Sabrina Sterzl[1], Djamshid A. Damry[1], Mathias U. Rothmann[1], Benoit Guilhabert[2], Michael J. Strain[2], Hark H. Tan[3], Laura M. Herz[1], Lan Fu[3], Martin D. Dawson[2], Antonio Hurtado[2], Chennupati Jagadish[3], Michael B. Johnston[1]*

Terahertz radiation encompasses a wide band of the electromagnetic spectrum, spanning from microwaves to infrared light, and is a particularly powerful tool for both fundamental scientific research and applications such as security screening, communications, quality control, and medical imaging. Considerable information can be conveyed by the full polarization state of terahertz light, yet to date, most time-domain terahertz detectors are sensitive to just one polarization component. Here we demonstrate a nanotechnology-based semiconductor detector using cross-nanowire networks that records the full polarization state of terahertz pulses. The monolithic device allows simultaneous measurements of the orthogonal components of the terahertz electric field vector without cross-talk. Furthermore, we demonstrate the capabilities of the detector for the study of metamaterials.

The terahertz (THz) band (0.1 to 30 THz) of the electromagnetic spectrum is where electronics meets optics, with THz photons sharing properties from the neighboring spectral regions. For example, in common with microwaves, THz radiation is non-ionizing and penetrates through most nonconducting materials, yet THz radiation can be directed by optical components similar to infrared light. This mixed property enables a wide variety of THz applications, including wireless communication, spectroscopy, sensing, and imaging (*1*).

Time-domain spectroscopy (TDS) with single or subcycle pulses of THz radiation is a powerful tool for materials characterization (*2*), because it directly measures both the amplitude $E(\omega)$ and phase $\phi(\omega)$ of electromagnetic radiation over a broad range of frequencies, ω, thereby allowing straightforward extraction of a material's complex dielectric properties. The pulsed nature of the technique also allows tomographic three-dimensional (3D) spatial mapping of dielectric properties of materials using a methodology similar to radar. Such spectral imaging is nondestructive and has been applied in a wide range of applications including pharmaceutical quality control, medical diagnostics, and production-line inspection. Furthermore, the pulsed nature of the TDS technique facilitates studying dynamic processes in materials with femtosecond time resolution (*3*, *4*).

The vast majority of THz-TDS systems are based on generation and detection of a linearly polarized component of single-cycle THz pulses. In the frequency domain, such data may be represented as $E(\omega)e^{i\phi(\omega)}$, where the two parameters $E(\omega)$ and $\phi(\omega)$ are the amplitude and phase spectra, respectively. Yet, a complete description of a THz pulse must also specify its polarization, which requires two additional parameters to describe the frequency dependence of polarization angle and ellipticity. So, formally the full state of a THz pulse may be described by a 4D Stokes vector or Jones vector for each frequency component of its broad spectrum (*5*). Thus, by encoding polarization information on a THz pulse, it is theoretically possible to double the information it transmits. In spectroscopy, measuring the full state of THz radiation facilitates extraction of anisotropic dielectric properties of materials (which could be affected by surface topography, crystal structure, stress, and magnetic fields) and is key to new techniques such as the THz optical-Hall effect (*6*), THz ellipsometry (*7*), and vibrational circular dichroism spectroscopy (*8*). In THz pulsed imaging applications, polarization information enables high-resolution THz tomography and helps correct the artifacts associated with birefringence and scattering from sample edges (*9*). Therefore, the capability of polarization measurement with THz-TDS is in high demand. Indeed, polarization-resolved THz-TDS systems have been demonstrated since the late 1990s (*10*). However, a lack of measurement schemes for fast and precise polarization sensing has impeded their applications. Currently, polarization detection with THz-TDS can be realized using wire-grid THz polarizers, rotatable polarized THz sources (*11*, *12*), or polarization-sensitive detectors (*13*, *14*).

In most cases, only one component of the THz electric field vector can be measured over

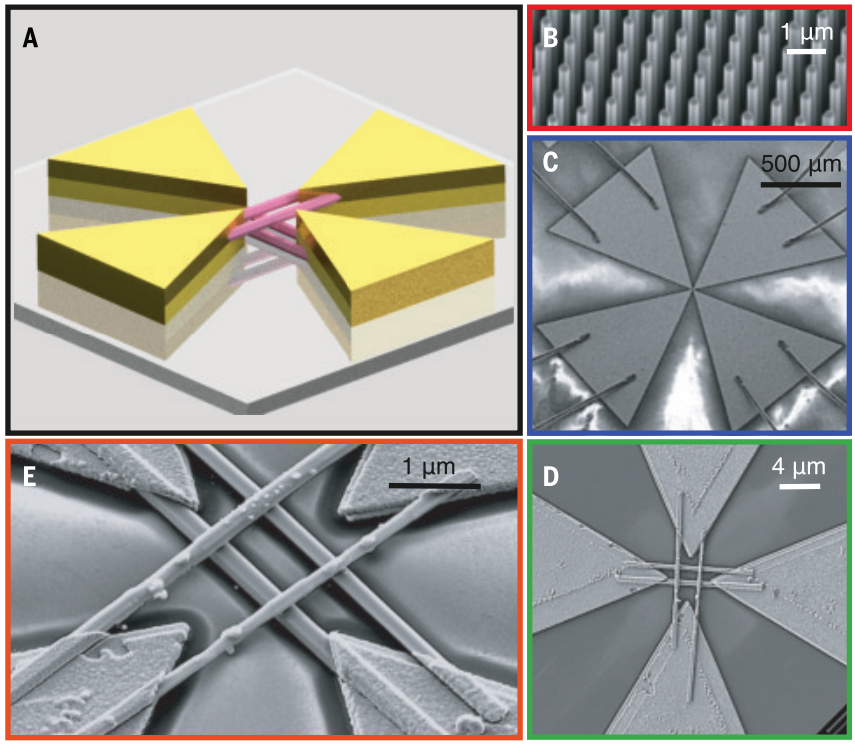

Fig. 1. Structure of the polarization-sensitive cross-nanowire THz detector. (**A**) Schematic illustration of device geometry. (**B**) Scanning electron micrograph (SEM) image of the as-grown InP nanowire array. (**C** to **E**) SEM images of the fabricated detector (blue: entire device; green: center of device; orange: close-up center of device under a tilted view of 25°).

[1]Department of Physics, University of Oxford, Clarendon Laboratory, Oxford OX1 3PU, UK. [2]Institute of Photonics, SUPA Department of Physics, University of Strathclyde, Technology and Innovation Centre, 99 George Street, Glasgow G1 1RD, UK. [3]Department of Electronic Materials Engineering, Research School of Physics, The Australian National University, Canberra, ACT 2601, Australia.
*Corresponding author. Email: michael.johnston@physics.ox.ac.uk

one time-domain scan. For determining the full polarization state, doubled data acquisition time is required, which is problematic for mapping and imaging applications. The use of a multicontact photoconductive antenna (*15*–*17*) for polarization-sensitive measurement is an exceptional case, because this detector type can simultaneously measure the THz electric field vector along multiple directions during a single time-domain scan. However, these devices are difficult to align and cross-talk between detection channels complicates extraction of the polarization state (*15*, *18*), thereby limiting their practical use. Seemingly, the field has reached a technological plateau, calling for a new approach. In this Report, we propose and demonstrate an innovative detector design that uses nanotechnology to measure THz polarization in full. The detector is alignment insensitive and free from the cross-talk, suggesting an ease of implementation in both scientific and industrial settings.

The active elements in our detector are single-crystal semiconductor nanowires that have been systemically studied in our previous work (*19*–*21*) confirming their good suitability for photoconductive THz detection. Here we used indium phosphide (InP) nanowires with a pure wurtzite crystal structure and an approximate average diameter and length of 280 nm and 10 μm, respectively (see materials and methods MM1). The detector architecture is shown in Fig. 1 and consists of two orthogonal gold bow-tie electrodes that are separately bridged by well-aligned nanowires in a "hashtag" configuration. The nanowires on each bow-tie electrode are parallel to the gap orientation, and thus the nanowires contacted by different bow-tie electrodes are orthogonal while being spatially separated perpendicular to the substrate to ensure that they are electrically isolated.

The device architecture was inspired by our previous findings that both single semiconductor nanowires (*22*) and bow-tie THz detectors exhibit extremely high polarization selectivity to absorption of both THz radiation and above-bandgap light. Thus, bow-tie THz detectors based on orthogonal semiconductor nanowires should offer little electromagnetic interference between polarization channels, making them perfect for full polarization characterization.

The cross-nanowire devices were realized through two steps of electron beam lithography and nanowire micropositioning using a "transfer print" technique to effectively manipulate the nanowire location and orientation in the device (see MM2 and MM3), enabling the creation of electrically isolated orthogonal polarization detection channels, thereby avoiding electrical cross-talk. In this work, we concentrate on a hashtag device design with a pair of nanowires per channel. However, the numbers of nanowires for each electrode can be altered; for example, a structure with a single nanowire per channel is presented in fig. S3.

After fabrication, the polarization-sensitive cross-nanowire detectors were characterized in a custom-built THz-TDS system (see MM4 and MM5). Briefly, each near-infrared pulse from a femtosecond laser was split into two: one used to generate a linearly polarized THz pulse in a THz emitter and the other to photoexcite electrons and holes in the cross-nanowire detector. The THz pulse from the emitter was focused on the detector, inducing a transient photocurrent (proportional to the THz field) in each detection channel, which was recorded as a function of time delay t between the THz pulse and optical pulse. The electric-field component of the THz pulse polarized parallel to each antenna (electrode) caused current to flow along its nanowires only after photoexcitation (*23*). Thus, to recover the electric field of the THz pulse in the time domain, the photocurrent data for each channel were differentiated as a function of t (see supplementary text ST1) (*24*). Frequency-domain data were obtained by Fourier transform of the time-domain data.

First, the spectral response of our nanowire detector was examined as shown in Fig. 2A. It can be seen clearly that the horizontal and vertical channels produced responses simultaneously with a current level of a few picoamps, spectral bandwidth of ~2 THz (defined as the cut-off frequency at the noise floor of the frequency spectrum), and low-noise performance, which are consistent with our earlier work (*20*). The current generated by the hashtag detector is limited by the nanosized active material volume but can be increased by adding more nanowires to the array or using larger-diameter nanowires. The two orthogonal channels have a strong linear response relative to the incident THz polarization, where the response current reaches

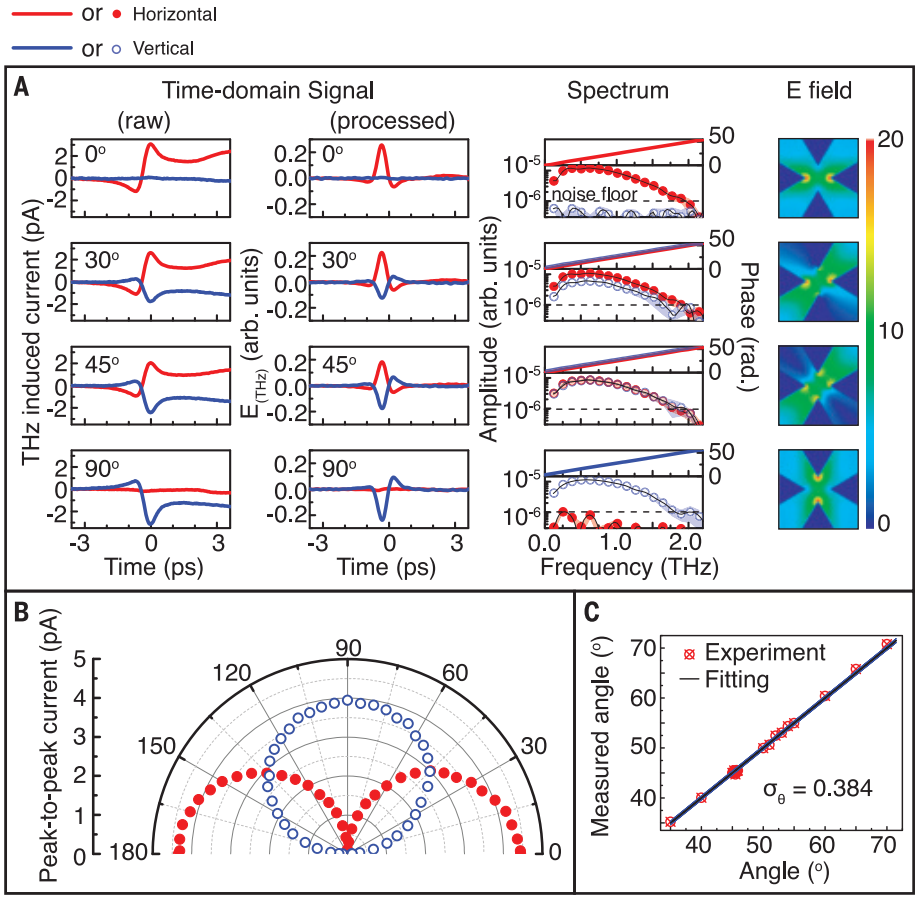

Fig. 2. Characterization of the polarization-sensitive cross-nanowire detector in THz-TDS. (**A**) Responses of the nanowire detector relative to the incident THz polarization (left: raw and processed time-domain THz electric field; middle: amplitude and phase spectrum of the THz electric field; right: simulated THz electric field distribution at 1 THz). 0°, 30°, 60°, and 90° are the angles at which the incident THz pulse is polarized. Red solid line: response from the horizontal-detection channel; blue solid line: response from the vertical-detection channel. (**B**) Relationship between the two orthogonal detection channels in the nanowire detector as a function of the incident THz polarization. Red dots: response from the horizontal-detection channel; blue circles: response from the vertical-detection channel. (**C**) Relative changes of the THz polarization measured by the nanowire detector (cross-circles) for different emitter rotation angles.

a maximum when the THz pulse is polarized parallel to the channel orientation and drops to nearly zero when polarized perpendicular to the channel orientation.

Finite-difference time-domain simulations (FDTDs) were performed to examine the electrode response to the incident THz polarization, which is also linear for each bow-tie structure (see Fig. 2A). The bow-tie antenna structure enhances the intrinsic THz-polarization sensitivity of the nanowires and collects the THz electric field over a much larger area (and concentrates it at the antenna center). Figure 2B illustrates more detailed angle-dependence responses (peak-to-peak current) of both orthogonal detection channels relative to the THz polarization, in excellent agreement with expected cosine and sine functions. This indicates that the two orthogonal channels are independent without any measurable cross-talk between them.

For comparison, we fabricated a multicontact photoconductive antenna, which had the same electrode structure as used in our nanowire detector but used a more conventional Fe^+-implanted InP substrate as the active material. This bulk reference device was measured under conditions identical to those for the nanowire detector. As expected, strong cross-talk dominates the signal and furthermore the degree of cross-talk is dependent on the size and position of the optical excitation spot (see ST3), making extraction of the THz polarization state nontrivial and alignment dependent.

The polarization selectivity of each channel of the nanowire hashtag detector was assessed by measuring the cross-polarized THz extinction ratio. This ratio was found to be 2500 (in power) for the horizontal channel (1440 for the vertical channel), which is a substantial improvement over the ratio of 256 in (*16*) and 108 reported in (*17*) (further analysis is provided in ST3). The high extinction ratio achieved by our hashtag detector is expected, as the aligned nanowires used in our detector are intrinsically polarization sensitive and cross-talk free. After the calibration (see ST4), we assessed the detector sensitivity to the change of the incident THz polarization angle as shown in Fig. 2C. The standard deviation of the measured angle values (calculated from the two-channel data) is 0.38°, indicating that the minimum detectable change of polarization angle is less than 0.4° for our nanowire detector.

To demonstrate the versatility of a polarization-resolved THz-TDS system equipped by our nanowire detector, we characterized a THz metamaterial. Metamaterials for the THz band have attracted considerable attention because of their simplicity of design and capability of manipulating the polarization state of THz radiation (*25*), which is difficult to achieve in natural materials. Here we studied a metamaterial (twisted split-ring resonator pair) that functions as a polarization converter. The schematic illustration of our measurement is shown in Fig. 3A, and the morphology of the metamaterial is presented in Fig. 3B (see MM7). When a linearly polarized THz pulse is transmitted through the metamaterial, a coupling effect will induce co- and cross-polarization components in the transmission direction. FDTD simulations were performed to examine the coupling effect for comparison with experimental results. The simulated and transmission amplitude spectra measured with the hashtag detector are compared in Fig. 3C and show excellent agreement. In particular, the copolarized transmission has a resonance splitting feature (at 1.06 and 1.4 THz) that is also observed in the measured spectra. The difference in the transmission ratio could be attributed to imperfect experimental conditions and/or the dielectric properties of the materials being slightly different from the values used in the simulation. A measurement on a similar metamaterial type has been reported (*26*), where

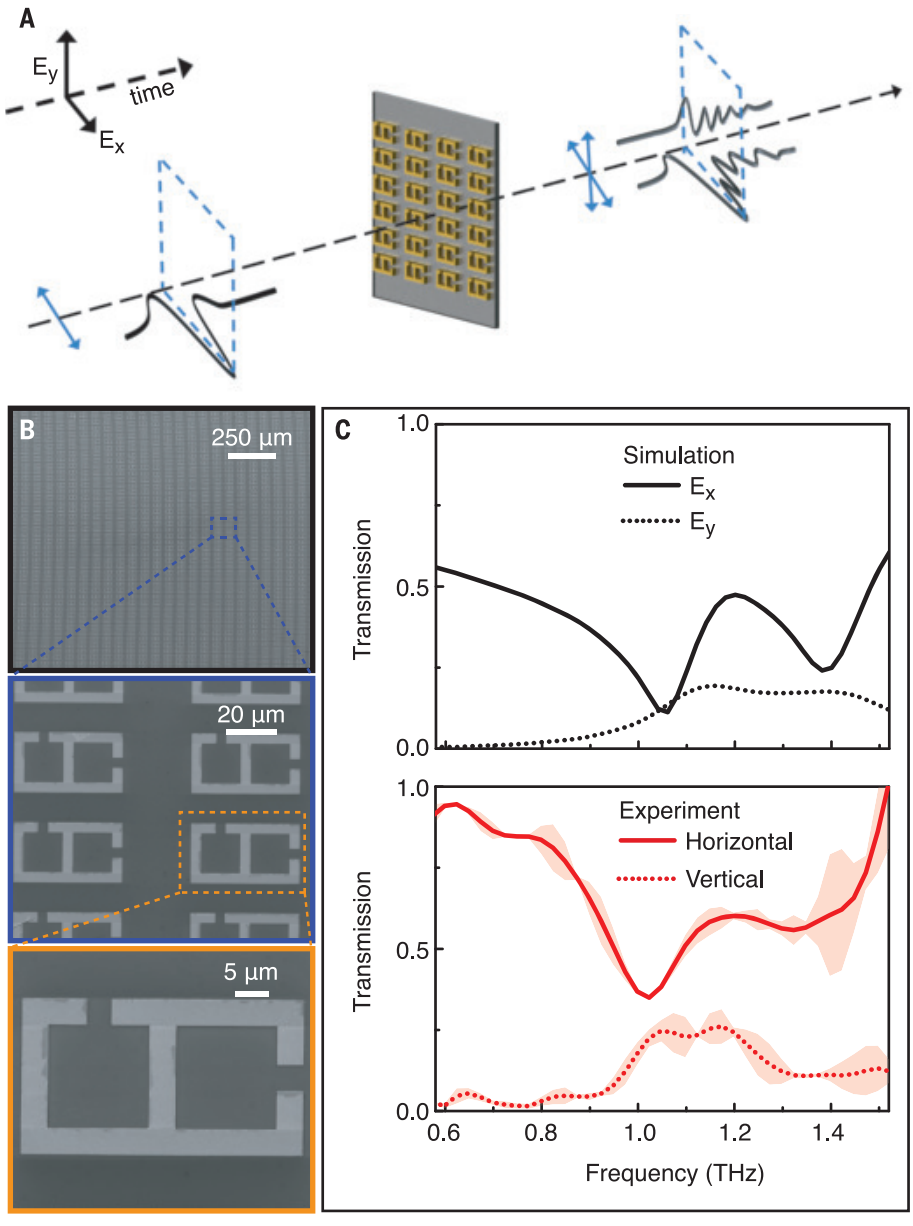

Fig. 3. Application demonstration of polarization-sensitive cross-nanowire detector. (**A**) Schematic representation of transmission measurement of a THz metamaterial. The arrowed blue solid lines show the polarization of the THz pulse before and after passing through the metamaterial. (**B**) SEM images of the fabricated metamaterial. (**C**) Simulated and measured transmission spectra of the THz metamaterial in co- (solid line) and cross- (dotted line) polarizations. Shaded area is the error bar showing the standard variation of repeats in the same measurement.

four wire-grid THz polarizers were used in the system. Our system just required a single scan while providing high polarization accuracy.

In this study, we used orthogonally crossed nanowire networks to develop an ultrafast detector capable of recording the full polarization state of THz radiation and demonstrated its capabilities in the characterization of metamaterials. The monolithic hashtag device is compact and can immediately replace conventional photoconductive receivers in most THz-TDS spectrometers and imaging systems, without any change to the optical layout while vastly improving the capabilities of such systems by including additional spectral polarization information without increased acquisition time. The detector architecture is simple and universal, so any quasi-1D semiconductor nanostructures (e.g., nanorods and nanopillars) could be exploited for further optimization of device performance, in terms of signal-to-noise ratio and accessing ultrabroad spectral bandwidth, thus paving the way to high-speed, high-accuracy THz pulsed imaging. Fast parallel data acquisition for far-field spectral imaging could also be achieved by forming arrays of the hashtag detectors. Furthermore, the detector concept could be scaled down as subwavelength detection units in near-field THz imaging systems for polarization-based super resolution (i.e., nanoscale spatial resolution), or use as an on-chip THz-TDS spectrometer. Therefore, the capabilities and geometry of the detector and its associated on-chip technologies open up a wide range of new scientific applications spanning physics, biology, chemistry, and engineering, while potentially enabling new approaches to industrial quality control, security imaging, and high-speed communications.

REFERENCES AND NOTES

1. S. Dhillon *et al.*, *J. Phys. D Appl. Phys.* **50**, 043001 (2017).
2. B. Ferguson, X. C. Zhang, *Nat. Mater.* **1**, 26–33 (2002).
3. C. Riek *et al.*, *Science* **350**, 420–423 (2015).
4. S. Schlauderer *et al.*, *Nature* **569**, 383–387 (2019).
5. E. Castro-Camus, M. B. Johnston, *J. Opt. A, Pure Appl. Opt.* **11**, 105206 (2009).
6. D. M. Mittleman, J. Cunningham, M. C. Nuss, M. Geva, *Appl. Phys. Lett.* **71**, 16–18 (1997).
7. K. N. Okada *et al.*, *Nat. Commun.* **7**, 12245 (2016).
8. W. J. Choi *et al.*, *Nat. Mater.* **18**, 820–826 (2019).
9. S. Watanabe, *Photonics* **5**, 58 (2018).
10. B. B. Hu, M. C. Nuss, *Opt. Lett.* **20**, 1716–1718 (1995).
11. Q. Chen, X. C. Zhang, *Appl. Phys. Lett.* **74**, 3435–3437 (1999).
12. C. D. W. Mosley, M. Failla, D. Prabhakaran, J. Lloyd-Hughes, *Sci. Rep.* **7**, 12337 (2017).
13. E. Castro-Camus *et al.*, *Opt. Express* **15**, 7047–7057 (2007).
14. N. Nemoto, T. Higuchi, N. Kanda, K. Konishi, M. Kuwata-Gonokami, *Opt. Express* **22**, 17915–17929 (2014).
15. D. S. Bulgarevich *et al.*, *Opt. Express* **22**, 10332–10340 (2014).
16. A. Hussain, S. R. Andrews, *Opt. Express* **16**, 7251–7257 (2008).
17. E. Castro-Camus *et al.*, *Appl. Phys. Lett.* **86**, 254102 (2005).
18. G. Niehues *et al.*, *Opt. Express* **23**, 16184–16195 (2015).
19. K. Peng *et al.*, *Nanotechnology* **28**, 125202 (2017).
20. K. Peng *et al.*, *Nano Lett.* **16**, 4925–4931 (2016).
21. K. Peng *et al.*, *Nano Lett.* **15**, 206–210 (2015).
22. S. A. Baig *et al.*, *Nano Lett.* **17**, 2603–2610 (2017).
23. Z. Yang *et al.*, *Science* **365**, 1017–1020 (2019).
24. E. Castro-Camus *et al.*, *J. Appl. Phys.* **104**, 053113 (2008).
25. T. J. Yen *et al.*, *Science* **303**, 1494–1496 (2004).
26. C. Li, C. C. Chang, Q. Zhou, C. Zhang, H. T. Chen, *Opt. Express* **25**, 25842–25852 (2017).

ACKNOWLEDGMENTS

We thank J. Liu, X. Bian, P. Pattinson, P. Parkinson, and M. Zerbini for useful discussions. We acknowledge the Australian National Fabrication Facility, ACT node (ANFF-ACT), for access to the facilities. Thanks to Z. Li's arrangement, simulation was undertaken with the assistance of resources from the National Computational Infrastructure (NCI Australia). **Funding:** This work was supported by the EPSRC (EP/M017095/1, EP/P006329/1, EP/R034804/1, EP/P013597/1 & EP/R03480X/1), ARC (Australia), and the European Union's Horizon 2020 research and innovation program under grant agreements 735008 (SiLAS) and 828841 (ChipAI). **Author contributions:** M.B.J. conceived the device concept. M.B.J., C.J., and L.F. established this project. K.P. worked on device design, fabrication, characterization, and simulation. D.J., B.G., M.J.S., M.D.D., and A.H. developed the transfer printing technique for the integration of nanowires. D.J. performed the transfer-print process under the supervision of AH. F.Z., L.F., and H.H.T. created the nanowires and ion-implanted wafers. S.S. characterized nanowire photoconductivity. D.A.D. assisted with the fabrication and system optimization. M.U.R. performed scanning electron microscopy under the supervision of L.M.H. K.P. and M.B.J. prepared the manuscript. All authors discussed and commented on the manuscript. **Competing interests:** M.B.J. and K.P. are inventors on UK patent application 2002340.7 submitted by Oxford University that covers the cross-nanowire device concept. **Data and materials availability:** All data needed to reach the conclusions of this Report are presented in the main text or the supplementary materials.

SUPPLEMENTARY MATERIALS

science.sciencemag.org/content/368/6490/510/suppl/DC1
Materials and Methods
Supplementary Text
Figs. S1 to S13
References (*27*–*29*)

29 January 2020; accepted 1 April 2020
10.1126/science.abb0924

CATALYSIS

Water-promoted interfacial pathways in methane oxidation to methanol on a CeO_2-Cu_2O catalyst

Zongyuan Liu[1]*, Erwei Huang[2]*, Ivan Orozco[2], Wenjie Liao[2], Robert M. Palomino[1], Ning Rui[1], Thomas Duchoň[3], Slavomir Nemšák[4], David C. Grinter[5], Mausumi Mahapatra[1], Ping Liu[1,2]†, José A. Rodriguez[1,2]†, Sanjaya D. Senanayake[1]†

Highly selective oxidation of methane to methanol has long been challenging in catalysis. Here, we reveal key steps for the promotion of this reaction by water when tuning the selectivity of a well-defined $CeO_2/Cu_2O/Cu(111)$ catalyst from carbon monoxide and carbon dioxide to methanol under a reaction environment with methane, oxygen, and water. Ambient-pressure x-ray photoelectron spectroscopy showed that water added to methane and oxygen led to surface methoxy groups and accelerated methanol production. These results were consistent with density functional theory calculations and kinetic Monte Carlo simulations, which showed that water preferentially dissociates over the active cerium ions at the CeO_2–$Cu_2O/Cu(111)$ interface. The adsorbed hydroxyl species blocked O-O bond cleavage that would dehydrogenate methoxy groups to carbon monoxide and carbon dioxide, and it directly converted this species to methanol, while oxygen reoxidized the reduced surface. Water adsorption also displaced the produced methanol into the gas phase.

Methane (CH_4), the main component of natural gas, is difficult to upgrade to value-added chemicals (e.g., aromatics, olefins, oxygenates) or even hydrogen because of its strong C-H bonds (104 kcal/mol). In nature, enzymes use oxygen-containing molecules such as water, oxygen, and carbon dioxide (CO_2) to directly convert CH_4 to methanol (CH_3OH) at ambient temperature, unlike commercial processes that require the energy-intensive formation of syngas (H_2 and CO) (*1*–*4*). Applying such biomimetic strategies to heterogeneous catalysts is often limited by the need for high temperatures, which lead to poor selectivity (*5*–*11*), but some oxide and metal-oxide surfaces can dissociate CH_4 at room temperature, which opens the possibility for a direct $CH_4 \rightarrow CH_3OH$ conversion (*12*, *13*). Indeed, a $Ni/CeO_2(111)$ catalyst can directly synthesize CH_3OH on exposure to a mixture of CH_4, O_2, and H_2O. The selectivity of the process is rather low (<40%) (*14*). $Cu_2O/Cu(111)$ and $CeO_2/Cu_2O/Cu(111)$ are very active for water dissociation (*15*, *16*). An inverse catalyst of the $CeO_2/Cu_2O/Cu(111)$ type displays a CH_4 to CH_3OH selectivity close to 70% in the presence of water (*16*).

Extensive studies have investigated the reaction mechanism, including the active sites, the nature of reaction intermediates, the operating pathway, and the role of O_2 and H_2O in the $CH_4 \rightarrow CH_3OH$ conversion. Some studies have proposed O_2 as the oxidizing agent for conversion of CH_4 to adsorbed methoxy groups ($^*CH_3O$) and CH_3OH through the generation

[1]Chemistry Division, Brookhaven National Laboratory, Upton, NY 11973, USA. [2]Chemistry Department, Stony Brook University, Stony Brook, NY 11794, USA. [3]Peter-Grünberg-Institut 6, Forschungszentrum Jülich, 52425 Jülich, Germany. [4]Advanced Light Source, Lawrence Berkeley National Laboratory, Berkeley, CA 94720, USA. [5]Diamond Light Source Limited, Diamond House, Harwell Science and Innovation Campus, Didcot, Oxfordshire OX11 0DE, UK.
*These authors contributed equally to this work.
†Corresponding author. Email: pingliu3@bnl.gov (P.L.); rodrigez@bnl.gov (J.A.R.); ssenanay@bnl.gov (S.D.S.)

of an active metal=O species on the catalyst surface at high temperature (450 to 500 K) (*10*, *14*, *17*–*19*). H_2O can help in the hydrogenation of $*CH_3O$ or block surface sites preventing its decomposition, thus facilitating the extraction of methanol (*10*, *11*, *14*). In the case of Cu-containing zeolites that mimic enzymes, CH_3OH generation is a sequential process that involves treatment or activation with O_2, reaction with CH_4, and finally extraction with water (*6*, *7*, *11*, *20*). For the active $CeO_2/Cu_2O/Cu(111)$ catalyst, the origin of the high selectivity (~70%) toward CH_3OH remains elusive.

We combined ambient-pressure x-ray photoelectron spectroscopy (AP-XPS) with density functional theory (DFT) calculations and kinetic Monte Carlo (KMC) simulation and obtained direct evidence for the essential role of H_2O in the selective production of CH_3OH upon exposure of CH_4, O_2, and H_2O over the $CeO_2/Cu_2O/Cu(111)$ catalyst. The spectroscopic measurements and theoretical modeling agreed that H_2O acts not only as an extractor of CH_3OH, as previously reported (*10*, *11*, *14*), but more

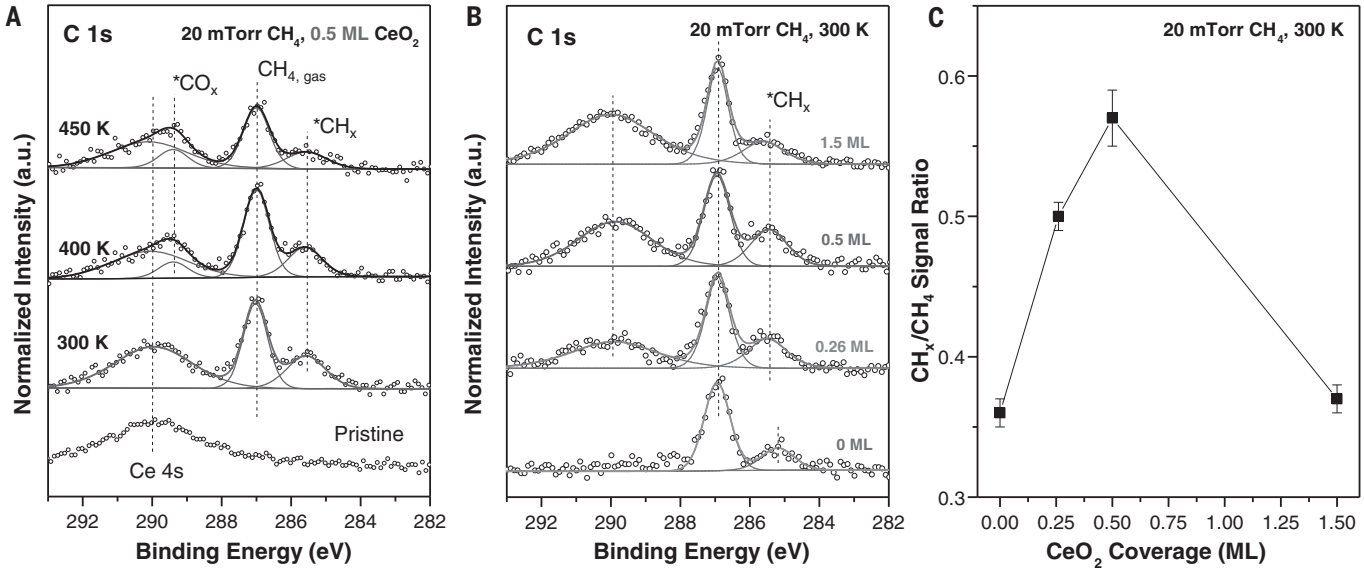

Fig. 1. Methane interaction with $CeO_2/Cu_2O/Cu(111)$. C 1s region of the AP-XPS spectra for introducing 20 mTorr of CH_4 to (**A**) $Cu_2O/Cu(111)$ surface covered with 0.5 ML CeO_2 at different temperatures, and (**B**) different coverages of ceria on $Cu_2O/Cu(111)$ surface at 300 K. a.u., arbitrary units. (**C**) Comparison of the surface $*CH_x$ amount derived from the integration of the corresponding C 1s normalized peak in (B).

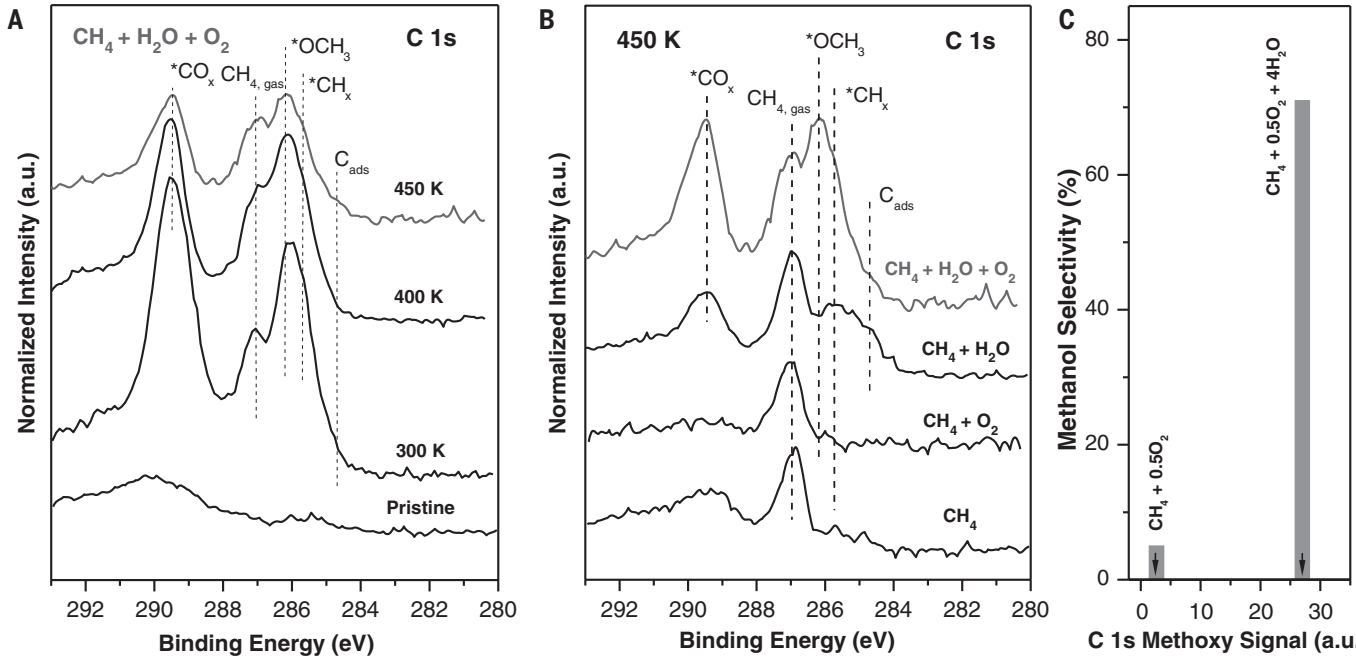

Fig. 2. Water effects on methoxy formation on $CeO_2/Cu_2O/Cu(111)$. C 1s region of the AP-XPS spectra for (**A**) the $CeO_2/Cu_2O/Cu(111)$ surface (θ_{CeO2} ~ 0.5 ML) when exposed to a gas mixture composed of 20 mTorr CH_4, 80 mTorr H_2O, and 10 mTorr O_2 at different temperatures; and (**B**) comparison of exposing $CeO_2/Cu_2O/Cu(111)$ surfaces (θ_{CeO2} ~ 0.5 ML) to different gas reactants at 450 K. (**C**) CH_3OH selectivity versus the amount of $*CH_3O$ generated with and without addition of water. The results for the catalytic tests were taken from (*16*).

importantly as a blocker and active chemical reagent. The addition of H_2O blocks the metal=O mediated mechanism proposed previously (*10*, *14*, *17*–*19*), prevents the complete dissociation of CH_4 to form CO or CO_2, and opens a previously unexplored *OH-mediated pathway, which enables the activation of CH_4 for direct CH_3OH formation at the CeO_2–Cu_2O/Cu(111) interface. Direct $CH_4 \rightarrow CH_3OH$ conversion by *OH introduces the possibility of more active and selective catalysts for CH_4 utilization.

Both Cu-containing enzymes (*3*, *4*) and zeolites (*6*, *10*, *11*) convert CH_4 into CH_3OH. The oxidation state of the copper in these systems is usually assumed to be +2 before reaction with CH_4 and +1 after CH_4 activation (*6*). In AP-XPS experiments, we found a very low reactivity of plain Cu_2O/Cu(111) systems toward CH_4 at room temperature. But this system and ceria are very active for water dissociation (*15*, *21*). The deposition of cerium on Cu_2O/Cu(111) under an atmosphere of O_2 (5×10^{-7} torr) leads to formation of two types of islands, as shown by scanning tunneling microscopy images (*22*). Large islands of ceria (30 to 50 nm in size and triangular in shape) were embedded in the substrate step edges and had a morphology different from that seen for the two most stable surfaces of bulk ceria: CeO_2(111) and CeO_2(110) (*22*). These islands had a height of ~0.3 nm, consistent with a single layer of cerium sandwiched between two layers of oxygen. In addition to the large ceria islands, a low concentration of ceria species of small (0.5 nm) to medium (5 nm) size was formed (*16*, *22*).

As shown in Fig. 1A, exposing a CeO_2/Cu_2O/Cu(111) surface [coverage θ_{CeO2} = 0.5 monolayers (ML)] to 20 mTorr of CH_4 at 300 K resulted in two peaks at ~287.0 and 285.3 eV in the C 1s region, which we attribute to the CH_4 gas phase and surface *CH_x species, respectively (*14*). The formation of *CH_x resulted from the dissociative adsorption of CH_4 at room temperature at a coverage of ~0.15 ML. The hydrocarbon fragment had a relatively strong surface bond given that it was still adsorbed on the surface at 450 K, which suggests a CH_x-surface bond strength greater than 30 kcal/mol. At 400 to 450 K, an additional feature grew at 289.4 eV that corresponded to *CO_x groups formed by the reaction between surface O sites and C atoms produced by the full decomposition of CH_4 (*14*). Thus, in contrast to plain Cu_2O/Cu(111), the CeO_2/Cu_2O/Cu(111) surface exhibited substantial reactivity toward CH_4.

The C 1s AP-XPS spectra acquired while exposing Cu_2O/Cu(111) and several CeO_2/Cu_2O/Cu(111) surfaces to 20 mTorr of CH_4 at 300 K are compared in Fig. 1B. After normalization to the intensity of the peak for gaseous CH_4, the most active CeO_2/Cu_2O/Cu(111) system was that with a ceria coverage near 0.5 ML (Fig. 1C). A 1.5-ML ceria system was not very active, probably because the ceria–copper oxide interface was substantially reduced and ceria deactivated when two-dimensional islands grew into three-dimensional ones (*22*). When these AP-XPS results are compared with data of catalytic activity for the conversion of CH_4 on CeO_2/Cu_2O/Cu(111) (*16*), one finds excellent agreement between the ability of the surface to activate CH_4 at room temperature and its activity for the conversion of the hydrocarbon to CH_3OH or a CO/CO_2 mixture. A CeO_2/Cu_2O/Cu(111) system with 0.5 ML of ceria exhibited the best performance for CH_4 activation and conversion.

Over Cu-containing zeolites, CH_3OH is produced by the sequential steps of activation in O_2, reaction with CH_4, and extraction with H_2O (*6*, *7*, *11*, *20*). After sequential addition of 10 mTorr of O_2 into the chamber at 450 K (CH_4/O_2 reaction feed), no changes were seen in the C 1s region for Cu_2O/Cu(111) or CeO_2/Cu_2O/Cu(111) surfaces. Specifically, no *CH_3O peak was detected around 286.5 eV. This result is consistent with the lack of CH_3OH formation over these surfaces where only CO and CO_2 are detected as reaction products in the absence of H_2O (*16*). Although O_2 dissociates readily on CeO_x/Cu_2O/Cu(111) (*23*), a metal–O or metal=O group is not an efficient agent for the formation of CH_3OH on these surfaces. A *CH_3O intermediate could be formed, but it probably would decompose very rapidly on some active sites of the surface (see DFT calculations below), producing mainly CO and CO_2 and ultimately giving no signal in AP-XPS (*16*).

The addition of H_2O to the CH_4/O_2 reaction mixture induced drastic changes in the chemical process. On CeO_2/Cu_2O/Cu(111), water dissociated to form OH on the surface at 300 and 450 K, as seen in AP-XPS spectra (fig. S1).

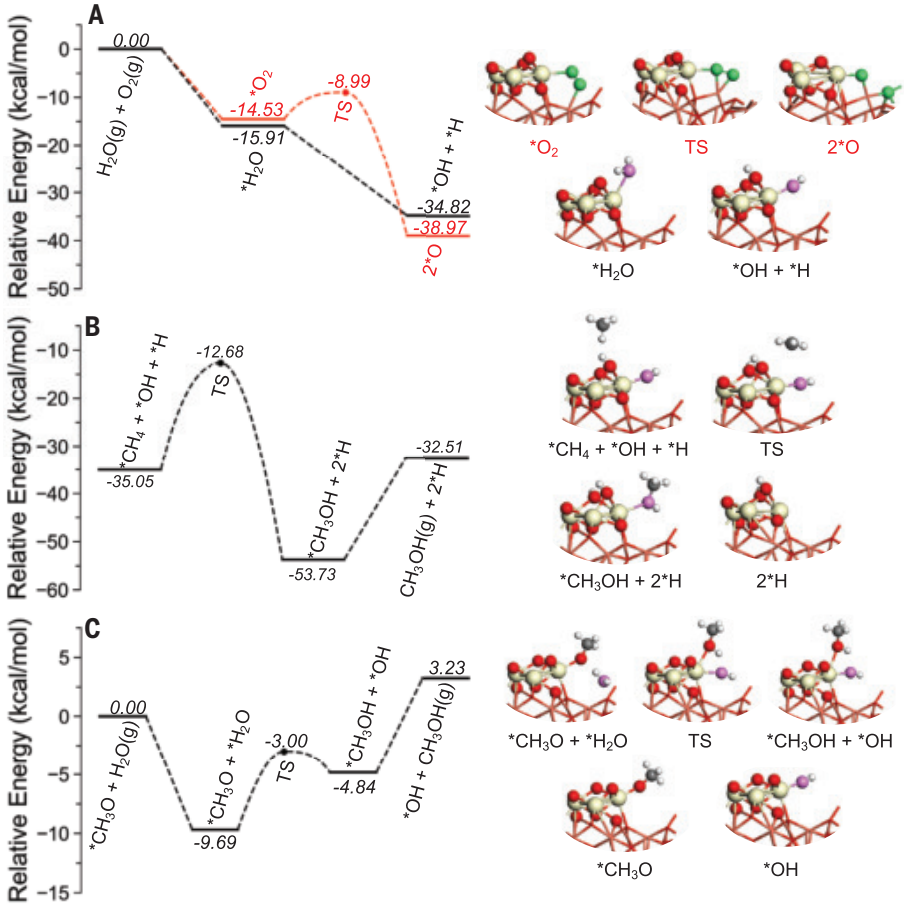

Fig. 3. DFT-calculated potential energy diagrams for the three key steps involved in CH_4 oxidation by O_2 and H_2O on CeO_2/Cu_2O/Cu(111). (**A**) O_2 and H_2O dissociation (red and black, respectively), showing the preferential H_2O dissociative adsorption and thus the blocked active Ce sites from O_2 by H_2O. (**B**) CH_4 oxidation by *OH, demonstrating the enabled one-step CH_3OH synthesis from CH_4 by dissociated fragments from H_2O. (**C**) Hydrogenation of *CH_3O by H_2O, indicating the facilitated CH_3OH formation or extraction by H_2O. The structures of intermediates and transition states (TS) are also included. Yellow, Ce; brown, Cu; red, O in CeO_2/Cu_2O/Cu(111) and *CH_xO (C); green, O in O_2; purple, O in H_2O; gray, C; white, H. Gas phase indicated by the "(g)" label. Units for numerical values: kcal/mol.

Signals for *OH species bound to Cu_2O (~531.1 eV) (*15*) and ceria (~532.1 eV) (*21*) were observed in the O 1s region (fig. S1). Figure 2A shows C 1s AP-XPS spectra collected while exposing a $CeO_2/Cu_2O/Cu(111)$ surface (θ_{CeO2} = 0.5 ML) to a set of $CH_4/O_2/H_2O$ reactants at temperatures between 300 and 450 K. In the presence of water, a clear change in the C 1s features can be seen, with signals not observed in the case of a dry experiment, in which only moderate amounts of $*CH_x$ and $*CO_x$ are detected (for an example, see Fig. 1A). The spectra in Fig. 2A were curve-fitted (fig. S2) well with peaks for $CO_{x,ads}$, $CH_{4,gas}$, CH_3O_{ads}, $CH_{x,ads}$, and C_{ads} (*24*). In test experiments for the adsorption of CH_3OH and its derivatives, the features around 286.2 eV corresponded to adsorbed CH_3O, in good agreement with previous XPS studies (*25*, *26*). As mentioned above, this species was not seen after exposing the surfaces to a simple CH_4/O_2 reaction mixture. Furthermore, in Fig. 2A, the adsorbed CH_3O was seen at temperatures of 400 and 450 K, which were the onset for a catalytic $CH_4 \rightarrow CH_3OH$ transformation over $CeO_2/Cu_2O/Cu(111)$ surfaces exposed to a $CH_4/O_2/H_2O$ mixture (*16*).

Figure 2B compares C 1s spectra collected after exposing a $CeO_2/Cu_2O/Cu(111)$ surface (θ_{CeO2} = 0.5 ML) to CH_4, $CH_4 + O_2$, $CH_4 + H_2O$, and $CH_4 + H_2O + O_2$ at 450 K, a temperature threshold for CH_3OH production (*16*). The amounts of $*CH_x$ and $*CH_3O$ present on the catalyst surface under pure CH_4 and a CH_4/O_2 mixture were negligible. Thus, a reaction feed of CH_4/O_2 produced mainly (~95%) CO and CO_2 as products (*16*). $*CH_3O$ and $*CH_x$ appeared when H_2O was added to the reaction feed, but the amount of $*CH_3O$ was larger when a $CH_4/O_2/H_2O$ mixture was used (fig. S3), and the $*CH_3O$ signal in AP-XPS correlated with the CH_3OH selectivity measured in catalytic tests (Fig. 2C). At high temperatures, CH_4 alone could induce a partial reduction of the ceria overlayer (fig. S4), but under a $CH_4/O_2/H_2O$ mixture, the ceria remained fully oxidized (fig. S5). Additionally, there was no reduction of the Cu_2O film in between ceria and Cu(111). Although the $CeO_2/Cu_2O/Cu(111)$ system has special properties for the dissociation of CH_4 (Fig. 1), some of its sites were probably too reactive to allow any of the $*CH_3O$ formed to avoid decomposition. The OH groups coming from water dissociation (fig. S1) were necessary to block these sites and, as shown below, they also could participate in an additional reaction path for the activation and conversion of CH_4.

Our AP-XPS measurements were fully consistent with theoretical calculations using DFT and KMC simulations under the experimental conditions (pressure ratio: $CH_4:O_2$ = 2:1 or $CH_4:O_2:H_2O$ = 2:1:8; temperature: 450 K; see supplementary materials for details). In the DFT calculations, following a previous study (*16*), the $CeO_2/Cu_2O/Cu(111)$ catalyst was modeled by depositing a Ce_3O_6 cluster on the 44 structure of $Cu_2O/Cu(111)$ (fig. S6A; see supplementary materials for details). According to the DFT results, the $CeO_2/Cu_2O/Cu(111)$ system should produce mainly CO_2 from a CH_4/O_2 mixture following a reaction path that is highly exothermic (figs. S7 and S8). Initially, upon exposure to CH_4 and O_2, an active Ce site (Ce-2 in fig. S6B) at the CeO_2–$Cu_2O/Cu(111)$ interface stabilized O_2 (binding energy E_{ads} = −14.53 kcal/mol) and enabled the facile O-O bond cleavage with the synergy of Cu from the Cu_2O film (reaction energy ΔE = −24.44 kcal/mol; activation barrier E_a = 5.54 kcal/mol) (Fig. 3A). However, in this case, none of the terminal metal=O oxo ligands, which were previously proposed as the active sites for $CH_4 \rightarrow CH_3OH$ conversion for the zeolite-based systems (*10*, *17*–*19*), survived. Instead, the doubly bridging oxo ligand formed (*O) over the interfacial Cu-Ce bridge sites (Fig. 3A and fig. S7).

The CH_4 also preferred the same Ce site, yet the KMC simulations show that it could not compete with O_2 because of weakened binding (E_{ads} = −2.54 kcal/mol) and the elevated barrier for dissociation (E_a = 11.76 kcal/mol) (*16*). Thus, all active Ce sites at the $CeO_2/Cu_2O/Cu(111)$ surface were occupied by *O from O_2 dissociation. The formed doubly bridging oxo Ce-O-Cu species were active to adsorb (E_{ads} = −1.15 kcal/mol) and activate CH_4 through the preferential C-O bond association. Either methoxy ($*CH_3O$) species (ΔE = −37.82 kcal/mol; E_a = 18.45 kcal/mol) (figs. S7 and S8) formed, or $*CH_3OH$ formed directly at the interface (E_a = 16.37 kcal/mol). The KMC simulations, however, demonstrated that the produced $*CH_3OH$ was not stable and preferentially dissociated to $*CH_3O$ with no barrier (ΔE = −14.53 kcal/mol).

The sequential dehydrogenation of $*CH_3O$ to formaldehyde ($*CH_2O$), formyl (*HCO), and the eventual production of CO_2 were highly favorable in terms of both thermodynamics and kinetics according to the DFT calculations (fig. S7), and hence none of the intermediates were likely to be stable. Indeed, under steady states, the $CeO_2/Cu_2O/Cu(111)$ surface remained clean on exposure to CH_4 and O_2, as demonstrated by the KMC snapshot (fig. S9). No $*CH_3O$ or other adsorbed surface species could be observed, which agreed well with the AP-XPS measurements in Fig. 2, B and C, for the experiment with a CH_4/O_2 reaction feed. With regard to the products in the catalytic tests (*16*), the KMC results were consistent with the experimental observations (Fig. 2C), showing that $CeO_2/Cu_2O/Cu(111)$ was highly selective to CO_2 and CO on exposure to CH_4 and O_2 rather than CH_3OH (Fig. 4A). Finally, during the dehydrogenation process, oxygen vacancies (figs. S7 and S8) were generated on the supported CeO_2 cluster, which could be quickly filled in presence of O_2, as reported previously (*16*).

The addition of H_2O to the mixture of CH_4 and O_2 changed the reaction network on the catalyst surface. First, H_2O blocked the adsorptions and dissociation of O_2 at the active interfacial Ce site (Fig. 3A), as seen under exposure of CH_4 and O_2. According to the DFT calculations, H_2O also preferred (E_{ads} = −15.91 kcal/mol)—as O_2 did—to adopt a tilted conformation because of the formation of a hydrogen bond with nearby bridging oxygen (Fig. 3A and figs. S10 and S11). The tilted adsorption was followed by a spontaneous O-H bond cleavage (Fig. 3A), which was much more facile than the O-O (E_a = 5.54 kcal/mol) and C-H bond cleavage (E_a = 11.76 kcal/mol) (*16*). Also, the pressure of H_2O was eight times higher than that of O_2 under reaction conditions considered in both experiment and KMC simulations. Thus, the KMC simulations showed that the adsorption rate of O_2 decreased by a factor of ~30 as a result of the addition of H_2O. In this case, 90% of active Ce sites were occupied by hydroxyl (*OH) from H_2O dissociation, and only 10% formed the Ce-O-Cu oxo species, as

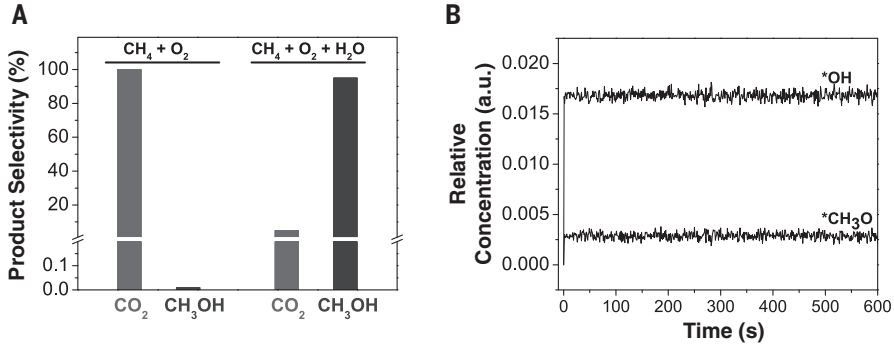

Fig. 4. KMC-simulated product selectivity and reaction intermediates. (**A**) Selectivity of CH_4 oxidation over $CeO_2/Cu_2O/Cu(111)$ on exposure to CH_4 and O_2, with a pressure ratio of 2:1, or CH_4, O_2, and H_2O, with a pressure ratio of 2:1:8, at 450 K. (**B**) Coverage of adsorbed surface species on $CeO_2/Cu_2O/Cu(111)$ under a mixture of CH_4, O_2, and H_2O.

was the case without H_2O. Thus, the adsorbed *OH groups blocked reactive Ce sites from interaction with O_2, and in the presence of H_2O, previously unavailable reaction paths are enabled to facilitate CH_3OH production (Fig. 3A and figs. S10 and S11).

The *OH species generated by H_2O dissociation at the interfacial Ce sites opened a highly effective pathway for a real catalytic transformation (Fig. 3B and fig. S10). Along this pathway, the direct conversion from CH_4 to $*CH_3OH$ was substantially populated by the active *OH at the Ce site (Fig. 3B and fig. S10) through the concerted C-O bond association and C-H dissociation (ΔE = −18.68 kcal/mol; E_a = 22.37 kcal/mol). This step represented the rate-limiting step along the path, and the negative shift in barrier by 2.31 kcal/mol effectively increased the CH_4 conversion by 93.79% and CH_3OH selectivity by 3.78%. This reaction was followed by the barrierless dissociation to $*CH_3O$, as it was in the CH_4 oxidation by O_2. The difference is that the presence of H_2O predominantly blocked $*CH_3O$ decomposition and thus the formation of CO_2. Instead, H_2O enabled the extraction of CH_3OH from $*CH_3O$ in addition to blocking O_2 adsorption and activating CH_4.

This process started with the formation of $*CH_3O\cdots HOH$ through hydrogen bonding (Fig. 3C and fig. S12). Such a structural motif drove the proton hopping from H_2O to $*CH_3O$ (ΔE = 4.85 kcal/mol; E_a = 6.69 kcal/mol) (Fig. 3C and fig. S12). It also produced gas-phase CH_3OH and the active *OH to replace the binding site for $*CH_3O$ at the interfacial Ce site, which is active for direct $CH_4 \rightarrow CH_3OH$ conversion (Fig. 3B and fig. S10). That is, the presence of H_2O favors CH_3OH formation via $*CH_3O$ hydrogenation and easy displacement from the surface into gas phase. The dissociated *H from CH_4 resulted in the hydroxylation of CeO_2 (figs. S10 and S11), which could easily be removed with the assistance of $*H_2O$ at the Ce site, leading to the formation of oxygen vacancy (O_v) and thus the reduced CeO_x (ΔE = −8.30 kcal/mol; E_a = 2.31 kcal/mol) (fig. S10). At this point, O_2 could preferentially fill the O_v and reoxidize CeO_x to CeO_2 (fig. S10), which is the dominant role of O_2 during this process owing to the preferential O_2 dissociation (E_a = 3.00 kcal/mol) over H_2O dissociation (E_a = 15.45 kcal/mol) at the O_v site.

According to the KMC simulations, under steady states of CH_4 oxidation by O_2 and H_2O, the $CeO_2/Cu_2O/Cu(111)$ surface was no longer clean. Instead, two stable surface species formed, *OH and $*CH_3O$ (Fig. 4B), which agreed very well with measurements of AP-XPS (Fig. 2B and fig. S1). Both surface species bound to the supported CeO_2 at the interface (fig. S13). The formation of *OH was associated with H_2O and CH_4 dissociation, and $*CH_3O$ was formed because of the interplay between the barrierless O-H bond cleavage of $*CH_3OH$ and the activated extraction of CH_3OH from $*CH_3O$ by H_2O (Fig. 3C and figs. S7 and S10).

The amount of *OH present on the catalyst surface was larger than the amount of $*CH_3O$ (Fig. 4B), a condition that was essential for preventing the full oxidation of the formed $*CH_3O$ species. The stabilized $*CH_3O$ and the $*CH_3O$ extraction enabled by addition of H_2O to the mixture of CH_4 and O_2 tuned the selectivity of $CeO_2/Cu_2O/Cu(111)$ from CO_2 to CH_3OH as the major product, according to the KMC simulations (Fig. 4A), which was also observed by the AP-XPS measurements and catalytic tests (Fig. 2C) (*16*). The addition of H_2O also facilitated CH_3OH production through oxidation of CH_4 by hindering the $*CH_3O$ dehydrogenation and promoting the displacement of CH_3OH according to the KMC simulation results (Fig. 3C and fig. S13). About one half of the dissociated *O at the active Ce sites led to CH_3OH production, and the rest remained as oxidizing agent to produce CO_2. Yet, because of the lower adsorption rate of O_2 than H_2O at the active Ce sites, 95% of CH_3OH was produced by reaction with H_2O, and the dominant role that O_2 played was to fill the O_v sites via facile dissociation.

The AP-XPS data were consistent with the results of the combined DFT and KMC simulations, showing that on the active CeO_2-Cu_2O interfaces, CH_4 was preferentially oxidized by O_2 into CO and CO_2 (fig. S14A). When H_2O was added to a CH_4/O_2 mixture, the selectivity was tuned toward CH_3OH (fig. S14B). The $CeO_2/Cu_2O/Cu(111)$ inverse catalyst exhibited a reactivity different from that reported for zeolite-based materials during the selective oxidation of CH_4. On the zeolite-based catalysts, O_2 is considered the oxidizing agent and H_2O is simply extracting the formed $*CH_3OH$.

However, on $CeO_2/Cu_2O/Cu(111)$, H_2O played three key roles: It acted as a site blocker. It preferentially occupied the active Ce sites at the CeO_2-Cu_2O interface, which hindered O_2 activation and thus the conversion of CH_4 to CO or CO_2 (Fig. 3A). And, more importantly, it was an active center, where the facile dissociation at the interfacial Ce sites produced the active *OH to promote direct $CH_4 \rightarrow CH_3OH$ conversion (Fig. 3B). In this case, H_2O participated in the reaction as the actual O-provider and enabled direct $CH_4 \rightarrow CH_3OH$ conversion. In this system, O_2 dominantly helped to reoxidize CeO_x, which was partially reduced during the reaction. Finally, as previously proposed, H_2O functioned as an extractor, preventing dehydrogenation of $*CH_3O$ and thus CO_2 formation, while facilitating hydrogenation and thus CH_3OH formation (Fig. 3C). The identification of the key roles played by H_2O while tuning selectivity during CH_4 conversion points to phenomena that must be taken into consideration when dealing with previously unexplored routes for designing efficient catalyst for selective $CH_4 \rightarrow CH_3OH$ oxidation.

REFERENCES AND NOTES

1. A. C. Rosenzweig, C. A. Frederick, S. J. Lippard, P. Nordlund, *Nature* **366**, 537–543 (1993).
2. S. Sirajuddin, A. C. Rosenzweig, *Biochemistry* **54**, 2283–2294 (2015).
3. M. O. Ross *et al*., *Science* **364**, 566–570 (2019).
4. R. Balasubramanian *et al*., *Nature* **465**, 115–119 (2010).
5. M. Ravi, M. Ranocchiari, J. A. van Bokhoven, *Angew. Chem. Int. Ed.* **56**, 16464–16483 (2017).
6. V. L. Sushkevich, D. Palagin, M. Ranocchiari, J. A. van Bokhoven, *Science* **356**, 523–527 (2017).
7. S. Grundner *et al*., *Nat. Commun.* **6**, 7546 (2015).
8. J. Shan, M. Li, L. F. Allard, S. Lee, M. Flytzani-Stephanopoulos, *Nature* **551**, 605–608 (2017).
9. C. Hammond *et al*., *Angew. Chem. Int. Ed.* **51**, 5129–5133 (2012).
10. M. H. Groothaert, P. J. Smeets, B. F. Sels, P. A. Jacobs, R. A. Schoonheydt, *J. Am. Chem. Soc.* **127**, 1394–1395 (2005).
11. P. Tomkins *et al*., *Angew. Chem. Int. Ed.* **55**, 5467–5471 (2016).
12. Z. Liang, T. Li, M. Kim, A. Asthagiri, J. F. Weaver, *Science* **356**, 299–303 (2017).
13. Z. Liu *et al*., *Angew. Chem. Int. Ed.* **56**, 13041–13046 (2017).
14. P. G. Lustemberg *et al*., *J. Am. Chem. Soc.* **140**, 7681–7687 (2018).
15. X. Deng, T. Herranz, C. Weis, H. Bluhm, M. Salmeron, *J. Phys. Chem. C* **112**, 9668–9672 (2008).
16. Z. Zuo, P. J. Ramírez, S. D. Senanayake, P. Liu, J. A. Rodriguez, *J. Am. Chem. Soc.* **138**, 13810–13813 (2016).
17. P. J. Smeets *et al*., *J. Am. Chem. Soc.* **132**, 14736–14738 (2010).
18. J. S. Woertink *et al*., *Proc. Natl. Acad. Sci. U.S.A.* **106**, 18908–18913 (2009).
19. G. Li *et al*., *J. Catal.* **338**, 305–312 (2016).
20. P. Tomkins, M. Ranocchiari, J. A. van Bokhoven, *Acc. Chem. Res.* **50**, 418–425 (2017).
21. J. Carrasco *et al*., *Angew. Chem. Int. Ed.* **54**, 3917–3921 (2015).
22. J. A. Rodriguez *et al*., *Angew. Chem. Int. Ed.* **48**, 8047–8050 (2009).
23. F. Yang *et al*., *J. Am. Chem. Soc.* **133**, 3444–3451 (2011).
24. Y. Lykhach *et al*., *ChemPhysChem* **11**, 1496–1504 (2010).
25. A. Siokou, R. M. Nix, *J. Phys. Chem. B* **103**, 6984–6997 (1999).
26. D. R. Mullins, *Surf. Interface Anal.* **50**, 913–920 (2018).

ACKNOWLEDGMENTS

Funding: The research carried out at Brookhaven National Laboratory (BNL) was supported by the U.S. Department of Energy (DOE), Office of Science and Office of Basic Energy Sciences, under contract DE-SC0012704. X-ray spectroscopy measurements were performed at beamline 9.3.2 at the Advanced Light Source (ALS) of Lawrence Berkeley National Laboratory, which is a U.S. DOE Office of Science User Facility under contract DE-AC02-05CH11231. The DFT calculations were performed using computational resources at the Center for Functional Nanomaterials, a U.S. DOE Office of Science Facility; at the Scientific Data and Computing Center, a component of the Computational Science Initiative at BNL under contract DE-SC0012704; at the National Energy Research Scientific Computing Center, a U.S. DOE Office of Science User Facility supported by the Office of Science of the U.S. DOE under contract DE-AC02-05CH11231; and at Stony Brook University, which was funded by National Science Foundation grant 1531492. S.D.S. is supported by a U.S. DOE Early Career Award. **Author contributions:** P.L., J.A.R., and S.D.S. came up with the general idea and supervised the execution of the project and the writing of the manuscript. Z.L. and E.H. worked on the main writing of the manuscript. Z.L., R.M.P., T.D., S.N., and D.C.G. performed synchrotron photoemission experiments at the ALS. I.O., N.R., and M.M. performed studies with XPS and morphology characterization. E.H. and W.L. performed the theoretical calculations. **Competing interests:** The authors declare no competing financial interests. **Data and materials availability:** All data are available in the main text or the supplementary materials.

SUPPLEMENTARY MATERIALS

science.sciencemag.org/content/368/6490/513/suppl/DC1
Materials and Methods
Figs. S1 to S14
Tables S1 and S2
References (*27*–*30*)

9 December 2019; accepted 26 March 2020
10.1126/science.aba5005

STELLAR PHYSICS

The Sun is less active than other solar-like stars

Timo Reinhold[1]*, Alexander I. Shapiro[1], Sami K. Solanki[1,2], Benjamin T. Montet[3], Natalie A. Krivova[1], Robert H. Cameron[1], Eliana M. Amazo-Gómez[1,4]

The magnetic activity of the Sun and other stars causes their brightness to vary. We investigated how typical the Sun's variability is compared with other solar-like stars, i.e., those with near-solar effective temperatures and rotation periods. By combining 4 years of photometric observations from the Kepler space telescope with astrometric data from the Gaia spacecraft, we were able to measure photometric variabilities of 369 solar-like stars. Most of those with well-determined rotation periods showed higher variability than the Sun and are therefore considerably more active. These stars appear nearly identical to the Sun except for their higher variability. Therefore, we speculate that the Sun could potentially also go through epochs of such high variability.

Stars like the Sun have a magnetic field in their interiors, which is driven by a self-sustaining dynamo process (*1*). When the magnetic field becomes unstable, it can emerge from the stellar surface, leading to the appearance of magnetic features such as bright faculae and dark star spots. As stars rotate, the transits of these magnetic features across their visible surface, and the temporal evolution of these features, lead to stellar brightness variations. Such variations have been extensively studied for the Sun (*2*), where they have an amplitude of up to 0.3% of the sunlight integrated over the entire spectrum, i.e., the total solar irradiance (TSI). Solar variability affects Earth's climate on decadal and longer time scales (*3*) and Earth's atmospheric chemistry on daily and monthly time scales (*4*). Sufficiently precise solar brightness measurements have only been available since the advent of dedicated spaceborne missions in 1978 (*5*). Records of sunspot areas and positions can be used to reconstruct brightness variations back to 1878 (*6*). Sunspot counts, the longest record of regular observations of solar magnetic activity, extend back to the onset of telescopic observations around the year 1610 (*7*). Solar activity can be reconstructed over longer periods, up to 9000 years, from cosmogenic isotopes (*8*).

We took an alternative approach by comparing the Sun's activity with other solar-like stars (*9*, *10*). Stellar magnetic activity and photometric variability are strongly correlated [e.g., (*11*)]. The same applies to the Sun, for which there is a close correlation between proxies for solar magnetic activity and photometric variability (*12*, *13*). There is an ongoing debate about whether solar photometric variability is smaller than the variability of other stars with near-solar effective temperatures and a similar level of magnetic activity (*10*, *14*, *15*). With the advent of planet-hunting missions, particularly the Kepler space telescope (*16*), this topic has received renewed attention. For example, the Sun has been found to be photometrically quieter (i.e., less variable) than most of the stars observed by Kepler (*17*). By contrast, the TSI has a similar level of variability compared with a sample of main-sequence stars with near-solar (and lower) effective temperatures in the Kepler field (*9*). Those studies could not constrain their samples to near-solar rotation periods because of the lack of available measurements. This may have affected their results, because the stellar rotation period and effective temperature are related to the action of the dynamo and therefore the level of magnetic activity (*1*).

To compare solar photometric variability with other stars, we focused on Kepler observations of main-sequence stars with near-solar fundamental parameters and rotation periods. The stellar fundamental parameters that we considered are the effective temperature $T_{\rm eff}$, surface gravity log *g*, and metallicity [Fe/H] (*18*, *19*). We adopted a parameter catalog (*19*) that is based on Kepler data release 25 (DR25). Rotation period measurements are available for thousands of stars observed during the Kepler mission (*20*, *21*). We adopted a catalog of 34,030 stars with determined rotational periods and 99,000 stars for which no rotation periods were detected [(*21*), their tables 1 and 2]; we refer to these as the "periodic" and the "nonperiodic" samples, respectively. From both

[1]Max-Planck-Institut für Sonnensystemforschung, 37077 Göttingen, Germany. [2]School of Space Research, Kyung Hee University, Yongin, Gyeonggi 446-701, Korea. [3]School of Physics, University of New South Wales, Sydney, NSW 2052, Australia. [4]Georg-August Universität Göttingen, Institut für Astrophysik, 37077 Göttingen, Germany.
*Corresponding author. Email: reinhold@mps.mpg.de

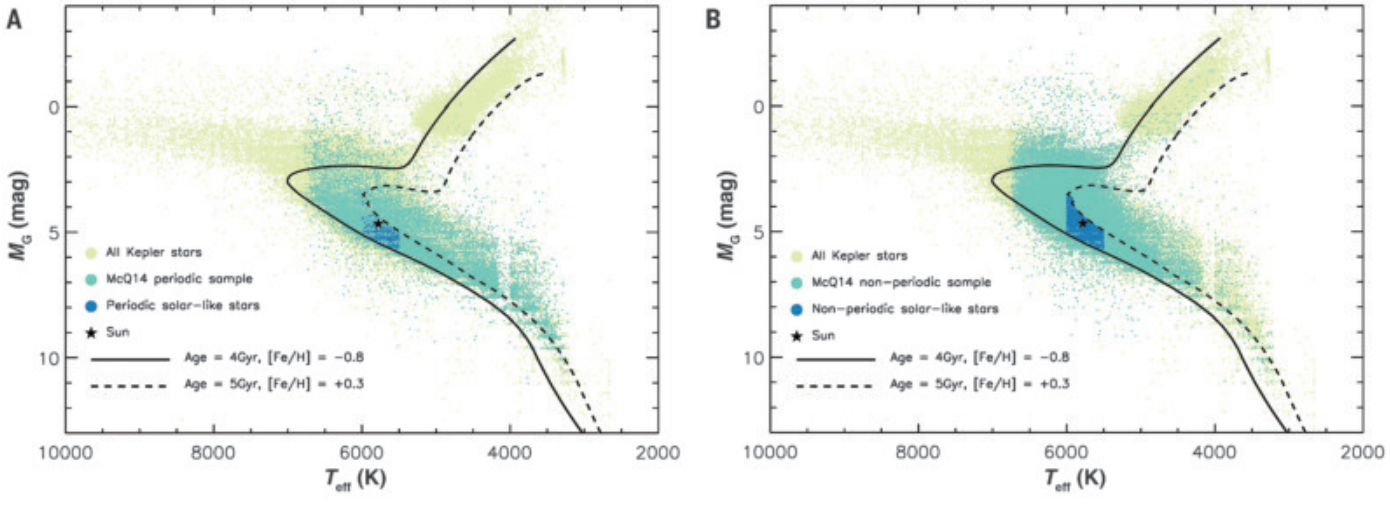

Fig. 1. HRDs of our samples. The periodic (**A**) and nonperiodic (**B**) samples (*21*) are shown in dark green (McQ14 in the legend), and the stars that meet our selection criteria are overplotted in blue. The solid black line is a 4-Gyr isochrone (*13*) with a metallicity [Fe/H] of −0.8, and the dashed black line is a 5-Gyr isochrone with a metallicity [Fe/H] of 0.3. The Sun is indicated by the small black star.

samples, we selected stars with T_{eff} in the range of 5500 to 6000 K (the value for the Sun, indicated with subscript ⊙, is $T_{eff,\odot}$ = 5780 K) and surface gravity log g > 4.2 (Sun: log $g_\odot$ = 4.44) to focus on solar-like main-sequence stars. The surface gravity cut removes evolved stars, which are inactive, so may have diluted the variability of solar-like stars found in previous analyses (*21*). For the periodic sample, we selected rotation periods in the range of 20 to 30 days (Sun: $P_{rot,\odot}$ = 24.47 days sidereal rotation period).

We further restricted the samples using astrometric data from the Gaia spacecraft (*22*). Using the sample stars' apparent magnitudes, distance measurements (*23*), and interstellar extinctions from Gaia data release 2 [Gaia DR2 (*24*)], we constructed a Hertzsprung–Russell diagram (HRD) by computing the absolute Gaia G-band magnitude M_G (Fig. 1). The absolute magnitudes of our samples were restricted by selecting stars from the HRD with near-solar ages between 4 and 5 gigayears (Gyr) (Sun: 4.57 Gyr) and metallicities in the range of −0.8 to 0.3 decimal exponents (dex). This was realized by fitting isochrones [i.e., evolutionary tracks of constant age (*13*)] to the HRD and then selecting periodic and nonperiodic stars between a lower isochrone of 4 Gyr and metallicity of [Fe/H] = −0.8 and an upper isochrone of 5 Gyr and metallicity of [Fe/H] = 0.3 (Fig. 1, A and B). Stellar variability depends only weakly on metallicity (*13*), so a stricter metallicity constraint does not affect our results; therefore, we used this broad range to improve the statistics. The Sun is slightly more luminous than most of the selected periodic and nonperiodic stars (Fig. 1), because 79% of these stars have metallicities lower than the solar value.

We considered stars in our periodic sample to be solar like, i.e., they had near-solar fundamental parameters and rotation periods. The nonperiodic stars are considered only pseudosolar because their rotation periods are not known. Furthermore, we discarded stars fainter than 15th magnitude (in the Kepler band) because of their high noise level, which could mask the stellar variability. After applying all of these selection criteria, our final samples contained 369 solar-like stars with determined rotation periods and 2529 pseudosolar stars without a detected period.

To quantify the magnetic activity of the Sun and the selected stars, we computed their photometric variability using the variability range R_{var}. This quantity is defined as the difference between the 95th and 5th percentile of the sorted flux values (normalized by its median) in a light curve, i.e., the temporal record of the stellar flux (*25*). Our R_{var} values are based on the Kepler Presearch Data Conditioning (PDC) and maximum a priori (MAP) detrended data (*26*). We selected the PDC-MAP data after considering how the different Kepler data products may affect our results (*13*).

We found that R_{var} in the periodic sample showed a weak dependence on effective temperature, rotational period, and metallicity (fig. S8) even though these were constrained to narrow ranges by our selection criteria. We therefore corrected the R_{var} measurements of the periodic stars for these dependencies and normalized them to the values of the solar fundamental parameters using a multivariate analysis (*13*). For four of the 369 periodic stars, this process returned negative R_{var} values, indicating an overcorrection. Those four stars were discarded. For the nonperiodic sample, R_{var} did not correlate with the fundamental parameters (fig. S9), so no correction was applied.

Figure 2 shows three example stellar light curves and solar TSI data (*13*) taken at the same epoch as the Kepler observations. TSI data have been demonstrated to be suitable for direct comparison with the variability observed in the Kepler passband (*9*, *13*). Although the star KIC 10449768 exhibits variability that

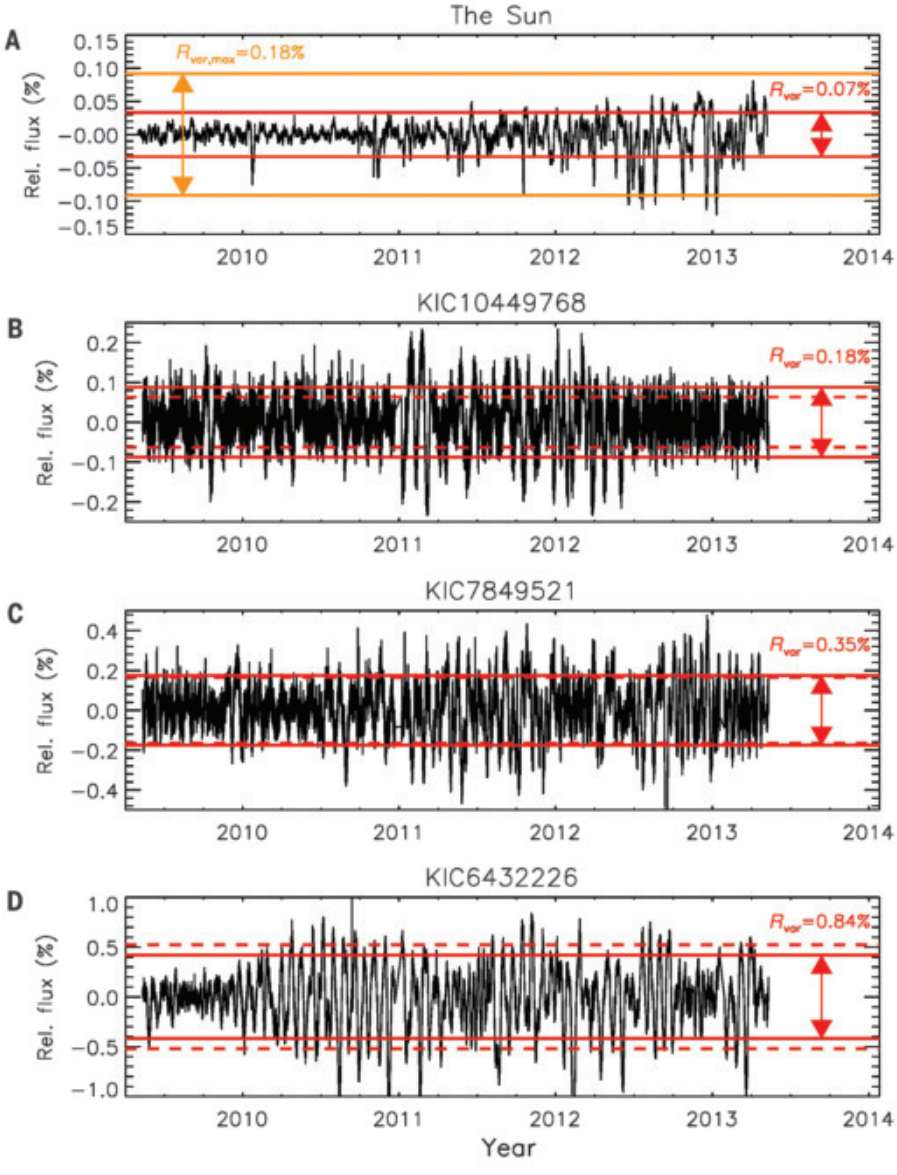

Fig. 2. Light curves of the Sun (A) and three stars from the periodic sample [(B to D)]. (**A**) Solar TSI data taken at the same epoch as the Kepler observations. The TSI data were detrended by cutting the 4-year time series into 90-day segments, dividing by the median flux, and then subtracting unity. (**B** to **D**) Three examples of stars (identified above each plot) with different variabilities. The variability ranges R_{var} are indicated by the differences between the horizontal red lines before (dashed) and after (solid) correction for the variability dependence on the fundamental parameters. The solid orange lines in (A) mark the maximum solar variability range [Fig. 3 and (*13*)]. The panels have different y-scales.

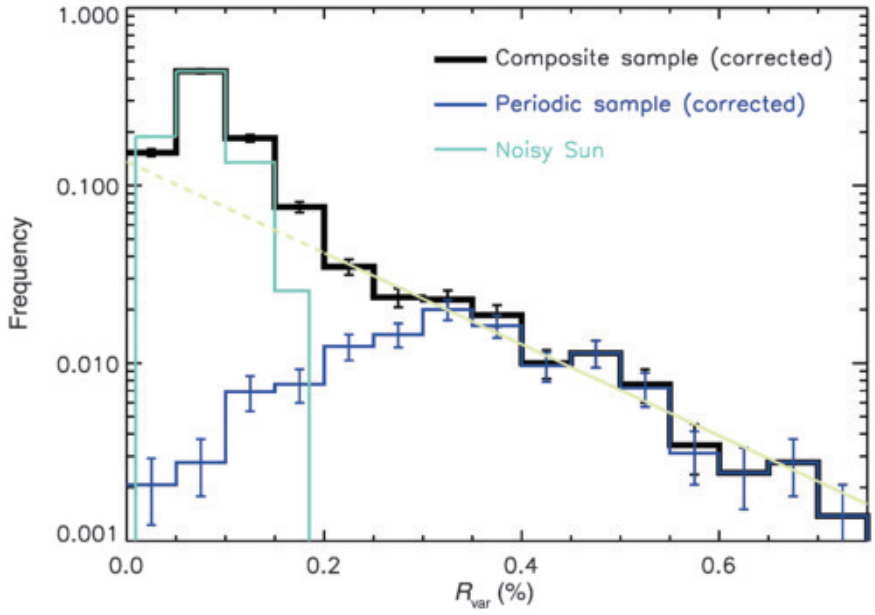

Fig. 3. Solar and stellar variability distributions on a logarithmic scale. The distributions of the variability range R_{var} are plotted for the composite sample (black), the periodic sample (blue), and the Sun over the last 140 years (green). Error bars indicate the Poisson uncertainties $\sqrt{N}$, where N is the number of stars in each bin, for the composite and the periodic samples. The yellow line shows an exponential model $a_0\,10^{a_1 R_{var}}$ fitted to the variability distribution of the (corrected) composite sample (R_{var} > 0.2%, solid line) and its extrapolation to low variabilities (R_{var} < 0.2%, dashed line). The solar distribution was normalized to the maximum of the composite sample. The first and last bins of the solar distribution were reduced in width to stop at the minimum and maximum values of solar variability over the last 140 years, respectively.

is similar to the maximum observed solar variability (*13*), the other two stars in Fig. 2 have much higher variability.

Figure 3 shows the distribution of R_{var} for the Sun, the periodic stars, and a composite sample of the periodic and nonperiodic samples combined. To compare the Sun with the stars observed by Kepler, we simulated how it would have appeared in the Kepler data by adding noise to the TSI time series (fig. S7). The variability range was then computed for 10,000 randomly selected 4-year segments from ~140 years of reconstructed TSI data (*13*).

The activity distribution of the composite sample (Fig. 3) does not separate into distributions of periodic and nonperiodic stars, but rather appears to represent a single physical population of stars. Fitting an exponential function $y = a_0\ 10^{a_1 R_{var}}$ to the variability distribution of the (corrected) composite sample with R_{var} > 0.2% yields $a_0 = 0.14 \pm 0.02$ and $a_1 = -2.27 \pm 0.17$. The subsample of periodic stars mostly populates the high-variability portion of the full distribution in Fig. 3, whereas the low-variability portion mostly contains stars from the nonperiodic sample. The solar R_{var} distribution is consistent with most of the low-variability stars, which is consistent with previous studies (*9*).

Determining the solar rotation period from photometric observations alone is challenging (*27*–*29*). The Sun would probably belong to the nonperiodic sample if it were observed by Kepler, and we found that the level of solar variability is typical for stars with undetected periods (Fig. 3). However, our composite sample contains stars that might have quite different rotation periods even though they have near-solar fundamental parameters.

By contrast, the variability of stars in the periodic sample has a different distribution. Although there are some periodic stars with variabilities within the observed range covered by the Sun, the variability amplitude for most periodic stars lies well above the solar maximum value of the last 140 years. Therefore, most of the solar-like stars that have measured near-solar rotation periods appear to be more active than the Sun. The variability of the periodic stars at the solar effective temperature, rotation period, and metallicity is R_{var} = 0.36% (fig. S8), which is ~5 times higher than the median solar variability $R_{var,\odot}$ = 0.07% and 1.8 times higher than the maximum solar value $R_{var,\odot} \lesssim 0.20\%$. All of these stars have near-solar fundamental parameters and rotational periods, suggesting that their values do not uniquely determine the level of any star's magnetic activity. This result is consistent with the detection of flares with energies several orders of magnitude higher than solar flares (i.e., superflares) on other solar-type stars (*30*, *31*).

We suggest two interpretations of our results. First, there could be unidentified differences between the periodic stars and nonperiodic stars (such as the Sun). For example, it has been proposed that the solar dynamo is in transition to a lower activity regime (*32*, *33*) because of a change in the differential rotation inside the Sun. According to this interpretation, the periodic stars are in the high-activity regime, whereas the stars without known periods are either also in transition or are in the low-activity regime. The second possible interpretation is that the composite sample in Fig. 3 represents the distribution of possible activity values that the Sun (and other stars with near solar fundamental parameters and rotational periods) can exhibit. In this case, the measured solar distribution is different only because the Sun did not exhibit its full range of activity over the last 140 years. Solar cosmogenic isotope data indicate that in the last 9000 years, the Sun has not been substantially more active than in the last 140 years (*8*). There are several ways for this constraint to be reconciled with such an interpretation. For example, the Sun could alternate between epochs of low and high activity on time scales longer than 9000 years. Our analysis does not allow us to distinguish between these two interpretations.

REFERENCES AND NOTES

1. A. Reiners, *Living Rev. Sol. Phys.* **9**, 1 (2012).
2. S. K. Solanki, N. A. Krivova, J. D. Haigh, *Annu. Rev. Astron. Astrophys.* **51**, 311–351 (2013).
3. G. Bond *et al.*, *Science* **294**, 2130–2136 (2001).
4. S. Wang *et al.*, *Geophys. Res. Lett.* **42**, 10,004–10,009 (2015).
5. G. Kopp, *J. Space Weather. Space Clim.* **4**, A14 (2014).
6. M. Dasi-Espuig, J. Jiang, N. A. Krivova, S. K. Solanki, *Astron. Astrophys.* **570**, A23 (2014).
7. I. G. Usoskin, *Living Rev. Sol. Phys.* **14**, 3 (2017).
8. C.-J. Wu, N. A. Krivova, S. K. Solanki, I. G. Usoskin, *Astron. Astrophys.* **620**, A120 (2018).
9. G. Basri, L. M. Walkowicz, A. Reiners, *Astrophys. J.* **769**, 37 (2013).
10. R. R. Radick, G. W. Lockwood, G. W. Henry, J. C. Hall, A. A. Pevtsov, *Astrophys. J.* **855**, 75 (2018).
11. C. Karoff *et al.*, *Nat. Commun.* **7**, 11058 (2016).
12. D. Salabert *et al.*, *Astron. Astrophys.* **608**, A87 (2017).
13. Materials and methods are available as supplementary materials.
14. P. Foukal, *Science* **264**, 238–239 (1994).
15. V. Witzke, A. I. Shapiro, S. K. Solanki, N. A. Krivova, W. Schmutz, *Astron. Astrophys.* **619**, A146 (2018).
16. W. J. Borucki *et al.*, *Science* **327**, 977–980 (2010).
17. R. L. Gilliland *et al.*, *Astrophys. J. Suppl. Ser.* **197**, 6 (2011).
18. D. Huber *et al.*, *Astrophys. J. Suppl. Ser.* **211**, 2 (2014).
19. S. Mathur *et al.*, *Astrophys. J. Suppl. Ser.* **229**, 30 (2017).
20. T. Reinhold, A. Reiners, G. Basri, *Astron. Astrophys.* **560**, A4 (2013).
21. A. McQuillan, T. Mazeh, S. Aigrain, *Astrophys. J. Suppl. Ser.* **211**, 24 (2014).
22. Gaia Collaboration, *Astron. Astrophys.* **595**, A1 (2016).
23. C. A. L. Bailer-Jones, J. Rybizki, M. Fouesneau, G. Mantelet, R. Andrae, *Astron. J.* **156**, 58 (2018).
24. Gaia Collaboration, *Astron. Astrophys.* **616**, A1 (2018).

25. G. Basri *et al.*, *Astrophys. J.* **713**, L155–L159 (2010).
26. J. C. Smith *et al.*, *Publ. Astron. Soc. Pac.* **124**, 1000–1014 (2012).
27. S. Aigrain *et al.*, *Mon. Not. R. Astron. Soc.* **450**, 3211–3226 (2015).
28. A. I. Shapiro *et al.*, *Nat. Astron.* **1**, 612–616 (2017).
29. T. Reinhold, K. J. Bell, J. Kuszlewicz, S. Hekker, A. I. Shapiro, *Astron. Astrophys.* **621**, A21 (2019).
30. H. Maehara *et al.*, *Nature* **485**, 478–481 (2012).
31. Y. Notsu *et al.*, *Astrophys. J.* **876**, 58 (2019).
32. T. S. Metcalfe, R. Egeland, J. van Saders, *Astrophys. J.* **826**, L2 (2016).
33. T. S. Metcalfe, J. van Saders, *Sol. Phys.* **292**, 126 (2017).

ACKNOWLEDGMENTS

We thank the three anonymous referees for constructive criticism and useful advice, which helped to greatly improve the paper. We also thank the International Space Science Institute, Bern, for their support of science team 446 and the resulting helpful discussions. This paper includes data collected by the Kepler mission. Funding for the Kepler mission is provided by the NASA Science Mission directorate. This work has made use of data from the European Space Agency (ESA) mission Gaia (https://www.cosmos.esa.int/gaia), which were processed by the Gaia Data Processing and Analysis Consortium (DPAC; https://www.cosmos.esa.int/web/gaia/dpac/consortium). Funding for DPAC has been provided by national institutions, especially the institutions participating in the Gaia Multilateral Agreement. **Funding:** T.R. and A.I.S. were funded by the European Research Council (ERC) under the European Union's Horizon 2020 research and innovation program (grant no. 715947). S.K.S. acknowledges support from the BK21 plus program through the National Research Foundation (NRF) funded by the Ministry of Education of Korea. E.M.A.-G. acknowledges support from the International Max-Planck Research School (IMPRS) for Solar System Science at the University of Göttingen. **Author contributions:** T.R., A.I.S., and S.K.S. conceived the study. A.I.S. and S.K.S. supervised the project. T.R. analyzed the Kepler data. B.T.M. investigated instrumental effects and cross-matched the Kepler and Gaia catalogs. A.I.S., S.K.S., N.A.K., R.H.C, and E.M.A.-G. contributed to the analysis of the data. T.R., A.I.S., S.K.S., and B.T.M. wrote the paper. All authors reviewed the manuscript. **Competing interests:** The authors declare no competing interests. **Data and materials availability:** The PDC-MAP Kepler data are available at https://edmond.mpdl.mpg.de/imeji/collection/1qSQkt89EYqXAA2S. Kepler data reduced with the PDC-msMAP pipeline are available at the Mikulski Archive for Space Telescopes at https://archive.stsci.edu/pub/kepler/lightcurves/. Sunspot data were taken from https://solarscience.msfc.nasa.gov/greenwch/sunspot_area.txt. SATIRE-T2 data can be found at http://www2.mps.mpg.de/projects/sun-climate/data/SATIRE-T2_TSI.txt. VIRGO level 2 1-min data were taken from ftp://ftp.pmodwrc.ch/pub/data/irradiance/virgo/1-minute_Data/. Our machine-readable catalog and software scripts are provided in data S1 in the supplementary materials.

SUPPLEMENTARY MATERIALS

science.sciencemag.org/content/368/6490/518/suppl/DC1
Materials and Methods
Figs. S1 to S10
Data S1
References (*34*–*61*)

13 June 2019; accepted 18 March 2020
10.1126/science.aay3821

CERAMICS

A general method to synthesize and sinter bulk ceramics in seconds

Chengwei Wang[1]*, Weiwei Ping[1]*, Qiang Bai[1]*, Huachen Cui[2,3]*, Ryan Hensleigh[2,3]*, Ruiliu Wang[1], Alexandra H. Brozena[1], Zhenpeng Xu[2,3], Jiaqi Dai[1], Yong Pei[4], Chaolun Zheng[4], Glenn Pastel[1], Jinlong Gao[1], Xizheng Wang[1], Howard Wang[1], Ji-Cheng Zhao[1], Bao Yang[4], Xiaoyu (Rayne) Zheng[2,3]†, Jian Luo[5]†, Yifei Mo[1]†, Bruce Dunn[6], Liangbing Hu[1,7]†

Ceramics are an important class of materials with widespread applications because of their high thermal, mechanical, and chemical stability. Computational predictions based on first principles methods can be a valuable tool in accelerating materials discovery to develop improved ceramics. It is essential to experimentally confirm the material properties of such predictions. However, materials screening rates are limited by the long processing times and the poor compositional control from volatile element loss in conventional ceramic sintering techniques. To overcome these limitations, we developed an ultrafast high-temperature sintering (UHS) process for the fabrication of ceramic materials by radiative heating under an inert atmosphere. We provide several examples of the UHS process to demonstrate its potential utility and applications, including advancements in solid-state electrolytes, multicomponent structures, and high-throughput materials screening.

Ceramics are widely used in electronics, energy storage, and extreme environments because of their high thermal, mechanical, and chemical stability. The sintering of ceramics is a technology that can be traced back to more than 26,000 years ago (*1*). Conventional ceramic sintering often requires hours of processing time (*2*), which can become an obstacle for the high-throughput discovery of advanced ceramic materials. The long sintering time is particularly problematic in the development of ceramic-based solid-state electrolytes (SSEs)—which are critical for new batteries with improved energy efficiency and safety (*3*, *4*)—because of the severe volatility of Li and Na during sintering (*5*–*9*).

Substantial effort has been devoted to the development of innovative sintering technologies, such as microwave-assisted sintering, spark plasma sintering (SPS), and flash sintering. Microwave-assisted sintering of ceramics often depends on the microwave absorption properties of the materials or uses susceptors (*10*, *11*). The SPS technique requires that dies are used to compress the ceramic while sintering (*12*), which makes it more difficult to sinter specimens with complex three-dimensional (3D) structures. Furthermore, SPS normally produces only one specimen at a time, though special tooling can and has been made to fabricate multiple samples. The more-recently developed flash sintering (*13*), photonic sintering (*14*), and rapid thermal annealing (RTA) (*15*) methods display a high heating rate of ~10^3 to 10^4°C/min. However, flash sintering typically requires expensive Pt electrodes and is material specific. Although flash sintering can be applied to many ceramics, flash sintering conditions depend strongly on the electrical characteristics of the material (*16*), which limits the general applicability of this method as well as its utility for high-throughput processing when a material's properties are unknown. Photonic sintering temperatures are normally too low to sinter ceramics (*14*, *17*). RTA has been used successfully to sinter ZnO (*15*), but this method can only provide a sintering temperature of up to ~1200°C with expensive commercial equipment.

To meet the needs of modern ceramics and foster material innovation, we report a ceramic synthesis method, called ultrafast high-temperature sintering (UHS), that features a uniform temperature distribution, high heating (~10^3 to 10^4°C/min) and cooling rates (up to 10^4°C/min), and high sintering temperatures (up to 3000°C). The ultrahigh heating rates and temperatures enable ultrafast sintering times of ~10 s (Fig. 1A), far outpacing those of most conventional furnaces. To conduct the process, we directly sandwich a pressed green pellet (Fig. 1B) of ceramic precursor powders between two Joule-heating carbon strips that rapidly heat the pellet through radiation and conduction to form a uniform high-temperature environment (fig. S1) for quick synthesis (solid-state reaction) and reactive sintering (Fig. 1C). In an inert atmosphere, these carbon heating elements can provide a temperature of up to ~3000°C (fig. S2), which is sufficient to synthesize and sinter virtually any ceramic material. The short sintering time also helps to prevent volatile evaporation and undesirable

[1]Department of Materials Science and Engineering, University of Maryland, College Park, MD 20742, USA. [2]Department of Mechanical Engineering, Virginia Tech, Blacksburg, VA 24061, USA. [3]Departments of Civil and Environmental Engineering and Mechanical and Aerospace Engineering, University of California, Los Angeles, CA 90095, USA. [4]Department of Mechanical Engineering, University of Maryland, College Park, MD 20742, USA. [5]Department of NanoEngineering, Program of Materials Science and Engineering, University of California San Diego, La Jolla, CA 92093, USA. [6]Department of Materials Science and Engineering, University of California, Los Angeles, CA 90095, USA. [7]Center for Materials Innovation, University of Maryland, College Park, MD 20742, USA.
*These authors contributed equally to this work.
†Corresponding author. Email: binghu@umd.edu (L.H.); yfmo@umd.edu (Y.M.); raynexzheng@vt.edu (X.Z.); jluo@ucsd.edu (J.L.)

interdiffusion at the interfaces of multilayer structures. Additionally, the technique is scalable because the processing is decoupled from the intrinsic properties of materials (unlike flash sintering; table S3), thereby allowing general and rapid ceramic synthesis and sintering. The UHS process is also compatible with the 3D printing of ceramic precursors, producing novel post-sintering structures in addition to well-defined interfaces between multilayer ceramic compounds. Furthermore, the speed of UHS enables the rapid experimental validation of new material predictions from computation, which facilitates materials discovery spanning a wide range of compositions. Several applications may benefit from this methodology, including thin-film SSEs and battery applications.

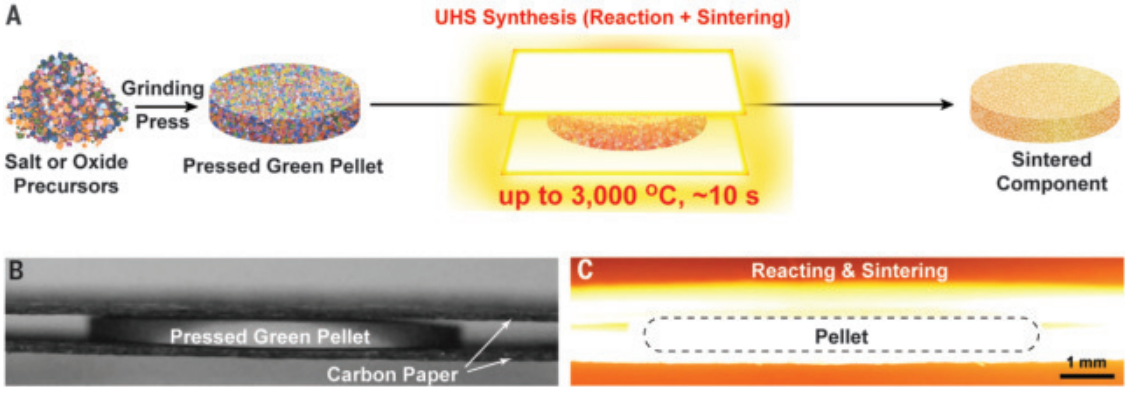

Fig. 1. Rapid sintering process and setup for ceramic synthesis. (**A**) Schematic of the UHS synthesis process, in which the pressed green pellet of precursors is directly sintered into a dense ceramic component at a high sintering temperature of up to 3000°C in ~10 s. (**B** and **C**) Photographs of the UHS sintering setup at room temperature without applying current (B), and at ~1500°C (C), in which the closely packed heating strips surrounding the pressed green pellet provide a uniform temperature distribution that enables rapid ceramic sintering.

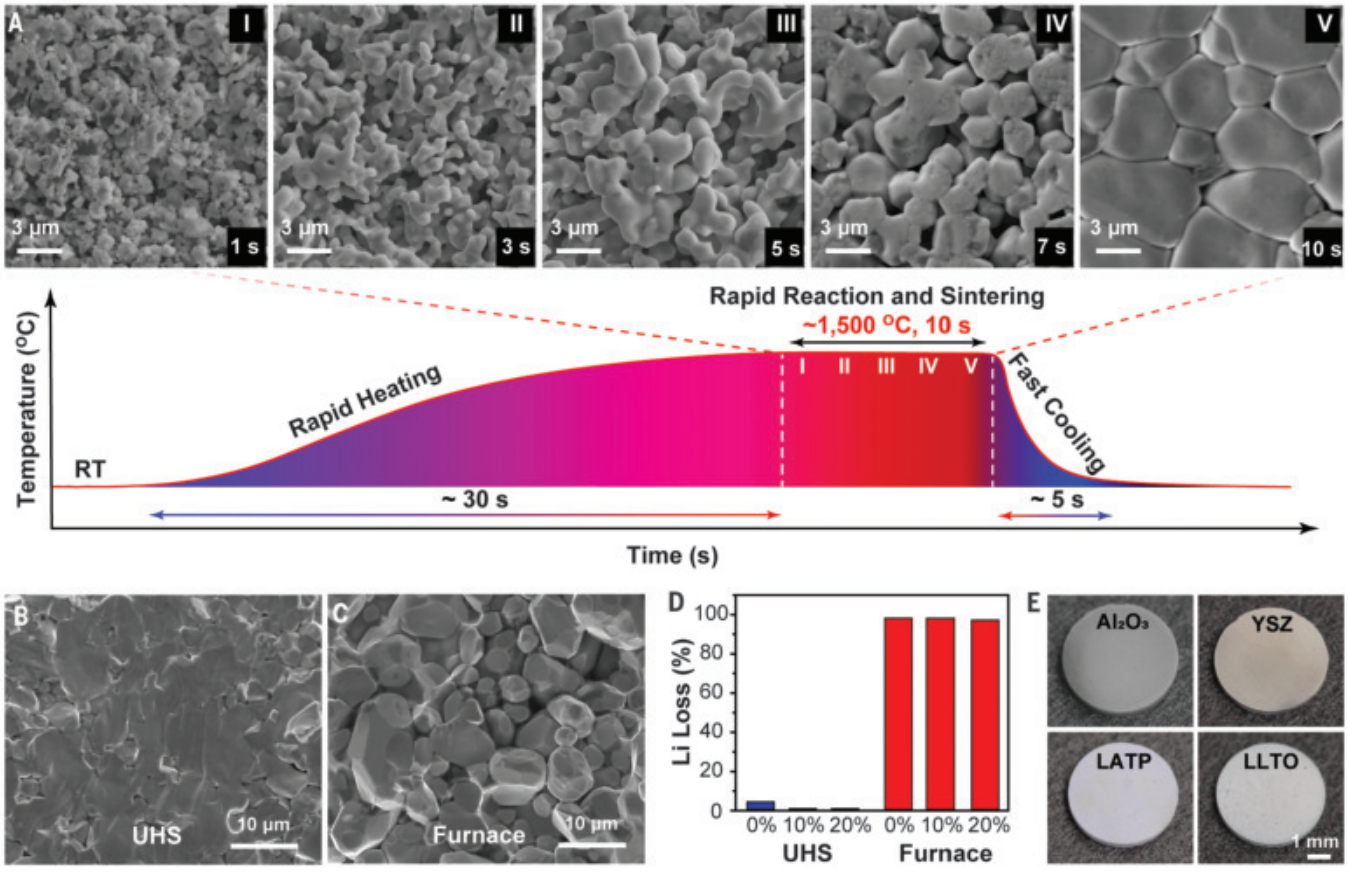

Fig. 2. Rapid sintering of ceramic materials. (**A**) Typical temperature profile of the UHS process. The whole process takes <1 min. The SEM images demonstrate the reaction process of the LLZTO ceramic over a 10-s isothermal hold of UHS sintering. RT, room temperature. (**B** and **C**) Fracture cross-sectional SEM images of UHS-sintered (B) and conventional furnace–sintered (C) LLZTO. (**D**) Li loss of different LLZTO samples sintered from precursors with 0, 10, and 20% excess Li by means of the the UHS technique and a conventional furnace. (**E**) Pictures of various ceramics sintered by the UHS technique in ~10 s.

In a typical UHS process, the heating elements ramp up from room temperature to the sintering temperature in ~30 s or less (Fig. 2A, bottom), a process that would typically take a conventional furnace several hours to complete (fig. S3). This temperature ramping stage is followed by ~10 s of isothermal sintering and then rapid cooling (in ~5 s). These times and conditions are attractive compared with those of other sintering methods (fig. S4 and table S3) (*11*, *12*, *16*). As a demonstration of the process, we synthesized Ta-doped $Li_{6.5}La_3Zr_{1.5}Ta_{0.5}O_{12}$ (LLZTO), a garnet-type Li-ion–conductive ceramic proposed for SSE applications (*18*). In the UHS technique, the precursors of LLZTO

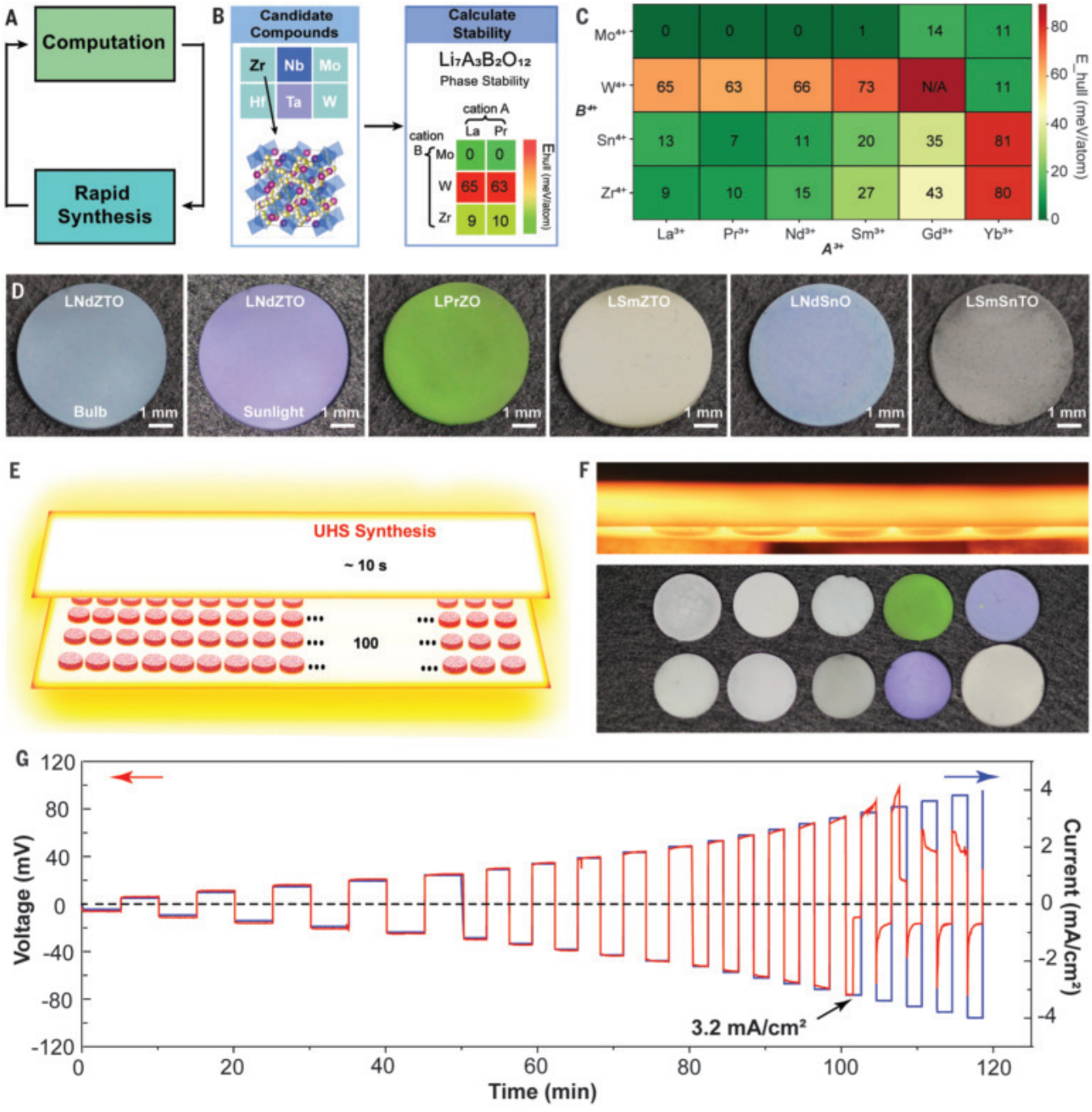

Fig. 3. Rapid sintering technique for ceramic screening. (**A**) Accelerated materials discovery enabled by computational prediction and rapid synthesis. (**B**) The computational workflow for predicting new garnet compositions. The phase stabilities of candidate compounds with different cation combinations were evaluated by the energy above hull (E_{hull}) in comparison with the lowest-energy phase equilibria. (**C**) The table lists the predicted garnet compositions with different stabilities. (**D**) Pictures of the garnet materials (featuring different colors from the usual white) sintered by means of the UHS technique and predicted by computation. The LNdZTO garnet can change color under different light sources (e.g., a fluorescent light bulb and sunlight) because of the Alexandrite effect (*34*). (**E**) Schematic of a 20 by 5 matrix for cosintering 100 ceramic samples with the UHS technique in just ~10 s. (**F**) Pictures of the UHS setup for cosintering 10 garnet samples. The top image is the side view of the UHS cosintering process. (**G**) The voltage and current profiles of the symmetric cell with a thick Li electrode cycled at different current densities.

quickly react and densify (Fig. 2A, top) in ~40 s (~30 s of temperature ramping and ~10 s of isothermal sintering), as the temperature of the heater approaches ~1500°C (movie S1). The high sintering temperature and short sintering time of the UHS technique produce a relatively small grain size of 8.5 ± 2.0 μm (Fig. 2B) and a high relative density of ~97% (fig. S5). By contrast, the conventional furnace–sintered garnet features a microstructure with larger grains of 13.5 ± 5 μm (Fig. 2C). This rapid sintering and densification observed in the materials produced by the UHS method may originate from (i) fast kinetics from the high sample temperature, (ii) additional chemical driving force beyond the normal capillary driving force for densification caused by the simultaneous reaction and sintering process, or (iii) the ultrahigh heating rates enhancing the densification rates (*15*, *19*).

In general, sintering involves competition between the coarsening and densification of particles. Surface diffusion can dominate at low temperatures and causes coarsening and neck growth without densification, whereas grain boundary and bulk diffusion are more important at high temperatures, leading to fast densification. The ultrahigh heating rates of UHS bypass the low-temperature region, thereby reducing the coarsening of particles and maintaining a higher capillary driving force for sintering, similar to that observed in other ultrafast heating schemes, such as flash sintering and other exotic heating methods (*15*, *19*). The lower activation energies (fig. S5) also suggest that sintering and grain growth mechanisms in the UHS process are somewhat different from those in conventional sintering methods (*20*). In some cases, particularly for some solid electrolytes of complex chemistries, a small fraction of a liquid can form at the high processing temperature in UHS, which further promotes densification as ultrafast liquid-phase sintering (*21*).

The long sintering time of conventional syntheses can lead to Li loss in garnet SSEs caused by the evaporation of Li and the formation of secondary phases that lead to lower ionic conductivity (*22*). In contrast, the UHS technique enables us to tune the sintering time in units of seconds, which provides excellent control in terms of the Li content and grain growth. As a comparison, we sintered a series of LLZTO precursor formulations featuring 0, 10, and 20% excess Li using either the UHS technique or a conventional furnace. Using inductively coupled plasma mass spectrometry, we observed severe Li loss in the furnace-sintered LLZTO samples (up to 99%) but <4% loss in the UHS samples. This was true even for the sample made without excess Li (Fig. 2D). The time-of-flight secondary ion mass spectroscopy results confirmed the uniform distributions of all elements in the UHS-sintered LLZTO (fig. S6). Both the densification and Li-evaporation rates increase with temperature as thermally activated processes, but the garnet densification rate likely increases faster than the evaporation rate. This leads to less Li loss with a much shorter sintering time sufficient for densification. The schematic time-temperature-transformation diagram (fig. S7) illustrates the evolution of density and composition of the LLZTO garnet in the UHS process. We identified a pure cubic garnet phase from x-ray diffraction (XRD) patterns of the UHS garnet, whereas the severe Li loss in the conventional furnace–sintered samples leads to a side reaction (fig. S8). Furthermore, the LLZTO samples synthesized with the UHS technique had an ionic conductivity of ~1.0 ± 0.1 mS/cm (fig. S9), which is among the highest reported for garnet-based SSEs (*8*, *18*, *23*).

We can apply our UHS method to synthesize a wide range of high-performance ceramics. As a demonstration, we successfully sintered alumina (Al_2O_3, >96% density), Y_2O_3-stabilized ZrO_2 (YSZ, >95% density, with an ultrafine grain size of 265 ± 85 nm), $Li_{1.3}Al_{0.3}Ti_{1.7}(PO_4)_3$ (LATP, >90% density), and $Li_{0.3}La_{0.567}TiO_3$ (LLTO, >94% density) directly from pressed green pellets of precursor powders and all in under 1 min (Fig. 2E). Al_2O_3 and YSZ are two typical structural ceramics with excellent mechanical properties and high sintering temperatures, whereas LATP and LLTO are Li-ion conductors used in solid-state batteries (*3*, *24*). The UHS materials featured pure phases that we identified with XRD, which was indicative of no side reactions (fig. S10). We used scanning electron microscopy (SEM) images to show that the well-sintered grains have low porosity and the fractured cross sections are uniform in microstructure (figs. S11 to S14). The pressureless sintering process and short processing time of the UHS technique also resulted in fewer solid diffusion–related side reactions or sample-carbon heater contamination issues (figs. S15 to S17) than often encountered in SPS (*25*). We hypothesize that the ultrahigh heating rate and short sintering time can kinetically minimize the likelihood of such side reactions. The technique is particularly suitable for high-throughput screening of bulk ceramics compared with different ceramic synthesis techniques.

The ability of the UHS method to rapidly and reliably synthesize a wide range of ceramics enables us to quickly verify new materials predicted by computation and accelerate the screening rate for bulk ceramic materials (Fig. 3A). We used lithium garnet compounds ($Li_7A_3B_2O_{12}$; A = La group, B = Mo, W, Sn, or Zr) as a model system to demonstrate this rapid screening ability that is enabled by computational prediction and the UHS process. We used density functional theory calculations to predict and evaluate the energies of a large number of compounds with other non-Li cation combinations based on garnet structures (Fig. 3B). The phase stabilities of these computer-generated hypothetical Li_7-garnet compounds (Fig. 3C) are described by the lower value of the energy above hull (E_{hull}), which we determined from the energy difference of the compound in comparison with the stable phase equilibria on the phase diagram (*26*). A material with a small E_{hull} (color-coded green) should feature good phase stability, and a high E_{hull} (color-coded red) suggests an unstable phase. Our compositional screening captured most known stoichiometric Li_7-garnets, such as $Li_7La_3Zr_2O_{12}$, $Li_7Nd_3Zr_2O_{12}$, and $Li_7La_3Sn_2O_{12}$ (*18*), which validated the computational method.

We selected the computationally predicted Zr- and Sn-based garnet compositions featuring small E_{hull} values (Fig. 3C) for experimental verification, including $Li_7Pr_3Zr_2O_{12}$ (LPrZO), $Li_7Sm_3Zr_2O_{12}$ (LSmZO), $Li_7Nd_3Zr_2O_{12}$ (LNdZO), $Li_7Nd_3Sn_2O_{12}$ (LNdSnO), and $Li_7Sm_3Sn_2O_{12}$ (LSmSnO). We also synthesized the corresponding 0.5 Ta-doped compositions in the B site [e.g., $Li_{6.5}Sm_3Zr_{1.5}Ta_{0.5}O_{12}$ (LSmZTO)]. New garnet compounds were well synthesized and sintered (figs. S18 to S22) in as little as 10 s, with uniform grain size and microstructure. The final relative densities were in the range of 91 to 96%, with a typical grain size of 2 to 10 μm. We confirmed the garnet structure (cubic phase for B site doped; tetragonal phase for nondoped) using XRD (fig. S23). Our garnet compounds exhibited different optical properties and were not the typical white color, owing to the different La-group elements (Fig. 3D). Our garnets also had ionic conductivities of ~10^{-4} S/cm (e.g., LNdZTO, fig. S24), which are comparable to those of LLZO garnets (*18*, *22*). We also attempted to synthesize some unstable garnet compounds that we predicted by computation, such as $Li_7Gd_3Zr_2O_{12}$. As expected, even though the SEM image shows well sintered grains (fig. S25A), the XRD pattern indicates that the composition did not form the garnet phase (fig. S25B), which verifies our computational predictions.

The fast sintering rate of UHS also enables cosintering of multiple materials simultaneously, which permits even faster screening of materials or devices. In practical ceramic synthesis, sintering can be the most time-consuming process, especially when the optimized sintering parameters have not been developed for new compositions. However, with the UHS sintering technique, 100 ceramic pellets can be rapidly cosintered using a 20 by 5 matrix setup (Fig. 3E), with an area of just ~12 cm by 3 cm (for a pellet size of 5 mm). This setup is practical for materials screening processes. As a demonstration of this scalability, we synthesized 10 garnet compositions

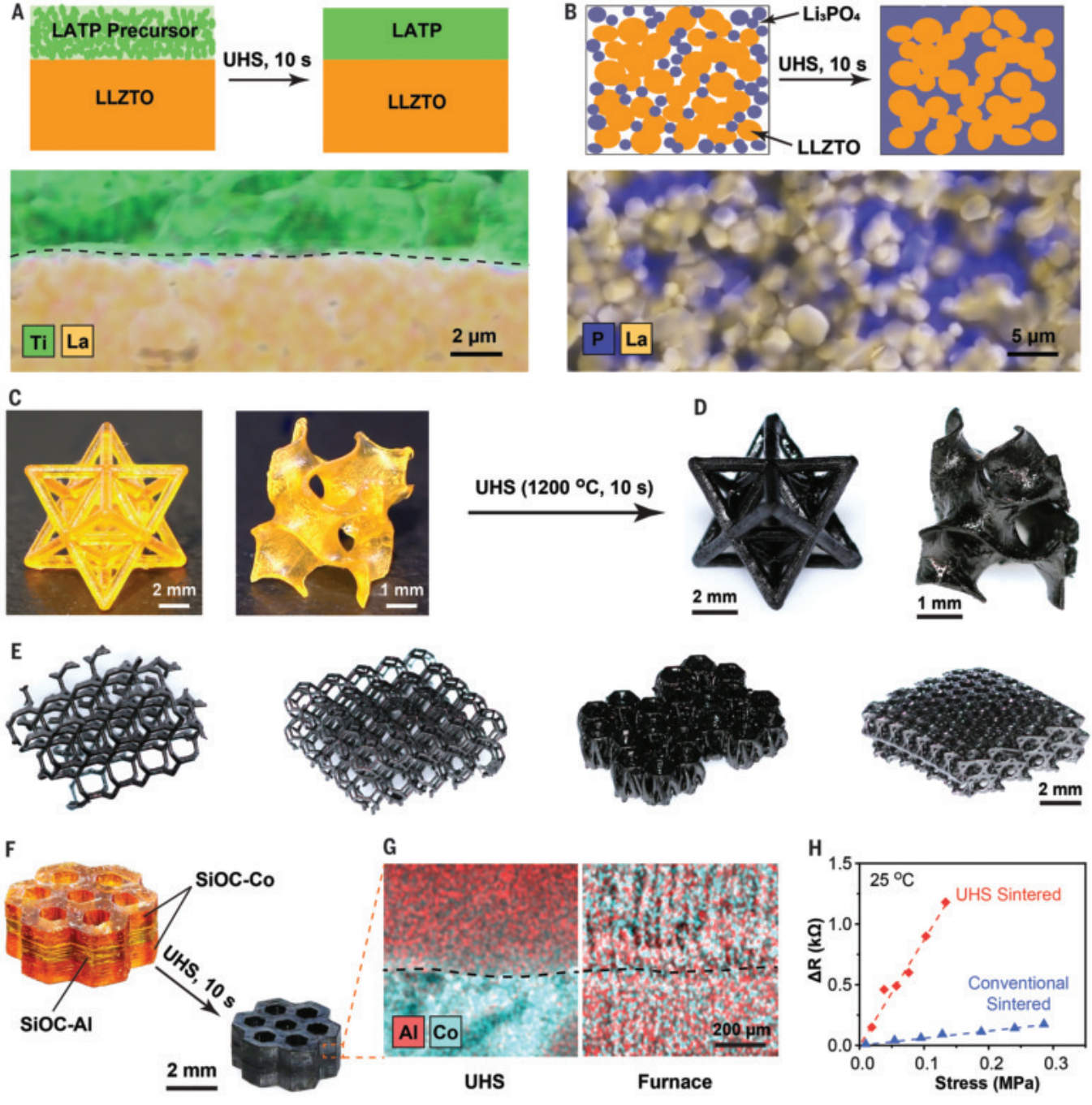

Fig. 4. Structures enabled by the UHS sintering technique. (**A** and **B**) Schematics and energy dispersive spectroscopy mapping of the cosintered LATP-LLZTO bilayer SSE (A) and the LLZTO-Li_3PO_4 composite SSE (B). (**C**) Photographs of the SiOC polymer precursor printed as a single material. (**D**) Photographs of the SiOC samples sintered by the UHS method, showing the uniform material shrinkage and maintained structures. (**E**) Four UHS-sintered complex structures with different repeating units. (**F**) The multilayer 3D-printed SiOC polymer precursor (doped with Al and Co) and the corresponding UHS-sintered structure. (**G**) Elemental mapping of the Co- and Al-doped boundary of the UHS-sintered and conventional furnace–sintered SiOC samples. (**H**) The piezoresistance versus the stress induced by the magnetic force of the 3D-printed magnetic flux density sensor device sintered by UHS and conventional sintering. ΔR is the change in the piezoresistance.

(see compositions listed in the supplementary materials) by cosintering directly from the corresponding green bodies (Fig. 3F). In comparison, although SPS is currently considered a high-throughput method to fabricate bulk ceramic specimens, it typically produces just one specimen in ~1 to 2 hours. Moreover, SPS cannot easily be carried out in parallel as it requires multiple expensive SPS instruments.

Ultrafast heating at high temperatures for only seconds can also reduce or eliminate the segregation of detrimental impurities and defects at grain boundaries. This process may have beneficial effects for solid electrolytes

and many other structural and functional ceramics. Using LLZTO garnet pellets as a proof of concept, we conducted a symmetric Li stripping-plating study to systematically characterize the electrochemical properties of the UHS garnet SSE. Because of the challenge in diagnosing the short circuit in the symmetric cell configuration (*27*), we applied in situ neutron depth profiling (NDP) (*28*) to confirm that the UHS LLZTO garnet SSE can conduct Li ions at high current densities without short-circuiting (fig. S26, A, B, and C). We show that the Li-LLZTO-Li symmetric cell with a thick (>100 μm) Li metal coating demonstrates a critical current density as high as 3.2 mA/cm^2 (Fig. 3G and fig. S26D), which is among the highest reported values for planar garnet-based SSEs (*18*, *29*). We have conducted long-term cycling of the Li-LLZTO-Li symmetric cell (fig. S27), which can cycle for >400 hours at a current density of 0.2 mA/cm^2, indicating excellent cycling stability.

Multilayer ceramics have advantages for various applications, including battery electrolytes, but they are challenging to sinter because of interdiffusion at high temperatures. We synthesized a LATP/LLZTO bilayer SSE without detectable side reaction or cross-diffusion using the UHS technique (Fig. 4A). The LLZTO garnet is stable against the Li metal anode, and the LATP features superior oxidation stability compared with the LLZTO (fig. S28) (*30*). Conventional furnace sintering results in severe interdiffusion and side reactions at the interface (fig. S29).

Introducing low–melting point materials into ceramics is a general approach to achieving a dense structure at a lower sintering temperature. We sintered a ceramic composite SSE by adding Li_3PO_4 to the LLZTO garnet, in which the Li_3PO_4 can melt at ~1200°C and weld with the LLZTO particles to form a dense composite pellet (Fig. 4B) by means of ultrafast liquid-phase sintering, with reduced side reactions and cross-doping compared with the conventional approach (fig. S30).

The UHS technique can also sinter ceramic structures with complex geometries. This is notable because the SPS technique is incompatible with 3D-printed structures. We successfully sintered polymer-derived ceramics (silicon oxycarbide, SiOC) with uniform shrinking and well-maintained structures (Fig. 4, C and D, and movie S2). Additionally, the structures can be stacked to form a more complex 3D lattice design (Fig. 4E). 3D-printed structures and devices with different spatially distributed materials have applications emerging from various combinations of mechanical, thermal, or other properties (*31*–*33*). However, cosintering of these structures is challenging because of cross-diffusion. To explore the capabilities of UHS for such complex designs, we 3D-printed multimaterial honeycomb structures featuring Al-doped SiOC (for piezoresistivity response) and Co-doped SiOC (for magnetic response, Fig. 4F) to form a magnetic flux sensor (fig. S31). The UHS sintering maintains the perfect registration of the structures with minimal diffusion of dopants caused by the short sintering time (Fig. 4G). Additionally, the 3D-printed magnetic flux sensor device effectively converts magnetic fields into voltage signals (fig. S31). In contrast, the conventional sintering method suffers from substantial diffusion between the different materials (Fig. 4G), which results in poor sensitivity of piezoresistive sensing (Fig. 4H and fig. S31).

The rapid sintering enables the potential for scalable, roll-to-roll sintering of ceramics because the precursor film can quickly pass through the heating strips to achieve continuous UHS. The thin, high-temperature carbon heater in the UHS technique is also highly flexible and can conformally wrap around structures for rapid sintering of unconventional shapes and devices (fig. S32). There are several other potential opportunities. First, UHS can be readily extended to a broad range of nonoxide high-temperature materials, including metals, carbides, borides, nitrides, and silicides, because of its extremely high temperature. Second, UHS may also be used to fabricate functionally graded materials (beyond the simple multilayers demonstrated in this work) with minimum undesirable interdiffusion. Third, the ultrafast, far-from-equilibrium nature of the UHS process may produce materials with nonequilibrium concentrations of point defects, dislocations, and other defects or metastable phases that lead to desirable properties. Finally, this UHS method allows a controllable and tunable temperature profile to enable the control of sintering and microstructural evolution.

REFERENCES AND NOTES

1. P. B. Vandiver, O. Soffer, B. Klima, J. Svoboda, *Science* **246**, 1002–1008 (1989).
2. E. M. Rabinovich, *J. Mater. Sci.* **20**, 4259–4297 (1985).
3. Z. Zhang *et al*., *Energy Environ. Sci.* **11**, 1945–1976 (2018).
4. A. Manthiram, X. Yu, S. Wang, *Nat. Rev. Mater.* **2**, 16103 (2017).
5. Y. Li, J. T. Han, C. A. Wang, H. Xie, J. B. Goodenough, *J. Mater. Chem.* **22**, 15357–15361 (2012).
6. M. Nyman, T. M. Alam, S. K. McIntyre, G. C. Bleier, D. Ingersoll, *Chem. Mater.* **22**, 5401–5410 (2010).
7. I. Garbayo *et al*., *Adv. Energy Mater.* **8**, 1702265 (2018).
8. X. Huang *et al*., *Energy Storage Mater.* **22**, 207–217 (2019).
9. R. Pfenninger, M. Struzik, I. Garbayo, E. Stilp, J. L. M. Rupp, *Nat. Energy* **4**, 475–483 (2019).
10. R. R. Mishra, A. K. Sharma, *Compos. Part A Appl. Sci. Manuf.* **81**, 78–97 (2016).
11. M. Oghbaei, O. Mirzaee, *J. Alloys Compd.* **494**, 175–189 (2010).
12. O. Guillon *et al*., *Adv. Eng. Mater.* **16**, 830–849 (2014).
13. M. Cologna, B. Rashkova, R. Raj, *J. Am. Ceram. Soc.* **93**, 3556–3559 (2010).
14. D. Angmo, T. T. Larsen-Olsen, M. Jørgensen, R. R. Søndergaard, F. C. Krebs, *Adv. Energy Mater.* **3**, 172–175 (2013).
15. Y. Zhang, J. Nie, J. M. Chan, J. Luo, *Acta Mater.* **125**, 465–475 (2017).
16. M. Yu, S. Grasso, R. Mckinnon, T. Saunders, M. J. Reece, *Adv. Appl. Ceramics* **116**, 24–60 (2017).
17. A. Albrecht, A. Rivadeneyra, A. Abdellah, P. Lugli, J. F. Salmerón, *J. Mater. Chem. C* **4**, 3546–3554 (2016).
18. V. Thangadurai, S. Narayanan, D. Pinzaru, *Chem. Soc. Rev.* **43**, 4714–4727 (2014).
19. W. Ji *et al*., *J. Eur. Ceram. Soc.* **37**, 2547–2551 (2017).
20. A. Sharafi, C. G. Haslam, R. D. Kerns, J. Wolfenstine, J. Sakamoto, *J. Mater. Chem. A* **5**, 21491–21504 (2017).
21. R. P. Rao *et al*., *Chem. Mater.* **27**, 2903–2910 (2015).
22. E. Yi, W. Wang, J. Kieffer, R. M. Laine, *J. Mater. Chem. A* **4**, 12947–12954 (2016).
23. Y. Jin *et al*., *Nat. Energy* **3**, 732–738 (2018).
24. J. C. Bachman *et al*., *Chem. Rev.* **116**, 140–162 (2016).
25. G. Bernard-Granger, N. Benameur, C. Guizard, M. Nygren, *Scr. Mater.* **60**, 164–167 (2009).
26. S. P. Ong, L. Wang, B. Kang, G. Ceder, *Chem. Mater.* **20**, 1798–1807 (2008).
27. P. Albertus, S. Babinec, S. Litzelman, A. Newman, *Nat. Energy* **3**, 16–21 (2018).
28. C. Wang *et al*., *J. Am. Chem. Soc.* **139**, 14257–14264 (2017).
29. N. J. Taylor *et al*., *J. Power Sources* **396**, 314–318 (2018).
30. Y. Zhu, X. He, Y. Mo, *J. Mater. Chem. A* **4**, 3253–3266 (2016).
31. A. Bandyopadhyay, B. Heer, *Mater. Sci. Eng. Rep.* **129**, 1–16 (2018).
32. R. Lakes, *Appl. Phys. Lett.* **90**, 221905 (2007).
33. X. Kuang *et al*., *Sci. Adv.* **5**, eaav5790 (2019).
34. I. P. Roof, M. D. Smith, E. J. Cussen, H. C. zur Loye, *J. Solid State Chem.* **182**, 295–300 (2009).

ACKNOWLEDGMENTS

We acknowledge the support of the Maryland NanoCenter, its Surface Analysis Center and AIM Laboratory, and the NIST Center for Neutron Research. We also acknowledge M. R. Zachariah and D. J. Kline from the University of California, Riverside, for their contributions to the temperature measurement. **Funding:** This work is not directly funded. J.L. acknowledges support from the Air Force Office of Scientific Research (AFOSR) (FA9550-19-1-0327) and X.Z. acknowledges support from the National Science Foundation (CMMI1727492) and AFOSR (FA9550-18-1-0299).

Author contributions: L.H. and C.W. developed the UHS concept and designed the overall experiments. Y.M. and Q.B. conducted the computational predictions and simulation analysis. X.Z. designed the 3D printing experiment. C.W. and W.P. carried out the UHS sintering experiments, electrochemical measurements, and SEM imaging. R.W. helped prepare the samples and conduct the XRD measurements. J.D. created the 3D illustrations. G.P. and J.G. performed XRD characterization. X.W. conducted the temperature profile measurement. H.W. and C.W. performed the NDP measurement. X.Z., H.C., R.H., and Z.X. conducted the material synthesis for 3D printing and characterization. B.Y., C.Z., and Y.P. conducted the measurements of thermal properties and temperature simulations. J.L. contributed to the mechanistic understanding and some sintering experimental designs and analysis. L.H., C.W., A.H.B., Y.M., X.Z., J.L., B.D., and J.-C.Z. collectively wrote and revised the paper. All authors discussed the results and commented on the manuscript. **Competing interests:** The authors declare no competing interests. A provisional patent application, titled "High Temperature Process for Ceramics and other Solid Materials," has been applied for through the University of Maryland (U.S. provisional patent 62/849578). **Data and materials availability:** All data are available in the manuscript or the supplementary materials.

SUPPLEMENTARY MATERIALS

science.sciencemag.org/content/368/6490/521/suppl/DC1
Materials and Methods
Supplementary Text
Figs. S1 to S32
Tables S1 to S3
References (*35*–*56*)
Movies S1 and S2

8 October 2019; accepted 1 April 2020
10.1126/science.aaz7681

NEUROSCIENCE

A noncanonical inhibitory circuit dampens behavioral sensitivity to light

Takuma Sonoda[1,2], Jennifer Y. Li[1]*, Nikolas W. Hayes[1,2], Jonathan C. Chan[3], Yudai Okabe[1], Stephane Belin[4], Homaira Nawabi[4], Tiffany M. Schmidt[1,5]†

Retinal ganglion cells (RGCs) drive diverse, light-evoked behaviors that range from conscious visual perception to subconscious, non–image-forming behaviors. It is thought that RGCs primarily drive these functions through the release of the excitatory neurotransmitter glutamate. We identified a subset of melanopsin-expressing intrinsically photosensitive RGCs (ipRGCs) in mice that release the inhibitory neurotransmitter γ-aminobutyric acid (GABA) at non–image-forming brain targets. GABA release from ipRGCs dampened the sensitivity of both the pupillary light reflex and circadian photoentrainment, thereby shifting the dynamic range of these behaviors to higher light levels. Our results identify an inhibitory RGC population in the retina and provide a circuit-level mechanism that contributes to the relative insensitivity of non–image-forming behaviors at low light levels.

Retinal ganglion cells (RGCs) relay light information to >40 brain areas (*1*–*3*), giving rise to both conscious visual perception (image-forming vision) and subconscious non–image-forming functions, such as circadian photoentrainment and the pupillary light reflex (PLR) (*4*, *5*). RGCs are thought to mediate these functions by the synaptic release of the excitatory neurotransmitter glutamate onto their postsynaptic targets. Previous immunohistochemical evidence has suggested the presence of inhibitory, γ-aminobutyric acid (GABA)–releasing (GABAergic) RGCs in several mammalian species (*6*–*9*). However, the identity of GABAergic RGCs and their function in visual behavior have remained elusive.

To label GABAergic projections from the retina to the brain, we used a mouse line, *Gad2-IRES-Cre*, in which Cre recombinase is coexpressed with the GABA synthesis enzyme *Gad2* (*10*). We then performed unilateral eye injections of an adeno-associated virus (AAV) that drives Cre-dependent expression of the fluorescent reporter tdTomato (AAV2/hSyn-FLEX-Chrimson-tdTomato) (Fig. 1A). Because RGCs are the only retinal neurons that project to the brain, any labeled tdTomato+ axons in the brain indicate the presence of *Gad2*-expressing RGCs. We observed tdTomato+ axons that were largely confined to non–image-forming brain areas, including the suprachiasmatic nucleus (SCN), the intergeniculate leaflet (IGL), and the ventral lateral geniculate nucleus (vLGN), which are involved in circadian entrainment, as well as the ipsilateral shell of the olivary pretectal nucleus (OPN), which is involved in the PLR (14 of 14 animals; Fig. 1, B to D) (*11*–*15*). No labeling was observed in the brains of wild-type animals injected with the same Cre-dependent virus (fig. S1). We observed less-frequent labeling in image-forming structures such as the medial posterior superior colliculus (10 of 14 animals) and projections to the shell of the contralateral dorsal LGN (dLGN) (9 of 14 animals) (fig. S2).

The melanopsin-expressing intrinsically photosensitive RGCs (ipRGCs) are the major type

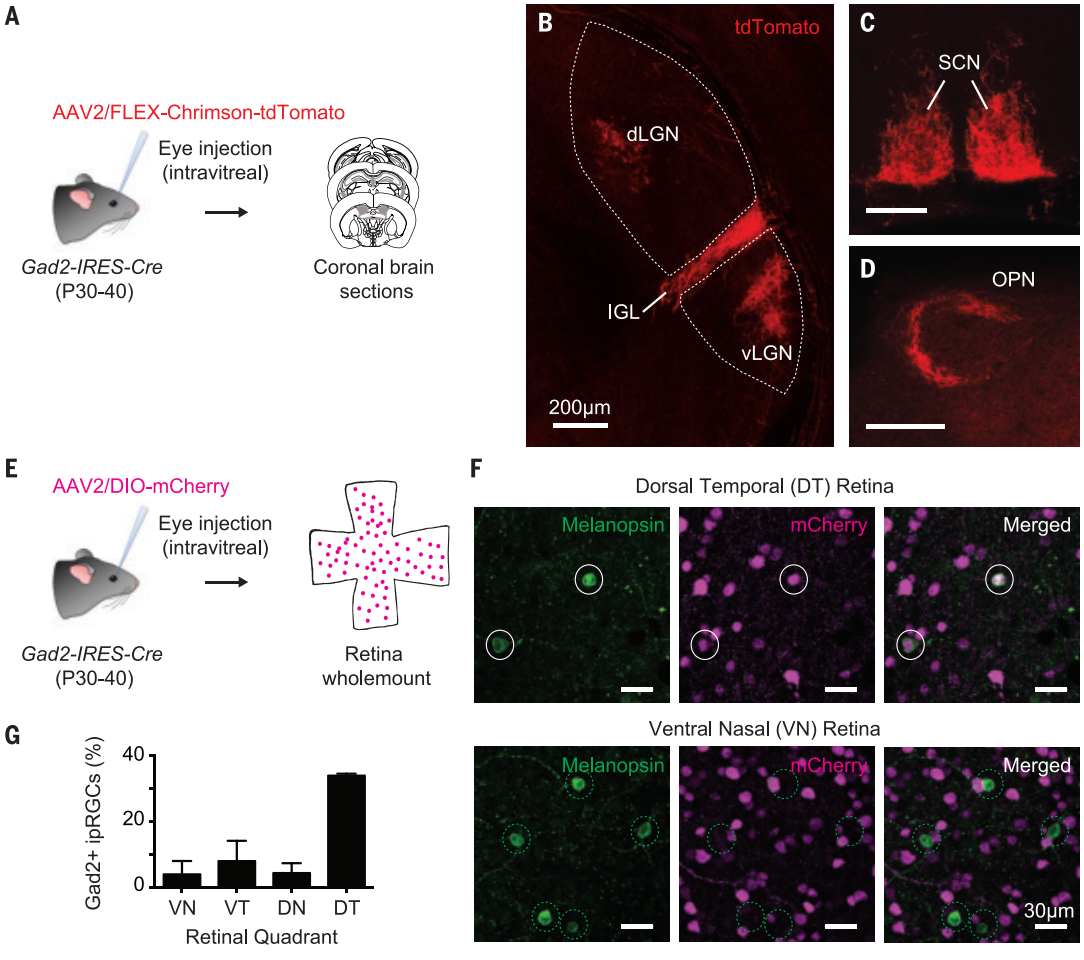

Fig. 1. ipRGCs are a potential source of inhibitory input to non–image-forming visual brain areas. (**A**) Intravitreal injections of AAV2/hSyn-FLEX-Chrimson-tdTomato in *Gad2-IRES-Cre* mice to label GABAergic cells in the retina. Coronal brain sections were made 1 to 2 months after infection. (**B** to **D**) tdTomato+ axons were consistently observed (14 of 14 animals) in the IGL (B), vLGN (B), SCN (C), and OPN (D). Scale bars, 200 μm. (**E**) Intravitreal injections of AAV2/hSyn-DIO-mCherry in *Gad2-IRES-Cre* mice to label GABAergic cells in the retina. Retinas were immunostained for melanopsin to label ipRGCs. (**F**) Melanopsin and mCherry labeling in dorsal-temporal (top) and ventral-nasal (bottom) quadrants of retinas in (E). Solid white circles indicate *Gad2*+ ipRGCs and dotted green circles indicate *Gad2*− ipRGCs. Scale bars, 30 μm. (**G**) Percentage of melanopsin immunoreactive cells that were *Gad2*+. n = 7 to 8 retinas per quadrant. Data are means ± SD. VN, ventral nasal; VT, ventral temporal; DN, dorsal nasal; DT, dorsal temporal.

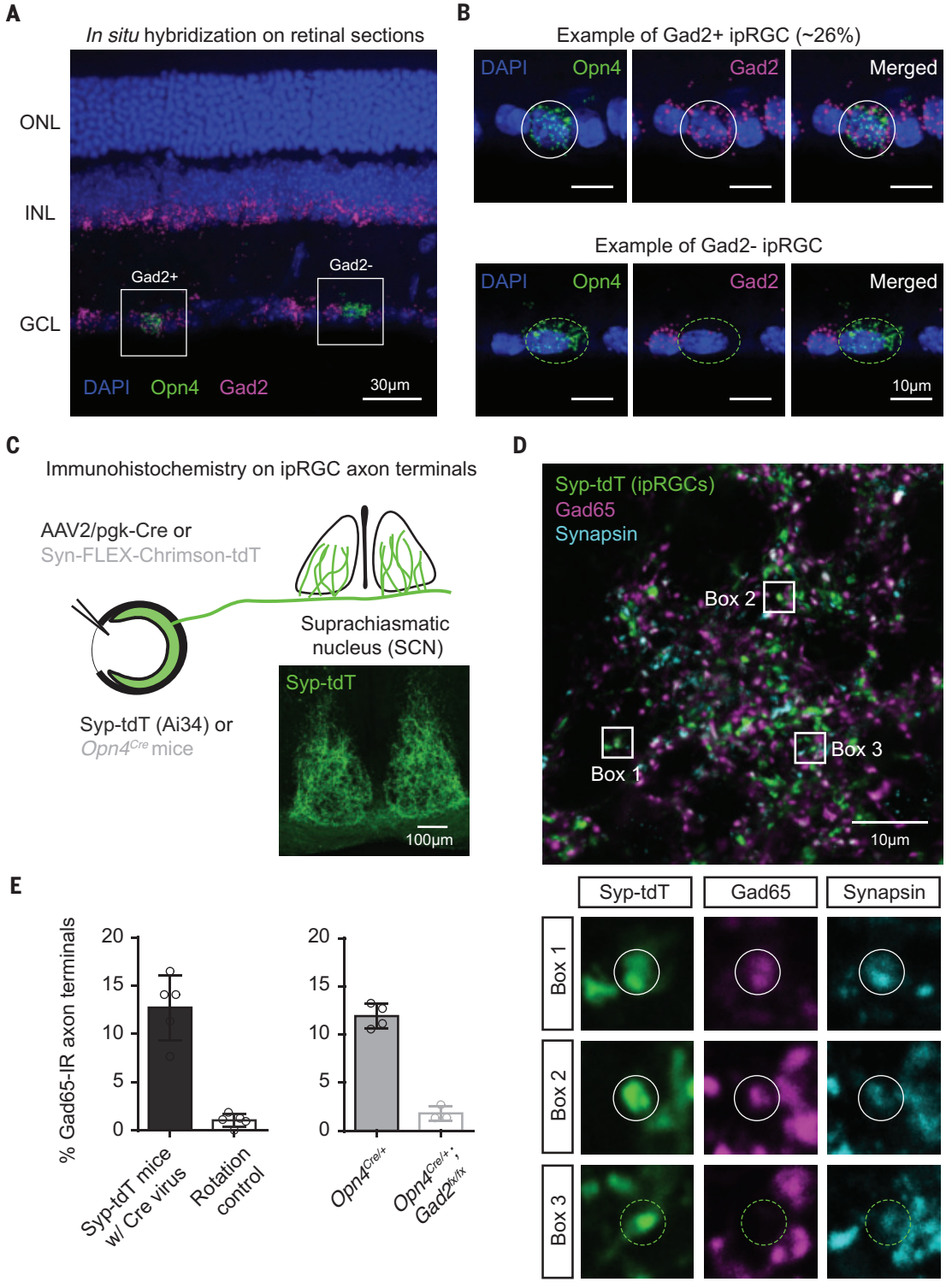

Fig. 2. ipRGCs express *Gad2*. (**A**) In situ hybridization for Opn4 (green) and *Gad2* (magenta). ONL, outer nuclear later; INL, inner nuclear layer; GCL, ganglion cell layer; DAPI, 4′,6-diamidino-2-phenylindole. (**B**) *Gad2*+ (top) and *Gad2*− (bottom) ipRGCs from (A). See figs. S5 and S7 for how the proportion of *Gad2*+ ipRGCs was estimated. (**C**) Strategies for labeling ipRGC axons in the SCN. Black text indicates that reporter mice, in which the synaptophysin-tdT fusion protein was expressed in the presence of Cre recombinase (Syp-tdT or Ai34), were intravitreally injected with the pgk-Cre virus. Gray text indicates that $Opn4^{Cre/+}$ animals were intravitreally injected with a virus driving Cre-dependent expression of Chrimson-tdT. (**D**) ipRGC terminals of Syp-tdt mice intravitreally injected with pgk-Cre virus (top) and immunolabeled for GAD65 (magenta) and synapsin to label axon terminals (cyan). Bottom panels show magnified images of ipRGC axon terminals that were GAD65 immunoreactive (boxes 1 and 2) and GAD65 negative (box 3). (**E**) Percentage of ipRGC terminals that were GAD65 immunoreactive (IR). n = 5 Syp-tdT mice injected with pgk-Cre virus, n = 4 $Opn4^{Cre/+}$ mice injected with FLEX-Chrimson-tdT virus, and n = 3 $Opn4^{Cre/+}$; $Gad2^{fx/fx}$ mice injected with FLEX-Chrimson-tdT virus. Error bars indicate SD.

[1]Department of Neurobiology, Northwestern University, Evanston, IL, USA. [2]Northwestern University Interdepartmental Neuroscience Program, Northwestern University, Chicago, IL, USA. [3]Microsoft, Redmond, WA, USA. [4]University Grenoble Alpes, Inserm, U1216, Grenoble Institut Neurosciences, 38000 Grenoble, France. [5]Department of Ophthalmology, Feinberg School of Medicine, Northwestern University, Chicago, IL, USA. *Present address: Department of Neurobiology, Duke University Medical Center, Durham, NC, USA.
†Corresponding author. Email: tiffany.schmidt@northwestern.edu

of RGCs that innervate non–image-forming structures—like the SCN, IGL, vLGN, and OPN shell—and are required for circadian photoentrainment and the PLR (*11*, *16*, *17*). To test whether *Gad2*+ RGCs are ipRGCs, we intravitreally injected *Gad2-IRES-Cre* mice with an AAV expressing a Cre-dependent mCherry reporter (AAV2/hSyn-DIO-mCherry) and immunolabeled these retinas for melanopsin (Fig. 1E). Of the melanopsin immunoreactive cells, 12% were mCherry+ (167 of 1437 cells from seven retinas), and the proportion of mCherry+ ipRGCs was highest (31%) in the dorsal-temporal quadrant of the retinas (Fig. 1, F and G). The individual densities of *Gad2*+ cells or of melanopsin immunopositive cells

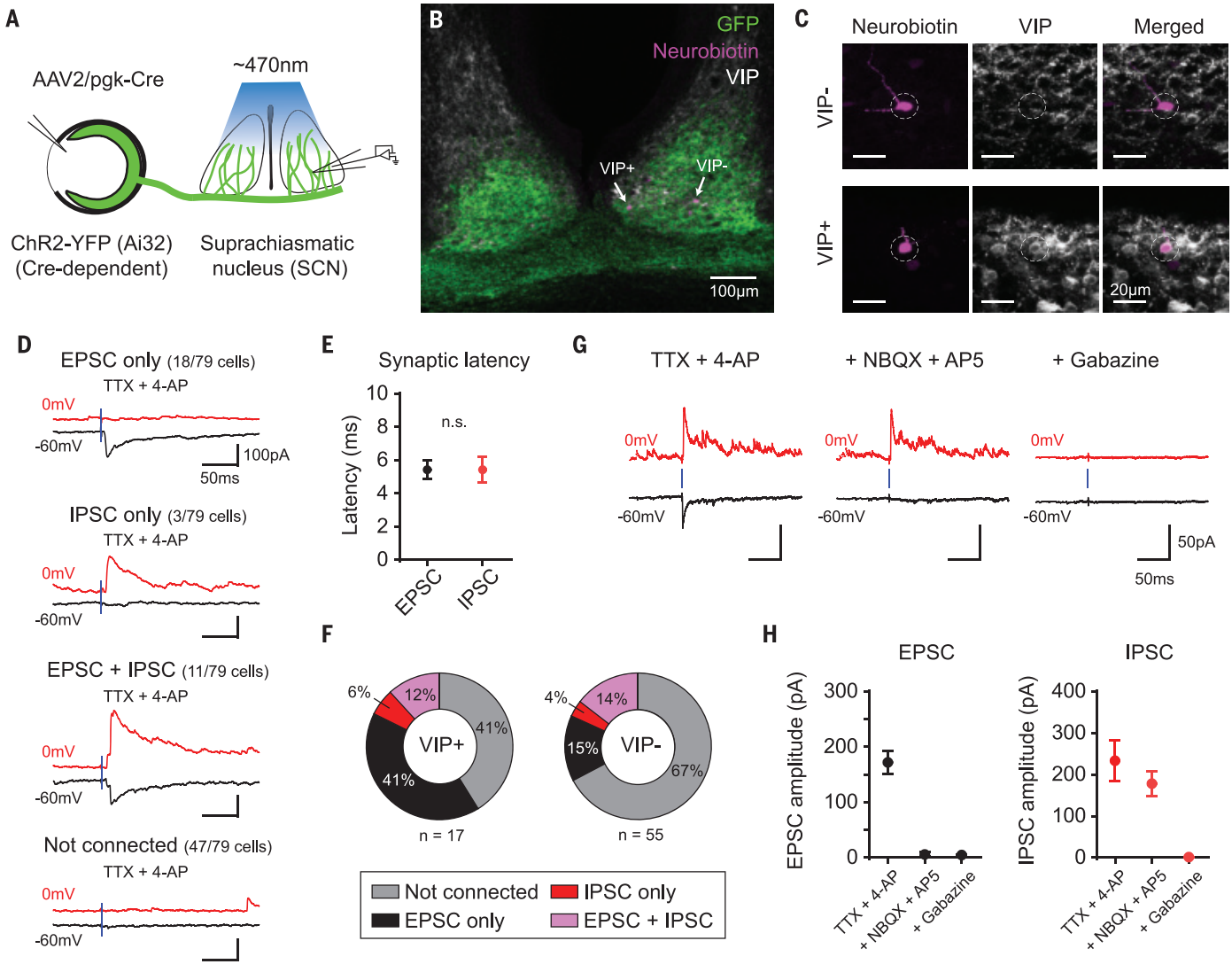

Fig. 3. Functional GABA release by ipRGCs. (**A**) SCN acute brain slices were prepared from ChR2-YFP (Ai32) mice intravitreally injected with pgk-Cre virus. Full field 470-nm light flashes were used to photoactivate ipRGC axons. (**B**) Neurobiotin-filled SCN neurons (magenta, indicated by arrows) in SCN slices labeled for VIP. ipRGC axons are labeled in green. (**C**) Magnified images of the VIP− (top panels) and VIP+ (bottom) neurons in (B). (**D**) EPSCs (black) and IPSCs (red) elicited in SCN neurons after photoactivating ipRGC axons in the presence of TTX and 4-AP (n = 79 cells). The blue line indicates delivery of a 1-ms light stimulus. TTX, tetrodotoxin; 4-AP, 4-aminopyridine. (**E**) Synaptic latency of EPSCs and IPSCs after photoactivation of ipRGC axons (n = 29 EPSCs and 14 IPSCs). n.s., not significant. (**F**) Proportion of VIP+ (left) and VIP− (right) SCN neurons that receive excitatory and/or inhibitory input from ipRGCs (n = 17 VIP+ and 55 VIP− SCN neurons). (**G**) Example recording from an SCN neuron that receives both excitatory and inhibitory ipRGC input. Bath application of NBQX and D-APV abolished the EPSC but did not affect the IPSC. Subsequent application of gabazine abolished the IPSC. (**H**) EPSC (black, left) and IPSC (red, right) amplitude in SCN neurons receiving both excitatory and inhibitory input from ipRGCs before and after application of NBQX and D-APV and then gabazine. n = 6 cells. All data are means ± SD.

alone were not higher in the dorsal-temporal retinas compared with other quadrants (fig. S3). Additionally, *Gad2* labeling was enriched in ipRGCs relative to the total RGC population because only 1% of the total RGCs and only 0.6% of the Brn3a+ (a marker of non-ipRGCs) RGCs were mCherry+ (fig. S4).

We performed RNA fluorescence in situ hybridization for *Gad2* mRNA in ipRGCs to determine whether we could detect it in ipRGCs. We identified ipRGCs in retinal sections by probing for *Opn4* mRNA (Fig. 2, A and B) and counting the number of *Gad2* puncta in that region of interest (figs. S5 to S7 and methods). We did not observe any labeling in the retinas of Opn4 knockout (KO) animals (fig. S6). To establish a threshold for *Gad2*+ ipRGCs, we performed the same experiment in animals lacking *Gad2* in ipRGCs ($Opn4^{Cre/+}$; $Gad2^{fx/fx}$). We estimate that *Gad2* mRNA is detectable above background in 26% of ipRGCs (fig. S7). We next immunolabeled ipRGC terminals in the SCN for GAD65 protein, which is encoded by the *Gad2* gene, in ipRGCs. Of the ipRGC nerve terminals in the SCN, 12% were GAD65 immunoreactive (Fig. 2, C to E). Less than 2% of ipRGC nerve terminals were GAD65 immunoreactive when we rotated the GAD65 channel (Fig. 2E), which indicates that colocalization levels were better than those that would be produced by chance. Likewise, <2% of ipRGC nerve terminals in $Opn4^{Cre/+}$; $Gad2^{fx/fx}$ animals were GAD65 immunoreactive.

We next investigated whether ipRGCs functionally release GABA. We expressed channelrhodopsin-2 (ChR2) in RGCs by delivering AAVs that drive Cre expression (AAV2/pgk-Cre) to the eyes of Ai32 mice (which drives Cre-dependent expression of ChR2) (*18*). We

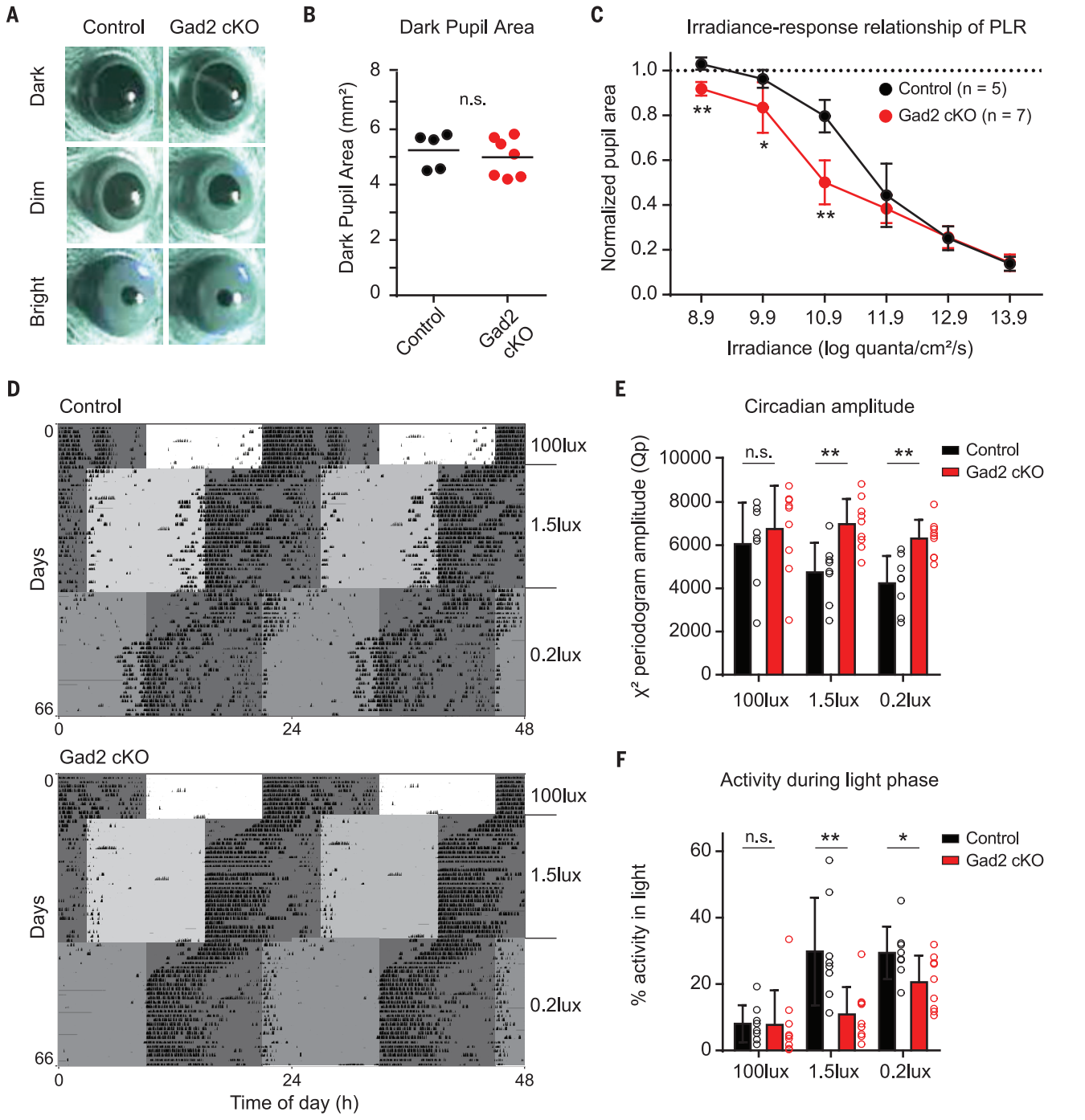

Fig. 4. GABA release by ipRGCs influences non–image-forming behaviors. (**A**) Representative PLR images from control (left panels, *Opn4*$^{+/+}$; *Gad2*$^{fx/fx}$) and *Gad2* cKO (right panels, *Opn4*$^{Cre/+}$; *Gad2*$^{fx/fx}$) mice in darkness (top), dim light (middle, 10.9 log quanta cm^{-2} s^{-1}), and bright light (bottom, 13.9 log quanta cm^{-2} s^{-1}). (**B**) Control (n = 5) and *Gad2* cKO (n = 7) pupil area in the dark. (**C**) Irradiance-response relationship of PLR in control and *Gad2* cKO mice. (**D**) Representative double-plotted actograms from control (top) and *Gad2* cKO (bottom) mice. Mice were initially exposed to a 12:12 LD cycle with 100 lux light during the light phase. The light level was subsequently lowered to 1.5 and 0.2 lux. The mice were exposed to a 6-hour phase advance each time the light level was lowered. (**E** and **F**) Circadian amplitude measured using the peak amplitude of the χ^2 periodogram (E) and percent activity during the light phase (F) in control (n = 8) and *Gad2* cKO (n = 9) mice. All data are means ± SD. n.s., not significant; *P < 0.05; **P < 0.01 (Mann-Whitney U test).

then made acute brain slices containing the SCN, which receives retinal input exclusively from ipRGCs in mice (*11*, *17*). We photoactivated the ipRGC axons (Fig. 3A) and voltage-clamped SCN neurons at −60 mV (E_{Cl}) to isolate excitatory postsynaptic currents (EPSCs) and then at 0 mV (E_{cation}) to isolate inhibitory postsynaptic currents (IPSCs). Tetrodotoxin (TTX) and 4-aminopyridine (4-AP) were included in the extracellular solution to ensure that the elicited postsynaptic currents were monosynaptic (*19*). Photoactivation of ipRGCs evoked synaptic currents in 32 of 79 (40%) SCN neurons including EPSCs only (18 of 32 cells), IPSCs but not EPSCs (3 of 32 cells), and both

IPSCs and EPSCs (11 of 32 cells). Therefore, just >43% of SCN neurons receiving direct input from ipRGCs receive inhibitory ipRGC input (Fig. 3D). The synaptic latency of EPSCs and IPSCs elicited in SCN neurons was not significantly different, which suggests that both types of postsynaptic currents arise from monosynaptic input from ipRGCs (Fig. 3E). When possible, we mapped the location of recorded SCN neurons (fig. S8) and immunolabeled recorded cells for vasoactive intestinal peptide (VIP) (Fig. 3, B and C). A higher proportion of VIP+ neurons in the SCN received monosynaptic ipRGC input (59%) compared with VIP– neurons (33%) (Fig. 3F). A larger percentage of VIP+ neurons received purely excitatory ipRGC input (41%) compared with VIP– neurons (15%), and a similar proportion of VIP+ and VIP– neurons received inhibitory ipRGC input (Fig. 3F).

Bath application of 2,3-Dioxo-6-nitro-1,2,3,4-tetrahydrobenzo[*f*]quinoxaline-7-sulfonamide (NBQX) and D-(-)-2-Amino-5-phosphonopentanoic acid (D-APV) abolished the evoked EPSCs (Fig. 3, G and H) in SCN neurons receiving excitatory and inhibitory ipRGC input, but it did not affect IPSC amplitudes. This further confirms that elicited IPSCs were likely not a result of a disynaptic inhibition arising from evoked glutamatergic ipRGC inputs onto a GABAergic interneuron. Subsequent bath application of gabazine (SR-95531) abolished the remaining light-evoked IPSCs in SCN neurons (Fig. 3, G and H).

To assess how GABA release by ipRGCs influences non–image-forming visual behavior, we crossed $Opn4^{Cre}$ mice (*20*) with $Gad2^{fx/fx}$ mice (*21*) to knock out *Gad2* specifically in ipRGCs ($Opn4^{Cre/+}$; $Gad2^{fx/fx}$, referred to as *Gad2* cKO). These animals showed normal ipRGC projections and visual acuity, which indicates that this manipulation does not affect the development of the visual system (figs. S9 and S10). We measured the PLR of *Gad2* cKO animals compared with littermate controls ($Opn4^{+/+}$; $Gad2^{fx/fx}$) across a range of light intensities and measured the irradiance-response relationship (Fig. 4, A to C). PLR amplitude and kinetics were both unaffected at bright light intensities in *Gad2* cKO animals (Fig. 4C and fig. S11), and baseline pupil size in darkness was also unchanged (Fig. 4, A and B). However, at low light levels, *Gad2* cKO mice showed significantly stronger pupil constriction (Fig. 4C) than that of their littermate controls, although the kinetics were not significantly different (fig. S11).

We next tested whether these changes in PLR were caused by a lack of *Gad2* in ipRGCs or, potentially, by developmental effects of *Gad2* excision early in development. We knocked out the *Gad2* gene specifically in RGCs of adult $Gad2^{fx/fx}$ mice through intravitreal delivery of an AAV that drives Cre expression under an RGC-specific promoter (AAV2/SNCG-Cre-HA) (*22*) (fig. S12 and methods). Less than 5% of amacrine cells were labeled in well-infected areas (fig. S12B). We then measured the PLR in response to dim (10.4 log photons cm^{-2} s^{-1}) and bright (13.4 log photons cm^{-2} s^{-1}) light stimuli. Mice in which *Gad2* was knocked out in RGCs exhibited significantly more sensitive PLR in response to dim light but not bright light (fig. S12, C and D) compared with control animals. These results suggest that these changes in PLR are not due to developmental defects from *Gad2* gene excision.

To determine whether GABA release by ipRGCs also influences circadian photoentrainment, we tracked voluntary wheel-running activity of littermate controls and *Gad2* cKO mice across multiple light levels. Mice were first exposed to a 12-hour–12-hour light-dark (LD) cycle with bright, 100-lux light during the light phase. We then performed a 6-hour phase advance of the LD cycle at 4-week intervals and simultaneously lowered the light intensity at each shift, first to 1.5 and then to 0.2 lux (Fig. 4D and fig. S13). The rate of re-entrainment in response to both 6-hour phase advances was the same in *Gad2* cKO compared to control animals (fig. S14). However, *Gad2* cKO animals had significantly higher circadian amplitudes in LD cycles at low (1.5 and 0.2 lux) but not high (100 lux) light levels (Fig. 4E). This indicates that the circadian photoentrainment of *Gad2* cKO animals remains more robust at lower light levels and is relatively insensitive to decreases in environmental light levels. There were no significant differences between *Gad2* cKO and control animals in total daily activity, activity onset time, or activity onset variability (fig. S15). Instead, *Gad2* cKO animals exhibited significantly less activity in the light phase at 1.5 and 0.2 lux, which likely accounts for their increased circadian amplitude at low light levels relative to controls (Fig. 4F).

Our results reveal a GABAergic circuit originating in the retina that decreases the sensitivity of the non–image-forming visual system at low light levels. Recent reports have shown that the ipRGCs providing input to non–image-forming brain regions are highly sensitive to dim light (*23*–*25*), and yet the non–image-forming behaviors driven by these inputs are relatively insensitive to light compared with image-forming vision (*26*, *27*). The mechanisms underlying this discrepancy between sensitive cellular inputs to non–image-forming brain regions and relatively insensitive behavioral outputs had remained a mystery. Our results suggest that a subpopulation of ipRGCs may serve to actively dampen the sensitivity of the non–image-forming visual behaviors by releasing the inhibitory neurotransmitter GABA, providing a circuit mechanism for this discrepancy. For the PLR, these inputs serve to maximize light entry into the eye at low light levels. For circadian behaviors, these inputs likely prevent unnecessary adjustments of the body's master clock to relatively minor perturbations in environmental light.

REFERENCES AND NOTES

1. J. R. Sanes, R. H. Masland, *Annu. Rev. Neurosci.* **38**, 221–246 (2015).
2. L. P. Morin, K. M. Studholme, *J. Comp. Neurol.* **522**, 3733–3753 (2014).
3. E. M. Martersteck *et al.*, *Cell Rep.* **18**, 2058–2072 (2017).
4. T. M. Schmidt, S. K. Chen, S. Hattar, *Trends Neurosci.* **34**, 572–580 (2011).
5. T. A. Seabrook, T. J. Burbridge, M. C. Crair, A. D. Huberman, *Annu. Rev. Neurosci.* **40**, 499–538 (2017).
6. P. C. Rogers, D. V. Pow, *Vis. Neurosci.* **12**, 1143–1149 (1995).
7. S. Davanger, O. P. Ottersen, J. Storm-Mathisen, *J. Comp. Neurol.* **311**, 483–494 (1991).
8. N. Lugo-García, R. E. Blanco, *Brain Res.* **564**, 19–26 (1991).
9. B. L. da Costa, J. N. Hokoç, R. R. Pinaud, R. Gattass, *Neuroreport* **8**, 1797–1802 (1997).
10. H. Taniguchi *et al.*, *Neuron* **71**, 995–1013 (2011).
11. A. D. Güler *et al.*, *Nature* **453**, 102–105 (2008).
12. R. Y. Moore, V. B. Eichler, *Brain Res.* **42**, 201–206 (1972).
13. F. K. Stephan, I. Zucker, *Proc. Natl. Acad. Sci. U.S.A.* **69**, 1583–1586 (1972).
14. G. E. Pickard, M. R. Ralph, M. Menaker, *J. Biol. Rhythms* **2**, 35–56 (1987).
15. L. J. Trejo, C. M. Cicerone, *Brain Res.* **300**, 49–62 (1984).
16. S. Hattar *et al.*, *J. Comp. Neurol.* **497**, 326–349 (2006).
17. S. B. Baver, G. E. Pickard, P. J. Sollars, G. E. Pickard, *Eur. J. Neurosci.* **27**, 1763–1770 (2008).
18. L. Madisen *et al.*, *Nat. Neurosci.* **15**, 793–802 (2012).
19. L. Petreanu, T. Mao, S. M. Sternson, K. Svoboda, *Nature* **457**, 1142–1145 (2009).
20. J. L. Ecker *et al.*, *Neuron* **67**, 49–60 (2010).
21. F. Meng *et al.*, *Proc. Natl. Acad. Sci. U.S.A.* **113**, 3645–3650 (2016).
22. A. Chaffiol *et al.*, *Mol. Ther.* **25**, 2546–2560 (2017).
23. S. Weng, M. E. Estevez, D. M. Berson, *PLOS ONE* **8**, e66480 (2013).
24. X. Zhao, B. K. Stafford, A. L. Godin, W. M. King, K. Y. Wong, *J. Physiol.* **592**, 1619–1636 (2014).
25. S. K. Lee, T. Sonoda, T. M. Schmidt, *Cell Rep.* **29**, 3349–3355.e2 (2019).
26. D. E. Nelson, J. S. Takahashi, *Brain Res.* **554**, 272–277 (1991).
27. M. P. Butler, R. Silver, *Proc. R. Soc. B* **278**, 745–750 (2010).

ACKNOWLEDGMENTS

We thank T. Bozza, R. Allada, and M. Gallio for helpful comments on the manuscript; S. Hattar for the gift of $Opn4^{Cre}$ mice; and Q. Wu for the gift of $Gad2^{fx}$ mice. **Funding:** This work was funded by a Klingenstein-Simons Fellowship in the Neurosciences to T.M.S., a Sloan Research Fellowship to T.M.S., NIH grant 1DP2EY022584 to T.M.S, NIH T32 EY025202 to support T.S., and NIH F31 EY030360-01 to T.S. **Author contributions:** Conceptualization, T.S., J.Y.L., and T.M.S.; Investigation, T.S., J.Y.L., N.W.H., Y.O., and T.M.S.; Formal analysis, T.S.; Software, J.C.C.; Writing – original draft, T.S. and T.M.S.; Writing – reviewing and editing, T.S., J.Y.L., and T.M.S.; Visualization, T.S., J.Y.L., N.W.H., J.C.C., and T.M.S.; Resources, J.C.C., S.B., and H.N.; and Funding acquisition, T.S. and T.M.S. **Competing interests:** The authors declare no competing interests. **Data and materials availability:** All data are available in the manuscript or the supplementary materials.

SUPPLEMENTARY MATERIALS

science.sciencemag.org/content/368/6490/527/suppl/DC1
Materials and Methods
Figs. S1 to S15
References (*28*–*30*)
MDAR Reproducibility Checklist

7 June 2019; resubmitted 31 January 2020
Accepted 13 March 2020
10.1126/science.aay3152

SUPERCONDUCTIVITY

Ferromagnetic order beyond the superconducting dome in a cuprate superconductor

Tarapada Sarkar[1], D. S. Wei[2,3], J. Zhang[4], N. R. Poniatowski[1], P. R. Mandal[1], A. Kapitulnik[2,3,5,6], Richard L. Greene[1]*

According to conventional wisdom, the extraordinary properties of the cuprate high-temperature superconductors arise from doping a strongly correlated antiferromagnetic insulator. The highly overdoped cuprates—whose doping lies beyond the dome of superconductivity—are considered to be conventional Fermi liquid metals. We report the emergence of itinerant ferromagnetic order below 4 kelvin for doping beyond the superconducting dome in thin films of electron-doped $La_{2-x}Ce_xCuO_4$ (LCCO). The existence of this ferromagnetic order is evidenced by negative, anisotropic, and hysteretic magnetoresistance, hysteretic magnetization, and the polar Kerr effect, all of which are standard signatures of itinerant ferromagnetism in metals. This surprising result suggests that the overdoped cuprates are strongly influenced by electron correlations.

Underdoped cuprates exhibit many ordered phases, including antiferromagnetism (*1*, *2*), charge order (*3*–*5*), and nematicity (*6*). The relationship of these phases to high-temperature (high-T_c) superconductivity has yet to be determined. Moreover, the nature of the much-studied pseudogap phase in the hole-doped cuprates, which appears to end at a critical doping, remains unresolved (*7*). The seemingly conventional overdoped region of the phase diagram [beyond the pseudogap endpoint in hole-doped materials or beyond the Fermi surface reconstruction (FSR) in electron-doped materials] has been studied less systematically, and its importance to the mechanism of superconductivity has largely been dismissed. However, some studies of this region suggest that the physics is not that of a conventional Fermi liquid. For example, in both hole-doped and electron-doped materials, the low-temperature normal-state transport properties are anomalous (*8*, *9*). An extended range of quantum critical transport appears to exist from the FSR doping to the end of the superconducting dome in all cuprates (*10*–*12*).

Here, we report ferromagnetic order in electron-doped $La_{2-x}Ce_xCuO_4$ (LCCO), which further challenges the conventional picture of overdoped cuprates. Hints of magnetism in overdoped hole-doped cuprates at temperatures below 1 K have been reported previously (*13*), and ferromagnetic fluctuations have been reported at higher temperatures (*14*). We provide comprehensive and robust evidence for static ferromagnetic order in LCCO (see below). The existence of a ferromagnetic phase beyond the end of the superconducting dome that competes with the d-wave superconductivity was hypothesized in (*15*); the fluctuations of this phase were invoked to explain the temperature dependence of the magnetic susceptibility (χ) in overdoped $(Bi, Pb)_2Sr_2CuO_{6+\delta}$. This raises the possibility that ferromagnetism is a universal feature of overdoped cuprate physics. However, obtaining direct evidence of static (or itinerant) ferromagnetic order associated with the CuO_2 planes in any cuprate remains experimentally challenging.

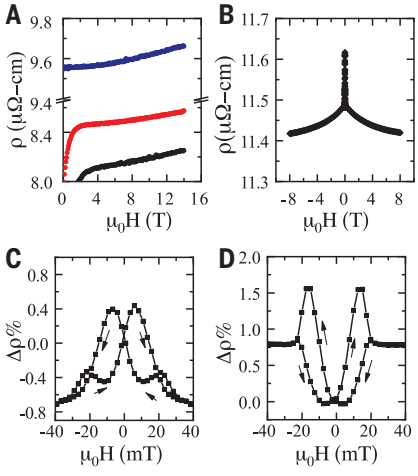

Fig. 1. Low-temperature magnetoresistance across the end of the superconducting dome in LCCO. Shown are the data for a sample on STO substrate. (**A**) *ab*-plane magnetoresistivity ($H \perp ab$-plane) for $x = 0.17$ ($T_c = 4$ K) at 2 K (black), 5 K (red), and 10 K (blue). (**B**) *ab*-plane magnetoresistivity ($H \perp ab$-plane) for $x = 0.18$ at 2 K. (**C** and **D**) *ab*-plane $\Delta\rho(\%) = [\rho(H) - \rho(0)]/\rho(0) \times 100$ for $x = 0.18$ ($T_c = 0$ K) at 2 K in low-field sweep from +400 Oe to −400 Oe for $H \perp ab$-plane (C) and $H \parallel ab$-plane (D). Arrows indicate the sweeping direction of the H field.

To investigate this highly overdoped regime, we measured electron-doped LCCO thin films, which can reliably be doped beyond the superconducting dome. In particular, we focused on the nonsuperconducting dopings ($x = 0.18$, 0.19) where a Fermi liquid–like quadratic temperature dependence of the resistivity is found at low temperatures (*16*).

In Figs. 1 and 2, we present the negative transverse magnetoresistance, anisotropic magnetoresistance, and magnetic field hysteresis in magnetization, magnetoresistance, and magneto-thermopower measurements on LCCO samples grown on $SrTiO_3$ (STO) substrates. Figure 1 shows the low-temperature transverse ($H \perp ab$-plane) magnetoresistance for both a superconducting ($x = 0.17$) and a nonsuperconducting ($x = 0.18$) sample. The magnetoresistance for $x = 0.17$ is positive and crosses over from linear to quadratic in field with increasing temperature, whereas the transverse magnetoresistance for $x = 0.18$ is negative with a strong low-field hysteretic dependence below ~4 K. Both of these features, the negative magnetoresistance and low-field hysteresis below 4 K, are hallmarks of itinerant ferromagnetism (*17*–*20*). Similar magnetoresistance data suggestive of ferromagnetic order are shown in Fig. 2, A and B, for $x = 0.19$, again below 4 K. As shown in Fig. 2D, we also observed hysteresis in the magneto-thermopower (*21*), reaffirming the presence of ferromagnetism and ruling out any current heating effect as the cause of the magnetoresistance hysteresis. In Fig. 2C we show a superconducting quantum interference device (SQUID) magnetization study of a $x = 0.19$ sample, which demonstrates hysteresis in the magnetization below 4 K, with a coercive field comparable to that of the magnetoresistance shown in Fig. 2, A and B. The hysteresis vanishes at 4 K (fig. S1). At 2 K, the magnitude of the magnetization is approximately 0.06 to 0.08 Bohr magneton per formula unit (μ_B/f.u.). The in-plane magnetization saturates, whereas the out-of-plane magnetization does not saturate (Fig. 2C); this shows that the ferromagnetic moments are in the plane, as confirmed by the polar Kerr effect results (Fig. 3) (*22*). Furthermore, we found an anisotropic magnetoresistance, which is a well-known effect intrinsic to ferromagnets, arising from spin-orbit coupling (*17*–*19*). These data are shown in Fig. 1, C and D, and fig. S4, where the magnetoresistance depends on the relative orientation of the current and the magnetization.

In Fig. 3, we show the polar Kerr effect measurements of an $x = 0.19$ LCCO film grown on an $(LaAlO_3)_{0.3}(Sr_2TaAlO_6)_{0.7}$ (LSAT) substrate. For these high-resolution measurements, we used a zero-area loop Sagnac interferometer that nulls out any reciprocal effects such as linear birefringence and is capable of detecting

[1]Maryland Quantum Materials Center and Department of Physics, University of Maryland, College Park, MD 20742, USA. [2]Geballe Laboratory for Advanced Materials, Stanford University, Stanford, CA 94305, USA. [3]Department of Applied Physics, Stanford University, Stanford, CA 94305, USA. [4]State Key Laboratory of Surface Physics, Department of Physics, Fudan University, Shanghai 200433, People's Republic of China. [5]Department of Physics, Stanford University, Stanford, CA 94305, USA. [6]Stanford Institute for Materials and Energy Sciences (SIMES), SLAC National Accelerator Laboratory, Menlo Park, CA 94025, USA.
*Corresponding author. Email: rickg@umd.edu

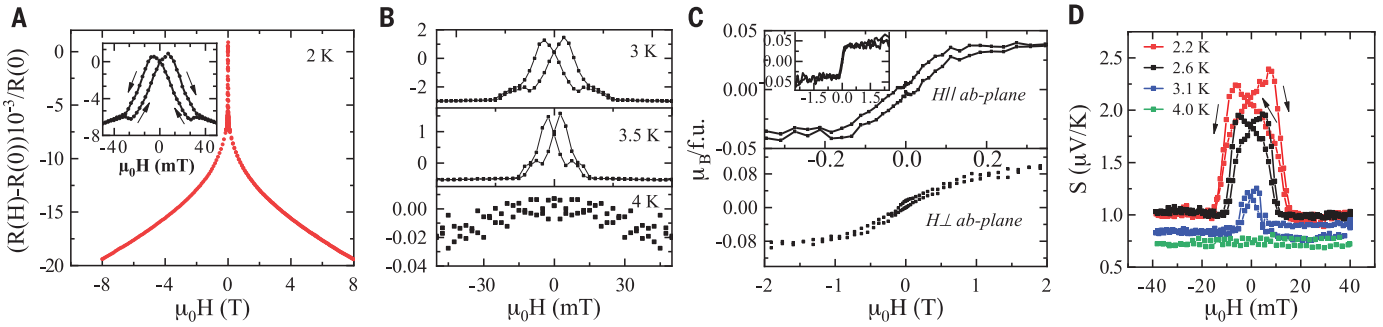

Fig. 2. Magnetotransport and magnetization for x = 0.19 in LCCO. Shown are the data for a sample on STO substrate. (**A**) *ab*-plane Δρ(%) = [ρ(*H*) − ρ(0)]/ρ(0) × 100 (*H* ⊥ *ab*-plane) at 2 K. Inset: Δρ(%) for low fields. Black arrows indicate the sweeping direction of the field. (**B**) Low-field *ab*-plane Δρ(%) (*H* ⊥ *ab*-plane) at 3 K, 3.5 K, and 4 K with the same sweeping direction as in (A) (the *y*-axis label is also the same). (**C**) Magnetization versus magnetic field with *H* || *ab*-plane and *H* ⊥ *ab*-plane at 2 K. The substrate background is removed in these plots (*22*). Inset: Magnetization in extended view for *H* || *ab*-plane. (**D**) *ab*-plane thermoelectric power with transverse sweeping field +400 Oe to −400 Oe.

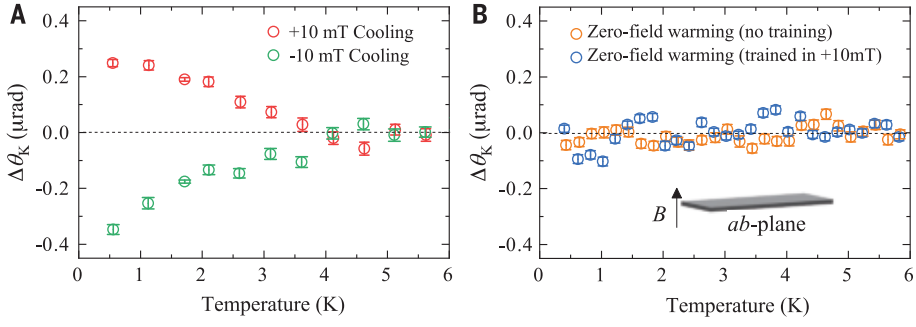

Fig. 3. Polar Kerr effect in LCCO. (**A**) Kerr angle measured in zero magnetic field after cooling down from 6 K in +10 mT (red) and −10 mT (green), plotted as a function of temperature for an LCCO sample with x = 0.19 (*H* ⊥ *ab*-plane, LSAT substrate). Data are averaged over 500-mK windows, and we subtract a temperature-independent background offset of ~0.7 μm stemming from electrical and optical contributions from the instruments. Error bars indicate SD. An onset of Kerr signal at 4 K and a complete reversal with opposite magnetic field indicate field-canted moments along the polar direction. (**B**) Kerr angle measured in zero magnetic field while warming after cooling down in zero magnetic field (orange) and after cooling down in +10 mT (blue). Data are averaged over 200 mK windows, and we subtract a temperature-independent background offset of roughly 0.7 μm. There is no discernible Kerr signal, indicating that the magnetic moments are in the *ab*-plane. Inset: Direction of the applied magnetic field for all Kerr measurements.

tiny magneto-optic effects on the order of tens of nanoradians, as described in (*23*). This technique has been used to detect time-reversal symmetry breaking in triplet superconductors (*24*, *25*) as well as the ferromagnetic phase transition of a thin film of $SrRuO_3$ (*26*). For all the Kerr measurements, we operated at a wavelength of 1550 nm with a spot size D ~ 10.6 μm and measured with an incident optical power P_{inc} ~ 30 μW. The details of these measurements are given in the Fig. 3 caption and (*22*). These results fully confirm the transport and magnetization results and indicate the onset of long-range ferromagnetic order at ~4 K. Moreover, the magnitude of the Kerr angle θ_K is consistent with the magnetic moment found from the magnetization results (*22*).

Taken together, the negative transverse magnetoresistance, anisotropic magnetoresistance, and hysteretic features in magnetoresistance, magneto-thermopower, and magnetization measurements, as well as the finite polar Kerr effect, provide compelling evidence for static ferromagnetic order below 4 K in overdoped LCCO. Great care was taken to ensure that the observed magnetism was intrinsic to the sample (*22*), including the reproduction of our results for more than 20 films grown on three different substrates. For example, magnetoresistance hysteresis similar to that shown in Figs. 1 and 2 for LCCO on an STO substrate was found for LCCO films on LSAT and $LaSrGaO_4$ substrates (fig. S3). Magnetization hysteresis of LCCO on LSAT is shown in fig. S1C; the Kerr effect was done for LCCO films on an LSAT substrate (Fig. 3).

The ferromagnetism we observe in overdoped nonsuperconducting LCCO resembles that found in weak itinerant ferromagnets such as UGe_2 (*27*) and Y_4Co_3 (*28*), in that they also exhibit a T^2 temperature dependence of the resistivity. The ferromagnetic order may exist above the doping x = 0.19, but we were unable to prepare such films. The onset of superconductivity at 5 K for x = 0.17 prohibits a lower-temperature magnetoresistance study for this and lower dopings. However, we measured an x ~ 0.175 film that might be superconducting below 1.8 K. This film shows a positive normal-state magnetoresistance at 1.8 K and no low-field hysteretic magnetoresistance (fig. S12), which means that it is not ferromagnetic at 1.8 K. On the basis of this result, the magnetoresistance data in Fig. 1, and a prior μSR study of LCCO (*29*), it is reasonable to predict the absence of any ferromagnetic order below x = 0.175. We attribute the observed ferromagnetism to the hypothesized (*15*) low-temperature ferromagnetic order in the copper oxide planes of overdoped cuprates.

A previous transport study observed quantum critical behavior of unknown origin at the end of the superconducting dome in LCCO based on the scaling of the resistivity with temperature and magnetic field. The work reported the low-temperature normal-state resistivity to vary as $T^{1.6}$ for a doping at the end of the dome (*30*). This power law of resistivity is very close to the power law expected to arise from quantum critical ferromagnetic fluctuations (*31*). In conjunction with the evidence for ferromagnetic order above the superconducting dome described in this work, these results are suggestive of a superconducting/ferromagnetic quantum critical point located at the end of the superconducting dome in LCCO.

Our study firmly establishes the existence of itinerant ferromagnetic order in the overdoped, nonsuperconducting, cuprate LCCO at temperatures below 4 K. This suggests the

presence of a ferromagnetic quantum critical point at the end of the superconducting dome, and a resultant competition between d-wave superconductivity and ferromagnetism. This competition may play a role in other unexplained aspects of the overdoped cuprates, such as the decrease of T_c beyond optimal doping and the anomalous loss of superfluid density (*32*). However, further work will be needed to learn more about the nature of the ferromagnetic phase and its impact on the properties of overdoped cuprates. Nonetheless, this striking observation of itinerant ferromagnetism may help to address the long-standing mystery of the cuprates and to reimagine the unexplored frontiers of their phase diagram. Finally, it is possible that this ferromagnetic order represents another intriguing similarity between the cuprates and twisted bilayer graphene, given that ferromagnetic order has recently been found beyond the superconducting dome in that system (*33*).

REFERENCES AND NOTES

1. P. A. Lee, N. Nagaosa, X.-G. Wen, *Rev. Mod. Phys.* **78**, 17–85 (2006).
2. B. Keimer, S. A. Kivelson, M. R. Norman, S. Uchida, J. Zaanen, *Nature* **518**, 179–186 (2015).
3. T. Wu *et al.*, *Nature* **477**, 191–194 (2011).
4. M. Hücker *et al.*, *Phys. Rev. B* **90**, 054514 (2014).
5. E. H. da Silva Neto *et al.*, *Sci. Adv.* **2**, e1600782 (2016).
6. R. Daou *et al.*, *Nature* **463**, 519–522 (2010).
7. M. R. Norman, D. Pines, C. Kallin, *Adv. Phys.* **54**, 715–733 (2005).
8. R. L. Greene, P. R. Mandal, N. R. Poniatowski, T. Sarkar, *Annu. Rev. Condens. Matter Phys.* **11**, 213–229 (2020).
9. A. Legros *et al.*, *Nat. Phys.* **15**, 142–147 (2019).
10. P. R. Mandal, T. Sarkar, R. L. Greene, *Proc. Natl. Acad. Sci. U.S.A.* **116**, 5991–5994 (2019).
11. T. Sarkar, P. R. Mandal, N. R. Poniatowski, M. K. Chan, R. L. Greene, *Sci. Adv.* **5**, eaav6753 (2019).
12. R. A. Cooper *et al.*, *Science* **323**, 603–607 (2009).
13. J. E. Sonier *et al.*, *Proc. Natl. Acad. Sci. U.S.A.* **107**, 17131–17134 (2010).
14. K. Kurashima *et al.*, *Phys. Rev. Lett.* **121**, 057002 (2018).
15. A. Kopp, A. Ghosal, S. Chakravarty, *Proc. Natl. Acad. Sci. U.S.A.* **104**, 6123–6127 (2007).
16. K. Jin, N. P. Butch, K. Kirshenbaum, J. Paglione, R. L. Greene, *Nature* **476**, 73–75 (2011).
17. J. M. D. Coey, *Magnetotransport in Magnetism and Magnetic Materials* (Cambridge Univ. Press, 2009).
18. M. Viret *et al.*, *Phys. Rev. B* **53**, 8464–8468 (1996).
19. T. R. McGuire, R. I. Potter, *IEEE Trans. Magn. Mater* **11**, 1018–1038 (1975).
20. H. Boschker *et al.*, *Phys. Rev. X* **9**, 011027 (2019).
21. Y. Pu, E. Johnston-Halperin, D. D. Awschalom, J. Shi, *Phys. Rev. Lett.* **97**, 036601 (2006).
22. See supplementary materials.
23. A. Kapitulnik, J. Xia, E. Schemm, A. Palevski, *New J. Phys.* **11**, 055060 (2009).
24. J. Xia, Y. Maeno, P. T. Beyersdorf, M. M. Fejer, A. Kapitulnik, *Phys. Rev. Lett.* **97**, 167002 (2006).
25. E. R. Schemm, W. J. Gannon, C. M. Wishne, W. P. Halperin, A. Kapitulnik, *Science* **345**, 190–193 (2014).
26. J. Xia, W. Siemons, G. Koster, M. R. Beasley, A. Kapitulnik, *Phys. Rev. B* **79**, 140407(R) (2009).
27. S. S. Saxena *et al.*, *Nature* **406**, 587–592 (2000).
28. A. Kolodziejczyk, J. Spalek, *J. Phys. F* **14**, 1277–1289 (1984).
29. H. Saadaoui *et al.*, *Nat. Commun.* **6**, 6041 (2015).
30. N. P. Butch, K. Jin, K. Kirshenbaum, R. L. Greene, J. Paglione, *Proc. Natl. Acad. Sci. U.S.A.* **109**, 8440–8444 (2012).
31. T. Moriya, K. Ueda, *Rep. Prog. Phys.* **66**, 1299–1341 (2003).
32. I. Božović, X. He, J. Wu, A. T. Bollinger, *Nature* **536**, 309–311 (2016).
33. A. L. Sharpe *et al.*, *Science* **365**, 605–608 (2019).
34. T. Sarkar *et al.*, Ferromagnetic order beyond the superconducting dome in a cuprate superconductor, Dryad (2020); https://doi.org/10.5061/dryad.05qfttf08.

ACKNOWLEDGMENTS

We thank M. Coey, J. Mannhart, J. Paglione, N. Butch, W. Fuhrman, and J. Higgins for helpful discussions and comments on the manuscript. **Funding:** The work at the University of Maryland is supported by NSF under grant DMR-1708334, AFSOR under grant FA9550-14-10332, and the Maryland Quantum Materials Center. Work at Stanford University was supported by the Department of Energy, Office of Basic Energy Sciences, under contract DE-AC02- 76SF00515. D.S.W. acknowledges support from the Karel Urbanek Postdoctoral Fellowship in Applied Physics at Stanford University. J.Z. acknowledges support from the Chinese Government Scholarship of China Scholarship Council. The Kerr effect experiments were funded in part by a QuantEmX grant from ICAM and the Gordon and Betty Moore Foundation through grant GBMF5305 to N.R.P. **Author contributions:** R.L.G. directed the overall project. A.K. directed the research at Stanford; T.S. performed the transport and magnetization measurements and analysis; P.R.M. performed the thermoelectric measurement; T.S. prepared the samples with assistance from N.R.P.; D.S.W. and J.Z. performed the Kerr effect measurements and analysis with assistance from N.R.P.; and R.L.G., T.S., N.R.P., and A.K. wrote the manuscript and discussed it with all other authors. **Competing interests:** The authors declare no competing financial interests. **Data and materials availability:** All data needed to evaluate the conclusions in the paper or the supplementary materials are available on Dryad (*34*).

SUPPLEMENTARY MATERIALS

science.sciencemag.org/content/368/6490/532/suppl/DC1
Materials and Methods
Supplementary Text
Figs. S1 to S12
References (*35*–*46*)

26 February 2019; resubmitted 23 October 2019
Accepted 25 March 2020
10.1126/science.aax1581

MESOSCOPIC PHYSICS

Evidence for an edge supercurrent in the Weyl superconductor $MoTe_2$

Wudi Wang[1], Stephan Kim[1], Minhao Liu[1]*, F. A. Cevallos[2], R. J. Cava[2], N. P. Ong[1]†

Edge supercurrents in superconductors have long been an elusive target. Interest in them has reappeared in the context of topological superconductivity. We report evidence for the existence of a robust edge supercurrent in the Weyl superconductor molybdenum ditelluride ($MoTe_2$). In a magnetic field *B*, fluxoid quantization generates a periodic modulation of the edge condensate observable as a "fast-mode" oscillation of the critical current I_c versus *B*. The fast-mode frequency is distinct from the conventional Fraunhofer oscillation displayed by the bulk supercurrent. We confirm that the fast-mode frequency increases with crystal area as expected for an edge supercurrent. In addition, weak excitation branches are resolved that display an unusual broken symmetry.

Topological superconductors support bulk supercurrents as well as edge states that carry unpaired excitations (*1*–*3*). A fundamental question is whether an edge supercurrent, distinct from the bulk supercurrent, can also exist. To this end, Weyl semimetals are especially attractive because Cooper pairing of electrons in the bulk (*4*–*9*) may induce pairing of edge excitations on the surface. Currently, γ-molybdenum ditelluride (γ-$MoTe_2$, where γ refers to the orthorhombic semimetallic phase) is the only Weyl semimetal that is known to be a superconductor (*10*, *11*); at ambient pressure, its critical temperature T_c is 100 mK (*12*). Here, we report evidence for an edge supercurrent in this material.

Crystals of γ-$MoTe_2$ were exfoliated to a thickness d = 60 to 120 nm and contacted by using evaporated gold (Au) probes (table S1) [(*13*), section 1]. To study its intrinsic superconducting properties, we avoided altogether injecting a supercurrent into the sample, in contrast with experiments (*13*) in which superconducting aluminium (Al) contacts were used to proximitize graphene (*14*) or mercury telluride (HgTe)/cadmium telluride (CdTe) quantum wells (*15*, *16*). With the temperature T fixed at 20 mK, we measured the differential resistance dV/dI versus the bias current I at selected values of the magnetic field B. We then plotted the resulting set of (typically) 150 traces of dV/dI as a color map of dV/dI in the B-I plane.

In a superconductor, the magnetic flux is quantized in units of the superconducting flux quantum ϕ_0. Usually, bulk measurements on a large crystal cannot resolve individual flux quanta; this would require special geometries such as submicrometer junctions or rings. Surprisingly, the color map in $MoTe_2$ (Fig. 1A, sample S1) reveals a critical current $I_c(B)$ that oscillates versus B with a scalloped profile suggestive of flux quantization; we call these oscillations the fast mode. In addition, there exists a slow mode that arises from Fraunhofer

[1]Department of Physics, Princeton University, Princeton, NJ 08544, USA. [2]Department of Chemistry, Princeton University, Princeton, NJ 08544, USA.
*Present address: Zitan Technologies, Tahoe Boulevard, Incline Village, NV 89450, USA.
†Corresponding author. Email: npo@princeton.edu

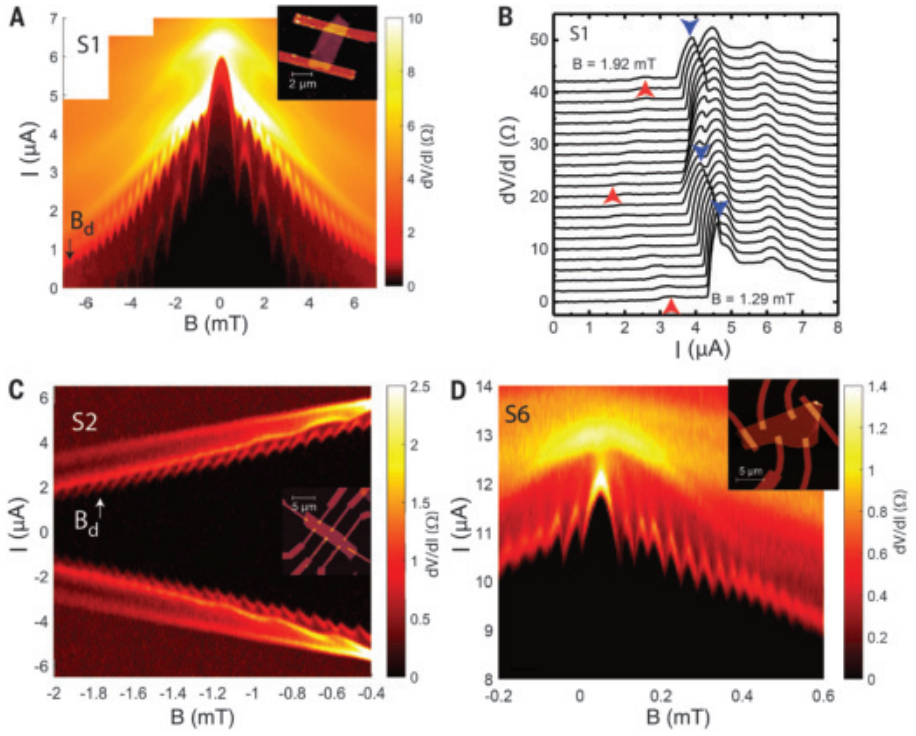

Fig. 1. Critical current maps in the Weyl superconductor $MoTe_2$. Shown are color maps of *dV/dI* versus *I* and *B* taken at *T* = 20 mK. (**A**) In sample S1, two oscillation modes are resolved. The fast mode, arising from amplitude modulation of an edge supercurrent, is observed as the scalloped boundary of the low-dissipation region. The slow mode, associated with the bulk supercurrent, displays the usual Fraunhofer diffraction pattern. (**B**) Shown are 22 traces of *dV/dI* versus *I* (shifted for clarity) taken in sample S1 in steps of 30 μT starting at 1.29 mT. Prominent peaks (blue arrows) track the fast mode, whereas the weak peaks (red arrows) track the slow mode. (**C** and **D**) In large-area crystals [samples S2 and S6 in (C) and (D), respectively], the fast mode is evident, whereas the slow mode is unresolved. (Insets) The Au contacts evaporated on each crystal. Arrows in (A) and (C) indicate the dephasing field B_d.

diffraction. The traces of *dV/dI* within a field interval comprising two periods of the fast mode are displayed in Fig. 1B. The large peaks (Fig. 1B, blue arrows) trace out the scalloped boundary, whereas the weaker peaks (Fig. 1B, red arrows) trace out the Fraunhofer diffraction pattern. In the color maps for two large-area samples S2 and S6 (Fig. 1, C and D, respectively), the fast mode is strikingly evident as the scalloped boundary surrounding the entire dissipationless region, whereas the slow mode is unresolved. We express the fast-mode frequency $f_1 = 1/\Delta B_1$ (where ΔB_1 is the period) in terms of the flux-penetration area $A_\phi \equiv f_1\phi_0$.

The slow mode displaying the familiar Fraunhofer diffraction pattern reflects the phase of the bulk supercurrent J_s^b, which winds at a frequency $f_2 = 1/\Delta B_2$ that is insensitive to the crystal area A_{phys} (fig. S3). The conditions that favor observation of either the slow mode (fig. S5) or the fast mode (fig. S6) are described in (*13*), section 3.

Hereafter, we focus on f_1 to show that the fast mode originates from an edge supercurrent J_s^e. As shown in Fig. 2A, f_1, expressed through A_ϕ, scales as $A_\phi = \eta(B)A_{phys}$ across five samples. The fraction $\eta(B)$ expresses the degree of flux penetration. In the Fig. 2A plot, the black symbols and black dashed line refer to the weak-field limit ($B < 1$ mT). Already in this limit, $A_\phi = f_1\phi_0$ scales linearly with A_{phys} with $\eta(B \sim 0) = 0.35$.

Inspection of f_1 reveals that it increases gradually with *B*. This chirp effect reflects increasing flux penetration (on the scale of the Pearl length $\Lambda = 2\lambda^2/d$, where λ is the London length). As indicated by the broad arrows and the red symbols in Fig. 2A, A_ϕ in each sample increases monotonically, reaching its physical area A_{phys} well before *B* reaches the critical field B_c. The plot of f_1 versus *B* for sample S1 in Fig. 2B shows that it saturates when *B* exceeds 6 mT. In all samples, $\eta(B \to B_c) \to 1$ but does not exceed 1. The partial screening implies that J_s^b is not confined to a monolayer, but extends over the entire crystal volume.

As shown in Fig. 2A, f_1 tracks the flux quanta as A_{phys} is increased ninefold at fixed *B* and also as $B \to B_c$ at fixed A_{phys}. Both trends suggest fluxoid quantization within a closed loop defined by J_s^e. We assume J_s^e flows along the side wall (of depth *d*) encircling the crystal, with a width δ_e (Fig. 2C), which we then estimated. A finite δ_e leads to a spread in the area $\Delta A_{phys} = \delta_e L_p$ and a phase uncertainty $\delta\varphi = 2\pi(\delta_e L_p/\phi_0)B$, where L_p is the crystal perimeter. Complete dephasing of the fast mode occurs (at the dephasing field B_d) when $\delta\varphi \to \pi$; $B_d = 0.6B_c$ to $0.8B_c$ is fixed by the experimental resolution (Fig. 1, A and C, arrows; and fig. S9). This yields $\delta_e = \phi_0/(2B_dL_p)$. From the observed $B_d = 7$ mT in sample S1 (1.8 mT in sample S2), we found $\delta_e < 10$ nm ($\delta_e \sim 1/200$ of the crystal width *w*). In the largest sample S6, the dephasing effect is especially clear (fig. S9).

To make the case for fluxoid quantization [(*13*), section 5], we assume that the edge condensate is described by a Ginzburg Landau (GL) wave function ($\hat{\Psi}_e$) distinct from that describing the bulk ($\hat{\Psi}_b$). The quantization of fluxoids within an enclosed area causes the edge superfluid velocity $\mathbf{v}_s$ to vary as $v_s = (2\pi\hbar/m^*L_p)(n - \phi/\phi_0)$, where $\hbar$ is Planck's constant $\hbar$ divided by 2π, m^* is the GL mass, and $n \in \mathbb{Z}$ (*13*). This leads to a set of free-energy branches $\Delta f_n(\phi)$, each centered at $\phi = n\phi_0$ (Fig. 2D). At an intersection, the system jumps between branches, leading to a sawtooth profile for $v_s(\phi)$. The result is a characteristic scalloped profile for the square of the wave function amplitude $\Psi_e^2 \equiv |\hat{\Psi}_e|^2$ which we write as

$$\Delta\Psi_e^2/\Psi_e^2 = -\mathcal{P}\,(n - \phi/\phi_0)^2,$$

$$\left(n - \frac{1}{2} < \phi/\phi_0 < n + \frac{1}{2}\right) \qquad (1)$$

with the prefactor $\mathcal{P} = (2\pi\xi)^2/L_p^2$, where ξ is the GL length [(*13*), section 5].

In the classic Little Parks (LP) experiment (*17*, *18*), the relative change corresponding to Eq. 1 is observed as a shift $\delta T_c(\phi)$ very near T_c (where the amplitude $\Psi_b = |\hat{\Psi}_b| \to 0$). Our experiment, performed at $T = T_c$, falls in a different regime; to drive both amplitudes Ψ_e and $\Psi_b \to 0$, we applied *I* close to I_c. The narrow width δ_e of the edge GL wave function $\hat{\Psi}_e$ renders it less susceptible than $\hat{\Psi}_b$ to field suppression as *I* approaches the boundary $I_c(B)$. Hence, the edge J_s^e carries an increasing share of *I*. At the boundary, $I_c \sim \Psi_e^2$ acquires the profile in Eq. 1, $\Delta I_c \sim \Delta\Psi_e^2$ (eq. S14).

Equation 1 predicts that the oscillation amplitude ΔI_c decreases steeply as $1/L_p^2$. We confirm that the observed decrease is consistent with the prediction (fig. S8). The model also explains a striking observation. As seen in samples S1, S2, and S6 in Fig. 1, the fast-mode minima occur high above the horizontal axis, $I = 0$, whereas the slow mode minima in S1 (also V2 in fig. S5) reach nearly to zero. This occurs because the former arises from a weak modulation of the amplitude squared $\Delta\Psi_e^2$, whereas the latter derives from phase winding.

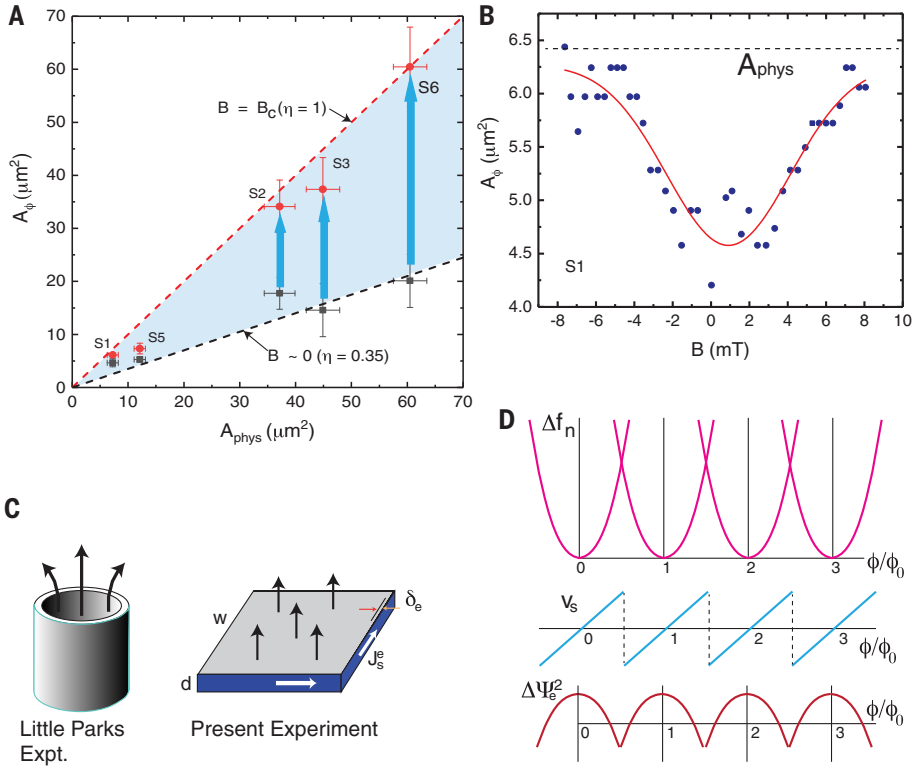

Fig. 2. Area scaling, frequency chirp, and scalloped profile. (**A**) Variation of the flux penetration area $A_\phi = \eta(B)A_{phys}$ in five samples measured at T = 20 mK, where $\eta(B)$ is the fraction of flux penetration in field B. In weak B, the data (black symbols) fall on the line with $\eta(B\sim 0) = 0.35$ (black dashed line). As B increases, $\eta(B)$ in each sample increases toward 1 (broad arrows). At the red circles, B equals 7.6, 1.1, 1.5, 3.6, and 0.6 mT in samples S1, S2, S3, S5, and S6, respectively. (**B**) The increase in A_ϕ versus B (in sample S1) saturates for $B > 6$ mT ($B_c \approx$ 10 mT). The red curve is a Gaussian fit. The dashed line indicates A_{phys}. (**C**) Sketch of fluxoids (black arrows) trapped in a superconducting cylinder in the Little Parks experiment (*21*) (left) and by the edge supercurrent J_s^e (white arrows) in $MoTe_2$ (right). The width δ_e of J_s^e is shown. (**D**) Changes in the superfluid kinetic energy lead to a set of branches of the free energy Δf_n, each centered at $\phi = n\phi_0$. Jumps between intersecting branches result in a sawtooth profile for v_s and oscillations in the edge condensate amplitude squared $\Delta\Psi_e^2$, observed as a characteristic scalloped boundary in the critical current $I_c(B)$.

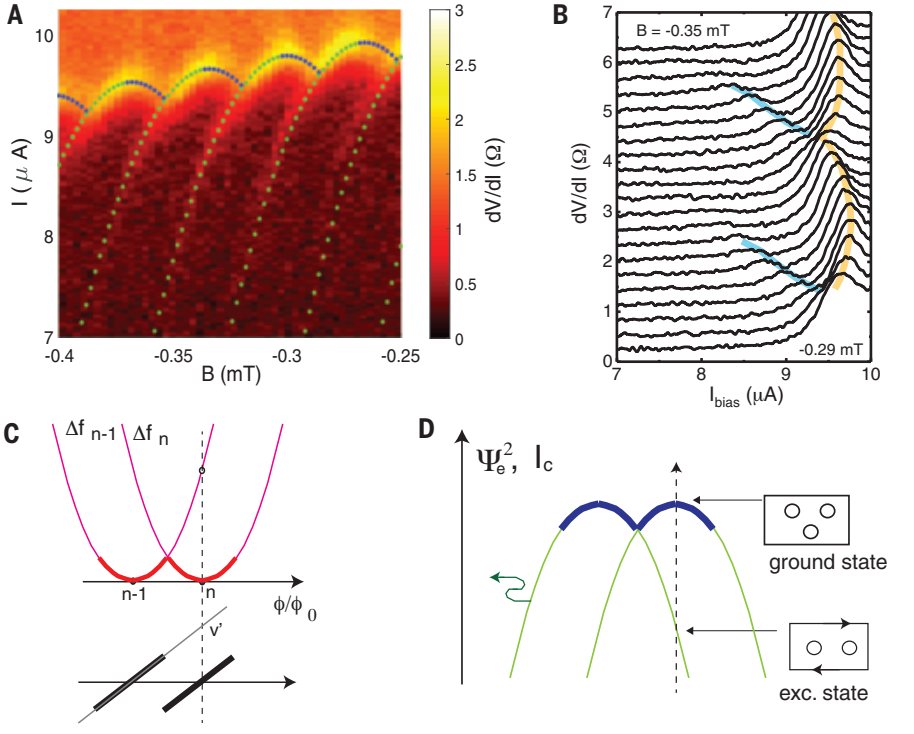

Fig. 3. Emergence of excitation branches. (**A**) High-resolution color map of dV/dI curves showing weak excitation branches trailing from each minimum in the scalloped boundary. The data are obtained at 20 mK in sample S6 with $B < 0$ and $I > 0$. Green dots represent fits to Eq. 1. (**B**) Shown are 21 traces of dV/dI versus I in the interval $-0.29 < B < -0.35$ mT (shifted vertically for clarity). The scalloped boundary (yellow curve) is traced by the large peak. At each cusp, a weak peak emerges and branches off to the left to trace out an excitation branch (blue curve). (**C**) Schematic plots of Δf_n and Δf_{n-1} (magenta parabolas) and the sawtooth profile of v_s. The corresponding curves of Ψ_e^2 are plotted in (D) (green parabolas). Bold blue arcs represent the scalloped boundary of $I_c(B)$. With ϕ fixed at $n\phi_0$ (dashed lines), the system occupies the lowest-energy branch, with $n = 3$ fluxoids and $v_s = 0$. When I is scanned at fixed B, the excited state (with 2 fluxoids and a large v'_s) is encountered at a current smaller than $I_c(B)$. This is observed as the excitation branch.

Next, we turned to a feature not observed in the LP experiment. The curves of Δf_n suggest that at low T, it is possible to detect excited states. Using high-resolution scans, we have resolved weak excitation branches trailing from the scalloped boundary (Fig. 3A). As shown by the green dots in Fig. 3A, the branches fit well to Eq. 1. The excitations are also directly visible in individual traces of dV/dI versus I (Fig. 3B). The large peak traces out the arcs of the scalloped boundary (Fig. 3B, yellow curve). At the cusp, a small peak (20× to 30× weaker in strength) emerges and traces out an excitation branch (Fig. 3B, blue curve). These excitations are also seen in sample S2 (fig. S9).

Our scenario for the excitation branch is sketched in Fig. 3, C and D. When ϕ is fixed at $n\phi_0$ (Fig. 3C, dashed line), the system lies at

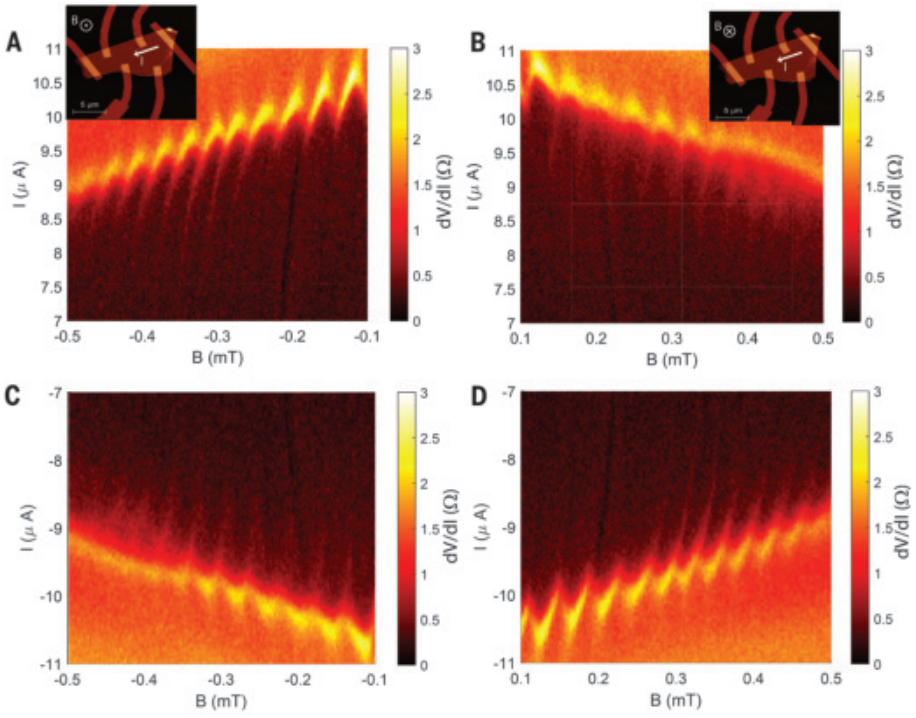

Fig. 4. Symmetry breaking in the excitation branches. Shown are the data for sample S6. (**A**) The color map is measured at 20 mK with $B < 0$ (inset) and $I > 0$ (flowing right to left). The observed excitation branches flow to the left (increasing $|B|$). (**B**) If B is reversed keeping $I > 0$ (inset), the excitation branches flow left, toward decreasing $|B|$, although the pattern is less sharply resolved than in (A). (**C**) If $B < 0$ and $I < 0$, the color map is similar to that in (B) except for the reversal in I. (**D**) For $B > 0$ and $I < 0$, we recover the color map from (A). The symmetry breaking follows the sign of the product $I \cdot B$. For $I \cdot B > 0$ [(B) and (C)], the branches flow toward decreasing $|B|$, whereas for $I \cdot B < 0$, the flow is toward increasing $|B|$ [(A) and (D)]. In (A) to (D), the patterns are nonhysteretic and independent of field-sweep direction. Sample S2 shows a similar symmetry breaking (*17*).

the minimum of Δf_n (Fig. 3C, magenta curves). Accordingly, the ground state has $v_s = 0$ with n fluxoids. The intersection of the branch Δf_{n-1} with the dashed line defines an excited state with $n - 1$ fluxoids and a large superfluid velocity v'_s. Expressed in terms of Ψ_e^2 (equivalently I_c), the free energy minima become the scalloped boundary (Fig. 3D, bold curves). As I is increased (along the Fig. 3D dashed arrow), we encounter the excited state at a value of I [$<I_c(B)$] that varies with ϕ, as in Eq. 1.

Last, we discuss an asymmetry exhibited by these branches. In Fig. 3A, branches that flow outward (toward increasing $|B|$) are observed, whereas branches flowing inward are conspicuously absent. As shown in Fig. 4, the flow direction is sensitive to the signs of I and B. Figure 4A, with outflowing branches, depicts the situation already discussed ($I > 0$, $B < 0$). When we reverse the sign of B (keeping $I > 0$) (Fig. 4B), the branches flow toward decreasing $|B|$ but are less clearly resolved. Likewise, in Fig. 4C ($I < 0$, $B < 0$), the flow is toward decreasing $|B|$. Last, with $I < 0$ and $B > 0$ (Fig. 4D), we recover the pattern in Fig. 4A. Empirically, we conclude that the branches flow outward if the product $I \cdot B < 0$ (Fig. 4, A and D), whereas they flow inward if $I \cdot B > 0$ (Fig. 4, B and C). The pattern favors one circulation of v_s over the other (but respects time-reversal invariance). These symmetry patterns, lying beyond the scenario discussed above, require the role of spin-orbit coupling and other topological properties of the edge modes to be better understood.

Aside from the symmetry breaking, the nature of pairing of edge excitations—what protects the edge condensate against hybridization with the bulk—and the role played by hinge states (*19*) are issues that invite further investigation. More broadly, this method may be extended to explore other topological superconductors (*1*–*3*) and chiral superconductors (*20*, *21*).

REFERENCES AND NOTES

1. L. Fu, C. L. Kane, *Phys. Rev. Lett.* **100**, 096407 (2008).
2. X.-L. Qi, T. L. Hughes, S. Raghu, S.-C. Zhang, *Phys. Rev. Lett.* **102**, 187001 (2009).
3. L. Fu, E. Berg, *Phys. Rev. Lett.* **105**, 097001 (2010).
4. S. Uchida, T. Habe, Y. Asano, *J. Phys. Soc. Jpn.* **83**, 064711 (2014).
5. H. Wei, S.-P. Chao, V. Aji, *Phys. Rev. B Condens. Matter Mater. Phys.* **89**, 014506 (2014).
6. G. Bednik, A. A. Zyuzin, A. A. Burkov, *Phys. Rev. B Condens. Matter Mater. Phys.* **92**, 035153 (2015).
7. T. Zhou, Y. Gao, Z. D. Wang, *Phys. Rev. B* **93**, 094517 (2016).
8. K. A. Madsen, E. J. Bergholtz, P. W. Brouwer, *Phys. Rev. B* **95**, 064511 (2017).
9. Y. Li, F. D. M. Haldane, *Phys. Rev. Lett.* **120**, 067003 (2018).
10. A. A. Soluyanov *et al.*, *Nature* **527**, 495–498 (2015).
11. Z. Wang *et al.*, *Phys. Rev. Lett.* **117**, 056805 (2016).
12. Y. Qi *et al.*, *Nat. Commun.* **7**, 11038 (2016).
13. Materials and methods are available as supplementary materials.
14. H. B. Heersche, P. Jarillo-Herrero, J. B. Oostinga, L. M. K. Vandersypen, A. F. Morpurgo, *Nature* **446**, 56–59 (2007).
15. S. Hart *et al.*, *Nat. Phys.* **10**, 638–643 (2015).
16. V. S. Pribiag *et al.*, *Nat. Nanotechnol.* **10**, 593–597 (2015).
17. W. A. Little, R. D. Parks, *Phys. Rev. Lett.* **9**, 9–12 (1962).
18. M. Tinkham, *Introduction to Superconductivity* (Dover, 2004), chap. 4.
19. Z. Wang, B. J. Wieder, J. Li, B. Yan, B. A. Bernevig, *Phys. Rev. Lett.* **123**, 186401 (2019).
20. D. A. Ivanov, *Phys. Rev. Lett.* **86**, 268–271 (2001).
21. J. R. Kirtley *et al.*, *Phys. Rev. B Condens. Matter Mater. Phys.* **76**, 014526 (2007).
22. P. Ong, Data for observation of an edge supercurrent in the Weyl superconductor $MoTe_2$. Harvard Dataverse (2020);

ACKNOWLEDGMENTS

We thank B. A. Bernevig, B. I. Halperin, A. Yacoby, and A. Yazdani for valuable discussions. **Funding:** The research was supported by the U.S. Army Research Office (W911NF-16-1-0116). The dilution refrigerator experiments were supported by the U.S. Department of Energy (DE- SC0017863). N.P.O. and R.J.C. acknowledge support from the Gordon and Betty Moore Foundation's Emergent Phenomena in Quantum Systems Initiative through Grants GBMF4539 (N.P.O.) and GBMF-4412 (R.J.C.). The growth and characterization of crystals were performed by F.A.C. and R.J.C., with support from the National Science Foundation (NSF MRSEC grant DMR 1420541). **Author contributions:** W.W., S.K., and M.L. jointly prepared the devices and performed all measurements. The detailed analyses were carried out by W.W., S.K., and N.P.O. The crystals were provided by F.A.C. and R.J.C. The manuscript was written by N.P.O., W.W., and S.K. **Competing interests:** The authors declare no competing interests. **Data and materials availability:** All data are archived in Dataverse (*22*).

SUPPLEMENTARY MATERIALS

science.sciencemag.org/content/368/6490/534/suppl/DC1
Materials and Methods
Supplementary Text
Figs. S1 to S10
Table S1
References (*23*, *24*)

6 February 2019; resubmitted 22 August 2019
Accepted 27 March 2020
10.1126/science.aaw9270

HIGH-LEVEL GLOBAL TALENTS RECRUITMENT

2020 Global Online Job Fair (www.edu.cn/cv)

May 08, 2020 North Area of East China Doctoral Talents Recruitment

May 09, 2020 Hong Kong, Macao, Taiwan and the China Great Bay Area Doctoral Talents Recruitment

May 15, 2020 High-level Global Talents Recruitment

Qualification for Applicants

Global scholars, Doctor and Post-doctor

Key Disciplines

Life Sciences, Health Sciences and Physical Sciences

Participating Approach

Please send your CV to consultant@acabridge.edu.cn for 2020 Global Online Job Fair

Scan to check the sessions

EVEN SEPARATED BY MOUNTAINS AND RIVERS, WE HAVE OUR BLOOD TIGHTLY CONNECTED

The Coronavirus pandemic has forced many of us to consider different ways of working and communicating. Chinese universities and colleges are now holding online job fairs to help overseas scholars explore career options in China.

Fight with One Heart to Combat COVID-19

In these challenging times, Chinese universities and colleges have shot videos, sending greetings and wishes to their overseas compatriots. Please scan below QR code to receive messages of love and well wishes from high schools in your motherland.

Overseas Chinese Scholars' Visit to Top Chinese Universities

Check the Details from www.edu.cn/zgx

- 10,000+ academic job vacancies in China
- Free one-to-one consultation service

Send your CV to consultant@acabridge.edu.cn

上海师范大学

中国石油大学

中南民族大学

ScienceCareers online @sciencecareers.org

SPECIAL JOB FOCUS:

Biotechnology

Issue date: May 22
Book ads by May 7

Ads accepted until May 15 if space allows

Deliver your message to a global audience of targeted, qualified scientists.

129,566
subscribers in print every week

33,295
yearly unique active job seekers searching for biotechnology jobs

16,250
yearly applications submitted for biotechnology positions

What makes *Science* the best choice for recruiting?

- Read and respected by 400,000 readers around the globe
- Your ad dollars support AAAS and its programs, which strengthens the global scientific community.

Why choose this job focus for your advertisement?

- Relevant ads lead off the career section with a special biotechnology banner.

Expand your exposure by posting your print ad online:

- Additional marketing driving relevant job seekers to the job board.

To book your ad, contact:
advertise@sciencecareers.org

The Americas
202 326 6577
Europe
+44 (0) 1223 326527
Japan
+81 3 6459 4174
China/Korea/Singapore/ Taiwan
+86 131 4114 0012

Science Careers
AAAS
SCIENCECAREERS.ORG

Produced by the *Science*/AAAS Custom Publishing Office.

FOR RECRUITMENT IN SCIENCE, THERE'S ONLY ONE *SCIENCE*.

Who's the Top Employer for 2019?

Science Careers' annual survey reveals the top companies in biotech & pharma voted on by *Science* readers.

Read the article and employer profiles and listen to podcasts at sciencecareers.org/topemployers

Neuroscience Postdoctoral Programme

Linköping University is one of Sweden's six large universities, currently enrolling 27,000 students. The Centre for Systems Neurobiology involves some 50 independent research groups, from the Faculty of Medicine and the Faculty of Science and Engineering, as well as the University Hospital.

The Centre for Systems Neurobiology is now seeking Postdoctoral Fellows within several neuroscience research areas: Animal behavior/Behavioral genetics (Per Jensen), Basic and translational psychiatric neuroscience (Rebecca Böhme, Paul Hamilton, Markus Heilig) Ion channel biophysics and pharmacology (Sara Liin, Antonios Pantazis), Neurodegenerative disease (Martin Hallbeck, Walker Jackson), Neuroendocrinology/ neuroimmunology (Anders Blomqvist, David Engblom), Neurophysiology and clinical neuromodulation (Magnus Thordstein), Sensory and cognitive systems (Anders Fridberger, Kajsa Igelström, Håkan Olausson, Mary Rudner), Stress and affective processing (Leah Mayo). Applications will be reviewed continuously.

For full consideration please apply as soon as possible.

LINKÖPING UNIVERSITY

For more details regarding the Centre, the different research labs involved in the programme, and to submit a letter-of-intent please go to: https://liu.se/en/research/center-for-systems-neurobiology. For information regarding the university and the region, please go to: liu.se, eastsweden.com.

SOMETIMES THE GRASS REALLY IS GREENER SOMEPLACE NEW.

Find your next job at ScienceCareers.org

There's scientific proof that when you're happy with what you do, you're better at what you do. Access career opportunities, see who's hiring and take advantage of our proprietary career-search tools. Get tailored job alerts, post your resume and manage your applications all in one place: sciencecareers.org

ScienceCareers
FROM THE JOURNAL SCIENCE AAAS

By **Anouschka Foltz**

Clocking your work

Four months into my second faculty job, I was shocked to discover that I had to record the hours I'd worked. I'd heard that others at the university were required to do that—but surely not faculty members, I thought. I was wrong. At the end of each month, I was expected to sign and submit a sheet that listed my start and end times each day. At first, I was annoyed that I had to waste my time on such a mundane task. But the practice of writing down my work hours was surprisingly illuminating, ultimately sending me down a path to better work-life balance.

In my previous 16 years in academia, it had been up to me to judge whether I was working hard enough. Usually, I felt I needed to work harder.

During my Ph.D., I always believed I could make my dissertation better with extra effort. My research never felt finished, and I had no idea how many hours I was supposed to work. That made it easy to go down rabbit holes and work more hours than necessary.

After graduating, I continued to work long hours, even though my employment contracts spelled out shorter workweeks. During my postdoc years, I was supposed to work precisely 39.5 hours per week, according to the labor agreement for public servants in Germany. But nobody asked how long I actually spent in the office, and I probably exceeded that on a regular basis.

"The data have completely altered my view of work-life balance."

When I started my first faculty position, my contract stated that I work anywhere from 36 to 48 hours per week. At first, I appreciated the flexibility, hoping for the occasional guilt-free 36-hour workweek. But my teaching and administrative workloads were so high that I regularly reached the 48-hour mark.

I was conscious of my work hours. I kept track mentally and made a point of taking some time off when I felt as though I'd worked too hard. But there were stretches of time during my first faculty job when my children didn't see me enough, or when—between work and parental duties—I had no time to spend with my husband.

In my second faculty position, I expected that my work hours would again be my business. So when I was told to track them, I was surprised. My contract stated that I work 40 hours per week, and couldn't I be trusted to do so?

Grudgingly, I opened a spreadsheet and started to record my hours. It would have been easy to add standard start and end times for each day—for instance, 9 a.m. to 5 p.m.—and be done with it. But my scientific tendencies kicked in, and I decided to keep careful track of my hours, even noting breaks.

I'm glad I did, because the data have completely altered my view of work-life balance. Recording my hours showed that I was racking up much longer workweeks than I realized. During the first month I started to track, for instance, I worked 15 hours more than was required of me—nearly two full workdays. That's far less than the insane hours that some academics work. But it was eye-opening for me.

With my tracking, I've found that I generally accumulate 1 week of overtime every 2 to 3 months. So now, every time I reach that milestone, I take a few days or even a whole week off. I spend that time at home with my family. Or I use the days to take a longer vacation, or to spend more time with relatives who visit. The breaks have improved my overall happiness and job satisfaction.

The data also help alleviate any guilt that I may have otherwise felt taking time off. I still have deadlines, tenure requirements, and the pressure to publish papers. And I still work a lot, sometimes even on weekends. But I now know how much I work—and that I deserve the time off.

When I am tenured, I won't have to submit my hours to my university any longer. But I'm going to continue to track them to help keep my work in bounds. To some academics, it may seem like a waste of time. But for me, it's been anything but.

I'd recommend opening a spreadsheet and tracking the hours that you spend at work. Even if you only do it for 1 or 2 weeks, you might be surprised what you'll discover. ■

Anouschka Foltz is an assistant professor at the University of Graz in Austria. Send your career story to SciCareerEditor@aaas.org.

ILLUSTRATION: ROBERT NEUBECKER

ScienceSignaling.org

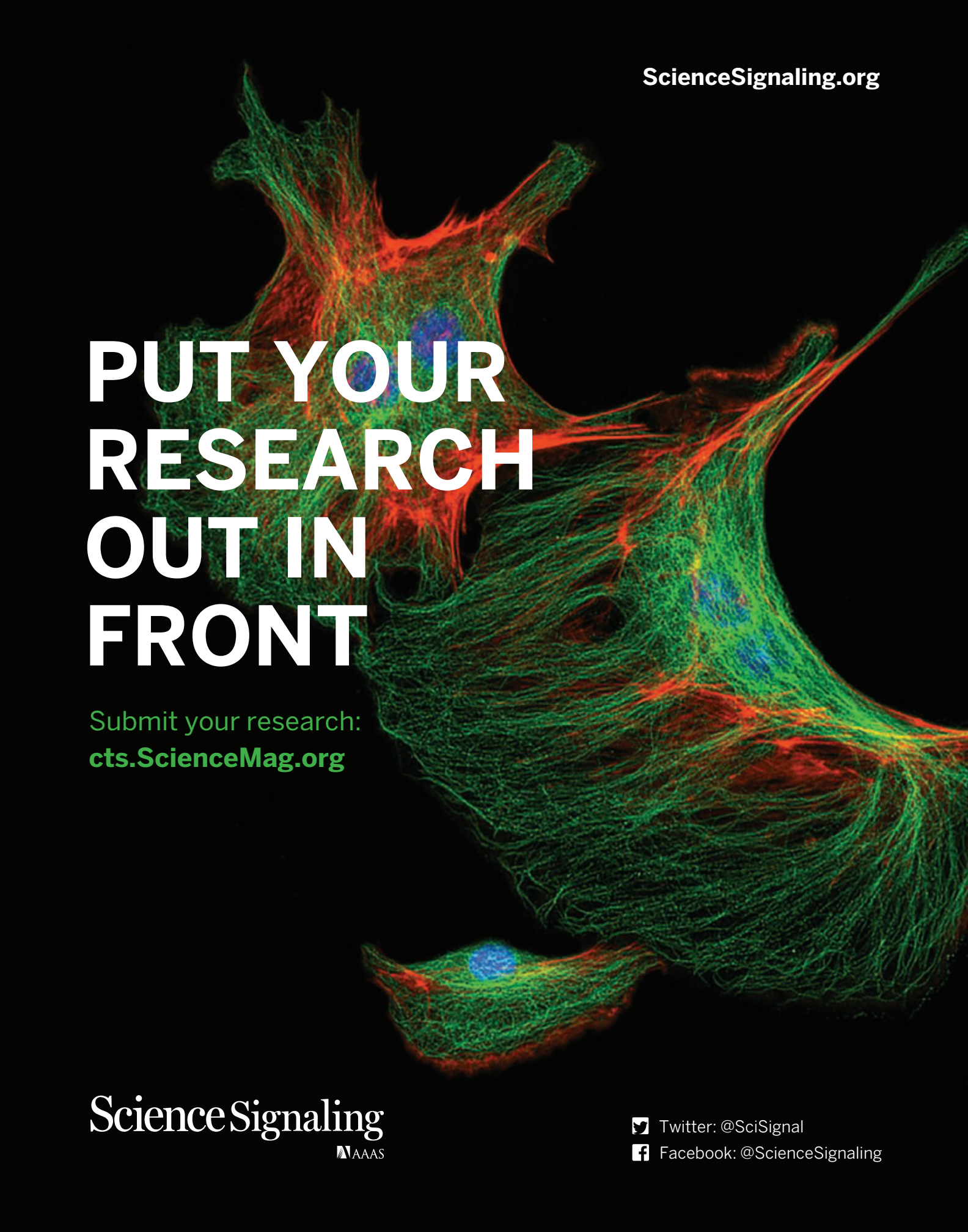

PUT YOUR RESEARCH OUT IN FRONT

Submit your research:
cts.ScienceMag.org

Science Signaling
AAAS

Twitter: @SciSignal
Facebook: @ScienceSignaling

Custom Protein Expression

Accelerate your scientific discovery

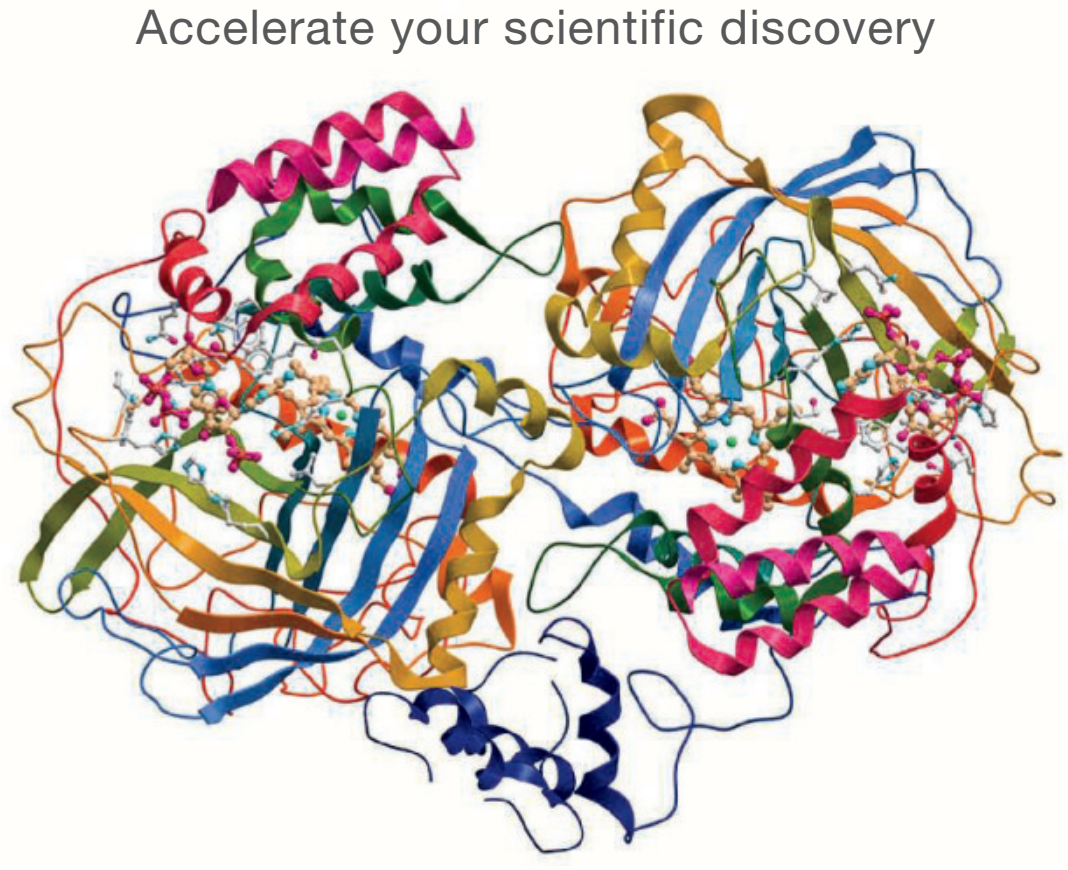

ProMab Biotechnologies offers an all in one platform for recombinant protein expression across multiple expression systems. From gene synthesis, addition of a protein/peptide tag of your choice, to large scale protein purification, ProMab has over 15 years of extensive CRO experience in developing proteins for academia and the pharmaceutical industry. Utilize ProMab's capabilities to accelerate your scientific discovery today.

ProMab's Advantages

Multiple Expression Systems:

- Mammalian
- Insect
- Bacterial
- Yeast

- Customizable protein/peptide synthesis
- Large scale production and purification
- Stable cell line development
- Quick turnaround time
- Dedicated technical support
- Downstream to antibody production

Additional services available.

All products are for research only

Discover more | www.promab.com

ProMab Biotechnologies, Inc.
2600 Hilltop Dr, Building B, Richmond, CA 94806
1.866.339.0871 | info@promab.com